Synthesis and characterization of Nano-sized Spinel and Orthoferrites and their application as Liquefied Petroleum Gas Sensor

THESIS SUBMITTED FOR THE AWARD OF THE DEGREE OF

Doctor of Philosophy

in

Applied Physics

by

Monika Singh
M.Sc.
Enrollment No. 595/11

Under the Supervision of

Dr Bal Chandra Yadav

DEPARTMENT OF APPLIED PHYSICS

SCHOOL FOR PHYSICAL SCIENCES

BABASAHEB BHIMRAO AMBEDKAR UNIVERSITY,

LUCKNOW-226025, U.P., INDIA

August 2017

DECLARATION

I hereby declare that the thesis entitled **"Synthesis and characterization of Nano-sized Spinel and Orthoferrites and their application as Liquefied Petroleum Gas Sensor"** has been prepared by me under the supervision of Dr Bal Chandra Yadav, Associate Professor, Department of Applied Physics, School for Physical Sciences, Babasaheb Bhimrao Ambedkar University, Lucknow. No part of this thesis has formed the basis for the award of any degree, diploma or fellowship previously. Further, I declare that the material embodied in the present work is based on original research work and the indebtedness to others has been duly acknowledged at relevant places.

Date: 25/08/2017

Place: Lucknow

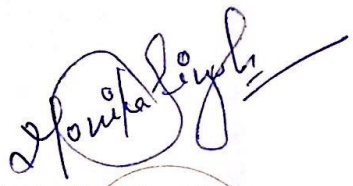

(Monika Singh)

Department of Applied Physics,

School for Physical Sciences,

Babasaheb Bhimrao Ambedkar University, Vidya Vihar,

Raebareli Road, Lucknow-226025, U.P., India

DEDICATED TO MY PARENTS AND MY FAMILY

CERTIFICATE

This is to certify that the thesis titled **"Synthesis and characterization of Nano-sized Spinel and Orthoferrites and their application as Liquefied Petroleum Gas Sensor"** submitted by Ms Monika Singh is an original research work and has not been previously submitted in part or full for the award of any other degree or diploma to this or any other university.

The thesis submitted to Babasaheb Bhimrao Ambedkar University, Lucknow satisfies all the requirements as stipulated in the *Doctor of Philosophy (Ph.D.) regulations-1999* as amended in *2008/2010/2013* and it is fit for submission and evaluation for the award of the degree of Doctor of Philosophy of the University.

B Yadav 28/08/2017

Date: 25/08/17 Supervisor

Dkumar 28/8/17

Head of the Department

ACKNOWLEDGEMENT

It is my great pleasure to express my gratitude and sincere thanks to my guide **Dr Bal Chandra Yadav,** who selflessly encouraged me to believe in myself and give a fruitful contribution in the research area. He is not only a generous personality but also an ocean of knowledge who always motivated his students as a mentor, as a parent and as a friend to do challenging and independent research work with great enthusiasms and hard work. I take this opportunity to place on record my heartfelt and sincere gratitude and deep indebtedness to him without whose guidance this work could not have been meaningfully concluded.

I am extremely thankful to Head of the Department **Dr Devesh Kumar** for all administrative support and moral support. I am very thankful to my teachers **Dr Ramesh Chandra, Dr A. K. Yadav, Dr Khem Bahadur Thapa, Mr Devendra Singh** and Lab staffs at Babasaheb Bhimrao Ambedkar University, for providing friendly and motivating environment during the course of this work.

I am thankful to **Dr Sarita Yadav** who constantly keeps a keen interest in my work and patiently helped me in thesis writing. I am very thankful to my junior **Mr Utkarsh Kumar** for always being so supportive in the lab throughout my experimental work.

I gratefully acknowledge to DAE-BRNS, Govt. of India for financial support in the form of the project, grant vide sanction number 2013/34/27/BRNS/2693. **Dr Manmeet Kaur,** senior scientist and others **Dr S.K. Gupta, Dr Shobhit Bhatacharya, Dr Niranjan** of Technical Physics Department, Bhabha Atomic Research Centre (BARC) Mumbai, MH, India are also highly acknowledged for providing the facilities available in the department. I am also obliged to **Dr Subodh Kumar**, BSIP, Lucknow and **Mr Ambrish Malaya,** senior project assistant, Indian Institute of Technology, Kanpur, Uttar Pradesh for technical help in obtaining micrographs. **Mr**

Rohtash Kumar, Research Scholar, JNU, Delhi for Raman Analysis. I am thankful to **Mr Totan Halder**, Research Scholar, Pondicherry University for helping in the characterization of samples.

I am very thankful to my senior **Dr Richa Srivastava, Dr Ravikant Tripathi, Dr Ravindra Kumar, Dr. Rakesh Sonker, Mr Saroj Radheysham and Dr Pranav Upadhyay** for their continuous moral support and encouragement. I would like to thanks **Ms Samiksha Sikarwar, Mr Kuldeep Kumar, Ms Priyanka Chaudhary**, **Ms Ruchi Mishra, Ms Yash Kaur**, **Mr Raj Kamal, Mr Surya, Mr. Ashish Kumar, Mr Ratindra, Mr. Narendra Kumar, Mr Deeptarko Rai** and other lab members for a joyful and healthy environment around me to work and to be with me throughout the work.

Finally, I would like to pay my highest regards to my parents **Shri Arun Pratap Singh** and **Smt. Pratima Singh**, my elder brother **Mr Mohit K Singh**, my sister **Malvika Singh** and my sister in law **Shreshtha Singh**, my younger brother **Mr Rohit K Singh**, my in laws **Mr Anil Kumar Singh** and **Smt. Sarla Singh** and my beloved husband **Mr Rajveer Singh Chauhan** for understanding my dreams and always being the part of my up and down phases of life. At last, I would like to give special thanks to my best friend **Mr Ashok Ranjan** in believing in me and for helping me throughout the experimental work. **.** I also acknowledge to my warden **Dr. Neetu Singh** for being so caring and loving towards me. Finally, I am also thankful to my close friends **Anoop Kumar Singh, Roshni Yadav, Anamika Singh, Shakti Singh, Abhishikta Bhaduri, Banani Kar** for being a part of this journey. I am thankful to all those helping hands that directly and indirectly encouraged me and helped me to complete my research work.

My final words of thanks will be for almighty God, for his constant support and companionship through all turmoil of my life.

Monika Singh

(Research Scholar)

LIST OF PUBLICATIONS

Paper published in the refereed journals:

1. **Monika Singh**, B. C. Yadav, Ashok Ranjan, Rakesh K Sonker, Manmeet Kaur, "Detection of liquefied petroleum gas below lowest explosion limit (LEL) using nanostructured hexagonal strontium ferrite thin film", **Sensors and Actuators B: Chemical** 249, (2017) 96-104. **Impact factor- 5.401**
2. **Monika Singh**, B. C. Yadav, Ashok Ranjan, Manmeet Kaur, S. K. Gupta, "Synthesis and characterization of perovskite barium titanate thin film and its application as LPG sensor", Sensors and Actuators B: Chemical 241, (2016). 1170-1178. **Impact factor - - 5.401**
3. Rakesh K. Sonker, **Monika Singh**, Utkarsh Kumar, B. C. Yadav, "MWCNT doped ZnO nano composite thin film as LPG sensing", Journal of Inorganic and Organometallic Polymers and Materials 26 (6), (2016) 1434-1440 . **Impact factor – 1.577**
4. Richa Srivastava, B. C. Yadav, **Monika Singh**, T. P. Yadav, Synthesis, "Characterization of Nickel Ferrite and Its Uses as Humidity and LPG Sensors", Journal of Inorganic Organomet Polymers and Materials 26(6) (2016) 1404-1412. **Impact factor – 1.577**
5. Satyendra Singh, B. C. Yadav, **Monika Singh**, Richa Kothari, "A review report on nanostructured ferrites as liquefied petroleum gas sensor", International Journal of Science, Technology & Society 1 (1) (2015) 5-21.

Communicated/ published in the refereed journals:

1. **Monika Singh**, Ashok Ranjan, Richa Srivastava B. C. Yadav, Manmeeet Kaur, P.K. Diwedi, "Study of Liquefied Petroleum Gas sensing properties of lead free Bismuth Sodium titanate prepared by sol-gel method" **Sensors and Actuators B: Chemical, Impact factor 5.401**

2. **Monika Singh**, Utkarsh Kumar, B. C. Yadav, Manmeeet Kaur, "Fabrication of pervoskite Lanthanum ferrite film by sol-gel method and its gas sensing properties".**Nanoscale**. **Impact factor 7.2**
3. **Monika Singh**, Utkarsh Kumar, Toton Halder, B.C. Yadav, "Ag substituted Nickel ferrite thin film and its application as LPG sensor below LEL" **Sensors and Actuators B: Chemical**. **Impact factor 5.401**
4. **Monika Singh**, Utkarsh Kumar, B.C. Yadav, "Ag substituted Cobalt ferrite thin film and its application as LPG sensor below LEL" **Sensors and Actuators B: Chemical Impact factor 5.401**
5. V. Manikandan, **Monika Singh**, B.C. Yadav, R.S. Mane, "Structural, dielectric and magnetic properties of Li substituted $CuFe_2O_4$. Journal of Material chemistry and physics of solids". **Impact Factor 2.1**
6. V. Manikandan, **Monika Singh**, B.C. Yadav, R.S. Mane, "Structural, dielectric and magnetic properties of Indium substituted $CuFe_2O_4$ and its gas sensing application". **Impact Factor 2.1**
7. Richa Srivastava, **Monika Singh**, Ruchita Chaudhary, "Gas sensing properties of La dopped Zincferrite". **Sensor Actuator A. Impact factor 2.49**

International Conferences/ workshop

1. **Monika Singh**, Ashok Ranjan, B.C. Yadav, Manmeet Kaur, "Study of Liquefied Petroleum Gas sensing properties of Zr doped Strontium ferrite prepared by sol-gel method" **International Conference on "New Scintillations on materials Horizon" (ICNSMH-2016)** Rohilkhand University, Bareilly, India. OPC-16, (21-23 Oct 2016) 103. Oral.
2. **Monika Singh**, Ashok Ranjan, B.C. Yadav, Manmeet Kaur, S.K. Gupta, "Synthesis and characterization of nano structured Barium titanate via sol-gel method and its application as LPG Sensor" **International Conference on "Plasma Science, Technology and Application 2016".** Amity University, Lucknow. PP-47, (20-21 Jan 2016) 106. Poster.
3. **Monika Singh**, Utkarsh Kumar, B.C. Yadav, "Synthesis and characterization of nanostructured BNT via sol-gel method and its application as LPG sensor"

International Conference on "Environmental systems and Sustainable Development" (15-16 Jan 2016) Pune. Poster

4. **Monika Singh**, Ashok Ranjan, B.C. Yadav, Manmeet Kaur, "Synthesis and characterization of nanostructured barium titanate via sol-gel" "3rd **International Conference on nanostructured materials and nano composites"** (**ICNM 2015**, 12-14 Dec), Mathura. Poster, 179, PP 60.
5. **R.k Sonker, S.R. Sabhajeet, Monika Singh, R. Yadav, R. Kumar, P. Kumar, B.C. Yadav, "**Characterization for NO_2 Gas Sensing Application" International workshop on **Bridging Development Divide for inclusive Growth through Science, Technology and Innovation**, BRIDGES 2015, 16-17 Jan, Lucknow, Pg no. 79.
6. **Monika Singh**, B.C. Yadav**,** "Synthesis and characterization of tin oxide film by sol-gel method and its application as humidity sensor**", International Conference on Nano Science and Nanotechnology-2013**, Poster, PP-317, 275.
7. International workshop on **Bridging Development Divide for inclusive Growth through Science, Technology and Innovation**, BRIDGES 2015, 16-17 Jan, Lucknow.
8. International Symposium on **Advances in Materials characterization**(ISAMC-2014), Lucknow July 2104.

Presentation in National/ Regional Conferences

1. **Monika Singh**, Ashok Ranjan, B.C. Yadav, Manmeet Kaur, S.K.Gupta, "Fabrication of nanostructured strontium ferrite and its application as LPG Sensor", **3rd Lucknow Science Congress and National Conference** on "Science for society: An Interdisciplinary Approach", 31st Oct- 2nd Nov 2015, , PP-48, Pg-81.
2. **Monika Singh**, B.C. Yadav**, "**Sol-gel processed Nanostructured Tin oxide and Zinc oxide as Humidity Sensors"**, 2nd Lucknow Science Congress** "Leveraging Science and Innovation for Development", BBAU, Lucknow, March 27-28, 2014, , PPBS-9, Pg-35.
3. Workshop on **Nano Science and Life**, 26th Feb-2nd March, 2015, B.H.U., India.
4. Workshop on **Nano materials with particular reference to Energy security**, March 11-17, 2014, B.H.U, Varanasi.
5. International workshop on **Innovation and technology** (IITI-2014) transfer to industries: Role of Universities, March 10-11 2014, Lucknow.

SUMMARY

Nanoscale materials are the materials having nanometer dimension and the scientific study of these objects, therefore, refers to the materials with sub nanometer dimension and the scientific study of these objects are known as Nanoscience. Nanoscience deals with the novel phenomenon of preparing, measuring its property and manipulating the dimension of an object up to the order of nanometer scale. Nanotechnology deals with using nanomaterials to develop products for practical application and for miniaturization of electronic devices. Nano-materials are the material of nanometer range and the nanometer order dimension can be achieved by constituting atom or molecule of few Angstrom order i.e. 10^{-10}. Nano-materials show enhanced and extraordinary characteristics from their bulk material [1-2]. It's changing extraordinary properties while size reduction, large surface to volume ratio and its application in different field elucidate the properties of nanomaterial. On the size reduction, the material undergoes several electronic transitions and due to which it shows relatively different property from the bulk material. The inverse relation between the particle size and surface area is a key underpinning in nanoscience world. This is due to the enhanced surface area of the material in comparison to the volume and quantum confinement [5]. The maximum number of atoms lies on the surface of the nanoparticle which possesses huge surface energy and causes unstable or metastable stage. So there is a change in its chemical, mechanical, and optical properties resulting in the increase in the surface area per unit mass. This increased surface area made the nanomaterial for versatile application in electronic and technical industry.

Nanomaterials can be synthesized in many ways in strategy synthesis, nature of synthesis, energy sources, and precursor method.

1. **By synthesis strategy,** there are two methods which are commonly used. Top down and bottom up approaches are the two strategies to synthesize nanoparticles. Top down approach is the one-way approach, in which block of material is taken then it is etched or milled into the desired shape. Carvings done on the pillar and breaking down of a block of rock into the

desired figure is an example of the top-down approach. The bottom-up approach is an analytic and universal approach in which smaller subunits (any atom or molecules) are united to make any useful product. Now in today's era, research is more focused on finding the advance bottom-up technique for synthesizing and characterizing nanomaterials range about 1-100 nm range.

2. **By nature of the process,** there are three types of synthesis method; physical, chemical, and biological method. A physical method is a method in which physical states like size, pores, shape and the phase of the material changes.
3. **On the basis of the energy** used as an input, the synthesis processes are categorized in terms of plasma, laser, electron beam, sputtering, ball milling, combustion, supercritical fluid etc.

4. **Precursor method** is widely used classification based on three phase. It is used to synthesize nanoparticles in the solid phase, liquid phase and gas phase [11].

We have been interested in carrying out our investigations with a new material that possess good sensitivity for the LPG concentration at the lower explosive limit (LEL) and beyond, with properties that are stable over time and thermal cycling after exposure to the various species likely to be present in the ambient. On the basis of a literature survey, I found there is no significant work done in the field of design and development of a LPG sensor operable at room temperature. Ferrites show very good surface reactivity and they have temperature dependent surface morphology. Also, they form composites with other metal oxides very easily. Therefore in this thesis, the synthesis of ferrites and their nanocomposites using soft chemical and mechanochemical routes were carried out. After thorough characterization of synthesized materials, these were employed as LPG sensor. In this thesis, the thorough experimental investigation was carried out in order to develop electrical type LPG sensor using thin/thick films of nanosized spinels and orthoferrites.

Requirements of a LPG Sensor

LPG is a combustible gas and it is widely used as a fuel for domestic heating and industrial use. Although it is one of the extensively used gases, it is hazardous. Hence, it is crucial to detect it in its early stages of the leakage and to perform the active suppression. For designing a robust gas sensor, the sensor material should possess following qualities given as under:

- The material should sensitive in lower explosive limit (LEL) for explosive gases.

- The material should have high sensitivity over a wide range of humidity and temperature.
- It should quickly respond to any fast changes in the ambient.
- The sensor material should have rapid response to the variation of gas concentration and good reproducibility of the electrical signal.
- The sensitivity should be independent of the ambient temperature.
- The material should not react with any chemical contaminants present in the application ambient.
- It should show stable characteristics for a long time.
- It should be less portable.
- The construction of the sensor should preferably be simple using IC technology and of low cost.
- The device should be operated by a battery.

Liquefied Petroleum Gas (LPG) Sensor

An LPG sensor is a chemical sensor which gives variation in its electrical properties when it interacts with the chemical gas species. The normally LPG are of two type propane (C_3H_8) rich in winters and butane (C_4H_{10}) rich in summer. The reason behind this is propane evaporates at –44 ºC and butane evaporate at +5 ºC. Small concentrations of other hydrocarbons may also be present The development of gas sensors in particular combustible gases is imperative due to the concern for safety requirements in homes and for the industry. LPG is extensively used in our country but potentially hazardous gas, because its leakage can cause an accident. So it's detection and monitoring of LPG are necessary for domestic appliances to avoid any mishap-pending. Also, it is very important to detect the leakage at the primary level at the LPG gas cylinder's store. If there is a little leakage of gas and if it catches fire by any means, it begins to burn and these burning starts increasing the temperature. Due to which gas inside the cylinders expand and the great explosion takes place. If leakage has been traced at primary level then such type of disasters can be avoided. Hence to avoid the disasters in houses or stores, reliable and cost effective sensing devices are the basic need of the time.

Material selection for the gas sensor fabrication is an important issue. Nanostructured spinel and orthoferrite oxide materials depicted in Table1, attracted the attention of researchers/scientists due to its larger surface to volume ratio and their adsorption efficiency

towards polar molecule and hydrocarbons on the surface of crystals. The adsorptions are reasonable so that the desorptions may fast and do not produce any structural change to crystallites. Therefore, they would be proven very good sensor materials. Here we have synthesized nanosized spinel and orthoferrite oxides using sol-gel and co-precipitation method and to perform its detail optical and spectroscopic characterizations. Further sensing investigations would be carried out with the exposure of LPG and other gases.

Table 1. Various types of ferrites on the basis of crystal structure are shown in the table.

S.No.	Type	General Formula	Crystal structure	Active sites	Replacement
1.	Spinel ferrite	AB_2O_4	Cubic	[A] & [B]	Mn, Zn, Ni, Mg, Co
2.	Garnet	RFe_5O_{12}	Cubic	a, c, and d	Y, Sm, Eu, Gd, Tb, Dy, Ho, Er, Tm and Lu
3.	Orthoferrite	$RFeO_3$	Perovskite	[A] & [B]	Y, Sm, Eu, Gd, Tb, Dy, Ho, Er, Tm and Lu
4.	Hexa ferrite	$AFe_{12}O_{19}$	Hexagonal	12k,2a,$4f_2$, $4f_1$, 2b	Pb, Sr, Ba

Sensor Parameters/ Sensor Attributes of LPG sensor

For optimizing and the performance of any device, it is necessary to know its sensing parameters. % Sensor response, sensitivity, selectivity, stability, response and recovery times, reproducibility and long-term stability are the operating parameters of a sensing device [84-87].

(i) % Sensor Response

Percentage sensor response of a sensor is defined as the ratio of the difference in the resistance of the film in the air and in presence of gas to the resistance in air.

$$\%\text{SR} = \frac{|R_a - R_g|}{R_a} * 100$$

(ii) Sensitivity

Sensitivity can be defined as the ratio of the magnitude of response of a sensor to a particular target analyte. There are several definitions of sensitivity depending upon the application. It is defined as the ratio of variation in the resistance of the film in the presence of gas and resistance of the film in air.

$$S = \frac{R_g}{R_a}$$

(iii) Response and Recovery Time

The response time of a sensor is defined as the time taken by the sensor to reach 90% of the final response value. Recovery time is defined as the time taken by the sensor to come to 90% value of the final value.

(iv) Reproducibility and Long Term Stability

Reproducibility of a sensor is defined as the efficiency of a sensor to reproduce the same output for the same amount of measuring input. Stability of a sensor is defined as the efficiency of a sensor to generate the same result after a long time without any change in its sensing parameters.

(v) Selectivity

Selectivity may be defined as the sensor response to a particular gas in a mixture of gases. This parameter defines the specific response of the sensor.

Sensing Mechanism of LPG Sensor

The gas sensing mechanism of ferrites based LPG sensor is based on the surface area of the material at which the LPG molecules adsorb and reacts with pre adsorbed oxygen molecules. When the ferrite is exposed to reducing gas like LPG, it reacts with the chemisorbed oxygen. On interaction with the alkanes of LPG, the adsorbed oxygen is removed forming gaseous species and

water. Consequently, the resistance changes, which is due to the change in the width of depletion layer after exposure to LPG. The overall reaction of LPG with the chemisorbed oxygen may take place as shown below:

$$C_nH_{2n+2} + O_2^- \longrightarrow C_nH_{2n}O + H_2O + e^- \text{.....(iii)}$$

Where C_nH_{2n+2} represent the various hydrocarbons. The formation of the barrier is due to a reduction in the concentration of conduction carriers and thereby, results in an increase in resistance of the sensing material with time. As the pressure of the gas inside the chamber increases, the rate of the formation of such product increases and a potential barrier to charge transport becomes strong which has stopped the further formation of water constituting the resistance constant.

The present thesis is divided into seven chapters. Chapter 1 introduces the materials, methods, characterization tools and describes the object of the present investigation. In view of this, the Chapter 1 deals about the nanoscience and nanotechnology of spinel and orthoferrite materials along with the introduction of LPG sensor. Detailed investigation on nanostructured perovskite type Barium titanate thin film with synthesis, characterization and application as LPG sensor is depicted in Chapter 2. In Chapter 3, the synthesis, characterization and LPG sensing properties of nanostructured hexagonal strontium ferrite thin film is described. Chapter 4 reports the study of liquefied petroleum gas sensing properties of lead-free bismuth sodium titanate prepared by the sol-gel method at room temperature. In Chapter 5, fabrication of perovskite lanthanum ferrite film by sol-gel and its gas sensing properties has been demonstrated. Chapter 6 describes the synthesis of porous Ag-substituted $NiFe_2O_4$ which were applied as LPG sensing material and has been demonstrated. A study of synthesis, characterization and LPG sensing properties of perovskite barium titanate, hexagonal strontium ferrite, lead-free bismuth sodium titanate, perovskite lanthanum ferrite and Ag-substituted $NiFe_2O_4$ is summarized in Chapter 7. This chapter also gives the guidelines for further research work in the field of spinel and orthoferrites materials and their applications as LPG sensor. A study of synthesis, characterization and LPG sensing properties of $BaTiO_3$, $SrFe_{12}O_{19}$, $Bi_{0.5}$ $Na_{0.5}TiO_3$, $LaFeO_3$ and Ag-substituted $NiFe_2O_4$ is summarized as below:

Chapter 1 contains an introductory part of ferrites i.e. Spinel and orthoferrite materials including nanoscience and nanotechnology and its application in the various field. It also focuses on the Gas sensor with a detailed description of LPG sensing mechanism and its attribute. Surface morphology with large surface area and more active sites or interstitial site is an important aspect of gas sensing. Adsorption and desorption are the two phenomena which are responsible for whole sensing mechanism.

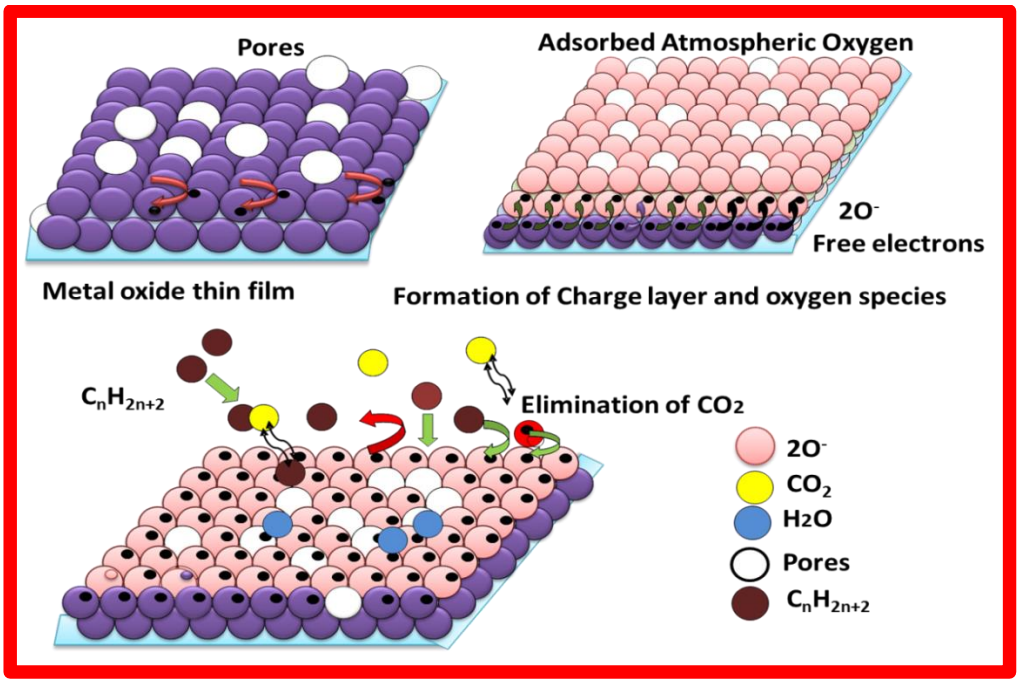

Fig. 1 Sensing mechanism of LPG Sensor

Chapter 2 describes the synthesis and characterization of perovskite Barium titanate thin film and its application as LPG Sensor. In this chapter preparation of nanostructured Barium titanate by the sol-gel method has been presented. The film was prepared by the spin-coating method and further, it was characterized by various characterizing tools. XRD confirmed the perovskite phase of the material. The prepared film was macro-porous which was used as a LPG sensor at room temperature. The sensing characteristic of the film was studied for 0.5 vol. of LPG to 4 vol.% of LPG. The maximum sensitivity was found for 4 vol.% of LPG i.e. 3.50 and % sensor response was found 250.85. Response time was found 30 s and recovery time was found 60 s. The aging effects were also checked after two weeks of sensing and after four weeks and the results were reproducible after this time period also. Graphical Abstract shown in Fig. 2 will give a glimpse of first chapter.

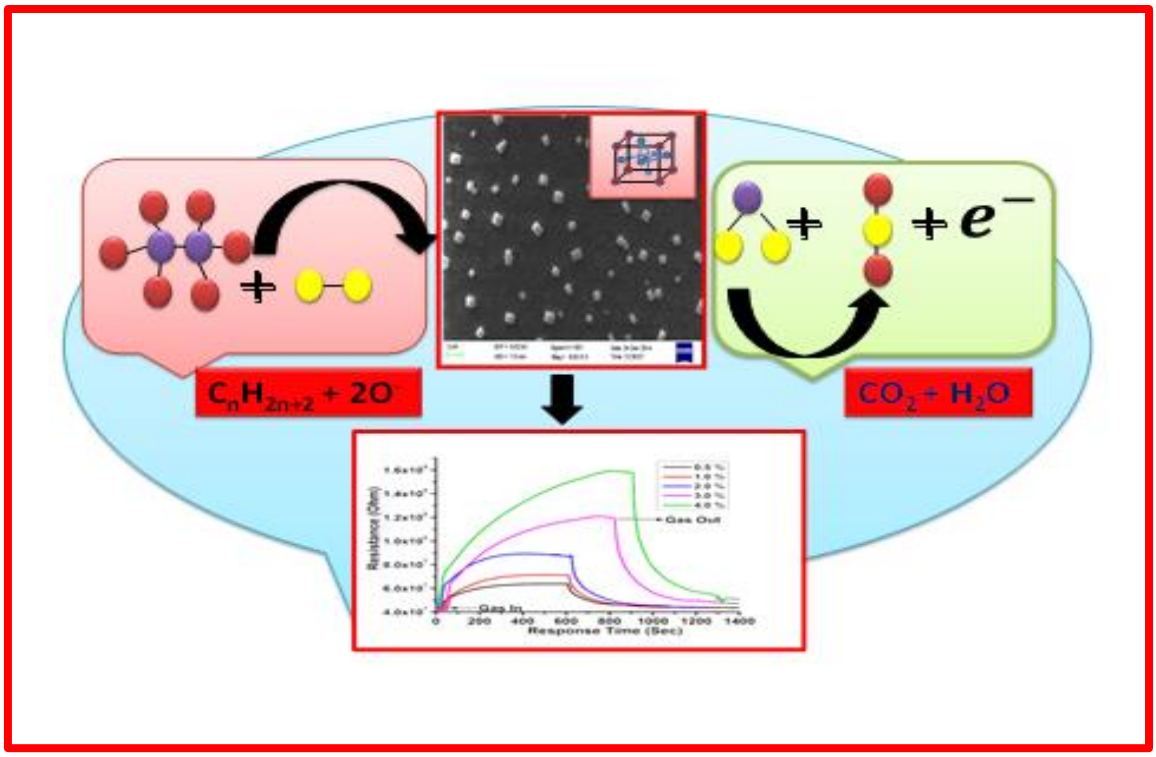

Fig. 2 Graphical Abstract of Barium titanate as LPG Sensor

Chapter 3 includes the detection of liquefied petroleum gas below lowest explosion limit (LEL) using nanostructured hexagonal Strontium ferrite thin film. In this chapter, we prepared hexagonal structured material by using co-precipitation method to reduce the size of the particle and better sensing response. We prepared the bulk amount of powder by this method and annealed it at high temperature 900 ºC to get the hexagonal phase of the ferrite. Hexagonal phase has four active sites which will give better LPG sensing response as LPG sensing depends on adsorption and desorption phenomenon. The minimum calculated size of the particle was found 18 nm. Sensitivity was found as 7 and % Sensor response as 602. Response time was found 40 s and recovery time was found 120 s. The Graphical Abstract of the work reported in this chapter is shown in Fig 3.

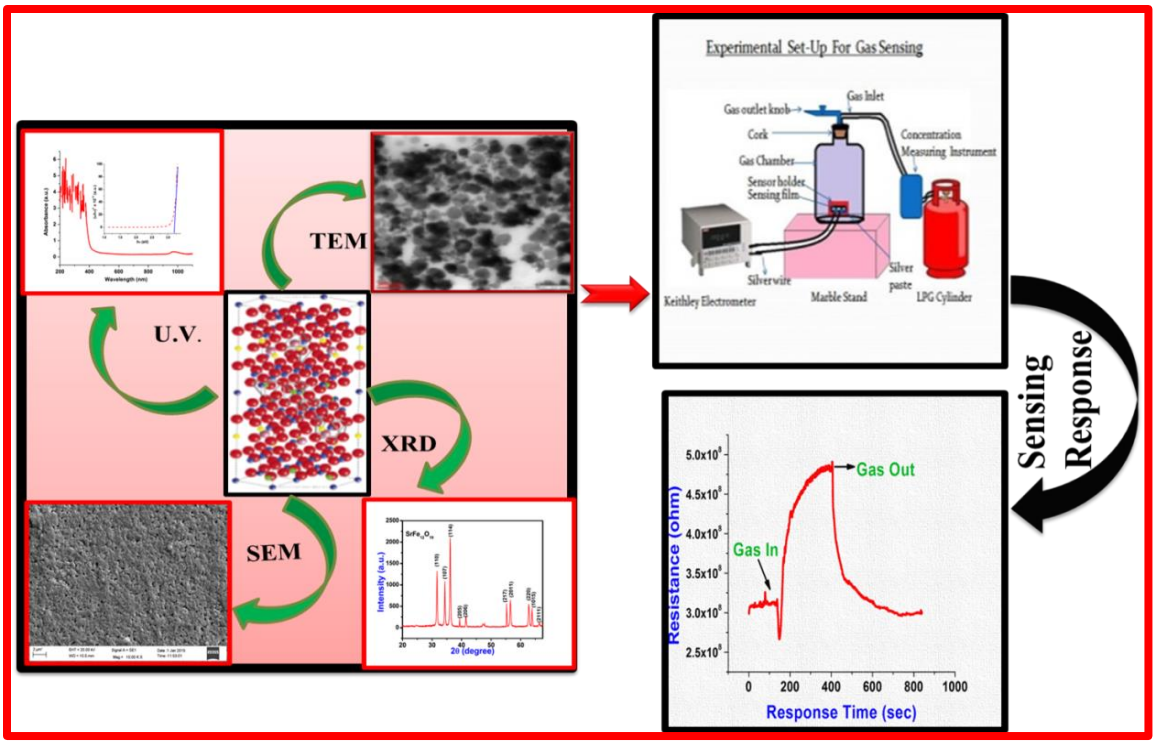

Fig. 3 Graphical Abstract of Strontium ferrite as LPG Sensor

Chapter 4 comprises of the study of Liquefied Petroleum Gas sensing properties of lead-free Bismuth sodium titanate prepared by sol-gel method. In this chapter, we again used the sol-gel method to replace Barium sites by some other material in Barium titanate. So we substituted Barium by Bismuth and Sodium at A-site to study its change in behaviour. Hence Bismuth sodium titanate was synthesized by using the sol-gel technique with a reduced size which belongs to orthoferrite family. The minimum crystallite size by XRD was found ~ 9 nm. The energy band gap was observed as 5.4 eV. Sensitivity was found 215 and % sensor response was found 115.4. Response time was found 22 s which was lesser than the previously reported response time. Graphical Abstract of BNT as LPG Sensor is presented by Fig.4.

Chapter 5 deals with the fabrication of perovskite Lanthanum ferrite film by sol-gel route and its gas sensing properties. The particle size was reduced to 8 nm and bandgap was found 5.3 eV. TEM revealed the particle size as 2.8 nm. Gas sensing properties were observed and the response time of this sensor was found as 12 s for 0.25 vol.% LPG and recovery time was 14 s. Maximum sensitivity was found as 3.3 for 3.5 vol.% LPG. Graphical Abstract of BNT as LPG Sensor is shown in Fig.5.

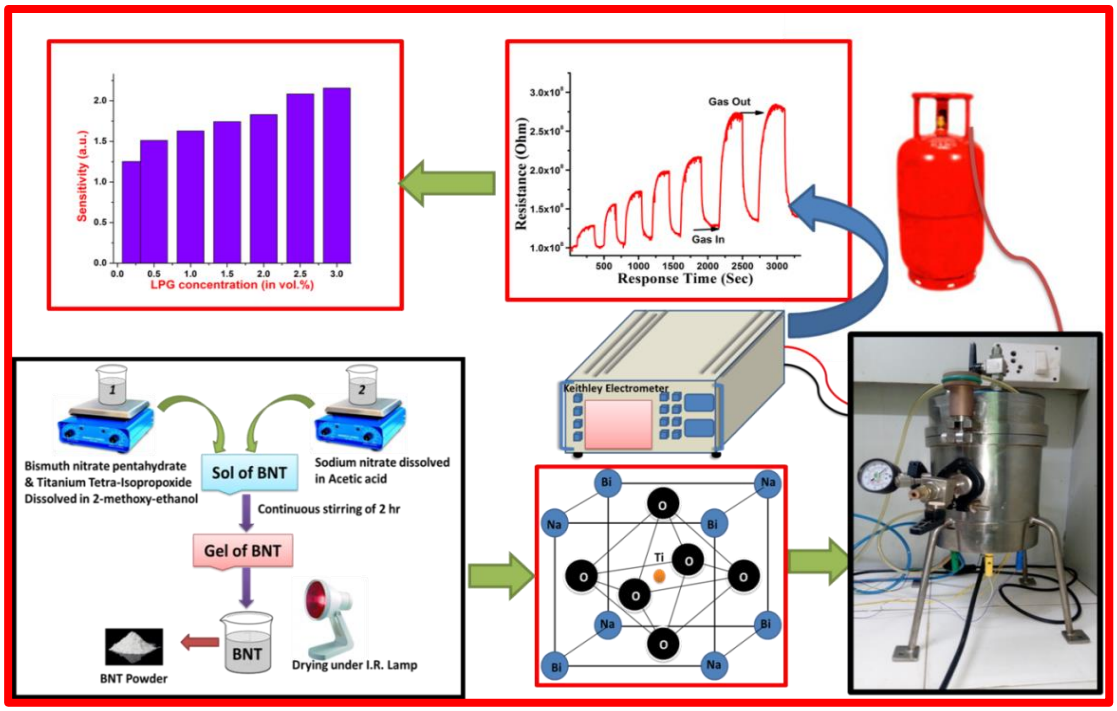

Fig.4 Graphical Abstract of BNT as LPG Sensor

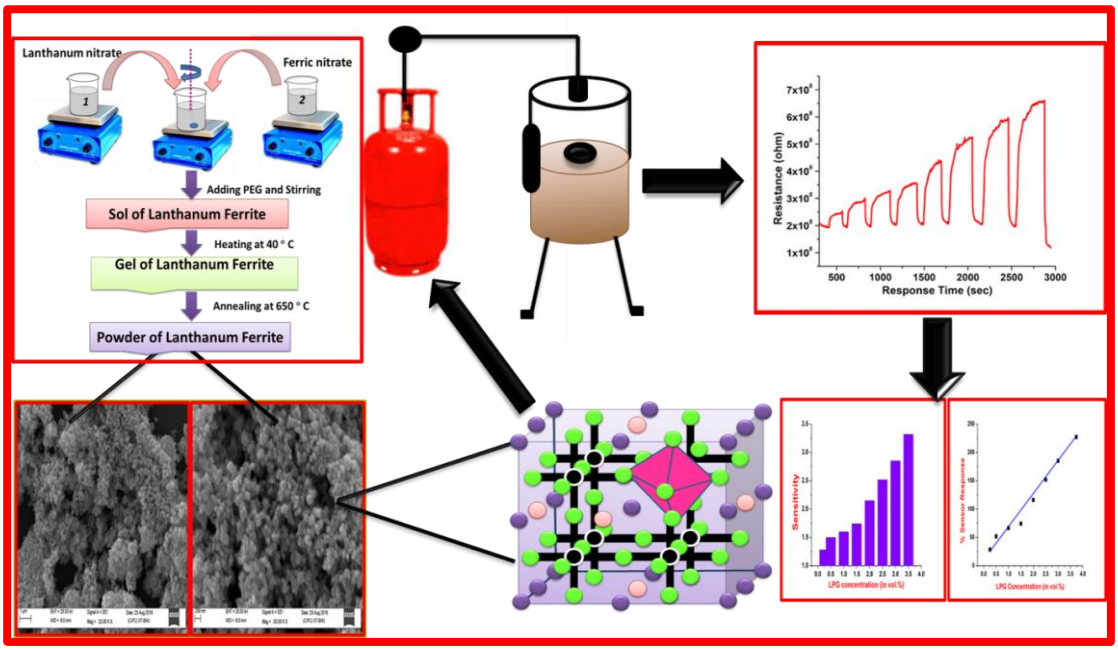

Fig.5 Graphical Abstract of Lanthanum ferrite as LPG sensor

Chapter 6 reports the Ag substitute Nickel spinel ferrite and further its application as LPG sensor below LEL. The comparisons in their microstructures were observed by SEM. Micrographs obtained, exhibited the better surface morphology of 0.45 Ag-substituted nickel ferrite than 0.2%

Ag-substituted nickel ferrite. As Ag-substitution increases, the porosity of material was found to be increased. XRD revealed the crystalline phase of Ag-substituted nickel ferrite. Similarly, there was a change in energy bandgap from 5.3 to 5.4 eV and also the optical behaviour of the samples. The maximum sensitivity was found 2.57 and 4.57 with % sensor response of 157.8 and 357.14 for 4 vol.% of LPG. The investigated LPG sensor produced a repeatable curve one after the other experiment hence this sensor was more reliable and a next step towards the development of a LPG sensor at commercial scale. Graphical Abstract of Ag substituted Nickel ferrite as LPG sensor is presented in Fig.6.

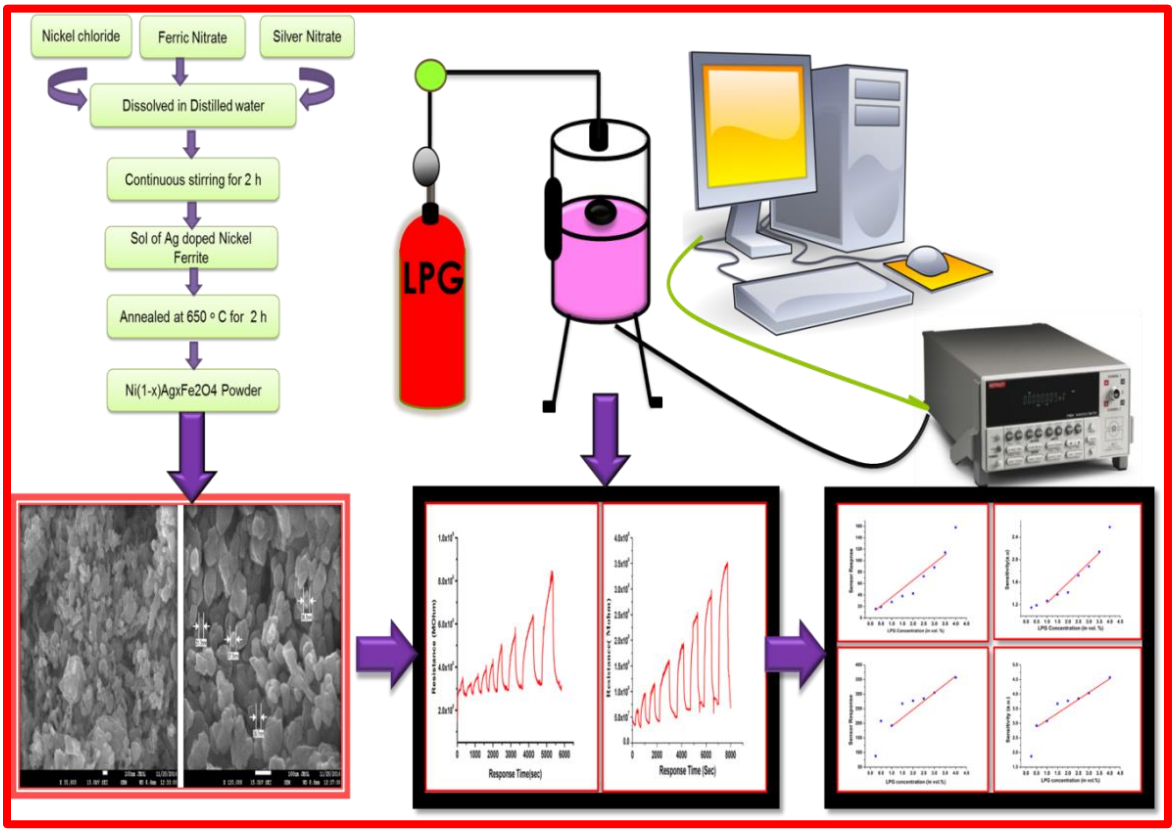

Fig.6 Graphical Abstract of Ag substituted Nickel spinel ferrite as LPG sensor

A chapter wise sketch of the Thesis including the sensing materials, dopants, bandgap, sensitivity, crystallite size, average grain size, pore size is depicted in Table 1.

Chapter No.	Materials	Method of Preparation	Band Gap (eV)	Particle Size	Sensitivity/ % Sensor Response	Response time
Chapter 1	Introduction	……...	……	……	…….	……
Chapter 2	$BaTiO_3$	Sol-gel	3.9 eV	11 nm	3.50/ 250.85	30 s
Chapter 3	$SrFe_{12}O_{19}$	Chemical Precipitation	3.2 eV	18 nm	7.02/ 602	40 s
Chapter 4	$Bi_{0.5}Na_{0.5}TiO_3$	Sol-gel	5.4 eV	9 nm	2.15/ 115.4	22 s
Chapter 5	$LaFeO_3$	Sol-gel	5.3 eV	8 nm	3.31/ 231	12 s
Chapter 6	Ag-substituted $NiFe_2O_4$	Sol-gel	5.3 & 5.4 eV	6 nm & 7 nm	2.57/ 157.89 & 4.57/ 357.15	10 s & 30 s
Chapter 7	Conclusion and future Scope	…….	……	……	…….	……

Table 1 A chapter wise sketch of the Thesis

From the Table 1, we infer that the Ag-substituted $NiFe_2O_4$ is an excellent material for LPG sensing application at room temperature and using this material a commercialized model of LPG sensor applicable for both indoor and outdoor detection may be designed.

Scope of Further Research Work

In future, research works for productive and efficient devices, the understanding about the role of nano-oxides for low-temperature applications would be desirable. These include incorporation of the recovery aspects achieved by the incorporation of catalysts onto the surface of a nano-oxide being used to detect a reducing gas.

- In the present work, Ag doping was done in nickel ferrite structure and had been optimized to improve the sensing parameters, while there is scope for integration of modifiers like of similar radius or some nanocomposite or CNT's for reducing the response and recovery times of LPG sensor.
- An effort may also be made for the synthesis of ferrites and multiferroic using other methods and their sensing applications.
- The magnetic and dielectric behaviour of spinel and orthoferrites are an interesting area. So attention may be focussed on twin character of ferrites.
- The effects of higher annealing temperature on the thin films, substrate, doping, substitution, magnetic field, etc. may be investigated in future.
- Detailed analysis of the evolution of the surface reactions with respect to temperature needs to be carried out, in order to exactly understand the reaction products from the surface interaction.
- Spectroscopic evaluation of the sensing mechanism using simulations has been important in future research.

Part of the thesis published and communicated in the refereed journals:

6. **Monika Singh**, B. C. Yadav, Ashok Ranjan, Rakesh K Sonker, Manmeet Kaur, "Detection of liquefied petroleum gas below lowest explosion limit (LEL) using nanostructured hexagonal strontium ferrite thin film", **Sensors and Actuators B: Chemical** 249, (2017) 96-104. **Impact factor- 5.401**
7. **Monika Singh**, B. C. Yadav, Ashok Ranjan, Manmeet Kaur, S. K. Gupta, "Synthesis and characterization of perovskite barium titanate thin film and its application as LPG sensor", Sensors and Actuators B: Chemical 241, (2016). 1170-1178. **Impact factor -- 5.401**

8. Rakesh K. Sonker, **Monika Singh**, Utkarsh Kumar, B. C. Yadav, "MWCNT doped ZnO nano composite thin film as LPG sensing", Journal of Inorganic and Organometallic Polymers and Materials 26 (6), (2016) 1434-1440 . **Impact factor – 1.577**
9. Richa Srivastava, B. C. Yadav, **Monika Singh**, T. P. Yadav, Synthesis, "Characterization of Nickel Ferrite and Its Uses as Humidity and LPG Sensors", Journal of Inorganic Organomet Polymers and Materials 26(6) (2016) 1404-1412. **Impact factor – 1.577**
10. Satyendra Singh, B. C. Yadav, **Monika Singh**, Richa Kothari, "A review report on nanostructured ferrites as liquefied petroleum gas sensor", International Journal of Science, Technology & Society 1 (1) (2015) 5-21.

Communicated/ published in the refereed journals:

8. **Monika Singh**, Ashok Ranjan, Richa Srivastava B. C. Yadav, Manmeeet Kaur, P.K. Diwedi, "Study of Liquefied Petroleum Gas sensing properties of lead free Bismuth Sodium titanate prepared by sol-gel method" **Sensors and Actuators B: Chemical, Impact factor 5.401**
9. **Monika Singh**, Utkarsh Kumar, B. C. Yadav, Manmeeet Kaur, "Fabrication of pervoskite Lanthanum ferrite film by sol-gel method and its gas sensing properties".**Nanoscale**. **Impact factor 7.2**
10. **Monika Singh**, Utkarsh Kumar, Toton Halder, B.C. Yadav, "Ag substituted Nickel ferrite thin film and its application as LPG sensor below LEL" **Sensors and Actuators B: Chemical**. **Impact factor 5.401**
11. **Monika Singh**, Utkarsh Kumar, B.C. Yadav, "Ag substituted Cobalt ferrite thin film and its application as LPG sensor below LEL" **Sensors and Actuators B: Chemical Impact factor 5.401**

REFERENCES

1. A. Alivisatos, Semicontuctor clusters, nanocrystal and Quantum dots, Science, 271 (5251) (1996) 933-937.
2. R. Feynman, There's Plenty of Room at the Bottom, Eng. Sci. 23 (1960) 22-36.
3. J.A. Thornton, J.E. Greene. Handbook of Deposition Technologies of thin films and coating (Rointan F. Bunshah, Ed.), Noyes publication, Park Ridge, New Jersey (1994) 275.
4. X. Wang, J. Zhuang, Q. Peng, Y. Li, A general strategy for nanocrystal synthesis, Nature 437 (7055) (2005) 121-124.
5. Satyendra Singh, B. C. Yadav, Monika Singh, Richa Kothari, A review report on nanostructured ferrites as liquefied petroleum gas sensor, International Journal of Science, Technology & Society 1 (1) 5-21.
6. M.R.A. Bhuiyan, M.M. Alam, M.A. Momin, M. J. Uddin, M. Islam, Synthesis and Characterization of Barium titanate ($BaTiO_3$) nanoparticle, Int. J. of Mat. and Mechanical Engineering, 1 (2012) 21-24.
7. A. Ghasemi, A. Morisako, X. Liu, Magnetic properties of hexagonal strontium ferrite thick film synthesized by sol-gel processing using SrM nanoparticle, Journal of magnetism and magnetic material, 320(18) (2008) 2300-2304.
8. K. Kanie, H. Sakai, J. Tani, H. Takahashi, A, Muramatsu, Synthesis of Bismuth Sodium Titanate Fine particles with different shapes by the Gel-sol method, Materials Transactions, 48 (8) (2007) 2174- 2178.
9. P. Song, Q. Wang, Z. Zhang, Z. Yang, Synthesis and gas sensing properties of biomorphic $LaFeO_3$ hollow fibers templated from cotton, Sens. Actuators B: Chem., 147 (2010) 248–254.
10. L. Satyanarayana, K.M. Reddy, S.V. Manorama, Nanosized spinel $NiFe_2O_4$: A novel material for the detection of liquefied petroleum gas in air, Materials Chemistry and Physics, 82 (2003) 21–26.
11. Satyendra Singh, B. C. Yadav, **Monika Singh**, Richa Kothari, A review report on nanostructured ferrites as liquefied petroleum gas sensor, International Journal of Science, Technology & Society 1 (1) 5-21.
12. T. P. Yadav Richa Srivastava, B. C. Yadav, **Monika Singh**, Synthesis, Characterization of Nickel Ferrite and Its Uses as Humidity and LPG Sensors, J Inorg Organomet Polym 2016, 1-9.

13. Rakesh K. Sonker, **Monika Singh**, Utkarsh Kumar, B. C. Yadav, MWCNT doped ZnO nano composite thin film as LPG sensing, Journal of Inorganic and Organometallic Polymers and Materials 26 (6), 1434-1440.
14. **Monika Singh**, B. C. Yadav, Ashok Ranjan, Manmeet Kaur, S. K. Gupta, Synthesis and characterization of perovskite barium titanate thin film and its application as LPG sensor, Sensors and Actuators B: Chemical 241, 1170-1178.
15. **Monika Singh**, B. C. Yadav, Ashok Ranjan, Rakesh K Sonker, Manmeet Kaur, Detection of liquefied petroleum gas below lowest explosion limit (LEL) using nanostructured hexagonal strontium ferrite thin film, **Sensors and Actuators B: Chemical** 249, 96-104.

PREFACE

Due to day by day increase in air pollution and the global warming, there is a great deal of interest for developing a gas sensor for checking air pollution, detecting harmful gases, monitoring other agro based products, home safety and hand held breath analyser etc. Lot of research work has been done on miniaturization of gas sensor which is economically cheap with high sensitivity, good sensor response and least response time and recovery time. There are various n-types and p-type metal oxide semiconductors gas sensor like ZnO, TiO_2, NiO, SnO_2, CuO, In_2O_3, Fe_2O_3 etc available in the market for the detection of harmful gases. However, after literature survey, I found that there is very less work be held on design and development of a LPG sensor operable at room temperature below LEL. The main goal of our present investigation is to design and fabricate a LPG sensor which would be robust, more sensitive with reduced response time, economically cheap and easy to fabricate than previously reported sensors. For this purpose, we have focused on ferrite materials which possess twin behaviour having a high surface area with reduced particle size and enhanced sensing features for the detection of Liquefied Petroleum Gas at room temperature below Lower Explosive Limit (LEL). Spinel and Orthoferrites oxides were prepared by simple pliable sol-gel and co-precipitation methods. Further, the structural, morphological and optical properties of the nanomaterial were optimized and LPG sensing applications were carried out.

The present Thesis is divided into seven chapters. Chapter 1 introduces the ferrite nanomaterial, gas sensor and its classification and LPG sensor and its sensing mechanism along with attributes. Chapter 2 contains the synthesis of perovskite Barium titanate via the sol-gel method and its application as LPG sensor. Chapter 3 describes the fabrication of hexagonal strontium ferrite film synthesized by co-precipitation method and detection of LPG sensor below

LEL. Chapter 4 deals with the study of LPG sensing properties and characterization of lead-free Bismuth sodium titanate. Chapter 5 describes the detailed investigation of nanostructured perovskite Lanthanum ferrite film synthesis, characterization and gas sensing application. Chapter 6 describes the effect of Ag (0.2% and 0.4%) doping in Nickel ferrite thin film and studying its morphology, optical and electrical behaviour of the film. Chapter 7 summarized the synthesis and characterization of $BaTiO_3$, $SrFe_{12}O_{19}$, $Bi_{0.5}Na_{0.5}TiO_3$, $LaFeO_3$ and Ag doped $NiFe_2O_4$. It encapsulates the summary and guideline for the further future plans.

LIST OF ABBREVIATIONS

S. No.	Name Compound	Full Name
1.	BNT	Bismuth Sodium Nitrate
2.	$BaTiO_3$	Barium Titanate
3.	Fe_2O_3	Ferric Oxide
4.	$SrFe_{12}O_{19}$	Strontium Ferrite
5.	$NiFe_2O_4$	Nickel Ferrite
6.	LPG	Liquid Petroleum Gas
7.	LEL	Lower Explosive Limit
8.	UEL	Upper Explosive Limit
9.	CVD	Chemical Vapor Deposition
10.	XRD	X-ray Diffraction
11.	SEM	Scanning Electron Microscope
12.	FE-SEM	Field Emission-Scanning Electron Microscope
13.	UV-vis	Ultra Violet-Visible spectroscopy
14.	TEM	Transmission Electron Microscope
15.	AFM	Atomic Force Microscope
16.	FTIR	Fourier Transformation Infrared Spectroscopy

17.	EDX	Electron Dispersive X-ray
18.	EPMA	Electron Micro Probe Analyzer
19.	NPs	Nanoparticles
20.	IPA	Isopropyl Alcohol
21.	NIOSH	National Institute for Occupation Safety and Health
22.	OSHA	Occupational Safety and Health Administration

LIST OF TABLE

LIST OF FIGURES

LIST OF APPENDIX

TABLE OF CONTENTS

Chapter 1

Introduction and Aim of Present Work

Ferrites are the class of ferromagnetic oxide material which possess iron oxide and metal oxide in a proper amount. Its twin behavior as an electrical insulator and magnetic conductor gained a lot of attention among the scientist and technologist. This chapter is an overview on different types of ferrites, spinel ferrites, pervoskite and its synthesis techniques along with its applications in daily life. It also focuses on types of gas sensors and LPG sensing with its sensing parameters. Significant developments on ferrite based gas sensor are reviewed and the advantages are discussed in detail. A brief outline of the present investigations is included in this.

CHAPTER 1

INTRODUCTION AND AIM OF PRESENT WORK

1. Motivation

1.1 Nanotechnology and Nanomaterial

The word 'Nano' is taken from the Greek word nanos which means "dwarf", describes a billionth of a unit 10^{-9}. Nanoscale materials are the materials having nanometer dimension and the scientific study of these objects, therefore, refers to the materials with sub nanometer dimension and the scientific study of these objects are known as Nanoscience. Nanoscience deals with the novel phenomenon of preparing, measuring its property and manipulating the dimension of an object up to the order of nanometer scale. Nanotechnology deals with using nanomaterials to develop products for practical application and for miniaturization of electronic devices. Nano-materials are the material of nanometer range and the nanometer order dimension can be achieved by constituting atom or molecule of few Angstrom order i.e. 10^{-10}. Nano-materials show enhanced and extraordinary characteristics from their bulk material [1-2]. It's changing extraordinary properties while size reduction, large surface to volume ratio and its application in different field elucidate the properties of nanomaterial. Generally, nanoparticles are unstable and they get agglomerate, therefore, it is essential to protect them. So as to protect them core shell structure or various capping agents are used for capping the molecules and avoiding them to form a mass [3]. Some sized based applications of nanoparticles have been discussed like particle size less than 5 nm are used for catalytic activities, particle size less than 20 nm is used for softening of hard magnetic materials, particles size less than 50 nm are used for changing the refractive index of the material which is useful for optoelectronic applications, particle size lesser than 100 nm can be used for mechanical strengthening of material and for super paramagnetism activity. Size regime plays an important role in nanoscience [4]. On the size reduction, the material undergoes several electronic transitions and due to which it shows relatively different property from the bulk material. The inverse relation between the particle size and surface area is a key underpinning in nano science

world. This is due to the enhanced surface area of the material in comparison to the volume and quantum confinement [5]. The maximum number of atoms lies on the surface of the nanoparticle which possesses huge surface energy and causes unstable or metastable stage. So there is a change in its chemical, mechanical, and optical properties resulting in the increase in the surface area per unit mass. This increased surface area made the nanomaterial for versatile application in electronic and technical industry.

1.1.1 Quantum Confinement

The macroscopic properties like boiling point, melting point etc. of any material is determined by average observation of the enough amount of material. As one mole contains 6.022×10^{23} molecules with 18 gm weight with respect to water and when the boiling point of water is observed, it is an average value of billions of molecules of water. This is not true in all the cases. When the size of the group of water molecules regime, its value changes. The same material shows different properties and behaviour. This is the fact that Newtonian (Classical) mechanics failed to explain many physical phenomena of nanomaterials [6].

Classical Physics states that a body can cross a potential barrier if it possesses enough energy. If the object has less energy then there is the null probability of finding that particle on another side. While according to Quantum Mechanics it is possible that lower energy particle can exist on other side but the only condition is the energy must be comparable to the size of the wavelength of the particle. It helps to provide a clear picture of nature at subatomic scales in terms of probabilities.

The phenomenon used to explain the size dependent characteristics of materials known as quantum confinement. Quantum confinement means to trap the particle and confine its motion in any direction. Quantum confinement effects are observed when the size of particles is comparable to de Broglie wavelength. Quantum mechanical laws are used to describe the behaviour of nanomaterial. When the size of the macroscopic material is reduced to micro and then to nano range, its properties began to change. There are some terms like Quantum well, Quantum wire, Quantum dots to describe nanomaterial according to their routine shape and size [7]. 2D materials are the nanomaterials which are confined from at least one dimension. They are also called “Quantum well”. Thin films are the best example of 2D material. Quantum well is widely used in various optoelectronic devices to

restrict the motion of particles on the 2D sheet. The 1D material is the nanomaterials which are reduced from any of the two dimensions. The particles travel in only one direction so they are also called “Quantum wire”. Nanotube, nanobelt and nanowire are an example of 1D material. They are used as an interconnector between several nano-devices to transport electrons. 0D nanomaterials are confined from all the three dimensions and the particles are restricted to move freely. They are well known as “Quantum dots”. They are used in electronic industry as tunable band gap semiconductors, nanocrystals semiconductor, transmitter, fluorescence material, etc [8]. In nanocrystals, the electron energy level is discrete (density of states). The Fig.1.1 shows the quantum confinement and density curve of all the dimension material corresponding to energy:

1.1.2 An approach to prepare the Nanomaterials

An approach to preparing the nanomaterials, Nanotechnology acts as an interdisciplinary among research and other subject areas like physics, chemistry, biology, materials science, engineering science, pharmacy etc. Nanocomposite materials are formed by the combination of two-phase or multiphase materials in which any of the nanomaterials should be of nano-dimensional. Nanomaterials can be a metal oxide, ceramic, polymers, ferrites, etc. Nanomaterial can be classified into three types on the basis of their source natural, incidental and engineered [9]. Engineered nanomaterials with controlled size and shape are the world widely used for various purposes. Nanomaterials can be synthesized in many ways in strategy synthesis, nature of synthesis, energy sources, and precursor method.

1. By synthesis strategy, there are two methods which are commonly used. Top down and bottom up approaches are the two strategies to synthesize nanoparticles. Top down approach is the one-way approach, in which block of material is taken then it is etched or milled into the desired shape. Carvings done on the pillar and breaking down of a block of rock into the desired figure is an example of the top-down approach. The bottom-up approach is an analytic and universal approach in which smaller subunits (any atom or molecules) are united to make any useful product. Top down is typically long term process in comparison to a bottom-up approach. Ball milling is one of the typical route for top down method while in bottom-up approach materials are synthesized by gas phase

condensation, chemical reduction of metal salt, an electrochemical method, decomposition of organometallic compounds etc. Now in today's era, research is more focused on finding the advance bottom-up technique for synthesizing and characterizing nanomaterials range about 1-100 nm range.

2. By nature of the process, there are three types of synthesis method; physical, chemical, and biological method. A physical method is a method in which physical states like size, pores, shape and the phase of the material changes. Condensation of various gases and all the mechanical size reduction process like ball milling, chemical vapour deposition, sputtering comes under physical process. A chemical method involves reduction and change in its chemical properties [10]. Metal salt reduction, electrochemical synthesis, co-precipitation etc. methods are the chemical process. The biological method employs to some biologically produce membrane used to control the growth of nanoparticle. Ferric oxide and silver oxide nanoparticles are synthesized by biological synthesis.

3. Energy is an essential part of daily life. On the basis of the energy used as an input, the synthesis processes are categorized in terms of plasma, laser, electron beam, sputtering, ball milling, combustion, supercritical fluid etc.

4. Precursor method is widely used classification based on three phase. It is used to synthesize nanoparticles in the solid phase, liquid phase and gas phase [11].

1.2 What changes occur in properties of nanomaterial due to size reduction?

Most of the nanomaterials are crystalline in nature and they possess a unique property. Nanomaterial show changes in chemical, physical, mechanical, magnetic, etc., properties while it is reduced from bulk to nano range. Some of the changes are discussed below:

1.2.1 Physical properties

Crystal structure of the nanomaterial is same as bulk material only the change is observed in lattice parameters. The interatomic spacing (d_{hkl}) is also decreased due to long electrostatic force and because of decrease in size; the melting point of the nanomaterial is also decreased.

1.2.2 Chemical Properties

Enhancement in the surface to volume ratio observed in nanomaterials causes the catalytic activity. Crystal structure of nanomaterial and size dependency is influenced by the synthesis technique used.

1.2.3 Electronic properties

Electronic structure of the nanomaterial is different f

rom the bulk material and a band gap is created when the difference in energy level is more than KBT. The density of energy state is also changed in the conduction band due to change in the electronic structure of the material. Ionization potential in nano dimension materials is high in comparison to the bulk material.

1.2.4 Magnetic/ dielectric properties

Nanoparticles made of semiconducting material like silicon, germanium etc., are not semiconductors. Ferrites show extraordinary magnetic and dielectric properties. Their magnetic properties depend on the sintering temperature and sometimes on the dopant concentration.

1.2.5 Mechanical properties

Mechanical properties like elastic strain, stress, Young modulus, hardness of the material, etc also varies as the material is reduced to nano dimension.

1.3 Application of Nanomaterial

Nanoscale materials are used in many fields. Nanotechnology is a boon to the modern world of science and technology. There are plenty of applications of the nano materials. Some are discussed below:

1.3.1 Automotive industry

They are used as sensors. Palladium nanoparticles are used in hydrogen sensor. They are used for painting and also used as a catalyst. They are used for manufacturing light weight devices.

1.3.2 Electronic industry

Miniaturization of electronic devices, compact size and less power consumption enhance the use of nanomaterial in the electronic industry. They can be used in FET, MEMs, LED display, Laser diode, coating materials, filters, fibers, etc [12-13]. They are used in the memory card and in various storing devices. They are also used in many optoelectronic devices.

1.3.3 Chemical industry

They are used as fillers in chemical industries. They are used for preparing dyes, ceramics, plastics, etc [14]. Nanocomposites are used for the coating material. They are also used as the magnetic fluid. They are also used in Lubricants.

1.3.4 Medical

Polymeric micelle nanoparticles are used in drug delivery. Iron nanoparticles are used for breaking clusters of bacteria in chronic bacterial infection. Silver nanoparticles are used in the treatment of cancer etc [15]. Nanodiamond nanoparticle of Carbon is used in joint implantation. Ceramic oxide nanoparticles used as an antioxidant for removing oxygen free particle from blood which helps in reducing traumatic injury. They are also used in chemotherapy.

1.3.5 Energy sources

Nanoparticles of the semiconductor are used in the solar cell [16]. They are also used in designing of solar panels, solar devices, etc. Nanoparticles are used for creating electrodes in the fuel cell. They are used in batteries, capacitors, etc.

1.3.6 Cosmetic

They are used in many sunscreen lotion creams. They are used in various gel, soap, handwash, etc. They are also used in toothpaste.

1.3.7 Food

Nanotechnology is also used in the food industry from growing of food to its packaging. Nanomaterials are developed for the change of flavours as well as hygienic food to eat it [17].

1.4 Synthesis techniques of nanomaterial

There are various methods for the preparation of nanomaterials. These methods are divided into two categories physical and chemical method [18]. Fig. 2 given below shows the classification of synthesis method.

1.4.1 Ball Milling

In late 1960 Benjamin and his co-workers developed this process. In ball milling, the mixture of powder is kept inside a chamber containing metallic balls. Fine, uniformly dispersed metal oxide nanoparticles are synthesized by mechanical alloying in ball milling method. Beside synthesis, high energy produced while ball milling is used to change chemical properties by modifying the reactivity of milled solid. These planetary balls are used for providing high energy to the solid salt and for mechanical alloying. Attritor planetary ball, horizontal ball mill are the apparatus used in this alloying process [19]. This method is mostly used in laboratories. The milling system contains a rotating disc and a bowl opposite to the direction of the disc for synchronizing centrifugal forces, powder mixture, surfactant, rotating the ball. The mixture of the powder is fractured and cold welded under high energy impact. These metallic balls are of used for high-speed milling and these balls are called the planetary ball. In the initial stage, the powder is partially flattered due to the collision of balls. In intermediate stage metastable structure is obtained by mechanical alloying process occurs followed by fracturing and cold welding process. In final stage reduction and refinement in particle size is done. Thus how a nanomaterial is formed.

1.4.2 Pyrolysis

Pyrolysis includes spray pyrolysis, aerogel pyrolysis and laser assisted pyrolysis. Spray pyrolysis is also called aerogel pyrolysis or vapour pyrolysis. There is a minor difference between spray pyrolysis and aerogel pyrolysis in the delivery of the reactant on the substrate. The main parts of aerogel pyrolysis instrument are (i) a generator, to obtain aerogel state from the liquid, (ii) furnace for particle formation and (iii) a particle collector, (iv) a flow meter to check the flow rate. In aerogel, pyrolysis nanoparticles are used in

vapour form to deliver it in the hot reactor while in spray pyrolysis these are in the small droplets form which is directly delivered from the nebulizer. Metal ions are dissolved in the aqueous solution to form a homogeneous precursor. This precursor is converted in aerogel in presence of oxygen, nitrogen or mixture of gases. Size dependency varies in aerogel by type of generator used, the volume of carrying gas and nature of the liquid. The formed aerosol is then carried inside the electric furnace where liquid droplets go through evaporation, solute precipitation, solute decomposition and finally sintering of oxide [21-22].

The nanomaterials obtained via this process are spherical in shape with minimal agglomeration, which is good for gas sensing. Major disadvantage of this method is the large size distribution of nanoparticles and requirement of large amount dilution for carrying gas to avoid cluster formation.

1.4.3 Sputtering

Sputtering is the physical process in which high-energy projectile particles are used for the ejection of the particle from matter target by transfer of momentum. John Thornton and Joseph Greene have described deposition technique method by the sputtering phenomenon. Sputtering deposition in a stable plasma system allows very fine control on deposition rate which is proportional to the discharge current between the electrodes and the sputter yield of the cathode material. Sputter yield is defined as the ratio of the mean of emitted number of atoms to the incident atoms [23].

Depending upon the process, the pressure range varies from 10^{-6} to 10^{-10} torr. An evacuated chamber with Ar gas and pressure from 1-100 m Torr is used to establishing a glow discharge. In sputtering positive ion is used and the substrate is always grounded. Glow discharge contains ions, neutral ions, positive ion negative ion, excited species, metastable species, and molecular species. This positive ion is bombarded with negative potential provided to the target. Sputter yield and sputter strength are the terms related to sputtering. Based on the deposition technique sputtering is divided into following categories:

1. Diode Sputtering

2. Reactive Sputtering
3. Bias Sputtering (Ion Implantation)
4. Magnetron Sputtering
5. Ion Beam Sputtering Depositions
6. Reactive Ion Implantation
7. Cluster Beam Deposition

1.4.4 Laser Ablation

Laser ablation technique was reported in early 1963 but it came into use for gas sensing application in around 1990s. Laser ablations as the name suggest the removal of a layer from the surface by laser treatment or laser irradiation. It is used to emphasize on non-equilibrium plasma or vapour conditions by intense laser pulse which is different from laser evaporation in which heating and evaporation of the material occur in an equilibrium condition. Its instrumentation requires two major parts a pulsed laser and an ablation chamber. An intense laser beam of high energy is used to elevate the temperature of the absorbing material and maximum absorption on the target surface. As a result, the layer on the surface vaporizes due to the intense laser beam. There is the possibility of condensed particles or cluster. These condensed particles are deposited on a substrate or collected on filter system containing glass fiber. Then dip coating or screen printing technique is used to coat substrate from collected nanoparticles. Laser ablated nanomaterials are extensively used for great sensing performance of the gas sensor [24-25].

1.4.5 Chemical Vapor Decomposition

Chemical vapour deposition (CVD**)** is a chemical process which is used to produce highly pure solid materials. It is the most reliable method for synthesis of nanomaterials. In this technique nucleation of particles in the vapour state take place rather than deposition of the film. The process is used to make a very thin film and is used in electronic industry and semiconductor industry. In a typical CVD process, the wafer (substrate) is exposed to one or more volatile precursors, which react and/or decompose on the substrate surface to produce the desired deposit and when the mixture of gas reactant is inserted inside the reacting chamber and chemical reaction among the gas molecule take place. Chemical

reaction types basic to CVD include pyrolysis (thermal decomposition), oxidation, reduction, hydrolysis, nitride and carbide formation, synthesis reactions, disproportionation, and chemical transport [26]. CVD can be classified into other as:

1. Chemical Vapour Deposition (CVD)
2. Plasma Enhanced CVD (PE-CVD)
3. Metal-Organic CVD (MO-CVD)
4. Atmospheric pressure CVD (AP-CVD)
5. Low-pressure CVD (LP-CVD)
6. Ultrahigh vacuum CVD (UHV-CVD)
7. Aerosol-assisted CVD (AA-CVD)
8. Direct liquid injection CVD (DLICVD)

1.4.6 Sol-gel Method

The most common method of synthesis of nanomaterial in the desired shape like a flower, fiber thin-film etc., can be obtained by the sol-gel method. It is very easy and cheap method which is widely used for the synthesis of the material. “Colloidal” is the solid particle ranging from 1-100 nm range. “Sol” is produced by dispersing colloidal solution in the liquid. An intermediate structure formed by polymeric chain and pores are known as “Gel”. Formation of sol takes place by dissolving alkoxide, inorganic metal salt into a suitable solvent. After continuous stirring, a homogeneous mixture is obtained. The two important reactions that occur in this process is hydrolysis followed by condensation of metal [27]. Usually, an alcoholic solvent is used for dissolving alkoxide.

$$\mathbf{M\text{-}OR + H_2O \rightarrow M\text{-}OH + ROH} \qquad \textbf{Hydrolysis}$$

$$\mathbf{M\text{-}OH + OR\text{-}M \rightarrow M\text{-}OM + H_2O} \qquad \textbf{Condensation}$$

The sol obtained after hydrolysis and condensation is low viscous liquid. Spin coating, dip coating and screen printing methods are further used for the fabrication of the thin films.

1.4.7 Chemical Co-Precipitation method

A precipitation and Co-precipitation comprises of three steps: chemical reaction, nucleation and crystal growth. In this method, different type of stoichiometric mixture of salt having one type of ion or multiple ions which are partially or sparingly soluble in the solvent are precipitated in chemical co-precipitation method [28]. This hydrate, hydrate oxide or formed salt solution hydrolyzed at a certain temperature and forms a precipitate in the form of hydroxides, oxalates, or formats, citrates when any precipitator like OH^-, $C_2O_4^{2-}$, CO_3^{2-} etc. is added. Then the anions from the formed product are separated and washed out by distilled water, ethanol, etc. as it may contain several impurities besides oxide. This mixture is filtered, dried and then heated to give the final product. Precipitate disturbs the ionic equilibrium of the solution or in other words, it induces supersaturation condition. Chemical reaction depends upon some parameters. They are as follows:

1. Maintenance of pH and settling time plays an important role in precipitation method
2. Use of sufficient amount of additive or precipitating agent for the completion of the reaction
3. Proper removal of the solid precipitate
4. Washing out and drying

It gives high-quality end product with the bulk amount of powder. So this method is mostly used for the synthesis of nanoparticles. It has drawback that it is not a controlled process i.e. morphology and size distribution differs batch wise. So it's not easy to maintain the reproducible size, structure and distribution of anions, etc.

1.4.8 Hydrothermal/ Solvothermal

The hydrothermal reaction is also known as thermal hydrolysis or hydrothermal hydrolysis. In the hydrothermal process, the aqueous reaction is carried out in an autoclave or high-pressure reactors (2000 psi) and high temperature ranging from 100-300 ºC. In this process water is used to accelerate the kinetics and act as a reactor for the hydrolysis reaction. Alkali and acid are used as a pseudo catalyst during the process. The sol of metal hydroxide or metal oxide is formed from aqueous solution at elevated temperature and pressure. It is very easy to control size variation and control particle size and structure by changing its parameters pH, ionic strength, solvent, cation concentration, anion

concentration, catalyst, time duration and stirring are the parameter to control size and morphology of the metal hydroxide or oxide. pH and reactant condition have an immense impact on phase transformation of the nanoparticle [29-30]. The hydrothermal reaction is a step by step procedure of the following subprocess which is given as under:

1. Hydrothermal oxidation
2. Hydrothermal precipitation
3. Hydrothermal deoxidization
4. Hydrothermal decomposition
5. Hydrothermal crystallization

It is a direct route method to obtain ultra-fine nanoparticles. No high-temperature annealing or calcination is required in this process as like in sol-gel method. Resulting sol can be directly used in green bodies after pressure filtration. Solvothermal is the same process as hydrothermal. Autoclave is used in a similar manner as in hydrothermal only difference is that in hydrothermal water is used as solvent and in solvothermal aqueous solvent or organic solvent is used other than water.

1.4.9 Electrochemical synthesis

An electrochemical synthesis is a low-temperature processing to obtain high purity material and controlled size and structure nanomaterials. It is done by passing an electric current between two electrodes separated by an electrolyte. The high potential gradient of 10^5 Vcm^{-1} is maintained between the two electrodes. Reactant dissolved in the electrolyte is deposited as a solid product. pH of the solution plays an important role in electrochemical synthesis and it is chosen such that the lower oxidation state is stable while higher oxidation state goes under oxidation. The activity of reactant decreases as the reaction proceeds [31]. The parameters on which an electrochemical synthesis depends are as follows:

1. Choice of a proper electrolyte
2. Choice of an electrode inert or reactive
3. Choice of temperature, composition of electrolyte
4. Concentration of used electrolyte and pH of the solution
5. Choice of cell divided or undivided

Moreover, based on the technique electrochemical synthesis can be classified into following:

1. Synthesis of Electro-migration
2. Electrolysis of fused salts
3. Alternative current synthesis by layer to layer composite of solid
4. Electro-generation of base
5. Anodic oxidation

1.4.10 Citrate gelation Method/ Penchini Method

In citrate gel method, the aqueous precursor is used for the synthesis of nanoparticles. The organic network is formed when metal ions are dissolved and stabilized in precursor solutions. After heat treatment, fine metal oxide particles are obtained. Citrate method is basically used for the preparation of multi-component compositions. They have the ability to prepare multi-component with homogeneous structure. Poly chelates are formed between the ligands of citric acid and metal ions. On heating, these poly chelates poly-esterification occurs with polyfunctional alcohol. Evaporation of the precursor containing metallic salts and citric acid shows an important role in poly chelation process. A viscous resin and a transparent glassy gel are obtained after heat treatment. Initially, Immobilization of different metal ions takes place from the mixture to form a rigid system to avoid the risk of segregation into different oxide compositions after calculations [32].

The process of the Penchini is same as the Citrate-gel method in which metal nitrates are dissolved in alcohol instead of citrate.

1.4.11 Emulsion Precipitation Method

This method involves the formation of stable emulsion systems prepared by adding surfactants to a water-oil system. Small numbers of atoms are added in the emulsion system. The stable precipitate is formed by the exchange of reactive species between the droplets of the emulsion. From the Einstein-Smoluchowski equation, the growth rate is directly proportional to the rate of exchange between droplets. Therefore, the nucleation of particle and its growth in emulsions is retarded avoiding agglomeration of large particles.

Droplet size can be controlled by the use of different surfactant. So the surfactant plays an essential role in microemulsion method. Other additives play a role as steric particle stabilizer after removal of water. To prepare an emulsion surfactant is added to the water followed by continuous mixing. Drop by drop this emulsion was added to alcohol solutions of alkoxides. Then this solution is stirred for 5-6 h. After removal of solvents, the residue was taken up in acetone to destroy the micelles. The solid product is obtained after drying of organic material and thus nano-crystalline nanoparticle is formed after calcination [33].

This method avoids agglomeration of the particles formed inside the bubbles. This process occurs unusually at low temperatures. It does not affect emulsion stability.

1.5.1 Allotropic form of Iron

Iron oxide plays an important role in spinel ferrite. So it is very essential to know the allotropes of iron and effect of annealing temperature on its structure**.** The purity of substance may exist in one or more than one crystalline form and each of its forms is stable at certain conditions like temperature, pressure, etc. This is also termed as Polymorphism or Allotrope. There is three main allotropes of iron found at different annealing temperatures; these are alpha (α), gamma (γ) and delta (δ). The melting point of pure iron is 1539 ºC and pure iron is soft and ductile.

From room temperature (RT) to 910 ºC pure iron possesses a BCC structure and is called Alpha iron (Fe_α). It possesses ferromagnetic behaviour up to 768 ºC. After heat treatment it becomes known- magnetic and ferromagnetism disappear but its BCC structure remains the same. The stable non-magnetic alpha iron is earlier known as beta (ß) iron. Gamma structure is formed above 910 ºC and allotropic change occurs from alpha to gamma structure, BCC is transformed into FCC structure. On further heating up to 1404 ºC again allotropic change occur and gamma iron is transformed to delta iron with BCC structure and is stable up to the melting point of iron [34]. All these processes are irreversible. The temperature at which above structural changes take place is called critical point or arrest point.

1.5.2 Types and Effect of Heat Treatment

Heat treatment refers to the phenomenon of heating and cooling of metal, ceramic, plastic, alloy etc., which alters change in its microstructure by changing its nature, size, font distribution and phase transformation and its properties. Heat treatment is done to achieve strain hardening, to remove gases from casting, to increase resistance, to soften the metal, to improve the magnetic properties, to improve the hardness of the steel and alloy, to produce single phase material, etc. When any material or alloy is allowed to heat above a certain temperature, a structural adjustment or stabilization occurs on cooling it at room temperature. Cooling rate plays an important role in this phenomenon.

The principal kinds of heat treatment are:

(i) **Annealing -** An annealing process consists of three stages: *(i)* heating the sample to the required temperature, *(ii)* holding or 'soaking' at that fixed temperature, and *(iii)* cooling, up to room temperature. Time is an important parameter in this process.

(ii) **Normalizing** - This is used to give more strength than annealing. The heating process is same as in annealing but in this cooling is done in the air so that cooling rate is much faster. Normalizing refines the grain and produces the homogeneous structure.

(iii) **Hardening** - It is a kind of heat treatment which is used to produce a non-equilibrium structure in an alloy. Tool-making alloys are hardened to increase its hardening strength. Under equilibrium conditions, alloy undergoes eutectoid transformation used to strengthen by hardening.

(iv) **Tempering-** Tempering and ageing are the kinds of heat treatment which are applied to hardened alloys; they involve certain phase transformations which make the metal structure approach the equilibrium. Tempering improves the ductility and toughness of quenched steel while decreases hardness.

(v) **Surface hardening-** Surface hardening of articles, like surface strengthening offers an additional advantage that large stresses appear in the surface layers of hardened articles. There are two ways of surface hardening (i) **selective heating of the surface layers**: e.g. flame hardening surface of the component is heated up to 850 ºC and induction hardening

surface of the component is heated up to 850-1000 ºC. (ii) **case hardening**- In this method C and/or N_2 are introduced in the surface layer. In carburizing the part is surrounded by material or atmosphere rich in carbon and on heating this carbon is first released and then absorbed in steel. More recently case carburizing is more effectively performed by heating steel [35].

1.6 Ferrite

1.6.1 Introduction to ferrites

Ferrites belong to a special class of magnetic material consisting of metal oxide particles and ferric oxide particles as their main compositions. The magnetic, electric and dielectric behaviours possessed by them have made ferrites more attractive to the current field of science and technology and from the research point of view. These important properties of ferrite find application in micro-electric devices, magnetic switches, sensors, microwave devices, electromagnetic circuits, transformer core, optoelectronic devices, antenna rods and in the field of medicines for drug delivery to chemotherapy, etc. Generally, Ferrites are ferri-magnetic materials having iron oxide as their main component along with the other metal oxides. A brief classification of magnetic material is given below to understand how ferrimagnetic materials differ from other magnetic material and also about its spin orientation [36-37].

1.6.2 Classification of ferrites on the basis of crystal structure

Ferrites comprise of a large number of magnetic oxide with remarkable structural, magnetic and electrical behaviour [38]. Its properties depend on the synthesis technique, sintering time and sintering temperature, pH, a chelating agent, etc. Ferrites can be classified into categories; firstly on the basis of magnetization and other on the basis of structure. On the basis of structure, ferrites can be classified into four types; spinel ferrite, perovskite, garnet, hexaferrite.

On the basis of magnetization, ferrites are of two types; hard magnet and soft magnet.

1.6.2.1 Spinel ferrite

1.6.2.1.1. Structure of spinel ferrite

The ferrite with AB_2O_4 structure is known as spinel. The unit cell of spinel ferrite consists of 32 oxygen, 16 trivalent ions and 8 divalent metal ions. The main feature of the

unit cell is the array of oxygen ions creates two kinds of interstices, which was occupied by the metallic ions. These interstices are referred to as tetrahedral or A- site and Octahedral or B- site. A site is called tetrahedral because it is located at the center of a tetrahedron whose corners are occupied by oxygen ions. B site is called octahedral because the oxygen ions around it occupy the corners of an octahedron [39]. Spinel ferrites can be either normal spinel $(M^{2+})A[Fe^{3+}\ Fe^{3+}]BO_4$ or inverse spinel with half of the trivalent ions in the A-sites and the other half together with divalent ions in the B-sites. The structure is complex, in that there are 8 molecules per unit cell ($8\times AFe_2O_4$) where A is the divalent metal ion. The 32 large oxygen ions form a face-centered cubic lattice in which two kinds of interstitial sites are present. The smaller metal ions occupy these interstitial spaces. These spaces are of two kinds. There are 32 octahedral sites surrounded by 6 oxygen ions. The crystallographic environments of A and B sites are therefore distinctly different. Only one by the eight part of the A sites and one by half part of the B-sites are occupied by the metal ions. $ZnFe_2O_4$ is an example of normal spinel, while $NiFe_2O_4$ is an example of inverse spinel [40].

1.6.2.1.2 Classification of spinel ferrite

On the basis of the distribution of cations in the two principal sites, tetrahedral site [A] and octahedral site [B], spinel ferrites are classified into three types:

1- Normal spinel ferrite

2- Inverse spinel ferrite

3- Mixed spinel ferrite

1) Normal spinel:

A ferrite is called normal spinel when the divalent metal ions occupy the tetrahedral [A] sites while $2Fe^{3+}$ ions are at the octahedral [B] site. The best examples of normal spinel ferrites are zinc ($ZnFe_2O_4$) and cadmium ferrites ($CdFe_2O_4$), in which the divalent metallic ions Zn^{2+} or Cd^{2+} are at the [A] site, while Fe^{3+} ions are at [B] sites.

2) Inverse spinel:

In inverse spinel ferrite, one trivalent ferric ion Fe^{3+} is at the tetrahedral [A] site while the remaining trivalent ferric ions Fe^{3+} and the divalent metallic ions M^{2+} are at the

[B] site. Actually, most of the simple ferrites, e.g. Nickel ferrite, cobalt ferrite ($CoFe_2O_4$) are of the inverse spinel structure.

3) Random spinel:

The divalent metal ions M^{2+} and trivalent Fe^{3+} ions are distributed at both tetrahedral [A] site and the octahedral [B] site, then the ferrite is termed as random spinel ferrite. The best-known example of random spinel ferrite is copper ferrite ($CuFe_2O_4$).

1.6.2.2 Orthoferrites

Jocker and Van Saten studied for the first time the magnetic properties of the perovskite structure. They are the class of ferrites with rare earth metal and are canted antiferromagnets. The structural formula of orthoferrite is ABO_3 where A represents rare earth metal ion. Eibschutz M et al. reported that pure $AFeO_3$ perovskite is called as orthoferrite to distinguish it from spinel or cubic structure [41]. The ferrite ABO_3 with perovskite structure consists of lanthanide series elements, A (where A = La, Gd, Tb Pr, Dy, Nd, Sm, Eu, Er, Tm, Yb, Ho and Lu) and first series of transition metals, B (where B = Ti, Fe, Co V, Cr, Mn, Ni and Cu). Small trivalent and tetravalent atoms occupy the center position of the cube and large divalent and trivalent molecules occupy the corner position of the cube. In the orthorhombic structure, the four octahedra in the unit cell are tilted in different directions, the extent of tilting being measured by non-linearity of B-O-B bond angles. In $AFeO_3$ perovskites, Fe-O-Fe bond angles decrease with diminishing ionic radius of the rare earth cation in the A sites. As a result, each B-site Fe 3+ cation has eight nearest A-site cations with next-nearest neighbour A-B distances. [42]

The ABO_3 perovskites exhibit different electronic and magnetic properties at a different temperature which depends on 3d electronic configurations of the transition metals. In octahedral coordination, cations with configurations 3dN (where N = 4, 5, 6 or 7, corresponding to Mn(III), Fe(III), Co(III) and Ni(III), respectively), may exist in either a spin-paired ground state or in states with maximum unpaired electrons according to Hund's rule.

1.6.2.2.1 Classification of ferrites on the basis of magnetization

At low-temperature ferrites behave as low band gap semiconductors and as well as insulators, due to this reasons engineers and researchers are keenly interested in innovating its properties, structure, characterization and its application [43]. The properties of ferrite can be altered by substituting different foreign cations at available sites or by incorporating any catalyst or by changing its sintering temperature, etc. So cation distribution in ferrite is essential to understand the magnetic as well as structural and other properties. Most of the magnetic materials of industrial interests are ferromagnetic materials. The ferromagnetic materials can be categorized into two; one is soft magnetic materials and the other is hard magnetic materials. This classification is based on their ability to be magnetized and demagnetized, not their ability to withstand penetration or abrasion

1. **Soft magnetic material**
2. **Hard magnetic material**

When domain wall can easily migrate, the ferromagnetic material can be easily magnetized at low magnetic field. These types of ferromagnetic materials are called soft ferrite. When domain wall is difficult to migrate, the magnetization of the ferromagnetic material occurs only when the high magnetic field is applied. In other words, these types of ferromagnetic materials are difficult to magnetize, but once magnetized, it is difficult to demagnetize. These materials are called hard ferrite. Soft ferrite materials are easy to magnetize and demagnetize, so are used for electromagnets, while hard materials are used for permanent magnets [44].

1.7 Sensor

The sensor is a device that produces a measurable output as a function of provided input. They are useful in-situ measurements such as in industrial process, scientific applications, daily necessity, offices, etc. They act as critical components in all measurement and controlled applications, responsible for converting any physical phenomenon such that temperature, pressure etc. into a measurable quantity through data acquisition (DAQ) system. It does not perform itself, it acts as a part of larger assembled system that may incorporate many other devices such as a transducer, detectors, data recorders, signal conditioners, signal processors, memory devices, actuators, etc.

Rapid growth in microelectronics and advancement in technology made machine more autonomous and intelligent day by day. It provoked a demand of artificial sensing organs which perform independently [45-46]. Thus people developed devices according to their requirement and now sensors are ubiquitous in our daily lifestyle. 3S factor plays an important role in remarking a sensor as a good sensor and these three factors are sensitivity, selectivity and stability. Sensors can be classified into three types:

1- **Physical sensor**- A physical sensor is based on the measurement factor where no chemical reaction occurs. Measurement can be in the form of absorbance, temperature, mass, refractive index, conductivity, etc. Temperature sensor, Pressure sensor etc. are well known physical sensor [47-49].
2- **Chemical sensor** – A chemical sensor is a sensor in which analyst participate to perform a chemical reaction and to give an analytic signal corresponding to the input. Various gas sensors and humidity sensors are well know chemical sensor [50-51].
3- **Biosensor**- Sensor that is used in biological applications is termed as biosensors. Immuno sensor, Microbial potentiometric sensor, etc. are the example of biosensors [52-53].

1.7.1 Chemical Sensor

Chemical sensors are a special variety of gas sensors, to detect and analyze which substance is present and in what concentration in our environment. With our senses, we can not only see, hear and feel but also smell and taste. Consequently, a chemical sensor is also known as artificial noses or artificial tongues. A Chemical Sensor interacts with the sample and transforms its chemical information to the analyst to produce analytically useful signals. The chemical information may be due to the chemical reaction of the analyte or due to physical measuring parameters of the system [54-56]. Many scientists gave their different definition for a chemical sensor according to their observations. It just concluded that chemical sensor is an interface between the chemical world and the electronic. Or it is just the primary link of the measuring chain.

Chemical sensors consist of two important units a receptor part and a transducers part [57-59]. Sometimes few sensors are provided with separator also. Receptor part of a sensor is a chemical interface; there is an occurrence of a chemical interaction of the analyte with

a surface of the sample producing a change in its physical/ chemical parameters. The chemical information provided by the analyst is transformed into a desirable form of energy which is further measured by the transducer. The transducer part is a device which converts one form of energy to another accordingly [60-61].

1.7.2 Gas Sensor

The gas sensor is the subclass of the chemical sensor. In 1927, Oliver W. Johnson introduced an explosive gas indicator of a portable gas cylinder which was considered as first commercial portable sensor which was not lesser than a miracle those days. This led to the beginning of fabrication of sensor and its commercialization all over the world [62]. After that researcher have developed various types of gas sensors such as electrochemical sensors, catalytic combustion sensors, calorimetric gas sensor, capacitive gas sensor, optical gas sensor, infrared sensors, and acoustic wave-based sensors, metal oxide based gas sensor etc. These sensors are applicable in various fields such as chemical engineering, research and development, architecture, medical, pharmaceutical, agriculture, etc [63-64].

1.7.3 History of the evolution of Gas Sensor

1. **Canary Bird**- In 1920s Canary bird, a very beautiful songful bird was used for detecting the harmful gases. The birds were very sensitive towards harmful gases from human beings also. So in an ancient time when these birds susceptible than human stop singing the song and then eventually they die, this was the significance of the presence of harmful gas around them.
2. **Davey's Lamp**- Later people started using Davey's lamp known as safety lamp also. In this lamp height of flame was used as the reference of the concentration of gas presented around. Oil was adjusted to a particular height and when the flame of the lamp becomes high then methane gas is predicted and when the flame of the lamp becomes dim then oxygen gas is predicted.

1.7.4 Why there is a need for Gas Sensors?

To monitor and control of the air pollution in the ambient and emission of toxic gases emitted from the industrial sector and daily household fuel arose the necessity of a gas sensor. These gases are risky for human being, animals and other living organisms. There are several types of gases used in industrial areas as the raw materials. Toxicity

should be checked and toxic gases should be banned near the living place so there is a need for the gas sensor. These need to be checked and LEL and UEL of each gas should be marked so that it couldn't be mixed in the air in huge amount preventing many infectious diseases, lungs problem, eyes problem, etc. It is really an important issue to control and monitor toxic gases in the surrounding, as it can cause a huge damage to property and human being. Certain gases can be toxic for humans, or corrosive gases, or explosive. Gases are also produced from the garbage and waste from the research and laboratories [65]. These problems need to be detected and these type of waste material need to be dumped in some place far from the living zone.

There are currently needs for three categories of gas monitoring:

1. For oxygen detection, to maintain breathable atmospheres for the entire living organism and for the control of combustion.
2. For detecting of flammable gases in the air in order to avoid any unwanted is happening of fire or any explosion. Such circumstances can be avoided by measuring its concentrations and its lower explosive limit and the upper explosive limit for a particular atmosphere.
3. For toxic gases in the air.

Therefore there is an essential requirement of gas sensors that can be used to detect these gases continuously to avoid any dangerous situation [66].

1.7.5 Classification of Gas Sensors

There is six types of gas sensors depending upon their transduction principle. They are as follows:

1. Electrochemical Gas Sensor
2. Acoustic Gas Sensor
3. Metal Oxide Gas Sensor
4. Colorimetric Gas Sensor
5. Capacitive Gas Sensor
6. Optical Gas Sensor

1.7.5.1 Electrochemical Gas Sensor

An electrochemical gas sensor consists of two major parts first is electrolyte/ gel used and another one is anode and cathode used. The anode is responsible for all the oxidation process while the cathode is responsible for the reduction process. Due to this phenomenon current is created and positive and negative ions are developed. Positive ions flow towards the cathode rod and the negative ions flow towards the anode rod. The output is directly proportional to the concentration or partial pressure of the gaseous species. Nowadays in the electrochemical gas sensor, liquid electrolyte is replaced by solid-state electrolyte but the whole working is same [67-68].

1.7.5.2 Acoustic Gas sensor

These sensors are based on the sound effects. These types of sensor consist of a piezoelectric substrate containing inter-digital electrodes. When RF voltage of particular frequency is given then the mechanical waves are produced in piezoelectric substrate. These Rayleigh surfaces then propagate and type of acoustic waves are generated and its frequency is determined. The mechanical energy is converted into electrical RF voltage [69-70]. Depending on this method, we can measure the properties, processes, or chemical species in the gas phase, liquid phase, vacuum or thin solid films. Acoustic gas sensor devices are already used in mobile industry, telephone industry and for sensor development. Acoustic wave devices are extremely sensitive to its surface perturbation [71]. There are different types of Acoustic wave gas sensor and they are as follows:-

1. Surface acoustic wave (SAW)
2. Shear horizontal surface Acoustic wave (SH-SAW)
3. Shear horizontal acoustic plate mode (SH-APM)
4. Flexural plate wave (FPW) or Lamb wave mode
5. Thickness shears mode (TSM) devices.

1.7.5.3 Metal Oxide Gas Sensor

The metal oxide gas sensor is also called chemo-resistor gas sensor. Semiconductors are found to be very sensitive to the very low concentration of gas. This type of sensor requires stain gauze, thick film, thin film, etc. In this sensor, the resistance of the film

changes when the gas interacts with the film and it gets adsorbed on the surface of the material. Then, the resistance of the film changes depending upon the type of the material used and type of gas exposed. Film interacts with the adsorbed oxygen molecule and the free electrons get attached to these molecules forming oxygen species and when any gas interacts, then there is a change in its parameters. The solid and gas interaction changes the resistance of the material and their sensing properties are studied. Response to the gas can be increased by adding dopant/ additive or by increasing the temperature of the substrate through the heater. There are various types of metal oxide gas sensor available in the market for both the reducing gas and for the oxidizing gas. Adsorption and chemisorption are the two phenomenon which is responsible for all the mechanism in metal oxide gas sensor [72-73].

1.7.5.4 Capacitive Gas sensor

The capacitive gas sensor is used to detect a change in the capacitive behaviour of the film by volatile analytes which are proportional to the concentration of target analyte. The capacitive gas sensor gives the output signal by converting the capacitance of the film in the form of voltage. It measures the changes in dielectric constant as a function of the inserted gas concentration between the two electrodes of the film. These type of sensor are dependent on inter digital electrode structures with two plates, forming a standard capacitor which corresponds to two plates of a standard capacitor. The basic concept behind this is the capacitance increases as the dielectric constant of the film decreases and it decreases as the dielectric of the film increases [74-75].

1.7.5.5 Calorimetric Gas Sensor

The calorimetric gas sensor is used to detect the combustible gas present in the surrounding. Its principle is based on the change in temperature in presence of gas. Generally, any substance burns at its ignition temperature, similarly the combustible gas also burns at their ignition temperature but the gas begins to ignite in presence of certain catalytic material even at very low temperature also. This type of sensor is also called catalytic sensor. It consists of two identical platinum coils coated with any ceramic in the form of a bead and a surface of the catalytic active metal. One bead is loaded with a catalyst like Pd, Pt, Rd, Th etc. The coils are maintained at a certain temperature by connecting

them in Wheatstone bridge. Wheatstone bridge is used to measure the output of the sensor. In the presence of air, the output is zero but in the presence of combustible gas, the temperature of the bead increases with the catalyst due to the exothermic reaction. Thus the imbalanced output of the bridge is balanced by a reduction in the electrical heating power. This power consumption is proportional to the concentration of gas. There are two types of catalytic sensor depicted as under:

1. Pellistor type
2. Thermo-electric type

Pellistor type sensor consists of active or inactive beads with platinum or palladium catalyst controlled by Wheatstone bridge while Thermo-electric gas sensor works on Sea back effect which occurs due to the temperature difference between two points producing voltage [76-77].

1.7.5.6 Optical gas sensor

In 1984, Butler reported the first hydrogen optical gas sensor. This sensor consisting of an optical fiber with palladium and titanium coating and was used for detecting hydrogen gas. Optical gas sensor gives higher sensitivity, stability, and selectivity than the non-optical gas sensor. Photons play an essential role in the optical gas sensor. They have residual mass with no charge so neither charge nor mass-based detection is done through it. This type of sensor is based on absorption and emission scattering of a gas species. An optical gas sensor consists of a light emitting element, optical fiber, a gas sensing element, a photodetector, and a filter for picking up fluorescence or phosphorescence phenomenon. The optical sensor having fiber optics is called optode [78]. These fibers are of two types; it can be dispersive and non-dispersive type. These fibers act as a sensing element which response to light. The infrared gas sensor is a type of optical gas sensor. In these sensors, measurand is determined by Refractive Index (Speed of the light), absorbance and fluorescence properties. The principle of optical sensors is used in Ellipsometry for determining dielectric properties of the material and interferometry in optical waveguide structures and in spectroscopy techniques for luminescence, phosphorescence, fluorescence phenomenon [79].

1.7.6 Application of Gas Sensor

There are many applications of gas sensor. Some of them are given as below:

1. The gas sensor is used in process control industries.
2. They are used for fire detection to avoid any miss-happening.
3. They are used for environmental monitoring.
4. They are used in mines for the detection of harmful gases.
5. They are used as breath sensor for detection of alcohol.
6. They are used for grading of agro-based in coffee industry or tea industry.
7. They are used as boiler sensor
8. They are used at home for safety purpose.

1.8 Liquefied Petroleum Gas (LPG) Sensor

Liquefied petroleum gas is an inflammable gas consists of a mixture of hydrocarbon gases including both the propane C_3H_8 and butane C_4H_{10}. Propane is an organic molecule containing three-carbon alkane group which is in gaseous form but it can be compressible to a transportable liquid form under certain condition. In summer butane-rich gas is used and in summer propane rich LPG is used. It also contains propylene and butylene in very less amount. Ethanethiol which is a powerful odorant is added to LPG ot trace its leakage. There are some other international standards like EN589, amyl mercaptane and tetra hydrothiophene may also be used as subsitute. LPG used as a fuel in heating appliances and vehicles and it is a substitute for petrol and diesel. It is increasingly used as a refrigerant in the refrigerator as an aerosol propellant which is a substitute for harmful gases like chlorofluorocarbons to reduce damage to the ozone layer caused by it. At moderate pressures and temperatures, LPG can be stored and transported in liquid form. When it is released in at relatively low temperature, it vaporizes and can be handled as a gas [80-81].

1.8.1 Lower Explosive Limit (LEL)

Lower explosive limit (LEL) is the lowest amount or percentage of a gas or a vapour present in the air which is capable of producing a flash of fire when any ignition source like an arc, flame, heat, etc. are brought near to it. For example, methane gas has an LEL

of 5%. If the atmosphere has less than 5% methane, an explosion cannot occur even if there is an ignition source present.

1.8.2 Upper Explosive Limit (UEL)

Upper explosive limit (UEL) is the highest amount or percentage of a gas or a vapour present in the air capable of producing a flash of fire when any ignition source like an arc, flame, heat, etc. are brought near to it. Concentrations higher than upper flammable limit (UFL) or UEL are "too rich" to burn. Flammability limits depend upon temperature, pressure, and the concentration of the oxidizer. Higher the temperature, lower will be LFL and higher UFL, while the LEL and UEL are increased on increasing the pressure. To avoid any risky condition there is need of standardization of LEL and UEL of each gas. National Institute for Occupational Safety and Health (NIOSH) and Occupational Safety and Health Administration (OSHA) Standardized the Lower Explosive Limit (LEL) of propane rich LPG as 21,000 ppm (2.1% by volume in air) and 19,000 ppm (1.9% by volume in air) for butane rich LPG. The Permissible Exposure Limit (PEL) for LPG as specified by NIOSH and OSHA standards is 1000 ppm [82-83].

1.8.3 Sensor Parameters/ Sensor Attributes of LPG sensor

For optimizing and the performance of any device, it is necessary to know its sensing parameters. % Sensor response, sensitivity, selectivity, stability, response and recovery times, reproducibility and long-term stability are the operating parameters of a sensing device [84-87].

(i) % Sensor Response

Percentage sensor response of a sensor is defined as the ratio of the difference in the resistance of the film in the air and in presence of gas to the resistance in air.

$$\%SR = \frac{\left|R_a - R_g\right|}{R_a} * 100$$

(ii) Sensitivity

Sensitivity can be defined as the ratio of the magnitude of response of a sensor to a particular target analyte. There are several definitions of sensitivity depending upon the application. It is defined as the ratio of variation in the resistance of the film in the presence of gas and resistance of the film in air.

$$S = \frac{R_g}{R_a}$$

(iii) Response and Recovery Time

The response time of a sensor is defined as the time taken by the sensor to reach 90% of the final response value. Recovery time is defined as the time taken by the sensor to come to 90% value of the final value.

(iv) Reproducibility and Long Term Stability

Reproducibility of a sensor is defined as the efficiency of a sensor to reproduce the same output for the same amount of measuring input. Stability of a sensor is defined as the efficiency of a sensor to generate the same result after a long time without any change in its sensing parameters.

(v) Selectivity

Selectivity may be defined as the sensor response to a particular gas in a mixture of gases. This parameter defines the specific response of the sensor.

1.8.4 Sensing Mechanism of LPG Sensor

LPG sensing is surface morphology based mechanism. The porous film plays an important step in sensing mechanism. Pores are also called as the active sites. Working principle of LPG Sensor is dependent on its electrical properties and change in its chemical properties when the sample is exposed to the gas. Adsorption plays an important role in this sensing mechanism process. Generally, Adsorption is simply defined as the attachment of the molecules or binding of molecules to the surface. Adsorption is of two types depending upon the bond i.e. Physisorption and Chemisorption [88-89]. Physisorption is a physical adsorption in which molecules are held weaker by Vander wall force while chemisorption is a chemical adsorption in which adsorbate get attached to the solid molecules by the formation of a chemical bond with the surface. This adsorption is stronger

than physisorption. Initially, physisorption occurs followed by chemisorption when the thin film comes in contact with the atmospheric oxygen molecule. The interaction of the gas with the material leads to transfer of electrons between the thin film and the reducing gas. These atmospheric oxygen molecules get adsorbed on the surface molecule to form oxygen species by the interacting with the conduction band electrons [90-91]. The kinematics involved in this process is as below:

$$O_2\,(air) \leftrightarrow O_2\,(ads) \qquad \text{------- (i)}$$

$$O_2\,(ads) + e^- \leftrightarrow O_2^-\,(ads) \qquad \text{------- (ii)}$$

This lead to decrease in concentration of electrons in the n-type material while in p-type material there is an accumulation of charge taking place [92]. When LPG is exposed to thin film a complex reaction occurs due to the formation of superoxide and peroxide which are highly active which is highly unstable. These complex hydrocarbons react with adsorbed oxygen species which are responsible for complex reactions below:

$$C_nH_{2n+2} + 2O^- \rightarrow H_2O + C_nH_{2n}{:}\,O + e^- \qquad \text{------- (iii)}$$

$$C_nH_{2n}{:}\,O + O^- \rightarrow CO_2 + H_2O + e^- \qquad \text{------- (iv)}$$

This reaction is termed as dehydration. Further oxidation of dehydrogenation mechanism occurred and CO_2 and water contents were released as the end product. Schematic diagram of LPG sensing mechanism is shown in Fig.1.20. As the rate of the reaction increased removal of electrons were taken place which leads to the formation of a potential barrier that was further responsible for the constant resistance of the film as presented in Fig.1.21.

When the film is put in the chamber in the air, then the stabilised resistance of the film is termed as R_a i.e. resistance in the air. After passing LPG when the film attains saturation point and constant resistance is obtained then this is termed as R_g i.e. resistance in gas. Again after this process when the chamber has removed the resistance of the film decrease again and tries to gain its initial R_a value. Again the new R_a value is not the same and it is slightly different due to the effect of humidity caused by water content. This water

content removed during sensing mechanism fills the pore and resistance of the film in air vary from the initial resistance. This water content can be removed by heating the film.

1) Depletion or Space Charge Layer: In n-type material depletion layer is formed by the ionized electrons from the conduction band which is further responsible for the formation of oxygen species. In p-type material, holes are the active elements. The extracted holes are responsible for the formation of charge layer. It is the most important layer in sensing phenomenon.

2) Accumulation layer: Accumulation layer is formed when electrons are injected into an n-type semiconductor surface. For example, when an acidic molecule such as H^+ donates an electron or accepts a hole from the surface state, this would lead to an accumulation of positive charges on the surface, that forms a double layer with the negatively charged semiconductor.

3) Inversion layer: It forms due to a local inversion of the surface from n to p or vice-versa, in the presence of a strong oxidizing agent [93-96].

1.9 Materials and its literature review

Research interest in the field of sensing technology is focused on ferrites. Ferrites operate at very low temperature and demonstrate better sensitivity and % sensor response than other metal oxides. Materials synthesized and discussed in this work are $BaTiO_3$, $SrFe_{12}O_{19}$, $LaFeO_3$, $Bi_{0.5}Na_{0.5}TiO_3$ and Ag doped $NiFe_2O_4$. Literature survey related to the material, its synthesis, characterizations with sensing parameters is depicted in Table 1.2. & 1.3.

1.9.1 International status

Table 1.2 Literature survey on various types on nanomaterials and their gas sensing applications at International level.

S.No.	Material	Method used for synthesis	Chemical used	Crystallite Size or Thickness /porosity	Properties or application of the content	Reference
1.	$BaTiO_3$	Solid state reaction/spin coating	Polyvinyl butyl, 2-2 butoxy ethoxy ethyl alcohol, PEG	200-500nm	Gas sensing properties	M.A. El Romh et al. [97]
2.	$CuO\text{-}BaTiO_3$	Oxide method	Oxide salt	1 μm	CO_2 Sensing at 729 K	Tatsumi Ishihna et al. [98]
3.	$SrTiO_3$/ $BaTiO_3$	Sol-gel/ spin coating	Titanium butoxide, Barium acetate, strontium acetate, acetic acid	40 nm by XRD	Ethanol Gas Sensor	Satreerat K. Hodak et al. [99]
4.	$BaTiO_3$/ $BaSbTiO_3$	Balling Method	$BaTiO_3$, Sb2O3, graphite powder, ethyl alcohol	100 μm	CO and N_2 Gas sensing	K.Park et al. [100]
5.	$BaTiO_3$ / $SrTiO_3$	Thermal decomposition	$BaTiO(C_2O_4)2$. 4H2O, PVA, Graphite powder, Ti powder, silicide, carbide	3.1-3.8 μm	Humidity sensing and Gas sensing	Burcu Ertung et al. [101]
6.	$BaTiO_3$ /$SrTiO_3$	Solution-based synthesis	Barium titanium, Strontium titanate, oleic acid and Isopropoxide	5-60 nm diameter of nanorod	Study of cubic perovskite nanorods	Jeffrey J. Urban et al. [102]
7.	$BaTiO_3$	Electro-chemical method	Barium hydroxide, ethanol	15 nm nanowire	Photo-luminescence spectrum of $BaTiO_3$	M.R.A Bhuiyan et al. [103]
8.	$BaTiO_3$	Hydrothermal	Barium chloride, Titanium Isopropoxide, ethanol	100-300 nm	Formation of Nanofibres by different polymer	Humar. A. Avila et al. [104]

9.	$BaTiO_3$	Sol-gel/dip coating	Barium acetate, Glacial acetic acid, tetra ethoxy titanate, ethanol	Very thin film 44 nm	Thermal, optical and dielectric properties	O. Harizanonv et al. [105]
10.	$BaTiO_{3-}$ Y_2O_3	Sol-gel	Barium acetate, Y_2O_3,glacial acetic acid	1-2 μm	DTA/TGA measurement, Positive Temperature Coefficient of resistivity(PTCR)	A.Kareiva et al. [106]
11.	$BaTiO_3$	Hydrothermal reaction	Barium Hydroxide, Titanium oxide	50-200 nm	Study of Raman Spectroscopy	Hiromichi et al. [107]
12.	La-doped $SrFe_{12}O_{19}$	Sol-gel	Sr nitrates, Fe nitrates, La nitrates	80-100nm by XRD, 200nm by TEM	Thermal and magnetic properties	T.T.V.Nga et al. [108]
13.	Sm-doped $SrFe_{12}O_{19,}$ PANI	Sol-gel	Sr nitrates, Fe nitrates, Sm nitrates, citric acid, HCl, ammonium sulphate	35 nm by XRD, 50-100 nm	Microwave absorption property and Electromagnetic properties were studied	Juhuo Lun et al. [109]
14.	Co-Ti doped $SrFe_{12}O_{19}$	Sol- gel ignition technique	Sr nitrates, Fe nitrates, Co nitrates, Titanium Isopropoxide, citric acid, ethylene glycol, NH_4OH	100 nm, 200 nm	Ferromagnetic Resonance Measurements	Simon et al. [110]
15.	$SrFe_{12}O_{19}$	Solid state thermal decomposition	SrC_2O_4, SCl_2, k2C2O4, Fe nitrate	25-30 nm	Ferromagnetic behavior	Abdollah Javidan et al. [111]
16.	La-doped $SrFe_{12}O_{19}$	Sol-gel/auto-combustion	Sr nitrates, Fe nitrates, La nitrates, de-ionized water	30-35 nm	Electrical characterization by calculating dielectric constant and dielectric loss	Muhammad Azim et al. [112]

					as a function of frequency	
17.	$SrFe_{12}O_{19}$	Pulsed Laser Deposition	---	16nm, 63nm, 21nm, 95nm thickness of film	Magnetic properties were studied by VSM	M. Khaleeq Rahmen et al. [113]
18.	$SrFe_{12}O_{19}$	Sol-gel/ auto combustion	Sr nitrates, Fe nitrates, citric acid	26.6 nm	Magnetic and thermal analysis	M. Ghobeiti-Hasab[114]
19.	$BaFe_{12}O_{19}$	Sol-gel method	Fe nitrate, Ba nitrate, coconut water	32 nm	Magnetic behaviour by SQID magnetometer	J.V.A Santos et al. [115]
20.	$SrFe_{12}O_{19}$/ polyimide	Screen printing and spin casting	Sr particle, benzophenone, tetracarboxylic dianhydride oxy dianicline		Magnetic and mechanical properties by micromachining	Laure K. Lagorce et al. [116]
21.	$SrFe_{12}O_{19}$	Sol-gel, spin coating	Sr nitrates, Fe nitrates, citric acid, ethylene glycol	33nm, 42nm, 57nm	Effect of citric acid on structural and magnetic properties	S.M. Madoudpanad et al. [117]
22.	$ZnFe_2O_4$/ $SrFe_{12}O_{19}$	Chemical co-precipitation	SrCO3, Zn cl2, Fecl3, HCl	---	Photocatylic activity	Taiping Xie et al. [118]
23.	$SrFe_{12}O_{19}$	Sol-gel using egg white binder	Fe nitrate, Sr nitrate, egg white protein	3-4 μm	Structural and magnetic properties by TGA-DTA	Tingting Li et al. [119]
24.	Mn-doped $SrFe_{12}O_{19}$	Protenic sol-gel	Fe nitrate, Sr nitrate, Mncl2, coconut water	46.4-52.6 nm	Magnetic properties by after Mn doping Hysteresis loop	W.M.S.Silva et al. [120]
25.	$BiFeO_3$/ $SrFe_{12}O_{19}$	RF Sputtering	Silica wafers, ceramic disk	5mm thickness	Electric and magnetic domain	Yukiko et al. [121]

26.	$SrFe_{12}O_{19}$	Sol-gel	Sr nitrates, Fe nitrates, citric acid	8-13 μm microtubules	Magnetic	Yongfei et al. [122]
27.	$SrFe_{12}O_{19}$	Co-precipitate and microemulsion	Sr nitrates, Fe nitrates, n-butanol, methyl ammonium hydroxide, sodium n-dodecyl sulphate	61 nm particle size	Thermal analysis and effect of annealing temperature	A. Dr mot a B. et al. [123]
28.	$LaFeO_3$	Simple synthesis route	La nitrates, Fe nitrates, Sorghum straw, citric acid	20-30 nm	Acetone sensing	Peng song et al. [124]
29.	$LaFeO_3$/ $YFeO_3$	Combustion method	Y_2O_3, La_2O_3, Fe nitrate	-----	Spin-phonon coupling by Raman	P.V. Cotinho et al. [125]
30.	Ag-$LaFeO_3$ – SWCNTs	Sol-gel /microwave synthesis	Fe nitrate, La nitrate, Ag nitrate, citric acid	45nm, 37nm,33nm,28nm,36 nm	Formaldehyde Gas sensing	Y.M.Zhang et al. [126]
31.	$LaFeO_3$/ SiO_2	Sol-gel	Fe nitrate, La nitrate, citric acid, Tetraethyl orthosilicate, Ammonia	------	TG-DTA Analysis, Nitrogen Adsorption isotherms at -196º C	Kamal M.S. Khalil et al. [127]
32.	$LaFeO_3$	Polymer pyrolysis method	Fe nitrate, La nitrate, Acrylic acid	34nm, 47nm,65m,74nm by XRD, 70 nm by TEM	Magnetic properties by VSM measurement	Sumalin Phokha et al. [128]
33.	$LaFeO_3$ with carbon modified	PANI pyrolysis method /stearic combustion method	Fe nitrate, La nitrate, sulfuric acid, aniline, stearic acid	-------	Core-shell model $LaFeO_3$ coated with carbon layer	Yaru Pei et al. [129]
34.	$LaFeO_3$- rGO	Stearic acid combustion method	Fe nitrate, La nitrate, Graphene oxide,	------	Electrochemical properties and kinematic characteristics	Yongjie Yuan et al. [130]
35.	TM (Mn, Co, Cu) doped $LaFeO_3$	Glycine nitrate process,	Fe nitrate, La nitrate, Mn	20-50 nm	TM doping properties	Qi Peng et al. [131]

		citrate auto-combustion process	nitrate, Co nitrate, Cu nitrate		based on visible light	
36.	$LaFeO_3$	Polyconden sation of Glucose, hydrotherm al method	Glucose, Fe nitrate, La nitrate, carbon sphere, distilled water	50 nm	Formaldehyde sensing	Hui hui Zhang et al. [132]
37.	$LaFeO_3$	Hydrother mal method	Fe nitrate, La nitrate, citric acid	19.2 nm	Acetone gas sensing	Hong Xio Xio et al. [133]
38.	Co-doped $LaFeO_3$	Chemical co-precipitatio n	Fe nitrate, La nitrate, $Co(CH_3COO)_2.4H_2O$, $(NH_4)_2Co_3$	21nm- 28nm	Ethanol gas sensing	Xiutao Ge et al. [134]
39.	NBT	Solid state	Na_2CO_3, Bi_2O_3, TiO_2	------	Anti-ferroelectric properties & Relaxor behavior	V.Dorcet et al. [135]
40.	BNT	Sol-gel	Na_2CO_3, Bi_2O_3, TiO_2, ethylene glycol, HNO_3	100-200nm	Thermal analysis by TGA & DTA	Chang Yeoul Kim et al. [136]
41.	Zr-doped BNT	Convention al oxide method	Na_2CO_3, Bi_2O_3, TiO_2, ZrO_2, ethanol	1 μm range	Study on Mechanical Properties	Anucha Watchraposo r et al. [137]
42.	Ca, Co, Mn doped $NiFe_2O_4$	Self-combustion	Ni nitrate, Fe nitrate, Ca nitrate, Co nitrate, Mn nitrate, NHO_3	100-500 nm	Gas sensing (LPG& Acetone)	N. Iftiimie et al. [138]
43.	BNT	Chemical solution deposition(CSD)	Bi nitrate, Na nitrate, Tetra butyl titanate, 2 methoxy ethanol,	----	Optical properties on Pt/ Ti/SiO2/Si(100) substrate	Ziping Cao et al. [139]
44.	NBT- $BaTiO_3$	TGG(Tem plated Grain growth)met	SrTiO3 plalets, Bi4Ti3O12 plalets	------	Dielectric, Piezoelectric and Electromechani cal properties	Huseyin Yitmaz et al. [140]

		hod & RTGG				
45.	BNT	Hydrothermal	NaOH, Bi_2O_3, TiO_2	400nm-nanaplate& 50-100 nm nanowire	Morphology-controlled synthesis and growth mechanism	Ran Lu Jie Yuan et al. [141]
46.	BNT	Sol-gel/ spincoating	Bi nitrate, $NaNO_3$, Titanium iso-propoxide	50-200 nm	Thermal analysis	T. Yu et al. [142]
47.	Cd substituted $NiFe_2O_4$	Sol-gel	Ni nitrate, Fe nitrate, Cd nitrate,	5.05 Å. 4.98 Å, 4.58 Å	n- type & p-type distinction by See back effect	Ande Ashok et al. [143]
48.	Co-doped $NiFe_2O_4$	Sol-gel/ auto combustion method	Ni nitrate, Fe nitrate, Co nitrate, NH4OH, Citric Acid	100 nm diameter of microstructure	P- Type Acetone sensor	Andris Sutka et al. [144]
49.	Al-doped $NiFe_2O_4$	Sol-gel method	Ni nitrate, Fe nitrate, $AlCl_3$ $.6H_2O$,citric acid, Ammonia	20-31 nm	Change in magnetic properties due to dopant	M.Mozaffari et al. [145]
50.	Zn-doped $NiFe_2O_4$	Sol-gel/ auto combustion	Ni nitrate, Fe nitrate, Zn Nitrate, NH4OH	62-66 % density	P- type Acetone gas sensing	A. Sutka et al. [146]

1.9.2 National Status

Table 1.3 Literature survey on various types on nanomaterials and their gas sensing applications at National level.

1.10 Present Challenges and Objective of the Thesis

S.No.	Material	Method used for synthesis	Chemical used	Crystallite Size or Thickness /porosity	Properties or application of the content	Reference
1.	$BaTiO_3$	Spray pyrolysis	Barium chloride, Titanium chloride	40 nm by XRD	Gas sensing (LPG) at room temperature, sensitivity 3.03 at 350ºC	Lalchand et al. [147]
2.	$BaTiO_3$ & CuO and CdO doped $BaTiO_3$	Solid state reaction	Barium hydroxide, titanium iso-isopropoxide, citric acid, cadmium nitrate, copper nitrate	65 nm for pure & 49 for doped by XRD	LPG Sensing and Influence of additives	G.N. Chaudhari et al. [148]
3.	$BaSrTiO_3$	Mechano-chemical Process/ Screen printing	Barium hydroxide, titanium dioxide, strontium hydroxide	264 nm by XRD	Ammonia Gas Sensing	G.H.Jain et al. [149]
4.	$BaTiO_3$	Solid state reaction/ Screen printing	BaCO3, TiO2, Terpinol	---	Humidity Sensing	R. Wagiran et al. [150]
5.	$BaTiO_3$	Sol gel/ spin coating	Barium acetate, glacial acetic acid and butoxide	0.5- 5 μm	I-V Characteristic, C-V Characteristics	Vijay Ramkrishna et al. [151]
6.	$BaTiO_3$	Ball milling	BaO, TiO_2	20-50 nm	Mechanochemical activation by thermal treatment	B.D. Stojonomic et al. [152]
7.	$BaTiO_3$	Spin coating	$BaTiO_3$ powder, HNO3	9.5 nm	Functional group identification by optical characterization	D. Lakshmi et al. [153]

8.	$SrFe_{12}O_{19}$	Sol-gel	Sr nitrates, Fe nitrates, D-Fructose	80-100nm, 40-70 nm	Thermal analysis by exothermic and endothermic reaction	Kanagesan et al. [154]
9.	$SrFe_{12}O_{19}$	Floating/ ball milling	Celeste, sodium carbonate blue dust	17 nm	B-H loop of sintered anisotropic strontium ferrite	R.K.Tiwary et al. [155]
10.	Ni & Zr-doped $SrFe_{12}O_{19}$	Sol-gel	Sr nitrates, Fe nitrates, Zr nitrate, Ni nitrate	2-4 % porosity	Effect of Ni- Zr Co-doping and dielectric and magnetic properties	Praveena et al. [156]
11.	Ca & Pb doped $SrFe_{12}O_{19}$	Solid state reaction	$SrCO_3$, $PbCO_3$, $CaCO_3$, $Fe2O_3$	---	Doping effect on dielectric and magnetic properties	Ashima Hooda et al. [157]
12.	Nd^+ doped $SrFe_{12}O_{19}$	Sol-gel	Sr nitrates, Fe nitrates, Nd nitrates, citric acid	31 nm	Magnetic measurement by VSM	Ankush Thakur et al. [158]
13.	$BaTiO_3$-$SrFe_{12}O_{19}$	Sol-gel	Barium acetate, n-buta0xide, 2-methoxy ethanol, Sr- nitrate, Fe nitrate	400-600 nm	Effect of constituent, phase variation, ferroelectric, dielectric and magnetic properties	Sadhana Katlakunta et al. [159]
14.	Al-doped $LaFeO_3$	Solid state reaction route	La_2O3, Al_2O_3, Fe_2O_3	---	Spontaneous polarization	S. Acharya et al. [160]
15.	Sr-doped $LaFeO_3$	Solution combustion method	La nitrates, Fe nitrates, Sr nitrates, diethyl oxalate, formaldehyde	0.067-0.028 μm	Change in surface area and properties on changing doping %	K.Surat et al. [161]
16.	$LaFeO_3$/ MWCNTs	Sonochemical/ sol-gel combustion	Fe nitrate, La nitrate, citric acid,	19.6 nm-19.4 nm	Microwave absorption	A. Mitra et al. [162]
17.	$LaFeO_3$/ TiO2	Hydrothermal method	Titanium isopropoxide, Fe nitrate, La nitrate, ethanol	60 nm	Photo-catalytic activity	R. Dhinesh Kumar et al. [163]
18.	$LaFeO_3$	Sol-gel/ dip coating	Fe nitrate, La nitrate, HNO_3	6.3 nm	Study of thermal stability, optical properties	M. Rajendran et al. [164]

19.	Ba doped BNT	Solid state reaction	Bi_2O_3, Na_2CO_3, $BaCO_3$	0.54- 0.56 μm	Dielectric and conductivity properties	Meera Rawat et al. [165]
20.	BNT	Ball milling	Na_2CO_3, Bi_2O_3, TiO_2, alcohol medium	100 nm	Phase transition by dielectric and internal friction	Venkata Raman et al. [166]
21.	NBT-BT	Pulsed laser deposition	Na_2CO_3, Bi_2O_3, TiO_2, $BaCO_3$	400nm – NBT & 50 nm BT thickness	Study of interdiffusion between the various layers	A.S. Daryapurkar et al. [167]
22.	BNT	Auto combustion technique/ solid state reaction	Na_2CO_3, Bi_2O_3, TiO_2	1.16 μm - 1.43μm	Dielectric properties	Tamaya Badapanda et al. [168]
23.	Ni, Co, Cd-doped $NiFe_2O_4$	Double sintered ceramic method	Nickel oxide, Cobalt oxide, Cd oxide, Iron oxide, Polyvinyl alcohol	33nm, 20nm, 18.49 nm	D.C. Resistivity determined by two probe method	B.A. Aldar et al. [169]
24.	Cu-doped $NiFe_2O_4$	Spray Pyrolysis	$NiCl_2.6H_2O$, $FeCl_3$, $CuCl_2$	46nm, 41nm,41nm	Ethanol gas sensing	Pratibha Rao et al. [170]
25.	Pd-doped $NiFe_2O_4$	Spray Pyrolysis	$NiCl_2.6H_2O$, $FeCl_3$, $PdCl_2$	46nm, 38nm, 35nm, 30nm	Ethanol Gas sensing	Pratibha Rao et al. [171]
26.	Zn doped $NiFe_2O_4$ incorporated with Pd	Sol-gel	$NiCl_2.6H_2O$, $FeCl_3 6H_2O$, $PdCl_2$, Zn $Cl_2.6H_2O$	39nm, 42nm,30nm ,31nm, 28nm	Ethanol Gas sensing	V.D.Kapse et al. [172]
27.	Zn-doped $NiFe_2O_4$	Co-precipitation method, sol-gel/ auto combustion	$NiCl_2.6H_2O$, $FeCl_3.6H_2O$, $ZnCl_2$. $6H_20$	-----	Ethanol Gas sensing	Deepshikha Rathore et al. [173]
28.	$NiFe_2O_4$ incorporated with Pd	Hydrothermal method	Ni nitrate, Fe nitrate, Aqueous Ammonia	11nm	N-type LPG Gas Sensor	L.Satyanaran et al. [174]
29.	$NiFe_2O_4$	Wet Co-precipitation method	Ni nitrate, Fe nitrate, NaOH	8-20 nm	Effect of sintering temperature, strain on structural, dielectric	Seema Joshi et al. [175]

					and magnetic properties	
30.	$NiFe_2O_4$ Si coated	Sol-gel Co-precipitation method	$NiCl_2.6H_2O$, $FeCl_3.6H_2O$, NaOH, oleic acid, silica gel	12-14 nm	Comparison of surface effect in SiO_2 coated & uncoated NiF	K.Nadeem et al. [176]
31.	Zn doped $NiFe_2O_4$	Sol-gel method	Ni nitrate, Fe nitrate, Zn Nitrate, citric acid, ethylene glycol	15-20 nm	Photocatalytic Degradation of Methylene blue	Rimi Sharma et al. [177]
32.	$NiFe_2O_4$	Co-precipitation method	Fe nitrate, Ni nitrate, citric acid	175- 275Å	p-type Chlorine Gas sensor	C.V. Gopal Reddy et al. [178]
33.	$LaFeO_3$	Auto combustion and modified penchini method	La nitrate, Iron nitrate, citric acid	46 nm	Butane sensor	K.K.Bhargav et al. [179]
34.	$LaFeO_3$	Microwave combustion synthesis	La nitrate, Iron nitrate, silver nitrate	57 nm	Magnetic behavior on silver doping	P.A. Desai et al. [180]

Nanostructured ferrites materials are the most propitious material for developing gas sensors because of their extraordinary property and twin behavior and there large much surface to volume ratio. We were aiming to investigate new materials which possess good sensing properties for the LPG concentration below LEL, with high sensitivity and % sensor response and low response time and recovery time. Stability of the sensor was checked by repeatability cycle after exposure to different LPG concentration and by ageing effect.

After literature survey, I found there is very less work going on design and development of an LPG sensor at room temperature below LEL. Ferrites show very good surface reactivity and possess different surface morphology and behaviour by varying parameters like pH, temperature, magnetic field etc. They are easy to synthesis, easy to dope easy to form nano-composite materials also. Therefore in this thesis ferrite material is synthesis by sol-gel and co-precipitation method. After this nano-sensors are fabricated using spin coating method are further it was characterized and used as LPG sensor. In this

thesis experimental investigation, films of nanosized spinels and orthoferrite and additives are used to enhance the properties of nanomaterial. Experiment is done at room temperature by measuring electrical properties of the sensor on exposure of LPG

The main goal of our present investigation is to design and fabricate an LPG sensor which would be robust, more sensitive with reduced response time, economically cheap and easy to fabricate than previously reported sensors.

1.11 Organization of the Thesis

This thesis contains eight chapters. Chapter 1 is the introductory part of nanomaterials, synthesis of nanoparticles and its application. It also focuses on the classification of ferrites and chemical gas sensor covering Liquefied Petroleum Gas Sensor in detail. Detailed investigation of synthesis and characterization of nanostructured perovskite Barium titanate used as an LPG sensor at room temperature is described in Chapter 2.It also contains the diagrammatic explanation of the set-up used throughout the experiment. Chapter 3 focuses on the synthesis of nanostructured hexagonal Strontium ferrite film using co-precipitation method followed by spin coating technique. A site substituted lead-free Bismuth sodium Titanate and its gas sensing properties has been depicted in chapter 4. Chapter 5 deals with the synthesis of silver (0.2 % and 0.4 %) substituted Nickel ferrite and also study on its change in the microstructure, optical properties and Gas sensing properties. Chapter 6 deals with the preparation and gas sensing properties of Lanthanum ferrite with reduced size and better response. Chapter7 summarize all nanostructured material $BaTiO_3$, $SrFe_{12}O_{19}$, $Bi_{0.5}$ $Na_{0.5}TiO_3$ Ag doped $NiFe_2O_4$ and $LaFeO_3$ synthesized during the work. It also contains a comparison chart showing a change in particle size, band gap, and percentage sensing response, sensitivity and response time. It also contains the guideline of the future work on multiferroic materials and their nanocomposite used as LPG sensor.

REFERENCES

1. A. Alivisatos, Semicontuctor clusters, nanocrystal and Quantum dots, Science, 271 (5251) (1996) 933-937.

2. R. Feynman, There's Plenty of Room at the Bottom, Eng. Sci. 23 (1960) 22-36.

3. J. Stohr, H.C. Siegmann, Magnetism: from fundamental to nanoscale dynamics, Springer 146 (2006) 33.

4. W. Kern, K. K. Schuegraf, Handbook of thin film Deposition and Techniques: Principles, Methods, Equipment and Applications (Krishna Seshan, Ed.) Norwich, N.Y. Noyes Publications/ William Andrew Pub. (2002) 11.

5. J.A. Thornton, J.E. Greene. Handbook of Deposition Technologies of thin films and coating (Rointan F. Bunshah, Ed.), Noyes publication, Park Ridge, New Jersey (1994) 275.

6. B. David, Nano type: the truth behind the nanotechnology buzz, Amherst, NY: Prometheus Books, (2006).

7. M.C. Roco, "Nanostructured Materials" (G.M.Chow and N.J. Noskovo, Eds), 3rdEdition, 3, Kluwer Academic, Boston, (1998) 71-92.

8. R.C. Shetty, Potential pitfalls of nanotechnology in its applications to medicine: immune incompatibility of nanodevices, Med. Hypotheses 65 (2005) 998-999.

9. J. Gangwar, B.K. Gupta, A.K. Srivastava, Prospects of Emerging Engineered Oxide Nanomaterials and their Applications, Defence Science Journal, 66 (4) (2016) 323-340.

10. W. Cao, O.K. Tan, Y. Duan, Y. Hu, W. Zhu, Nanomaterial Synthesis for Gas Sensing, Encyclopedia of Sensors, 6 (2006) 403-433.

11. X. Wang, J. Zhuang, Q. Peng, Y. Li, A general strategy for nanocrystal synthesis, Nature 437 (7055) (2005) 121-124.

12. W. Reddick and G. Amaratunga, Silicon surface tunnel transistor, Appl. Phys. Lett., 67(4) (1995) 494–496.

13. H. S. Lee, W. S. Um, K. T. Hwang, H. G. Shin, Y. B. Kim, and K. H. Auh, Ferroelectric properties of Pb(Zr,Ti)O_3 thin films deposited on annealed IrO_2 and Ir bottom electrodes, Journal of Vacuum Science and Technology A, 17(5) (1999) 2939–2943.

14. D.W, Johnson American Ceramic Society, Advances in ceramics: Ceramics Powder Science, Westerville, 21 (1987) 3-19.

15. E. Kanazawa, G. Sakai, K. Shimanoe, Y. Kanmura, Y. Teraoka, N. Miura, N. Yamazoe, Metal oxide semiconductor N_2O sensor for medical use. Sens. Actuat. B: Chem. 77 (2001) 72–77.

16. U. Kumar, S. Sikarwar, R. K. Sonker, B.C. Yadav, Carbon Nanotube: Synthesis and Application in the Solar cell, J. of Inorganic and organometallic polymers and material, 26(6) (2016) 1231-1242.

17. T.V. Duncan, Applications of nanotechnology in food packaging and food safety: Barrier materials, antimicrobials and sensors, Journal of Colloid and Interface Science 363 (2011) 1–24.

18. K. Kimura, in "Fine Particles: Synthesis and characterization and Mechanism of Growth" (Sugimoto Tadao, Ed.), Marcel Dekker, New York, (2000) 513.

19. O.K. Tan, W. Cao, Y. Hu, W. Zhu, Nanostructured oxides by high-energy ball milling technique: application as gas sensing materials, Solid-State Ionics 172 (2004) 309-331.

20. Y. Chen, C.P. Lie, H. Chen, Y. Chen, One-dimensional nanomaterial synthesized using high energy ball milling and annealing process, Science and Technology of Advanced Materials 7 (2006) 839-846.

21. A. Tischner, T. Maier, C. Stepper, A. Köck, Ultrathin SnO_2 gas sensors fabricated by spray pyrolysis for the detection of humidity and carbon monoxide. Sens. Actuat. B-Chem. 134 (2008) 796–802.

22. A.M. More, J. L. Gunjakar, C.D. Lokhande, Liquefied petroleum gas (LPG) sensor properties of interconnected web-like structured sprayed TiO_2 films, Sens. Actuators B 129 (2008) 671-677.

23. P.C. Zalm, Quantitative Sputtering, Surface and Interface Analysis, 11(2) (1983) 1-24.

24. D. B. Geohegan, Physics and Diagnostics of Laser Ablation plumepropagation for high Tc super conductor film growth, Thin solid film, 220 (1992) 138-145.

25. D.B. Geohegan, A. Puretzky, Laser Ablation plume thermalization dynamics in background gases: combined imaging, optical absorption and emission spectroscopy and ion probe measurements, Appl. Surf. Sci. 96-98, 131-138.

26. K.L. Choy, Chemical vapour deposition of coatings. Prog. Mater. Sci., 48 (2003) 57–170.

27. B.C. Yadav, S. Singh, A. Yadav, Nanonails structured ferric oxide thick film as room temperature liquefied petroleum gas LPG sensor, Applied Surface Science, 257 (2011) 1960-1966.

28. A. Drmota, M. Drofenik, A. Zidars, Synthesis and characterization of nano-crystalline strontium hexaferrite using the coprecipitation and microemulsion methods with nitrate precursors, Ceramics International, 38 (2012) 973–979.

29. R.E. Riman, W.L. Suchanek, M.M. Lencka, Hydrothermal crystallization of ceramics, Ann. Chim. Sci. Mat, 27(6) (2002) 15-36.

30. M. Zawadzki, J. Wrzyszcz, Hydrothermal synthesis of nanoporous Zinc aluminate with high surface area, Mate. Res. Bull. 35 (2000) 109-114.

31. L. GR, H. Xu, X. F. Lu, J. X. Feng, Y. X. Tong, C. Y. Su, Electrochemical synthesis of nanostructured materials for electrochemical energy conversion and storage, Nanoscale, 5 10 (2013) 4056-69,

32. M. Zayat, D. Levy, Blue $CoAl_2O_4$ particles prepared by the sol-gel and citrate gel methods, Chem. Mater., 12 (2000) 2763-69.

33. K. Takatori, T. Tani, N. Watanabe and N. Kamya, Preparation and characterization of nanostructured ceramic powder synthesised by emulsion combustion method, J. Nanoparticles, Res, 1 (1999) 197-201.

34. S. L. Kakani, A. Kakani, Alloys system, Phase diagram and phase transformation, Material Science, New Age International Publisher, Ch-9, (2004) 304.

35. S.L. Kakani, A. Kakani, Heat Treatment, Material Science,New Age International publisher, Ch-10, (2004) 322-333.

36. B.D. Cullity, Introduction to MagneticMaterials, Addition Wesley, Reading, M.A., (1972).

37. J. Livage, M. Henry, C. Sanchez, Sol-gel chemistry of transition metal oxide, Progress in Solid-State Chemistry,18 (1988) 259-341.

38. M. Marezio, J. P. Remeika, P. D. Dernier, The crystal chemistry of the rare earth orthoferrites, Acta Cryst., B, 26 (1970) 2008-2022.

39. M. Eibschutz, S. Shtrikman, D. Treves, Mossbauer studies of Fe ^{57} inorthoferrites, Phys. Rev., 156 (1967) 562-577.

40. N. Rezlescu, E. Rezlescu, F. Tudorache and D. Popa, Some spinel oxide compounds as reducing gas sensors, Sens. Trans. Journal 28 (2007) 1134-1142.

41. D.S. Mathew, R.S. Juang, An overview of the structure and magnetism of spinel ferrite nanoparticles and their structurein microemulsions, Chemical Engineering Journal, 129(1-3) (2007) 51-65.

42. M. Sugimoto, The past, present and future of ferrite, Journal of American Ceramic Society, 82(2) (1990) 269-280.

43. R. Valenzuela, Novel Application of Ferrites, Physics Research International, 2012 (2012) 1-9.

44. P. Kanhere, Z. Chen, A Review on Visible Light Active Perovskite-Based Photocatalysts, Molecules 19 (2014) 19995-20022.

45. H.J. Kim, J.H. Lee, Highly sensitive and selective gas sensors using p-type oxide semiconductors: Overview, Sens. Actuators B: Chem., 192 (2014) 607– 627.

46. J. Cadena, G.J. Riu, F.X. Rius. Gas sensors based on nanostructured materials. Analyst, 132 (2007) 1083-1099.

47. M. Schenk, A.R. Reichelt, An electron microphone as a force sensor for combined scanning probe microscopy. Ultramicroscopy, 65 (1996) 109–118.

48. F. He, Q. Huang, M. Qin, A silicon directly bonded capacitive absolute pressure sensor. *Sens. Actuator A: Phy.*, 35 (2007) 507–514.

49. C.T. Huang, C.L. Shen, C.F. Tang, S.H. Chang, A wearable yarn-based piezo-resistive sensor. *Sens. Actuator A: Phy.*, 141(2) (2008)396–403.

50. C.V.G. Reddy, S. V. Manorama, V.J. Rao, Preparation and characterization of ferrites as gas sensor materials, J. Mater. Sci. Lett. 19 (2000) 775-778.

51. S. Singh, B.C. Yadav, R. Prakash, B. Bajaj, J.R. Lee, Synthesis of nanorods and mixed shaped copper ferrite and their applications as liquefied petroleum gas sensor; App. Surf. Sci., 257 (2011) 10763-10770.

52. C. Peng, Principle and Application of Biomedical Sensors, Higher Education Press, Beijing, China, (2000) 157–160.

53. L.A. Mercante, V.P. Scagion, F.L. Migliorini, L.H.C. Mattoso, D.S. Correa Electrospinning-based (bio) sensors for food and agricultural applications: A review, Trends in Analytical Chemistry 91 (2017) 91-103.

54. G. Korotcenkov, B.K. Cho, Metal oxide composites in conductometric gas sensors: Achievements and challenges, Sens. Actuators B: Chem., 244 (2017) 182–210.

55. L. Gajdosik, Tin oxide Gas Sensors, Encyclopedia of Sensors, 10 (2006) 361-373.

56. K. Shimanoe, M. Yuasa, T. Kida, and N. Yamazoe, Semiconductor gas sensor using nano-sized oxide for high-sensitive detection of environment-related gases, in Proceedings of the IEEE International Conference on Nanotechnology Materials and Devices (2011)38–43.

57. G. Neri, Metal Doping in semiconductor Gas Sensors, Encyclopedia of Sensors, 6 (2006) 1-13.

58. T. Seiyama, A. Kato, K. Fujiishi, M. Nagatani, A new detector for gaseous components using semiconductive thin films. Anal. Chem., 34 (1962)1502–1503.

59. D.E. Williams, Semiconducting oxides as gas-sensitive resistors. Sens. Actuators B: Chem., 57 (1999) 1–19.

60. A.A. Tomchenko, G.P. Harmer, B.T. Marquis, J.W. Allen, Semiconducting metal oxide sensor array for the selective detection of combustion gases. Sens. Actuators B: Chem., 93 (2003) 126–134.

61. N. Yamazoe, K. Shimanoe, Theory of power laws for semiconductor gas sensors. Sens. Actuators B: Chem., 128 (2002) 566–573.

62. C. Massie, G. Stewart, G. M. Gregor, and J. R. Gilchrist, Design of a portable optical sensor formethane gas detection, Sens. Actuators B: Chem., 113 (2) (2006) 830–836.

63. S.C. Gadkari, M. Kaur, V.R. Katti, V.B. Bhandarkar, K.P. Muthe, S.K. Gupta, Solid State Sensors for H_2, H_2S and NH_3, Encyclopedia of Sensors, 10 (2006) 21-43.

64. R. Binions, H. Davies, A. Afonja, S. Dungey, D. Lewis, D. E. Williams, D.E, I.P. Parkin, Zeolitemodified discriminating gas sensors. J. Electrochem. Soc. 156 (2009) J46–J51.

65. R.K. Sonker, M. Singh, U. Kumar, B.C. Yadav, MWCNT doped ZnO nanocomposite thin film and it's sensing, Journal of Inorganic and Organometallic Polymers and Materials, 26 (6) (2016) 1434-40.

66. T. Takada, T. Fukunaga, and T. Maekawa, New method for gas identification using a singlesemiconductor sensor, Sens. Actuators B: Chem., 66(1–3) (2000) 22–24.

67. J.F. Currie, A. Essalik, and J.C. Marusic, Micromachined thin film solid state electrochemical CO_2, NO_2 and SO_2 gas sensors, Sens. Actuators B: Chem., 59, (2–3) (1999) 235–241.

68. R. Sathiyamoorthi, R. Chandrasekaran, T. Mathanmohan, B. Muralidharan, T. Vasudevan, Study of electrochemical-based gas sensors for fluorine and chlorine, Sens. Actuators B: Chem., 99 (2–3) (2004) 336–339.

69. I.D. Avramov, M. Rapp, A. Voigt, U. Stahl, M. Dirschka, Comparative studies on polymer coated SAW and STW resonators for chemical gas sensor applications. In Proceedings of 2000 IEE/EIA International Frequency Control Symposium and Exhibition, Kansas City, USA, 7–9, 58–65.

70. W. H King, Piezoelectric Absorption Detector, Analytical Chemistry, 36 (1964) 1735–1739.

71. M. Hoummadyy, A. Campitelliyz, W. Wlodarski, Acoustic wave sensors: design, sensing mechanisms and applications, Smart Mater. Struct. 6 (1997) 647–657.

72. E. Comini, Metal oxide nano-crystals for gas sensing. Analyt. Chim. Acta, 568 (2005) 28–40.

73. G. F. Fine, L. M. Cavanagh, A. Afonja, R. Binions, Metal Oxide Semi-Conductor Gas Sensors in Environmental Monitoring, Sensors, 10 (2010) 5469-5502.

74. C. Hagleitner, A. Heirlemann, H. Baltes, Single-Chip CMOS Capacitive Gas Sensor for Detection of Volatile Organic Compounds, IEEE Sensors Conference, 2 (2002) 1428-1431.

75. T. Ishihara, K. Kometani, Y. Mizuhara, Y. Takita, Capacitive type gas sensor for the selective detection of Carbondioxide, Sens. Actuators B: Chem., 13 (1-3) (1993) 470-472.

76. J. Courbat, D. Briand, J. Wollenstein, N.F. de Rooji, Colorimetric gas sensor based on optical waveguides made on plastic foil, Procedia Chemistry, 1(1) (2009) 576-579.

77. K. Schmitt, K. Trantik, C. Pannek, G. Sulz, J. Wollenstein, Colorimetric Gas Sensing with enhanced Sensitivity, Procedia Engineering,168 (2016) 1237-1240.

78. L. N. Acquaroli, R. Urteaga, and R. R. Koropecki, Innovative design for optical porous silicon gas sensor, Sens. Actuators B: Chem., 149(1) (2010) 189–193.

79. Z. Yunusa, M. Nizar H. A. Kaiser, Z. Awang, Gas Sensors: A Review, Sensors & Transducers, 168(4) (2014) 61-75.

80. C. Selvapriya, S. Sathya Prabha, M. Abdulrahim, K.C. Aarthi, LPG leakage monitoring and multilevel alerting system, International Journal of Engineering sciences & research technology, 2(11) (2013) 3287-3290.

81. A. Singh, A. Singh, S. Singh, P. Tandon, B.C. Yadav, R.R. Yadav, Synthesis, characterization and performance of zinc ferrite nanorods for room temperature sensing applications, Journal of Alloys and Compounds 618 (2015) 475–483.

82. M. Singh, B.C. Yadav, A. Ranjan, R.K. Sonker, M. Kaur, Detection of liquefied petroleum gas below lowest explosive limit (LEL) using nanostructured hexagonal strontium ferrite thin film, 249 (2017) 96-104.

83. A. Makeenkov, I. Lapitskiy, O. Kanischev, A. Somov, Infrared sensor for monitoring of LEL of flammable gases and vapours of flammable liquids, Procedia Engineering, 87 (2014) 995-998.

84. J. Huang, Q. Wan, Gas sensors based on semiconducting metal oxide one-dimensional nanostructures. Sensors, 9 (2009) 9903–9924.

85. C. Wang, L. Yin ,L. Zhang, D. Xiang, R. Gao, Metal Oxide Gas Sensors: Sensitivity and Influencing Factors, Sensors, 10 (2010) 2088-2106.

86. S. Capone, P. Siciliano, Gas Sensors from Nanostructured Metal Oxides, Encyclopedia of Nanoscience and Nanotechnology, 3 (2004) 769–804.

87. O.K. Varghese, C.A. Grimes, Metal Oxide Nanostructures as Gas Sensors, Encyclopedia of Nanoscience and Nanotechnology, 5 (2004) 505–521.

88. X. Liu, S. Cheng, H. Liu, S. Hu, D. Zhang, H. Ning, A Survey on Gas Sensing Technology, Sensors, 12 (2012) 9635-9665.

89. R.B. Waghulade, P.P. Patil, R. Pasricha, Synthesis and LPG sensing properties of nano-sized cadmium oxide, Talanta 72 (2007) 594-599.

90. B.C. Yadav, S. Singh, A. Yadav; Nanonails structured ferric oxide thick film as room temperature liquefied petroleum gas LPG sensor, Applied Surface Sci., 257 (2011) 1960-1966.

91. B.C. Yadav, S. Singh, A. Yadav, Nanonails structured ferric oxide thick film as room temperature liquefied petroleum gas LPG sensor, Applied Surface Science, 257 (2011) 1960-1966.

92. B.C. Yadav, S. Singh, A. Yadav, T. Shukla, Experimental investigations on nano-sized ferric oxide and its LPG sensing International Journal of Nanoscience,10(1) (2011) 1-5

93. A. W. Tuantranont, E. C. Sberveglieri, W. Wlodarski, Characterization of n-type and p-type semiconductor gas sensors based on NiO_x doped TiO_2 thin films. Thin Solid Films, 517 (2009) 2775–2780.

94. N. Barsan, N. and U. Weimar, Conduction model of metal oxide gas sensors, J. Electroceramic., 7(3) (2001) 143-167.

95. S. Singh, B.C. Yadav, M. Singh, R. Kothari, A review report on Nanostructured ferrites as Liquefied petroleum gas sensor, International Journal of Science, Technology and Society, 1(1) (2015) 5-22.

96. G. Korotcenkov, B.K. Cho Metal oxide composites in conductometric gas sensors: Achievements and challenges, Sens. Actuators B: Chem., 244 (2017) 182–210.

97. M.A. El Romb, D. Fasquelle, S. Deputier, M. Mascot, Elaboration and characterization of doped barium titanate films for gas sensing, AIP Conference Proceedings 1627 (2014) 25.

98. T. Ishihara, K. Kazuhiro, Y. Mizuhara, Y. Takita, Mixed oxide capacitor of CuO-$BaTiO_3$ as new type CO_2 Gas Sensor, J. of the Am. Ceram. Soc.75 (3) (1992) 613-618.

99. S. K. Hodak, T. Supasai, A. Wisitsoraat and Jose H. Hodak, Design of low-cost gas sensor based on $SrTiO_3$ and $BaTiO_3$ Films, J. of Nanosci. and Nanotechno. 10 (2010) 7236-7238.

100. K. Park, D.J. Seo, Gas sensing characteristics of $BaTiO_3$-based ceramics, Mater. Chem. Phys. 85 (2004) 47-51.

101. B. Ertug, The fabrication of porous Barium Titanate Ceramics via pore forming agents (PFAs) for thermistors and sensor applications, Powder metallurgy, Dr. Katsuyoshi Kondoh (Ed.) In Tech, (2012).

102. J.J. Urban, W.S. Yun, Q. Gu, H. Park, Synthesis of Single-Crystalline Perovskite Nanorods Composed of Barium Titanate and Strontium Titanate, J. Am. Chem. Soc. 9 124(7) (2002) 1187.

103. M.R.A. Bhuiyan, M.M. Alam, M.A. Momin, M. J. Uddin, M. Islam, Synthesis and Characterization of Barium titanate ($BaTiO_3$) nanoparticle, Int. J. of Mat. and Mechanical Engineering 1 (2012) 21-24.

104. H. A. Ávila, M. M. Reboredo, M. Castro, R. Parra, Nanofibers Obtained by Electrospinning of $BaTiO_3$ Particles Dispersed in Polyvinyl Alcohol and Ethyl cellulose, Materials Research. 16(4) (2013) 839-843.

105. O. Harizanov, A. Harizanova, T. Ivanova, Formation and Characterization of sol-gel barium titanate, Mat. Sci. and Engineering B 106 (2004) 191-195.

106. A. Kareiva, S. Tautkus, R. Papalaviciute, Sol-gel synthesis and characterization of barium titanate powders, J. of Mat. Sci. 34 (1999) 4853-4857.

107. H. Hayashi, T. Nakamura, T. Ebina, In-situ Raman spectroscopy of BaTiO3 particles for tetragonal–cubic transformation, Journal of Physics and Chemistry of Solids 74 (2013) 957–962.

108. T.T.V. Nga, T.D. Hien, N.P. Duong, T.D. Hoang, Structural and Magnetic Properties of SrLaxFe12-xO19 (x = 0 { 0.15) prepared by Using a Sol-Gel Method Journal of the Korean Physical Society, 52(5) (2008) 1474-1477.

109. J. Luo, Y. Xu, D. Gao, Synthesis, characterization, and microwave absorption properties of polyaniline/Sm-doped strontium ferrite nanocomposite, Solid State Sciences 37 (2014) 40-46.

110. S. Thompson, N.J. Shirtcliffe, E.S.O'Keefe, S. Appleton, C.C. Perry, Synthesis of $SrCoxTixFe(12-2x)O_{19}$ through sol–gelauto-ignition and its characterization, Magnetism and Magnetic Materials 292 (2005) 100–107.

111. A. Javidan, S. Rafizadeh, S.M.H. Mashkani, Strontium ferrite nanoparticle study: Thermal decomposition synthesis, characterization, and optical and magnetic properties, Materials Science in Semiconductor Processing 27 (2014) 468–473.

112. M. Azim, S. Atiq, S. Naseem, Structural and electrical characterization of lanthanum-doped strontium hexaferrites, Sci. Int. (Lahore), 24(4) (2012) 341-345.

113. M.K. Rahman, K.A. Bhatti, M.S. Rafique, A. Latif, S. Zia, Deposition and characterization of strontium hexaferrite ($SrFe_{12}O_{19}$) by PLD technique, Optics & Laser Technology 47 (2013) 361–365.

114. M. G. Hasab, Z. Shariati, Magnetic Properties of Sr-Ferrite Nano-Powder Synthesized by Sol-Gel Auto-Combustion Method, Molecular, Nuclear, Materials and Metallurgical Engineering 8(10) (2014) 1122-1125.

115. J.V.A. Santos, M.A. Macedo, F. Cunha, J.M. Sasaki, J.G.S. Duque, $BaFe_{12}O_{19}$ thin film grown by an aqueous sol–gel process, Microelectronics Journal 34 (2003) 565–567.

116. L. K. Lagorce, M. G. Allen, Magnetic and Mechanical Properties of Micromachined Strontium Ferrite/Polyimide Composites, Journal of microelectromechanical systems, 6(4) 1997.

117. S.M. Masoudpanah, S.A.S. Ebrahimi, Effect of citric acid content on the structural and magnetic properties of $SrFe_{12}O_{19}$ thin films, Thin Solid Films 520 (2011) 199–203.

118. T. Xia, L. Xua, C. Lib, Y. Wang, Magnetic composite $ZnFe_2O_4/SrFe_{12}O_{19}$, Preparation characterization, and photocatalytic activity under visible light, Applied Surface Science (2013) 684– 691.

119. T. Li, Y. Li, R. Wu, H. Zhou, X. Fang, S. Su, A. Xia, C. Jin, X. Liu, A solution for the preparation of hexagonal M-type $SrFe_{12}O_{19}$ ferrite using egg-white: Structural and magnetic properties, Magnetism and Magnetic Materials 393 (2015) 325–330.

120. W.M.S. Silva, N.S. Ferreira, J.M. Soares, R.B. daSilva, M.A. Macêdo, Investigation of structural and magnetic properties of nanocrystalline Mn-doped $SrFe_{12}O_{19}$ prepared by proteic sol–gel process, Journal of Magnetism and Magnetic Materials 395 (2015) 263–270.

121. Y. Yasukawa, X. Liu, A. Morisako, Observation of magnetic/electric domains and control of electric polarization by magnetic field in $BiFeO_3/SrFe_{12}O_{19}$ bilayers Journal of Magnetism and Magnetic Materials 327 (2013) 95–102.

122. Y. Wang, Q. Li, C. Zhang, B. Li, Effect of Fe/Sr mole ratios on the formation and magnetic properties of $SrFe_{12}O_{19}$ microtubules prepared by sol–gel method Journal of Magnetism and Magnetic Materials 321 (2009) 3368–3372.

123. A. Drmota, M. Drofenik, A. Z nidars, Synthesis and characterization of nano-crystalline strontium hexaferrite using the co-precipitation and micro emulsion methods with nitrate precursors, Ceramics International, 38 (2012) 973–979.

124. P. Song, H.H. Zhang, D. Han, J. Li, Z. Yang, Q. Wang, Preparation of biomorphic porous $LaFeO_3$by sorghum straw-biotemplate method and its acetone sensing properties, Sens. Actuators B: Chem., 196 (2014) 140–146.

125. P.V. Coutinho, F. Cunha, P. Barrozo Structural, vibrational and magnetic properties of the orthoferrites $LaFeO_3$and $YFeO_3$: A comparative study, Solid State Communications 252 (2017) 59–63.

126. Y.M. Zhang, J. Zhang, J.L. Chen, Z.Q. Zhu, Q.J. Liua, Improvement of response to formaldehyde at Ag–$LaFeO_3$ based gassensors through the incorporation of SWCNTs, Sens. Actuators B: Chem., 195 (2014) 509–514.

127. K.M.S. Khalil, W.A. Elhamdy, A.E.A.A. Said, A.A. Elsamahy, Porous $LaFeO_3$/Silica Nanocomposites via Sol-Gel Mixing Involving Citric Acid, Chemistry, Colloids and Surfaces A: Physicochem. Eng. Aspects 506 (2016) 840–848.

128. S. Phokha, S. Pinitsoontorn, S. Rujirawat, S. Maensiri, Polymer pyrolysis synthesis and magnetic properties of $LaFeO_3$ nanoparticles, Physica B 476 (2015) 55–60.

129. Y. Pei, Y. Li, J.Y. Che, W. Shen, Y. Wang, S. Yang ,S. Han, Study on the high-temperature electrochemical performance of perovskite-type oxide $LaFeO_3$ with carbon modification, International journal of hydrogen energy 40 (2015) 8742-8749.

130. Y. Yuana, Z. Donga, Y. Lia, L. Zhang, Y. Zhao, B. Wanga, S.Han, Electrochemical properties of $LaFeO_3$-rGO composite, Progress in Natural Science: Materials International 27 (2017) 88–92.

131. Q. Peng, B. Shan, Y. Wen, R. Chen, Enhanced charge transport of $LaFeO_3$ via transitionmetal (Mn, Co, Cu) doping for visible light photoelectron chemical water oxidation, International journal of hydrogen energy 40 (2015) 15423-15431.

132. H. Zhang, P. Song, D. Han, Q. Wang, Synthesis and formaldehyde sensing performance of $LaFeO_3$ hollow nanospheres, Physica E 63 (2014) 21–26.

133. H. Xiao, C. Xue, P. Song, J. Li, Q. Wang, Preparation of porous $LaFeO_3$microspheres and their gas-sensing property, Applied Surface Science 337 (2015) 65–71.

134. X. Ge, Y. Liu, X. Liu, Preparation and gas sensitive properties of $LaFe_{1-Y}Co_YO_3$ semiconducting materials, Sens. Actuators B: Chem., 79 (2001) 171-174.

135. V. Dorcet, G. Trolliard, P. Boullay, The structural origin of the antiferroelectric properties and relaxor behavior of $Na_{0.5}Bi_{0.5}TiO_3$, Journal of Magnetism and Magnetic Materials 321 (2009) 1758–1761.

136. C.Y. Kim, T. Sekino, K. Niihara, Synthesis of bismuth sodium titanate nanosized powders by solution/ sol-gel process, Journal of American Ceramic Society 86(9) (2003) 1464-67.

137. A. Watcharapasorn, S. Jiansirisomboon, T. Tunkasiri, Microstructures and Mechanical Properties of Zirconium-Doped Bismuth Sodium Titanate, Ceramics Chiang Mai J. Sci. 33(2) (2006) 169-17.

138. N. Iftimie, E. Rezlescua, P. D. Popaa, N. Rezlescua, Journal of optoelectronics and advanced materials, Gas sensitivity of nanocrystalline nickel ferrite 8(3) (2006) 1016–1018.

139. Z. Caoa, A. Ding, X. He, W. Cheng, P. Qiu, Optical properties of BNT thin films grown on Pt/Ti/SiO2/Si(100) substrates by a CSD processing, Journal of Crystal Growth 270 (2004) 168–173.

140. H. Yilmaz, S.T. Mckinstry, G. l. messing, (Reactive templated grain growth of textured sodium bismuth titanate ($Na_{1/2}$ Bi $_{1/2}$ TiO_3-$BaTiO_3$) ceramics— II dielectric and piezoelectric properties, Journal of electroceramics, 11 (2003) 217–226.

141. R. Lu, J. Yuan, H. Shi, B. Li, W. Wang, D. Wang, M. Cao, Morphology-controlled synthesis and growth mechanism of lead-free bismuth sodium titanate nanostructures via the hydrothermal route, Cryst Eng Comm, 15, (2013) 3984–3991.

142. T. Yu, K.W. Kwok, H.L.W. Chan, Preparation and properties of sol–gel-derived $Bi_{0.5}$ $Na_{0.5}$ TiO_3 lead-free ferroelectric thin film, Thin Solid Films 515 (2007) 3563–3566.

143. A. Ashok, T. Somaiah, D. Ravinder, C. Venkateshwarlu, C.S. Reddy, K.N. Rao, M. Prasad, Electrical Properties of Cadmium Substitution in Nickel Ferrites, World Journal of Condensed Matter Physics, 2 (2012) 257-266.

144. A. Sutka, G. Mezinskis, A. Lusis, M. Stingaciu, Sensors and Actuators B: Chemical, Gas sensing properties of Zn-doped p-type nickel ferrite, 171–172 (2012) 354– 360.

145. M. Mozaffari , Z. Abooalizadeh, J. Amighian, Investigation of magnetic properties of Al substituted nickel ferrite nanopowders synthesized by the sol–gel method, Journal of Magnetism and Magnetic Materials 323 (2011) 2997–3000.

146. A. Sutka, R. Pärna, G. Mezinskis, V. Kisand, Effects of Co ion addition and annealing conditions on nickel ferrites gas response, Sens. Actuators B: Chem., 192 (2014) 173–180.

147. L. A. Patil, D. N. Suryawanshi, I. G. Pathan, D.G. Patil, Effect of firing temperature on gas sensing properties of nanocrystalline perovskite $BaTiO_3$ thin films prepared by spray pyrolysis techniques, Sens. Actuators B: Chem., 195 (2014) 643-650.

148. G.N. Chaudhari, D.R. Bambole, A.B. Bodade, Structural and gas-sensingbehaviour of nanocrystalline $BaTiO_3$ based liquid petroleum gas sensors, Vacuum, 81 (2006) 251-256.

149. G.H. Jain, L.A. Patil, U.P. Mulik, K.R Patil, studies on gas sensing performance of pure and modified barium strontium titanate thick film resistors, Bull. Mater. Sci. 30(1) (2007) 9-17.

150. R. Wagiran, W.S. Wan Zaki, S.B. M. Noor, A.H. Shaari, I. Ahmad, Characterization of Screen printed $BaTiO_3$ thick film humidity sensor, Int. J of Eng. and Techno., 2(1) (2005) 22-26.

151. V.R. Chinchamalatpure, S.A. Ghosh, G.N. R. Chaudhari, Synthesis and Electrical Characterization of BaTiO3 Thin Films on Si(100), Materials Sciences and Applications, 1 (2010) 187-190.

152. B.D. Stojanovic, A. Z. Simoes, C. O. Paiva-Santos, C. Jovalekic, V.V. Mitic, J.A. Varela, Mechanochemical synthesis of barium titanate, Journal of the European Ceramic Society 25 (2005) 1985–1989.

153. D. Lakshmi, V. M. Priya, J. Shanthi, International journal of information technology & computer sciences study of barium titanate thin films by spin coating technique, 2(1) (2014) 301-303.

154. K. Samikannu, J. Sinnappan, S. Mannarswamy, T. Chinnaswamy, K. Thirunavukarasu, Synthesis and Magnetic Properties of Conventional and Microwave

Calcined Strontium Hexaferrite Powder, Materials Sciences and Applications, 2 (2011) 638-642.

155. R.K. Tiwary, S.P. Narayan, O.P. Pandey, Preparation of Strontium hexaferrite magnets from celestite and blue dust by mechanochemical route, Mining and Metallurgy 44 B (2008) 91–100.

156. P. Kuruva, P.R. Matli, B. Mohammad, S. Reddigari, S. Katlakunta, Effect of Ni–Zr codoping on dielectric and magnetic properties of $SrFe_{12}O_{19}$ via sol–gel route, Journal of Magnetism and Magnetic Materials 382 (2015)172–178.

157. A. Hooda, S. Sanghi, A. Agarwal, R. Dahiya, Crystal structurefinement, dielectric and magnetic properties of Ca/Pb substituted $SrFe_{12}O_{19}$ hexaferrites, Journal of Magnetism and Magnetic Materials 387 (2015) 46–52.

158. A. Thakur, R.R. Singh, P.B. Barman, Synthesis and characterizations of Nd^{3+} doped $SrFe_{12}O_{19}$ nanoparticles, Materials Chemistry and Physics 141 (2013) 562-569.

159. S. Katlakunta, P. Raju, S. S. Meena , S. Srinath, R. Sandhya, P. Kuruva, S.R. Murthy, Multi ferric properties of microwave sintered $BaTiO_3$–$SrFe_{12}O_{19}$ composites, Physica B, 448 (2014) 323–326.

160. S. Acharya, P.K. Chakrabarti, Some interesting observations on the magnetic and electric properties of Al^{3+} doped lanthanum orthoferrite ($La_{0.5}Al_{0.5}FeO_3$), Solid State Communications 150 (2010) 1234-1237.

161. K. Suresha, T.S. Panchapagesan, K.C. Patil, Synthesis and properties of $La_{1-x}Sr_xFeO_3$, Solid State Ionics 126 (1999) 299-305.

162. A. Mitra, A.S. Mahapatra, A. Mallick, P.K. Chakrabarti, Enhanced microwave absorption and magnetic phase transitions of nanoparticles of multiferroic $LaFeO_3$ incorporated in multiwalled carbon nanotubes (MWCNTs), Journal of Magnetism and Magnetic Materials 435 (2017) 117–125.

163. R. D. Kumar, R. Thangappan, R. Jayavel, Synthesis and characterization of $LaFeO_3/TiO_2$ nanocomposites for visible light photocatalytic activity, Journal of Physics and Chemistry of Solids 101 (2017) 25–33.

164. M. Rajendran, M. G. Krishna, A.K. Bhattacharya, Low temperature preparation of orthoferrite thin-films by an inorganic sol-gel process, Thin Solid Films 385 (2001) 230-233.

165. M. Rawat, K. L. Yadav, A. Kumar, P. K. Patel, N. Adhlakha, J. Rani, Structural, dielectric and conductivity properties of Ba^{2+} doped $(Bi_{0.5}\ Na_{0.5})TiO_3$ ceramic. Adv. Mat. Lett. 3 (4) (2012) 286-292.

166. V. R. Mudinepalli, N. R. Reddy, W. C. Lin, K.V. Siva Kumar, B.S. Murty, Phase transitions of the ferroelectrics $(Bi_{0.5}\ Na_{0.5})TiO_3$by dielectric and internal friction measurement. Adv. Mater. Lett. 6(1) (2015) 27-32.

167. A.S. Daryapurkar, J.T. Kolte, P. Gopalan, Growth and Characterization of $Na_{0.5}Bi_{0.5}$ TiO_3 Thin Films with $BaTiO_3$ Buffer Layer (Study of Au/$Na_{0.5}\ Bi_{0.5}\ TiO_3$/$BaTiO_3$/Pt Capacitor), Ferroelectrics, 44(1) 46-55.

168. T. Badapanda, S. Venkatesan, S. Panigrahi, P. Kumar, Processing and Application of Ceramics, Structure and dielectric properties of bismuth sodium titanate ceramic prepared by auto-combustion technique, 7(3) (2013) 135–141.

169. B. A. Aldar, R. K. Pinjari, N. M. Burange, Electric and Dielectric behavior of Ni-Co-Cd Ferrite, IOSR Journal of Applied Physics (IOSR-JAP).

170. P. Rao, R.V. Godbole, S. Bhagwat, Copper doped nickel ferrite nano-crystalline thin films: A potential gas sensor towards reducing gases, Materials Chemistry and Physics 171 (2016) 260-266.

171. P. Rao, R.V. Godbole, S. Bhagwat, Nanocrystalline Pd:$NiFe_2O_4$ thin films: A selective ethanol gassensor, Journal of Magnetism and Magnetic Materials 416 (2016) 292–298.

172. V.D. Kapse, S.A. Ghosh, F.C. Raghuwanshi, S.D. Kapse, U.S. Khandekard Nanocrystalline $Ni_{0.6}Zn_{0.4}Fe_2O_4$: A novel semiconducting material for ethanol detection, Talanta 78 (2009) 19–25.

173. D. Rathore, R. Kurchania, R.K. Pandey, Fabrication of $Ni_{1-x}Zn_xFe_2O_4$ (x = 0, 0.5 and 1) nanoparticles gas sensor for some reducing gases, Sens. Actuators A: Phy., 199 (2013) 236– 240.

174. L. Satyanarayana, K. M. Reddy, S. V. Manorama, Nanosized spinel $NiFe_2O_4$: A novel material for the detection of liquefied petroleum gas in air, Materials Chemistry and Physics 82 (2003) 21–26.

175. S. Joshi, M. Kumar, S. Chhoker, G. Srivastava, M. Jewariya,V.N. Singh, Structural, magnetic, dielectric and optical properties of nickel ferrite nanoparticles synthesized by co-precipitation method, Journal of Molecular Structure 1076 (2014) 55–62.

176. K. Nadeem, H. Krenn, W. Sarwar, M. Mumtaz, Comparison of surface effects in SiO_2 coated and uncoated nickel ferrite nanoparticles, Applied Surface Science 288 (2014) 677– 681.

177. R. Sharma, S. Singh, Structural, magnetic and electrical properties of zinc doped nickel ferrite and their application in photocatalytic degradation of methylene blue, Physica B, 414 (2013) 83–90.

178. C.V.G. Reddy, S.V. Manorama,V.J. Rao, Semiconducting gas sensor for chlorine based on inverse spinel nickel ferrite, Sens. Actuators B: Chem., 55 (1999) 90–95.

179. K.K. Bhargav, A. Maity, S. Ram, S.B. Majumder, Low temperature butane sensing using catalytic nano-crystalline lanthanum ferrite sensing element, Sensors and Actuators B 195 (2014) 303–312.

180. P.A. Desai, A. A. Athawale, Microwave Combustion Synthesis of Silver Doped Lanthanum Ferrite Magnetic Nanoparticles, Defence Science Journal, 63(3) (2013) 285-291.

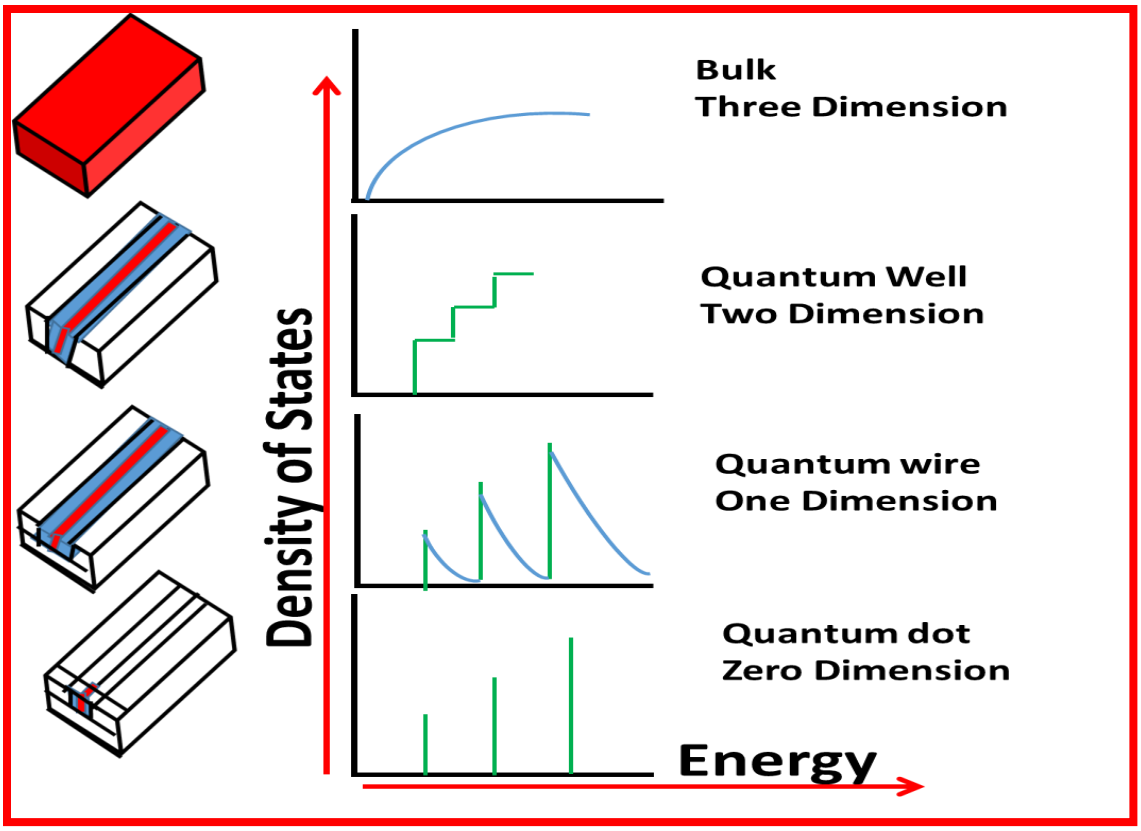

Fig.1.1 3D, 2D, 1D and 0D materials along with their density of state curves

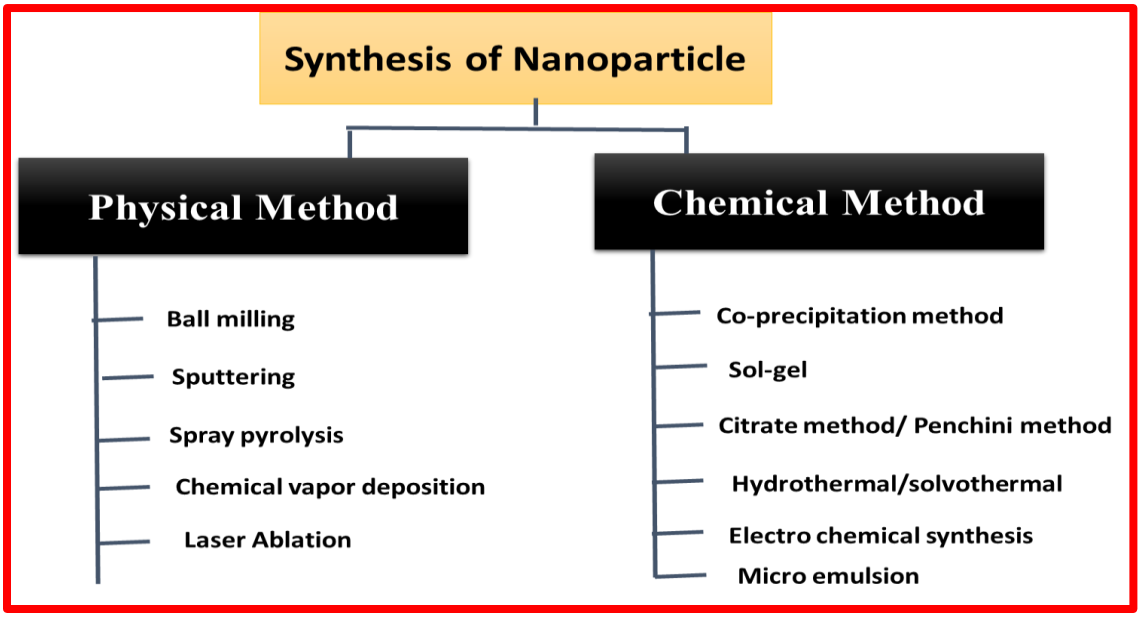

Fig.1.2 Classification of synthesis of nanomaterial

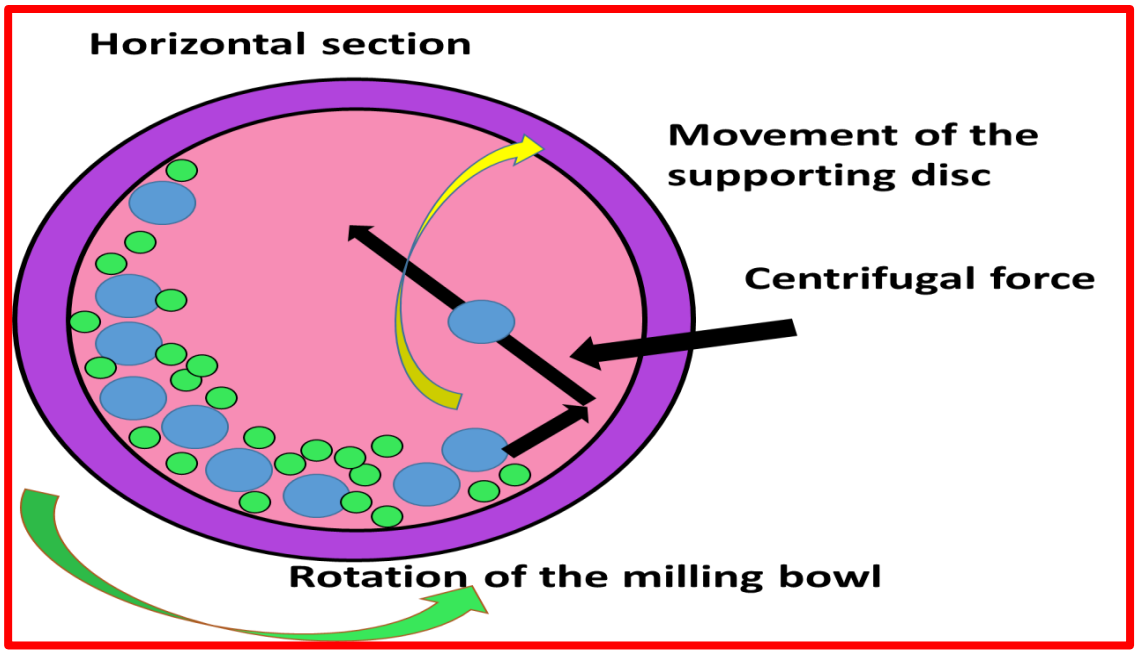

Fig.1.3 Ball milling phenomenon showing opposite direction of the disc and planetary ball

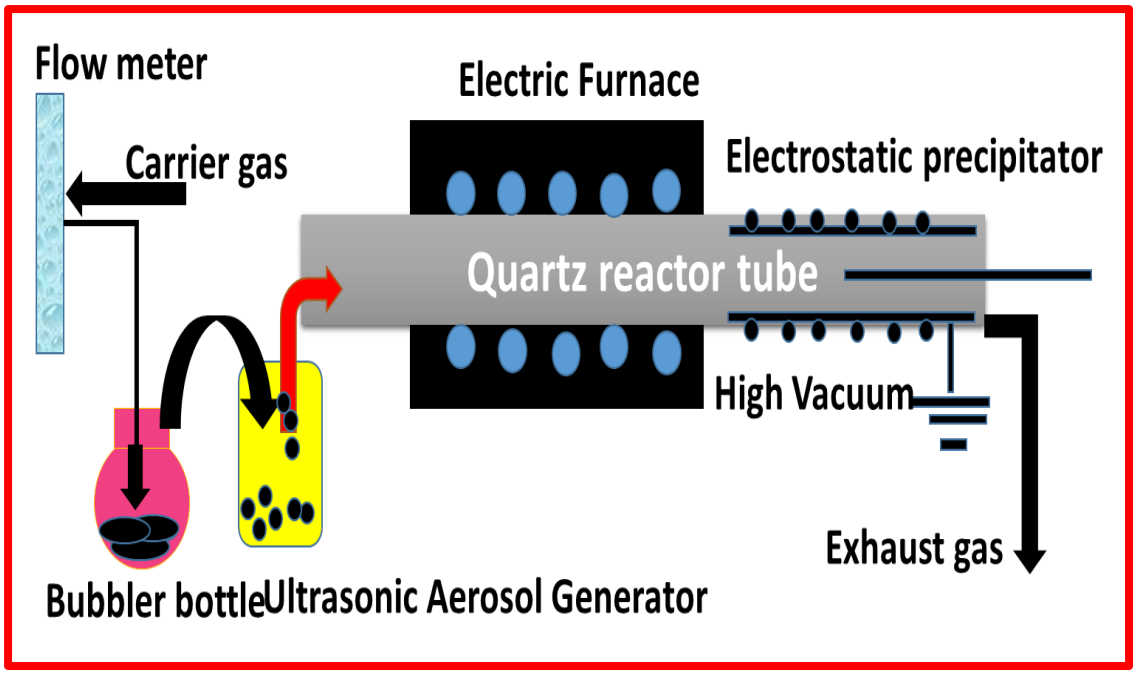

Fig. 1.4 Schematic diagram of Pyrolysis Method

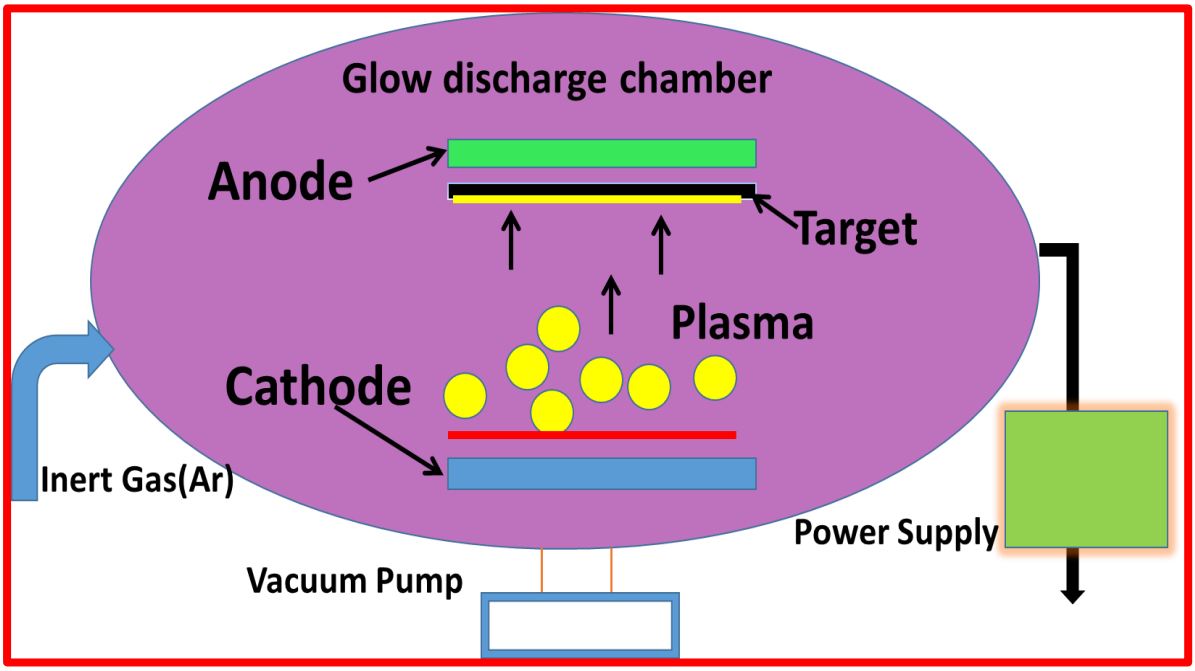

Fig. 1.5 Schematic diagram of Sputtering

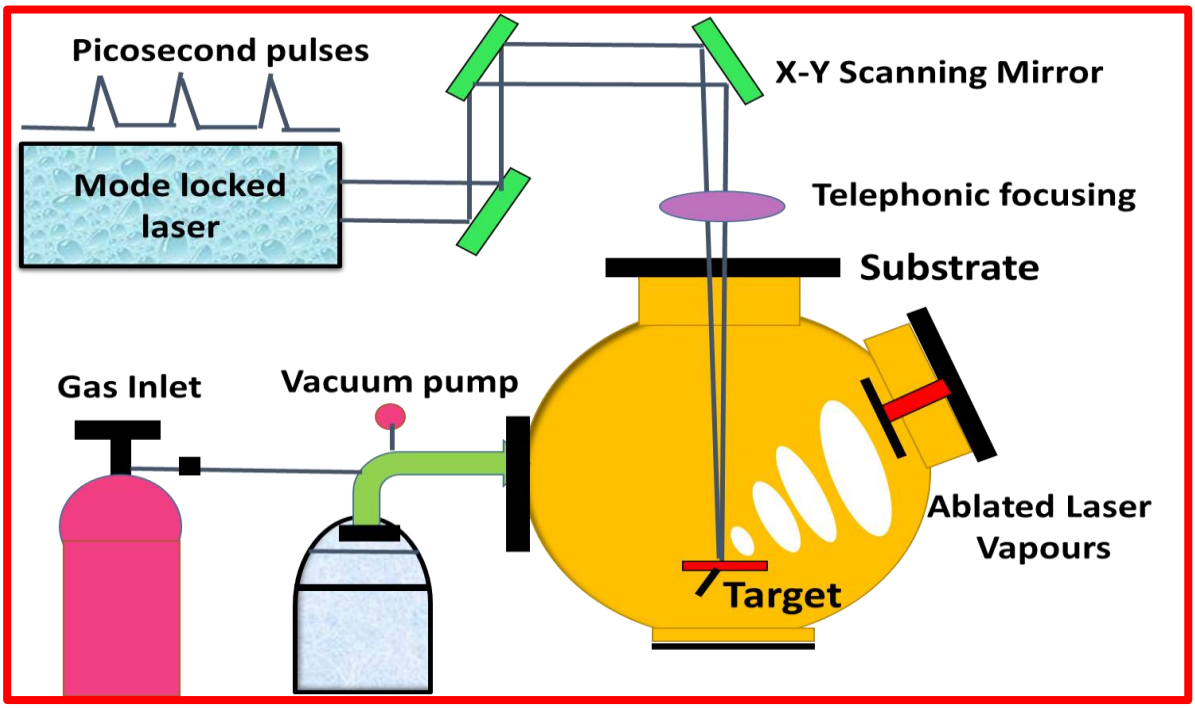

Fig.1.6 Schematic diagram of Laser Ablation Method

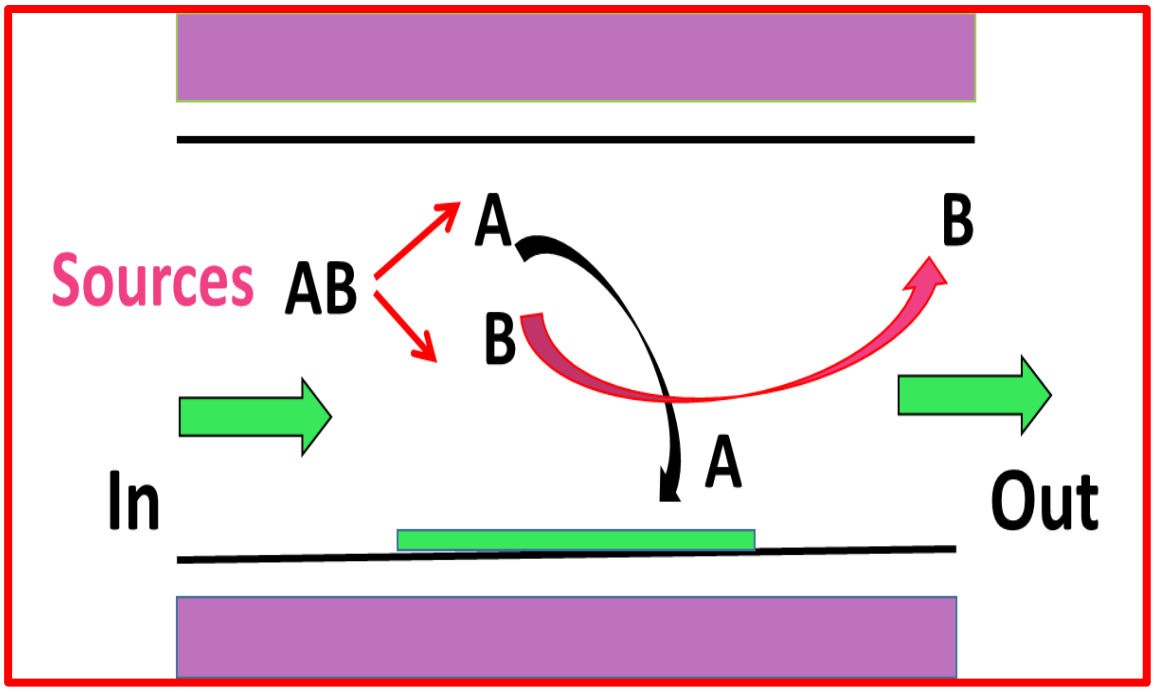

Fig.1.7. Schematic diagram of mechanism of Chemical Vapour Deposition

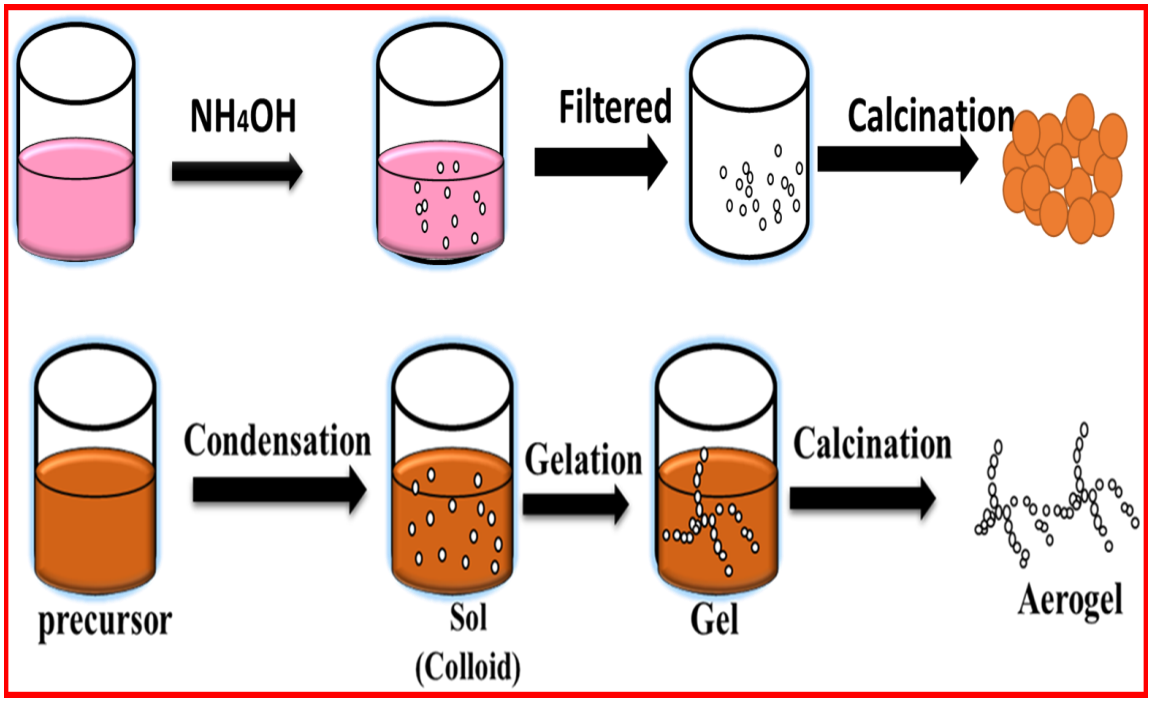

Fig. 1.8 Comparison between co-precipitation method and sol-gel method

.

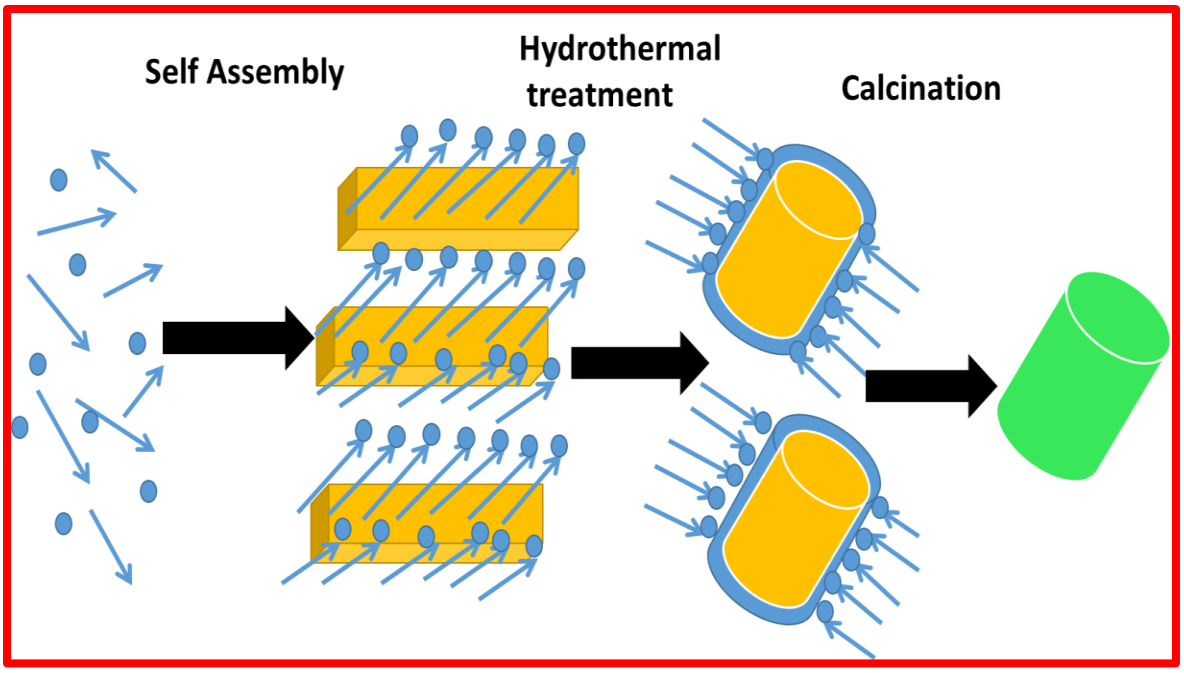

Fig.1.9 Schematic diagram of mechanism of Hydrothermal Process

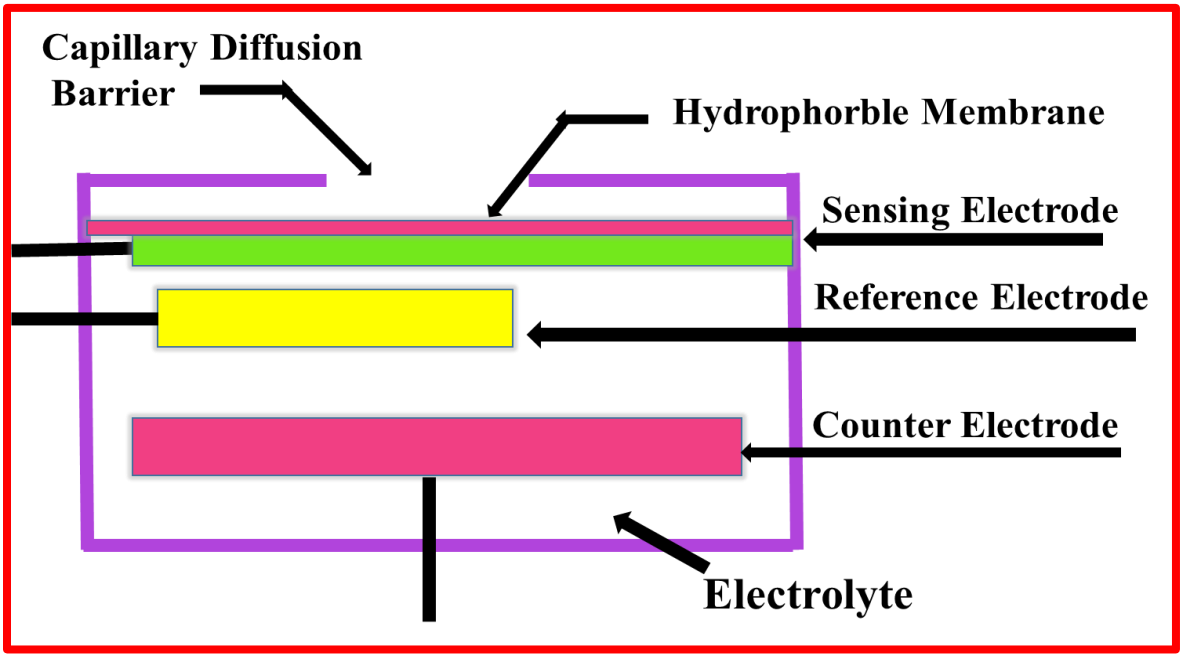

Fig.1.10 Schematic diagram of mechanism for electrochemical process

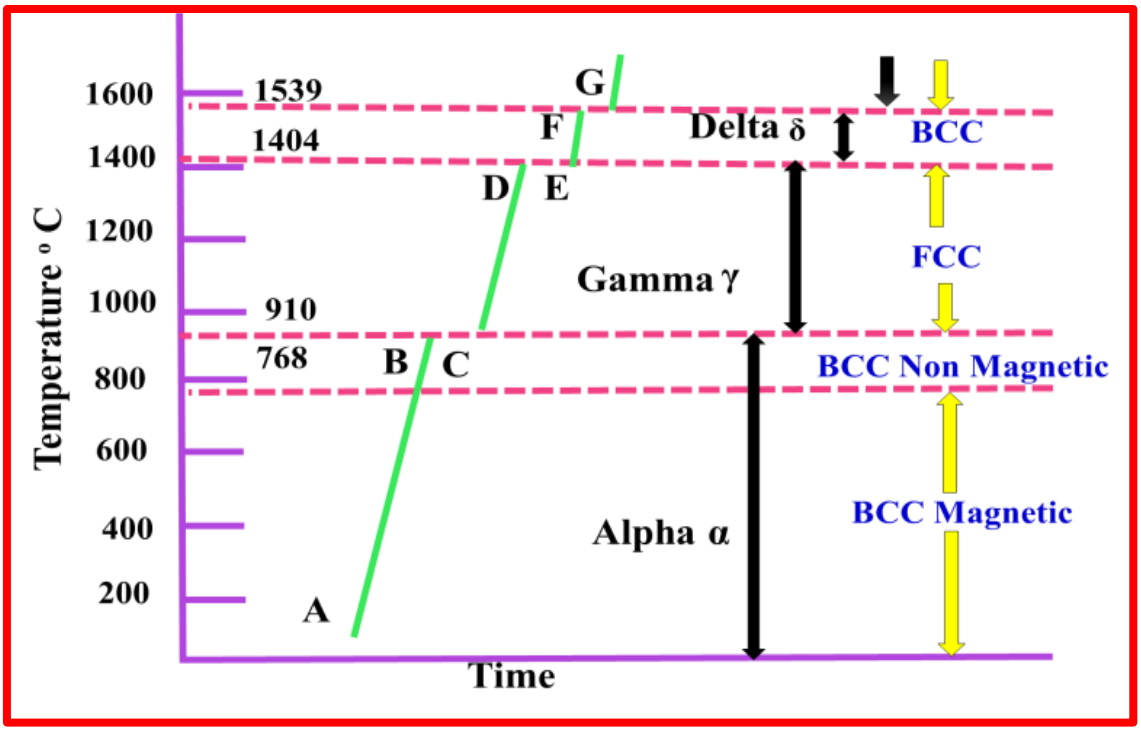

Fig.1.11 Ideal heating curve for pure iron

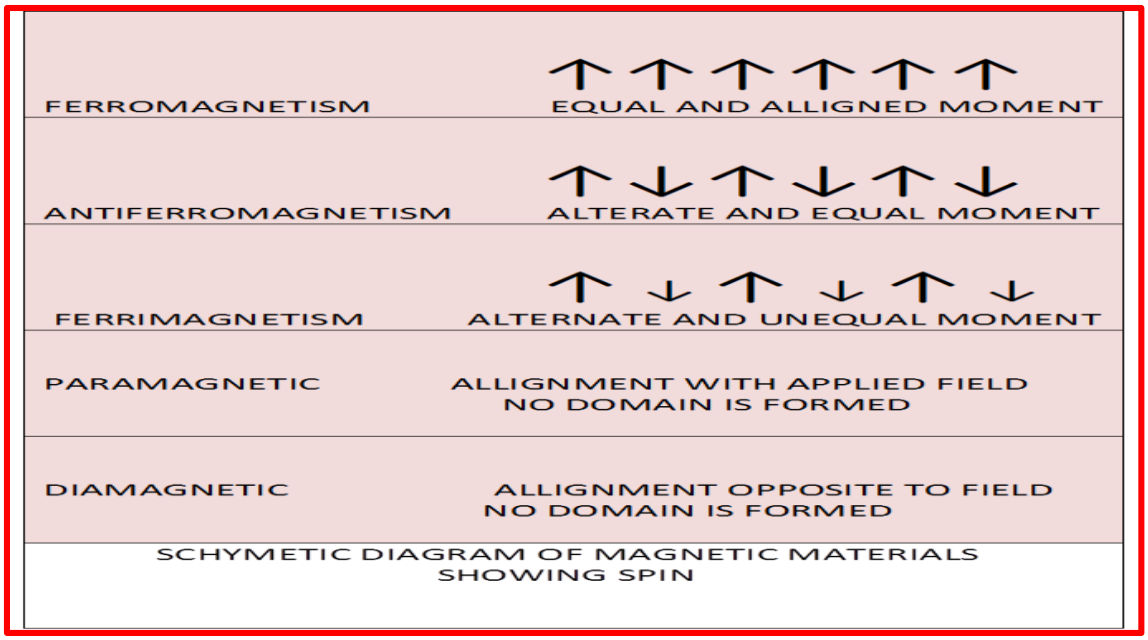

Fig. 1.12 Schematic diagram of magnetic materials showing spin

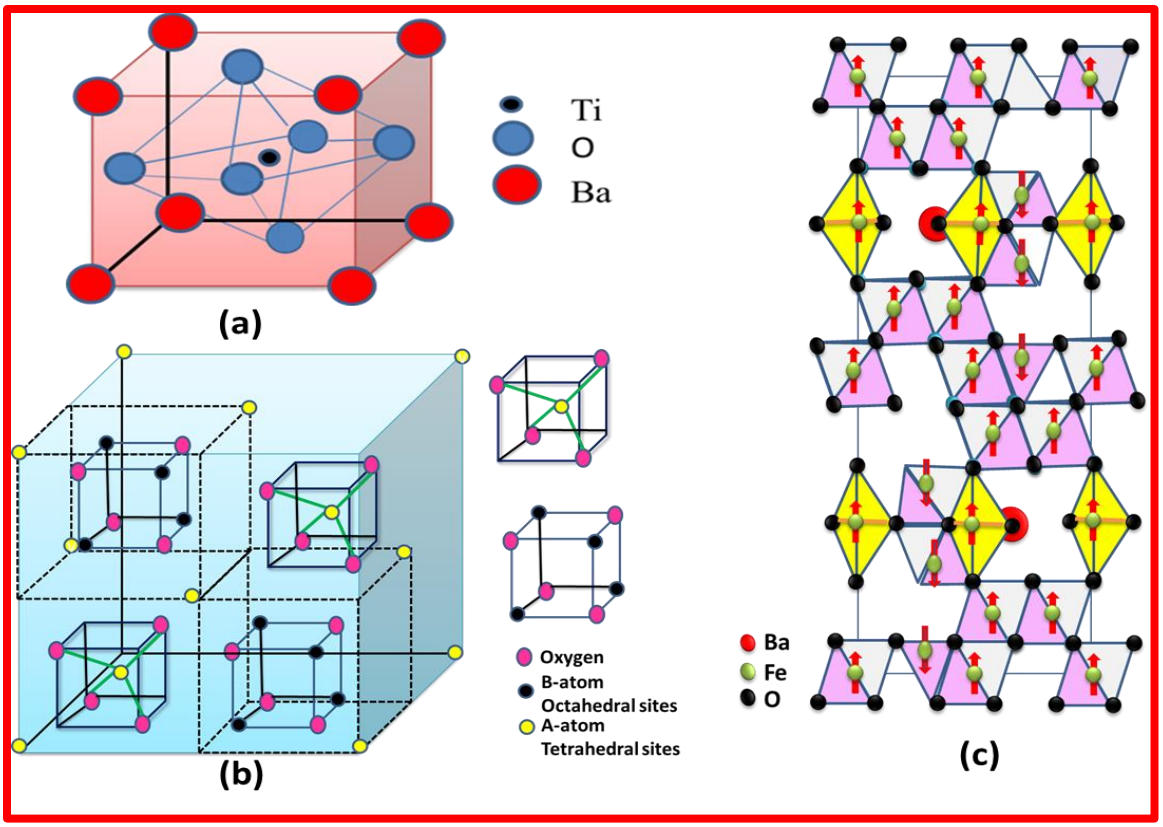

Fig.1.13 Crystal structures of (a) Perovskite, (b) Spinel ferrite & (c) Hexaferrite

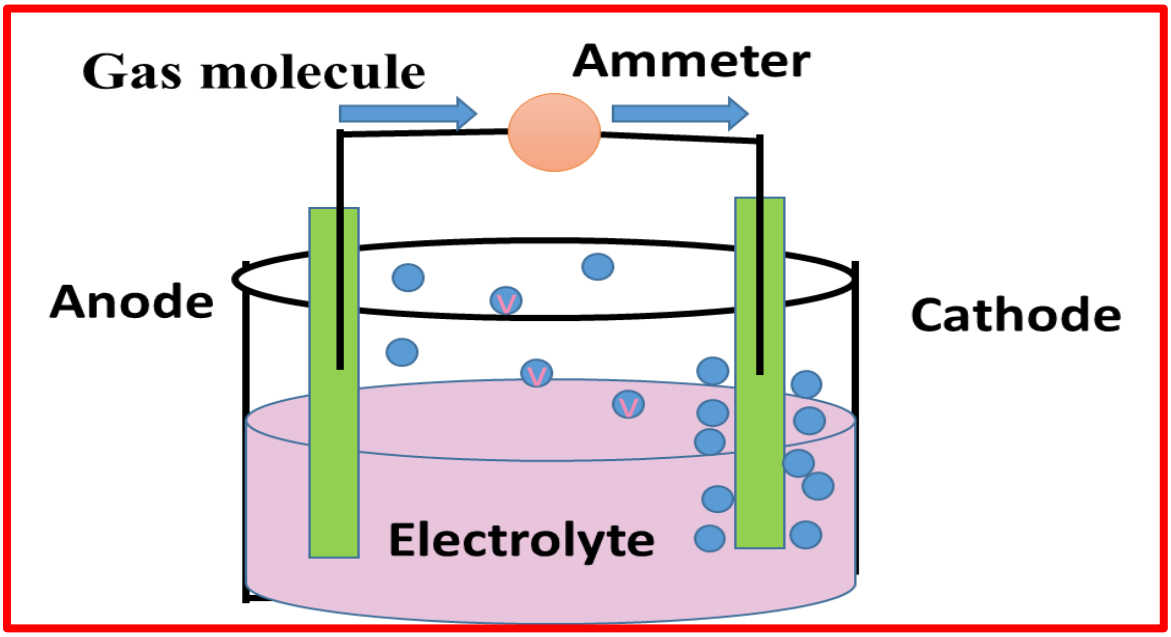

Fig.1.14 Schematic diagram of electrochemical gas sensor

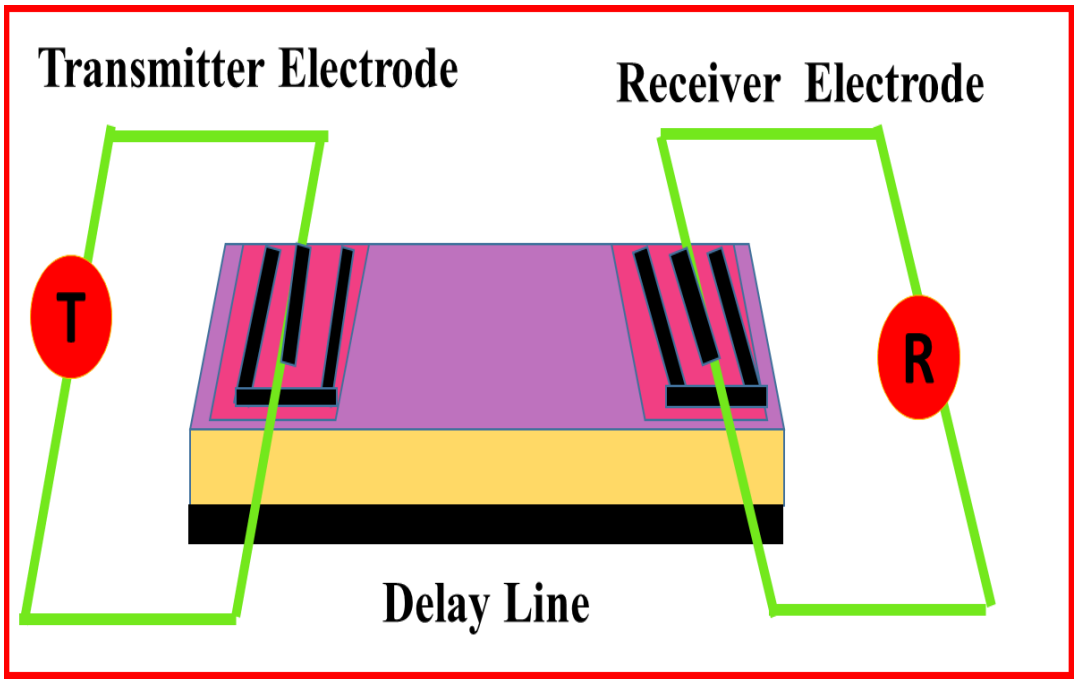

Fig.1.15 Schematic diagram of surface acoustic gas sensor

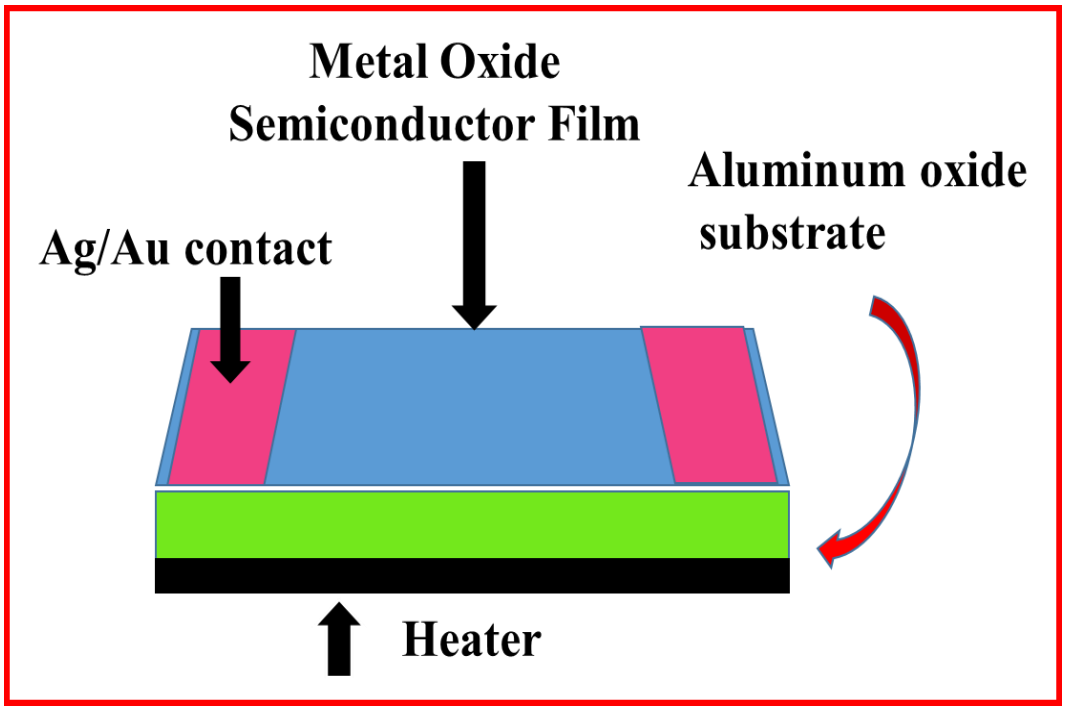

Fig 1.16 Schematic diagram of metal oxide gas sensor

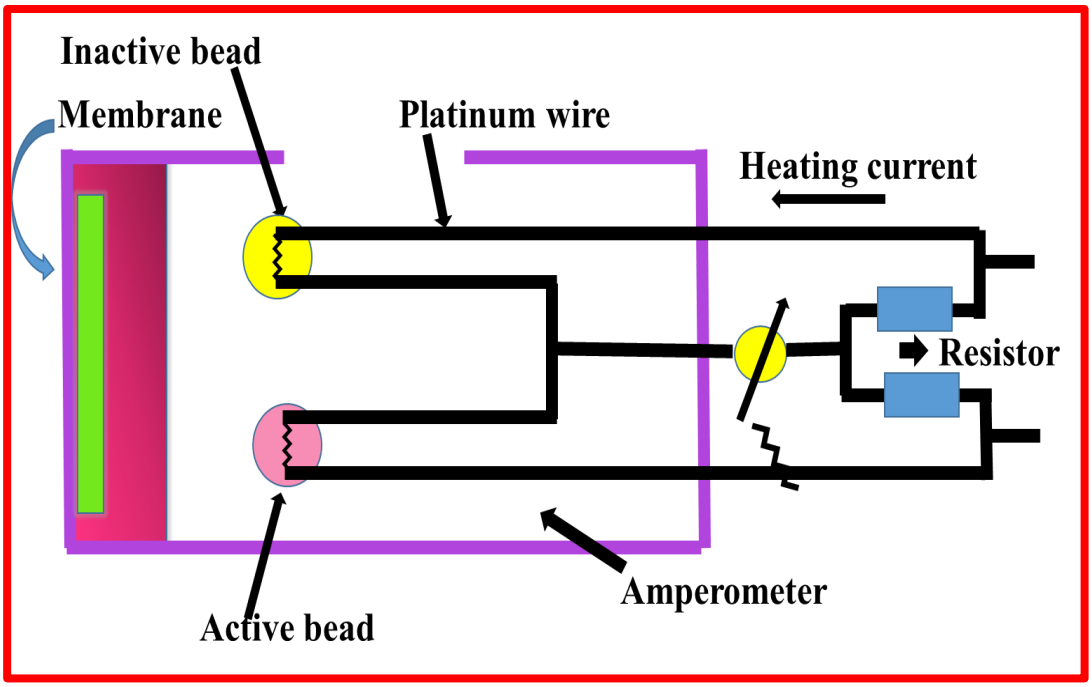

Fig.1.17 Schematic diagram of calorimetric gas sensor

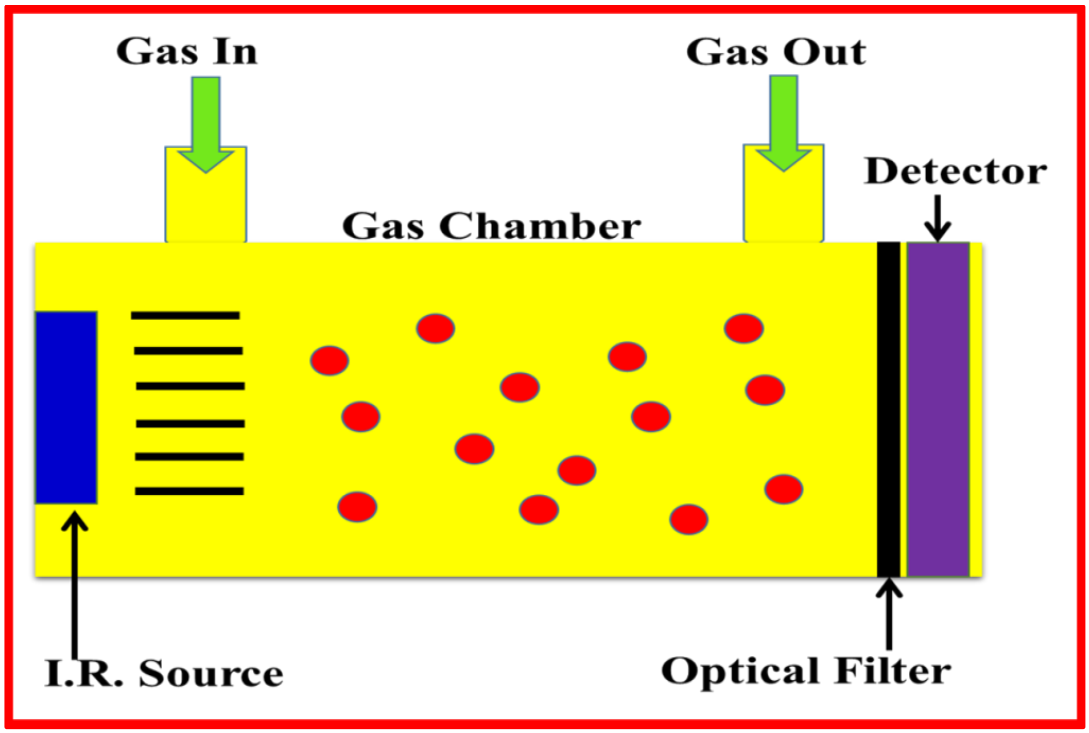

Fig.1.18 Schematic diagram of optical gas sensor

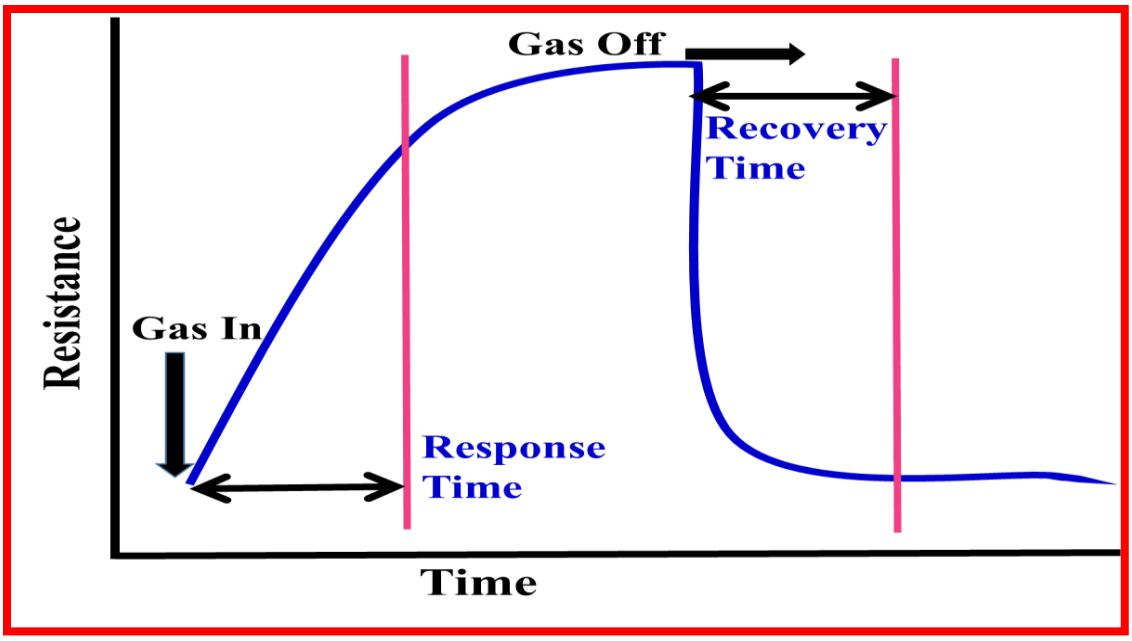

Fig. 1.19 Schematic response of a gas sensor

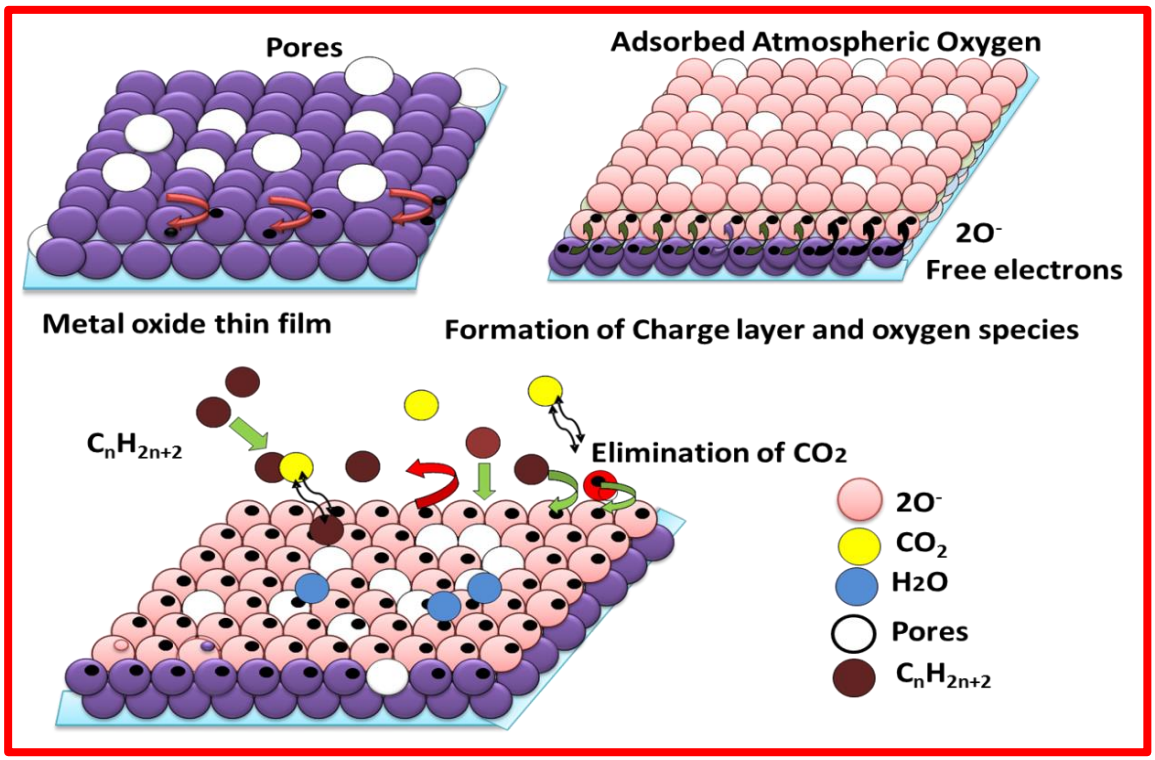

Fig.1.20 Schematic diagram of mechanism of LPG sensing

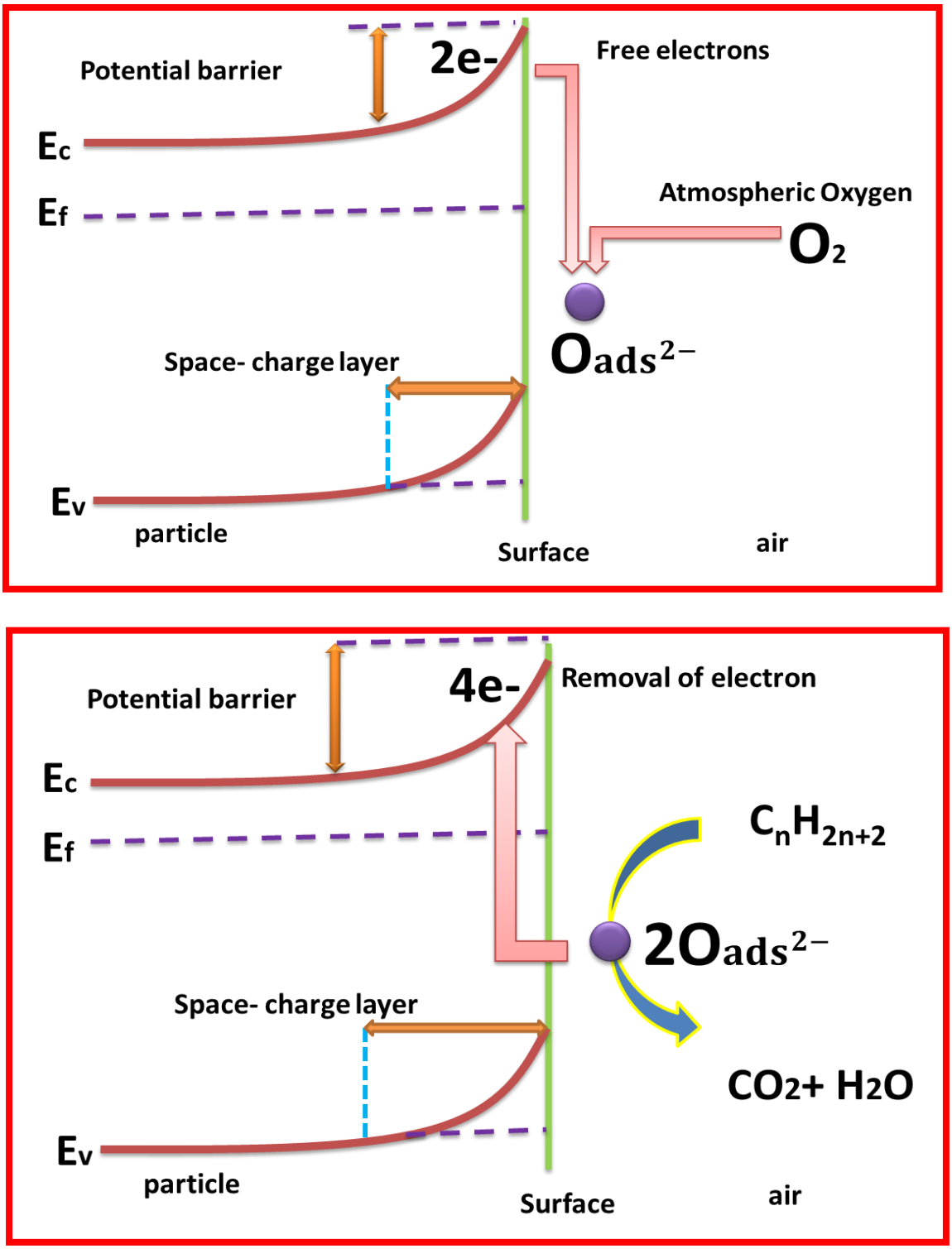

Fig. 1.21 (a) The mechanism of film in term of band gap for n-type material in presence of atmospheric gas and **(b)** is showing mechanism in presence of LPG

Table 1.1. Various types of ferrites on the basis of crystal structure are shown in the table.

S.No.	Type	General Formula	Crystal structure	Active sites	Replacement
1.	Spinel ferrite	AB_2O_4	Cubic	[A] & [B]	Mn, Zn, Ni, Mg, Co
2.	Garnet	RFe_5O_{12}	Cubic	a, c, and d	Y, Sm, Eu, Gd, Tb, Dy, Ho, Er, Tm and Lu
3.	Orthoferrite	$RFeO_3$	Perovskite	[A] & [B]	Y, Sm, Eu, Gd, Tb, Dy, Ho, Er, Tm and Lu
4.	Hexa ferrite	$AFe_{12}O_{19}$	Hexagonal	12k,2a,$4f_2$, $4f_1$, 2b	Pb, Sr, Ba

Chapter 2

Synthesis and characterization of perovskite Barium titanate thin film and its application as LPG Sensor

This chapter reports the successful preparation of perovskite Barium titanate ($BaTiO_3$) nanocomposite thin film using spin coating technique. Surface morphological, structural, compositional and optical properties of the film were investigated by various techniques such as SEM, XRD, TEM, EDS, UV-Spectroscopy, Raman spectroscopy and FTIR. SEM images show the macro porous cubic structure of the film. The minimum crystallite size was evaluated as 11 nm by XRD and confirmed by TEM. Energy band gap of $BaTiO_3$ was evaluated as 3.9 eV. Raman spectroscopy confirmed the formation of $BaTiO_3$ at 540 cm^{-1}. LPG sensing was carried out for 0.5 to 4 vol. % of LPG and the sensor was found suitable for the detection of LPG at lowest explosive limit (LEL).

CHAPTER 2

SYNTHESIS AND CHARACTERIZATION OF PEROVSKITE BARIUM TITANATE THIN FILM AND ITS APPLICATION AS LPG SENSOR

2.1 Introduction

For more than 60 years barium titanate has attracted most of the researchers for practical interest and research work, due to its attractive properties. Rochelle salt and potassium dihydrogen phosphate instigated and accelerated the study on barium titanate. Then an era came when escalation in 100 of new ferroelectric materials occurred. A decade of 70's was known as the age of diversification in which concept of ferroelectric domain and its changing properties were studied and widely used in various applications [1-2].

Barium titanate is the first piezoelectric perovskite ceramic transducer ever developed which is isostructural with mineral perovskite ($CaTiO_3$) [3]. It is a ferroelectric perovskite ceramic which undergoes three phase transition with its decreasing temperature from cubic phase to tetragonal and then from tetragonal to orthorhombic and from orthorhombic to rhombohedral phase [4-5]. Chemically and mechanically $BaTiO_3$ is very stable as well as it exhibits ferroelectric properties at and above the room temperature.

Barium titanate is a porous ceramic formed by either ionic or covalent bond. There are two types of porous ceramics i.e. reticulate ceramic and foam ceramic. Reticulate ceramic has voids surrounding by a web of ceramic while foam ceramic has closed void into a ceramic matrix [6]. Miniaturization of electronic devices enhanced the use of nanomaterial in daily life. Porous nanomaterial of $BaTiO_3$ has various applications in electro-optics, laser frequency doubling, high capacitor memory cell, MEMS, MLC's, sensors, waveguide, etc [7]. Barium titanate also possesses amazing optical properties and ferroelectric polarization in presence of electric field so barium titanate is widely used in electro-optics and photonic applications [8].

$BaTiO_3$ is used in photovoltaic devices. Conventional solar cell works on the classical phenomenon of the p-n junction but there were certain limitations such as lattice mismatch, band alignment etc. To overcome such problems, ferroelectric photovoltaic cells are developed. $BaTiO_3$ is widely used as it is easy to sandwich between the electrodes to get rectifying behaviour and good performance solar cell [9-10]. It is used as core material in nanoshell replacing silica nanoparticles [11]. $BaTiO_3$ is also used as condenser material because their temperature characteristic curves are flat. Condensers are used for coupling bi-pass and filter [12]. Barium titanate is used in fabricating ceramic filters [13], as Positive Temperature Coefficient (PTC) thermistors [14], supersonic devices, in transducers for pick up, microphone, etc as audio-frequency acoustic devices [15]. Due to its porous property researchers are focusing on the ceramic gas sensor and humidity sensor. Ceramic gas sensors are classified into two categories. First is a semiconducting ceramic gas sensor which works on elevated temperature about 300-400 $^{\circ}$C and the latter one is a protonic gas sensor which works on normal room temperature [16]. Both the sensors based on the mechanism of adsorption. In humidity sensor, there is adsorption of water molecules on the surface of the $BaTiO_3$ film while in gas sensor there is adsorption of gas molecules.

A lot of work has been done focusing on the synthesis and applications of $BaTiO_3$ ceramic. $BaTiO_3$ can be prepared by various techniques such as vacuum evaporation, hydrothermal, laser ablation, precipitation, solid-state route method, sputtering, sol-gel method etc [17]. Nanocrystalline Barium titanate has better properties than ceramic barium titanate. Now a day's sol-gel method is mostly used by the researchers due to its several advantages. Sol-gel is a simple and pliable method in which a solute is dissolved in alkaloid followed by hydrolysis and polycondensation to form a sol and then gel [18]. For the present investigation perovskite type $BaTiO_3$ was synthesized using the sol-gel method and thin film was fabricated on a glass substrate. After characterizing thoroughly, it was employed for LPG sensing below LEL and found better results over the previously reported research work [7-8]. LPG is an explosive gas which contains hydrocarbons. It is hazardous to mankind causing several problems related to breathing and health. So leakage of LPG and it's detection in the environment is an important predicament for the mankind. So a lot of research work is going on for developing LPG sensor sensitive for the lower explosive limit (LEL) [19]. The present work deals with the LPG sensing below LEL. LEL of a gas

is defined as the lowest explosive limit of any gas which gets explodes when any flammable material is brought near to it. OSHA (Occupational Safety and Health Administration Calibration) has calibrated 1.8 % LEL for butane gas and 2.2 % LEL for propane gas.

2.2 The Structure of Barium titanate

Barium titanate possesses a typical unit cell ABO_3 structure. Perovskite consists of a transition metal ion in its center with corner sharing of O_6 octahedral as shown in Fig. 2.1 Most of the ferroelectric perovskite consists of non-magnetic transition element with empty d-shell. These non-magnetic elements form a molecule by forming a covalent bond with neighboring oxygen ions. A typical ABO_3 unit cell consists of a corner-linked network of oxygen octahedral with Ti^{4+} ion occupying B sites with octahedral cage and Ba^{2+} ions situated in A sites created by linked octahedral.

2.3 Literature Review

Lalchand A. Patel et al synthesized $BaTiO_3$ by spray pyrolysis method on a quartz substrate and the crystallite size was found as 40 nm by XRD. Further, he studied the effect of firing temperature on gas sensing properties of nanocrystalline $BaTiO_3$ and found 3.03 sensitivity at 350 $^{\circ}C$ [20]. G. N. Chaudhari et al studied the structural and gas sensing properties of undoped $BaTiO_3$ and doped $BaTiO_3$ with CuO/ CdO. XRD shows the cubic structure and no extra peaks of the additives were found. The crystallite size was estimated as 65 nm for pure and 49 nm for doped $BaTiO_3$. Sensitivity versus operating temperature graph was recorded for LPG, H_2, H_2S and CO [21]. M.A. El Romh et al elaborated the doped $BaTiO_3$ thick film by solid state spin coating method and characterized by XRD and SEM. Grain size was found as 200-500 nm. Also, they studied its dielectric and gas sensing properties [22]. Tatsumi Ishihara et al. synthesized the CuO-$BaTiO_3$ using oxide method and crystallite size was reported in the range of 1μm. Further, he performed CO_2 gas sensing at optimum temperature 729 k [23]. B. Liao et al. reported the synthesis of CuO-$BaTiO_3$ by co-precipitation method and fabricated a pn junction. Also, they studied its I-V characteristic regarding the CO_2 sensing [24]. G.H. Jain et al. investigated the gas sensing properties of pure and modified barium strontium titanate prepared by screen printing method. They also studied its quantitative, electrical conductivity and thermal analysis of it [25]. Satreerat K. Hodak et al. designed low-cost $SrTiO_3$/$BaTiO_3$ gas sensor for sensing

ethanol vapor using the sol-gel method on alumina substrate and obtained 30-100 sensitivity in the range 100-1000 ppm [26]. K. Park et al. fabricated tetragonal $BaTiO_3$ ceramic and used as a gas sensor. They investigated CO and N_2 sensing and found comparatively better results for CO gas sensing than N_2 gas [27]. R. Wagiran et al. synthesized thick film of $BaTiO_3$ using ball milled screen printing method and performed its electrical properties and humidity sensing [28]. Burcu Ertug et al. fabricated porous barium titanate ceramics via pore-forming agents i.e. PFAs for the thermistor and sensor application for humidity and various reducing gases and explained that nano $BaTiO_3$ are better sensor than bulk $BaTiO_3$ [29].

2.4 Experimental Methods

2.4.1 Materials Required

Barium acetate, titanium tetra-isopropoxide and 2- methoxy ethanol were purchased from Sigma-Aldrich Chemical Co. and useful for synthesizing nanostructured $BaTiO_3$.

2.4.2 Synthesis technique for preparation of Barium titanate powder

Barium titanate was synthesized by using sol-gel method [30]. Barium acetate and Titanium tetra-isopropoxide were used as a starting material and 2-methoxy ethanol was used as a solvent. Firstly Barium acetate (5.476 gm) was dissolved in 2-methoxy ethanol and titanium isopropoxide (6.939 ml) was dissolved in 2-methoxy ethanol separately followed by stirring for 2 h. Then both the solutions were mixed to form a stock solution. This stock solution was further stirred continuously for 2 h and thus a sol of Barium titanate was obtained. The sol so obtained under I.R. lamp to obtain a gel of Barium titanate. Further, this gel was dried at 80 $^{\circ}$C inside the oven and then it was annealed at 650 ^{o}C for 2 h in a programmable electric furnace to obtain Barium titanate powder. The crystalline powder was crushed into the fine powder by using mortar and pestle. The flowchart of synthesis of Barium titanate powder is given as under:

2.4.3 Preparation of thin film of Barium titanate

Sol-gel spin coating technique is the best among the other techniques for depositing the thin films of uniform thickness [31]. For this purpose glass substrate of dimension 1×1 cm^2 was prepared and cleaned in an ultrasonic cleaner (WUC-AO2H) by distilled water and ethanol followed by acetone. A thick solution of $BaTiO_3$ was made by dissolving it in glacial acetic acid in 1:2 ratio and it was stirred for 2 h and further it was sonicated for 2 h. Then the solution was spun on the glass substrate using a photoresist spinner (METREX RC100) at a speed of 3000 rpm and for 30 sec at 60°C and dried for 10 min on a hot plate. Again spin coating was done at 3000 rpm for 30 sec and again dried for 10 min on a hot plate. This process was repeated by 2 times for obtaining a homogeneous thin film. Later the film was finally dried at 80 °C for 15 min on the hot plate and annealed at 200 °C for 2 h.

2.4.4 Experimental setup for LPG Sensing

The thin film of Barium titanate has been fabricated according to prescription depicted as in section 2.3. The thin film was employed as LPG sensor. Detailed experimental setup in shown in Fig. 2.3, which consists of a controlled gas chamber, cylinder of LPG, marble slab, hot plate, Keithley electrometer model no. 6517 B and volume measuring unit.

2.4.5 Characterization Techniques

XRD pattern of the prepared powder of Barium titanate was recorded by glancing angle X-ray Diffractometer (Benchtop X-ray Diffraction, 5^{th} generation Miniflex), equipped with monochromatic Cu-Kα as the radiation source. Surface morphological study of the material had been done by SEM (Zeiss EV040) coupled with EDX. TEM analysis was carried out by FEI Technai G2 Spirit TWIN, Netherland and also it was verified by Zeta nano sizer model no. (Nano ZS90). Optical characterization of the sample was performed by using UV-Visible spectrophotometer (Evolution 201). The FTIR spectra of $BaTiO_3$ sample was recorded by the instrument, Thermo Nicolet, (Model No. 6700, USIC).

Raman peaks of Barium titanate was analyzed by En Specter R532. Particle size analysis was carried out by Zeta Sizer (Nano-ZS90).

2.5 Result and Discussions

2.5.1 X-ray Diffraction Analysis

XRD pattern of the prepared powder of Barium titanate was recorded by glancing angle X-ray Diffractometer equipped with high source-detector with 600 W X-ray source. Fig. 2.4 shows the X-Ray diffraction pattern of Barium titanate film. The analysis of XRD pattern matched with JCPDS no. #892475 reveals that the formation of cubic phase of the film with lattice parameter a = 4.017. The intensity peak is found at 2θ = 32.17. The peaks at 2θ = 22.208 (100), 3.217 (110), 38.898 (111), 45.590 (200), 50.812 (210), 56.127 (211), 65.779 (220), 70.323 (300), 74.788 (310) and 79.011 (311) confirms the formation of perovskite Barium titanate [32]. Other small peaks are due to $BaCO_3$ content which was formed when the reaction of Barium hydroxide was taken place with CO_2 liberated during the annealing process. The minimum crystallite size of the Barium titanate thin film was calculated as 11 nm by using Debye Scherer's equation through broadening of the intensity peak, crystallite size corresponding to each peak was calculated and the average crystallite size was found as 18 nm [33-35].

2.5.2 Surface Analysis and EDX

Surface morphological study of the material has been done by SEM equipped with LaB_6 gun operated at 20 kV and EDX. SEM micrographs show the porous nature of the material with cubic structure and the grains are evenly distributed leaving vacant spaces among them known as pores [36-38]. These pores serve as adsorption centers and quite favorable for the gas sensing mechanism. SEM micrographs at different scales 20 μm, 10 μm and 2 μm are shown in Fig. 2.5 (a), (b) and (c). Accordingly, macroporous $BaTiO_3$ with higher surface area and adsorption site causes the variation in sensing properties when coming in contact with air and LPG.

Elemental dispersive X-ray (EDX) spectrum is shown in Fig. 2.6 and it confirms the formation of Barium titanate with compositions as Ba 59%, Ti 20%, O 21% in our sample. Some impurity of Co is present in a negligible amount.

2.5.3 TEM analysis and Particle Size Analysis

TEM analysis was carried out by FEI Technai G2 Spirit TWIN, Netherland Figs. 2.7 (a) and (b) shows the TEM images of Barium titanate, loaded on the carbon coated copper grid at scales 100 nm and 50 nm. The sample was prepared by dispersing the Barium titanate powder in ethanol. The solution was sonicated several times by ultrasonic machine and few drop of floating solution was dropped on the grid. The image at 100 nm scale reveals the crystalline structure in agglomerated form and the minimum grain size was found as 6.7 nm. Particle sizes of $BaTiO_3$ are heterogeneous with diameter 10 nm, 16 nm, 23 nm, 29 nm, 30 nm, etc. so the average size of the particles varies.

The particle size of Barium titanate was analyzed by dissolving it in distilled water and methanol solution using Zeta nanosizer (Nano ZS90) and corresponding data were plotted as shown in Fig 2.8. It measured the acoustic wave attenuation (db/cm) vs. frequency in the range 1-100 MHz. The average size of the particle was found as 24 nm from the particle size distribution curve verifying the TEM result.

2.5.4 UV-visible Absorption Spectroscopy

The optical absorbance spectra of Barium titanate film deposited separately on a glass substrate (200-1100 nm) are shown in Fig. 2.9. The graph represents the variation of optical absorbance for the thin film with the variation in wavelength. Further, this data was used for analyzing the optical bandgap energy (E_g) using the following relation:

$$\alpha h\upsilon = A(h\upsilon - E_g)^n$$

where A is a constant. υ is the transition frequency and the "n" is exponent representing nature of band transition (n = 1/2 and n = 3/2 corresponding to indirect allowed and forbidden transitions). The optical band gap of Barium titanate has been calculated from the intercept of energy axis obtained by extrapolating the plot on energy axis [hυ verses $(\alpha h\upsilon)^2$] as shown in figure found as 3.9 eV [39].

2.5.5 FTIR analysis

The FTIR spectra of the barium titanate sample were recorded by the instrument; Thermo Nicolet, (Model No.6700, USIC) at room temperature for wavenumber 4000 to 400 cm^{-1}. The IR spectrum is obtained by using KBr pellet mixed in 1:20 ratio. FTIR spectrum of the sample taken in transmittance mode is presented in Fig. 2.10. The vibrational peak assigned to 438 cm^{-1}, 540 cm^{-1}, 860 cm^{-1},1421 cm^{-1}, 1634 $cm^{-1}$and 3412 cm^{-1} are the peaks of $BaTiO_3$ showing the stretching in Ti-O (normal and bending mode), Ti-OH, COO^- , OH- and Ba-OH bonds [40-41]. The region from 400 to 600 cm^{-1} corresponds to infrared absorption region. The strong peaks at 438 cm^{-1} are due to Ti-O bending vibration along polar axis and 540 cm^{-1} is due to stretching vibrations. Vibrational peaks assigned at 860 cm^{-1} and 1421 cm^{-1} are due to bending vibrations in COO- group which aroused due to the acetic acid ligand. The peaks corresponding to 1634 $cm^{-1}$and 3412 cm^{-1} due to OH stretching vibrations and OH deformation vibration arised due to H_2O content and methoxy ethanol [42].

2.5.6 Raman Spectrum

Raman spectrum of Barium titanate was analyzed by En Specter R532 with a laser power of 30 nW and wavelength of 532 nm. Barium titanate possesses 5 atoms and 15 degrees of freedom per unit cell. Raman Spectra in spectral range from 200 cm^{-1} to 1000 cm^{-1} were recorded [43-44]. There are three modes of the barium titanate as shown in the Fig. 2.11.The modes are called as Raman active modes. These modes are broad which indicates the polycrystalline nature of the sample. Peaks at 270 cm^{-1}, 304 cm^{-1}, 514 cm^{-1}, 720 cm^{-1} represent the Raman shift of barium titanate [45-46]. The intense and broad peak at 270 cm^{-1} and 304 cm^{-1} is due to the vibration in TiO_6 group. Peak assigned at 514 cm^{-1} is due to the vibration occurred by displacement of the oxygen atom.

2.5.7 LPG sensing mechanism

LPG sensing mechanism is based on the variation in electrical properties of the film used when exposed to the gas [47-48] .The interaction of the gas with the material leads to

transfer of electrons between the barium titanate and the reducing gas. The atmospheric oxygen molecules get adsorbed to the surface and they form oxygen species by interacting with the conduction band electrons. The kinematics involved in this process is as below.

$$O_2\,(air) \leftrightarrow O_2\,(ads)\,, \qquad \text{------- (i)}$$

$$O_2\,(ads) + e^- \leftrightarrow O_2^-\,(ads) \qquad \text{------- (ii)}$$

This lead to decrease in concentration of electrons. When LPG was exposed to barium titanate film a complex reaction occurred due to the formation of superoxide and peroxide of titanium which are highly unstable. These complex hydrocarbons react with adsorbed oxygen species which are responsible for complex reaction [49-51] as below:

$$C_nH_{2n+2} + 2O^- \rightarrow H_2O + C_nH_{2n}{:}\,O + e^- \qquad \text{------- (iii)}$$

$$C_nH_{2n}{:}\,O + O^- \rightarrow CO_2 + H_2O + e^- \qquad \text{------- (iv)}$$

This reaction is termed as dehydration. Further oxidation of dehydrogenation mechanism occurred and CO_2 and water contents were released as the end product. As the rate of the reaction increased removal of electrons were taken place which leads to the formation of a potential barrier that was further responsible for the constant resistance of the film [52-53]. Sensitivity, % Sensor response, response time, recovery time and reproducibility are the sensing parameter of a sensor. Time taken by a sensor to reach stable value is called response time of the sensor. The sensitivity of the sensor is defined as the ratio of the increment of the output with respect to input measurand.

2.5.8 Sensing behaviour of Barium titanate film

Barium titanate unit cell consists of a corner-linked network of oxygen octahedral with Ti^{4+} ion occupying B sites with octahedral cage and Ba^{2+} ions situated in A sites created by linked octahedral. LPG sensing properties were examined by variations in electrical resistance with time for different concentrations of LPG and plotted in Fig. 2.12. Each curve shows that on exposure of LPG, there is variation in the resistance of the film. Initially, the resistance of the film was stabilized at 41.5 MΩ when the film was exposed to 0.5 vol % of LPG and then the resistance of the film initially increases very sharply and

attains a constant value of 61.48 MΩ. Then the outlet of the chamber was opened and the resistance of the film was found to be decreased and finally attained its initial value around 42.4 MΩ. This slight variation in the resistance was due to water content produced due to a chemical reaction that occurs when LPG interact with the film. As gas concentration increases from 0.5 to 4 vol.% there is a linear change in sensor response for each concentration as shown in table.2.1. The average of the percentage response sensor also increases in a similar way as sensitivity which is shown in Fig. 2.13 (b) and Fig. 2.13 (a). As the concentration of LPG increases the number of gas molecules increases in the chamber and they were absorbed by the dangling bonds on the surface of the film as a result sensitivity increases. The value of maximum sensitivity was found as 3.5 and percentage sensor response was 250 for 4 vol. % LPG. Minimum response time was found 30 sec for 0.5% LPG and recovery time was found 60 sec for 0.5% LPG.

2.5.9 Reproducibility and ageing effect

Reproducibility of a sensor is defined as the ability of the sensor to reproduce the same result after some time. Reproducibility graph of $BaTiO_3$ thin film sensor is shown in the Fig. 2.14 for 3 vol.% of LPG which shows that the results are reproducible and the barium titanate as an LPG sensor is reliable. After all the observations from 0.5 vol.% to 4 vol.% of LPG again the observation was taken for 3 vol.% of LPG. The film was already saturated due to water content produced after so many observations and due to room temperature variation. The resistance of the film is high in the air but the resistance in presence of LPG is nearly same. Therefore, there was a decrement in the sensing response and sensitivity of the film after repeating the experiment on the same day. The ability of a sensor to produce same output over an interval of time for some fixed input measurement is called the ageing effect of the sensor. The ageing effect of the barium titanate film was observed after two months and four months for 0.5 % LPG. Before taking the sensing again, the film was dried under I.R. lamp for five min to remove the humidity of the film. Now the film becomes more porous with more activation sites due to which the resistance of the film decreases after two and four weeks from the initial resistance. Similarly, the resistance of the film in presence of LPG also changes. But the response time and sensitivity were merely same after two and four weeks of sensing. The comparative study

through open literature is depicted in Table 1 which shows that our result is the best among other reported works. Average sensitivity is 3.5 and sensor response is 250 with operating temperature 25 $^{\circ}$C.

2.6 Conclusion

Nanostructured Barium titanate was synthesized by sol-gel method and film was prepared by spin coating technique. XRD, FTIR and Raman studies confirmed the formation of barium titanate and minimum size was calculated as 11 nm from XRD, SEM and TEM were used for surface morphological phase analysis. Particle size calculated by TEM was varied from 6-30 nm. Optical characterization was done and band gap was found was estimated as 3.9 eV. The peak at 540 cm^{-1} in Raman Spectra confirmed the formation of $BaTiO_3$. FTIR revealed the information about the bond stretching between the molecules. The film of Barium titanate was further used as LPG sensor. The value of maximum sensitivity was found 3.5 which is maximum till date reported in the open literature (Table 2.1) and percentage sensor response was found as 250 % for 4 vol.% LPG. The linear sensing characteristic curve showed that the $BaTiO_3$ based LPG sensor is quite appropriate for developing a commercial LPG sensor operable at room temperature.

REFERENCES

1. L.E. Cross and R.E. Newnham, History of Ferroelectrics, High Technology Ceramic-Past Present and Future: The Ceramics and Civilization, American *Ceramic* Society, Westerville, 3 (1987) 289-305.
2. S. Singh, B.C. Yadav, M. Singh, R. Kothari, A review report on Nanostructured ferrites as Liquefied petroleum gas sensor, Int. J. of Sci., Techno. and Soc., 1(1) (2015).
3. G. Arlt, The influence of microstructure on the properties of ferroelectric ceramics, Ferroelectrics, 104 (1990) 217-227.
4. N. Verma, S. Singh, B.C. Yadav, Experimental investigations on barium titanate nanocomposite thin films as an optoelectronic humidity sensor, J. of Experimental Nanosci. 1 (2012) 1-9.
5. T. Takenaka, Piezoelectric properties of some lead-free ferroelectric ceramics, Ferroelectrics, 230 (1999) 87-98.
6. M.W. Barsoum, Fundamentals of Ceramics, The McGraw-Hill Companies, Inc. (1997) 149-411.
7. Y.M. Chiang, D. Birnie, W.D. Kingery, Physical Ceramics: Principles for Ceramic Science and Engineering, John Wiley & Sons, Inc. (1997).
8. K. Abe, T. Tanaka, S. Miura, K. Okazaki, Study on Langev in type $BaTiO_3$ ceramic vibrator, Bulletin of Institute for Chemical Research, Kyoto University, 31 (1953) 295–304.
9. W. Wang, F. Liu, C.M. Lau, L. Wang, G. Yang, D. Zheng, Z. Li, Field-effect $BaTiO_3$-Si solar cells, Applied Physics Letters 104 123901 (2014).
10. Y. Okamoto, Y. Suzuki, J. of Physical Chemistry, Mesoporous $BaTiO_3/TiO_2$ Double Layer for Electron Transport in Perovskite Solar Cells, 120 (2016) 139995-14000.
11. E.F. Takina, G. Ciofania, M. Genomic, V. Piazzac, B. Mazzolaia, V. Mattolia, Synthesis and characterization of new barium titanate core–gold shell nanoparticles, Colloids and Surfaces A: Physicochem. Eng. Aspects 415 (2012) 247– 254.
12. T. Tanaka, Barium titanate ceramic and their application, Bulletin of Institute for Chemical Research, Kyoto University, 32(2) (1954) 43-53.

13. S. Fujishima, Transactions on ultrasonics, ferroelectrics, and frequency control, The History of Ceramic Filters, 47 (2000) 1-7.

14. M.M. Vijatovic, J.D. Bobić, B.D. Stojanović, Science of Sintering, History and Challenges of Barium Titanate: Part II, 40 (2008) 235-244.

15. J.B. Mac Chesney, P.K. Gallagher, F.V. DiMarcello, Stabilized Barium Titanate Ceramics for Capacitor Dielectrics, J. of the American Ceramic Society, 46(5) (1963) 197-202.

16. Y.K. Mishra, G. Modi, V. Cretu, V. Postica, O. Lupan, T. Reimer, I. Pawlowicz, V. Hrkac, W. Benecke, L. Kienle, R. Adelung, the Direct growth of freestanding ZnO Tetrapod Networks for multifunctional Applications in Photocatalysis, UV-Photodetection and gas sensor, Appl. Mater. Interfaces, 7(26) (2015) 14303-14316.

17. V.R. Chinchamalatpure, S.A. Ghosh, G.N. Chaudhari, Synthesis and Electrical Characterization of $BaTiO_3$ thin films on Si (100), Mat. Sci. and Applications (2010) 187-190.

18. B.D. Stojanovi, A.Z. Simoes, C.O. Paiva-Santos , C. Jovaleki, V.V. Miti, J.A. Varel, Mechanochemical synthesis of barium titanate, Journal of the European Ceramic Society 25 (2005) 1985–1989.

19. A. Kareiva, S. Tautkus, R. Papalaviciute, Sol-gel synthesis and characterization of barium titanate powders, J. of Mat. Sci. 34 (1999) 4853-4857.

20. L.A. Patil, D.N. Suryawanshi, I.G. Pathan, D.G. Patil, Effect of firing temperature on gas sensing properties of nanocrystalline perovskite $BaTiO_3$ thin films prepared by spray pyrolysis techniques, Sens. Actuators B: Chem., 195 (2014) 643-650.

21. G.N. Chaudhari, D.R. Bambole, A.B. Bodade, Structural and gas-sensing behavior of nanocrystalline $BaTiO_3$ based liquid petroleum gas sensors, Vacuum, 81 (2006) 251-256.

22. M.A. El Romb, D. Fasquelle, S. Deputier, M. Mascot, Elaboration and characterization of doped barium titanate films for gas sensing, AIP Conference Proceedings 1627, 25 (2014).

23. T. Ishihara, K. Kazuhiro, Y. Mizuhara, Y. Takita, Mixed oxide capacitor of CuO-$BaTiO_3$ as new type CO_2 Gas Sensor, J. of the Am. Ceram. Soc. 75(3) (1992) 613-618.

24. B. Liao, Qin Wei, K. Wang, Y. Liue, Study on CuO- $BaTiO_3$ semiconductor CO_2 sensor, Sens. Actuators B: Chem., 80(3) (2001) 208-214.

25. G.H. Jain, L.A. Patil, U.P. Mulik and K.R Patil, studies on gas sensing performance of pure and modified barium strontium titanate thick film resistors, Bull. Mater. Sci. 30(1) (2007) 9-17.

26. S.K. Hodak, T. Supasai, A. Wisitsoraat, J.H. Hodak, Design of low-cost gas sensor based on $SrTiO_3$ and $BaTiO_3$ Films, J. of Nanosci. and Nanotechno. 10 (2010) 7236-7238.

27. K. Park, D.J. Seo, Gas sensing characteristics of $BaTiO_3$-based ceramics, Mater. Chem. Phys. 85 (2004) 47-51.

28. R. Wagiran, W.S. Wan Zaki, S.B. Mohd Noor, A.H. Shaari and I. Ahmad, Characterization of Screen printed $BaTiO_3$ thick film humidity sensor, Int. J of Eng. and Techno., 2(1) (2005) 22-26.

29. B. Ertug, The fabrication of porous Barium Titanate Ceramics via pore forming agents (PFAs) for thermistors and sensor applications, Powder metallurgy, Dr. Katsuyoshi Kondoh (Ed.) In Tech, (2012).

30. B.R. Li, X.H. Wang, L.T. Li, Synthesis and sintering behavior of $BaTiO_3$ prepared by different chemical methods, Mater. Chem. Phys. 78 (2002) 292-298.

31. C.J. Brinker, G.W. Scherer, Sol-gel Science, The Physics and Chemistry of Sol-gel Processing, Academic Press, Inc., United States of America (1990).

32. N. Sahu, B. Parija, S. Panigrahi, Fundamental understanding and modeling of spin coating process: A review, Indian J. Phys. 83 (4) (2009) 493-502.

33. W.L. Zhong, Y.G. Wang, P.L. Zhang, B.D. Qu, the Phenomenological study of the size effect on the phase transitions in ferroelectric particles, Phys. Rev. B 50 (1994) 698-703.

34. C.J. Xiao, Z.H. Chi, W.W. Zhang, F.Y. Li. S.M. Feng, C.Q. Jin, X.H. Wang, X.Y. Deng, L.T. Li., The phase transitions and ferroelectric behavior of dense nano crystalline $BaTiO_3$ ceramics fabricated by pressure assisted sintering, J. of Physics and Chemistry of Solids, 68 (2007) 311-314.

35. M.H. Frey, D.A. Payne, Grain-size effect on the structure and phase transformations for barium titanate, Phys. Rev. B 54 (1996) 3158-3168.

36. Z.G. Ye, Relaxor ferroelectric complex pervoskites: structure, properties and phase transitions, Key Eng. Material. 155-156 (1998) 81-122.

37. H. Hayashi, T. Nakamura, T. Ebina, In situ Raman spectroscopy of $BaTiO_3$ particles for tetragonal- cubic transformation, J of Phys. and Chem. of Solids 74 (2013) 957-962.

38. Michael Veith, Sanjay Mathur, Nicolas Lecere, Volker Huch and Timo Decker, Sol-gel synthesis of nanoscaled $BaTiO_3$, $BaZrO_3$ and $BaTi_{0.5}Zr_{0.5}O_3$ Oxides via single-source alkoxide precursor and Semi- Alkoxide Route Routes, J. of Sol-Gel Sci. and Tech. 15 (2000) 145-158.

39. D. Lakshmi, V. Meena Priya, J. Shanthi, International journal of information technology & computer sciences study of barium titanate thin films by spin coating technique, 2(1) (2014) 301-303.

40. O. Harizanov, A. Harizanova, T. Ivanova, Formation and Characterization of sol-gel barium titanate, Mat. Sci. and Engineering B, 106 (2004) 191-195.

41. M.R.A. Bhuiyan, M.M. Alam, M.A. Momin, M. J. Uddin, M. Islam, Synthesis and Characterization of Barium titanate ($BaTiO_3$) nanoparticle, Int. J. of Mat. and Mechanical Engineering, 1 (2012) 21-24.

42. M.K. Trivedi, G. Nayak, S. Patil, R.M. Tallapragada, O. Latiyal, Industrial Engineering and Management, Impact of Biofield Treatment on Atomic and Structural Characteristics of Barium Titanate Powder, (2015) 1-16.

43. Lagos L. Patricio, Hermans Z. Rodolfo, Nicolas Velasco, Tarrach Guido, Frank Schlaph of, Christian Loppacher, Lukas M. Eng, Identification of ferroelectric domain structures in $BaTiO_3$ for Raman Spectroscopy, Surface Science, 532-535 (2003) 493-500.

44. R.Y. Sato-Berru, E.V. Mejia-Uriarte, C. Frausto-Reyes, M. Villagran- Muniz, H. Murrieta S., J.M. Saniger, Application of principal component analysis and Raman spectroscopy in the analysis of polycrystalline $BaTiO_3$ at high pressure, Spectrochimica Acta Part A 66 (2007) 557-560.

45. Y. Yuan, S.R. Zhang, X.H. Zhou, B. Tang, B. Li, High-Temperature Capacitor Materials based on modification $BaTiO_3$, J. of Electronic Materials 38(5) (2009).

46. U.D. Venkateswaran, V.M. Naik, R. Naik, High-pressure Raman studies of polycrystalline $BaTiO_3$, Phys. Rev. B 58 (1998) 14256-14260.

47. P. Rao, R.V. Godbole, D.M. Phase, R.C. Chikate, S. Bhagwant, Ferrite thin films: Synthesis, characterization, and gas sensing properties towards LPG, Mat. Chem. and Phys. (2015) 333-338.

48. B.C. Yadav, S. Singh, A. Yadav; Nanonails structured ferric oxide thick film as room temperature liquefied petroleum gas LPG sensor, Applied Surface Sci., 257 (2011) 1960-1966.

49. C.E. Simion, A. Sackmann, V.S. Teodorescy, C.F. Rasti, A. Stanoiu, Room temperature ammonia sensing with barium strontium titanate under humid air background, Sens. Actuators B: Chem., 220 (2015) 1241-1246.

50. S. Singh, B.C. Yadav, R. Prakash, B. Bajaj, J. Rock Lee, Synthesis of nanorods and mixed shaped copper ferrite and their applications as liquefied petroleum gas sensor; Applied Surface Sci. 257 (2011) 10763-10770.

51. R. Srivastava, B.C. Yadav, M. Singh, T.P. Yadav, Synthesis, Characterization of Nickel Ferrite and Its Uses as Humidity and LPG Sensors, J. Inorg Organomet Polym, 26(6) (2016) 1404-1412.

52. O. Lupan, V. Cretu, M. Deng, D. Gedamu, I. Pawlowicz, S. Kaps, Y. K. Mishra, O. Polonsky, C. Zamponi, L. Kienle, V. Trofin, I. Tiginyanu, R. Adeling, the Versatile growth of freestanding orthorhombic α- Molybdenum trioxide nano and microstudies by rapid thermal processing for gas nanosensor, J. Phys. Chem. C, 118 (2014) 15068-15078.

53. A. Singh, A. Singh, S. Singh, P. Tandon, B.C. Yadav, R.R. Yadav, Synthesis, characterization and performances of zinc ferrite nanorods for room temperature sensing applications, J. of Alloy and Compounds, 618 (2015) 475-483.

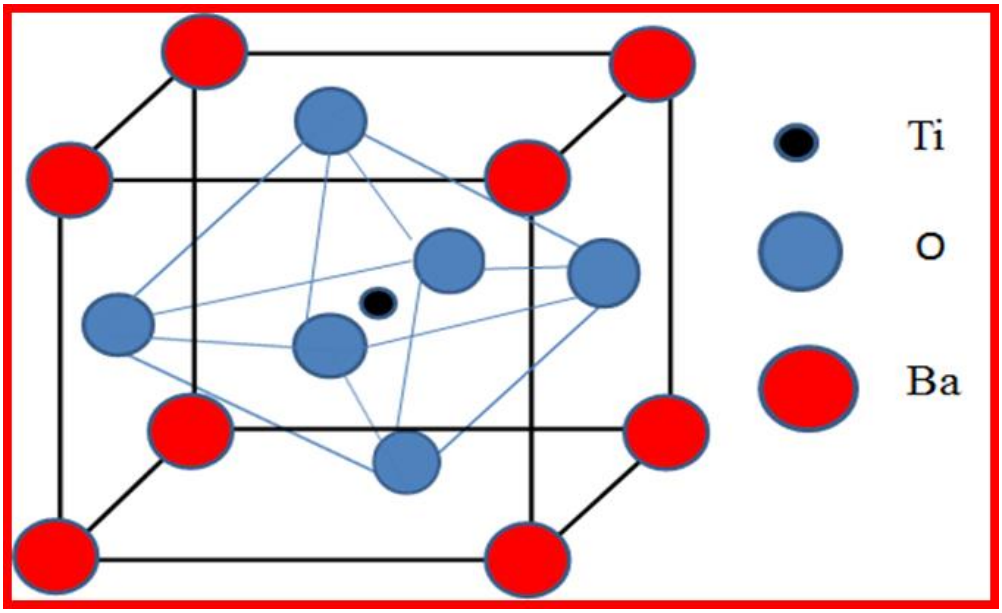

Fig. 2.1 Structure of perovskite ABO_3 unit cell structure of Barium titanate

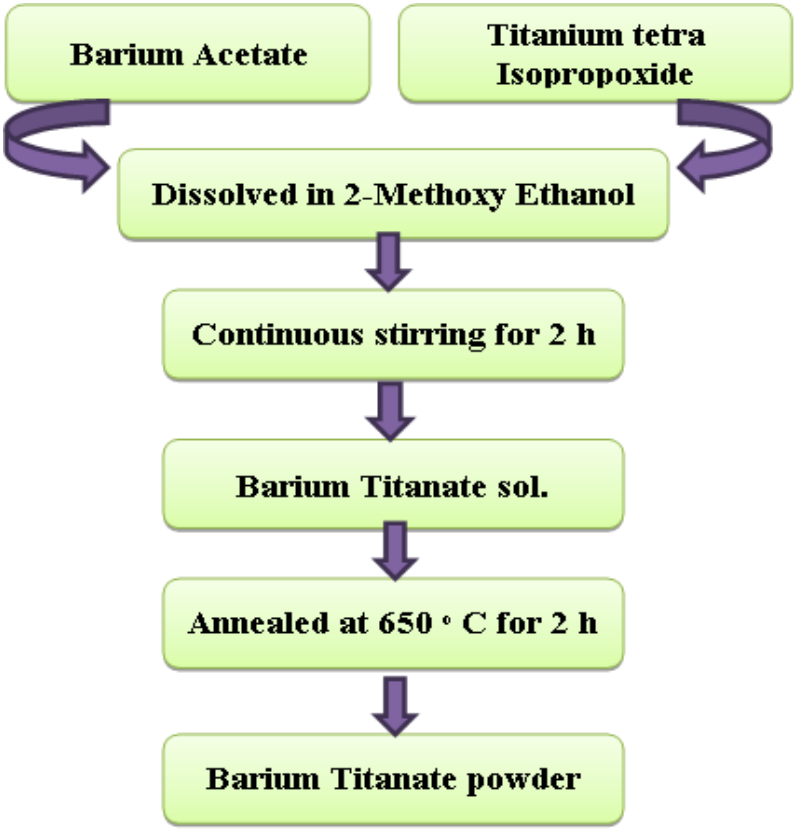

Fig. 2.2 Flowchart for synthesis of Barium titanate powder by sol-gel method

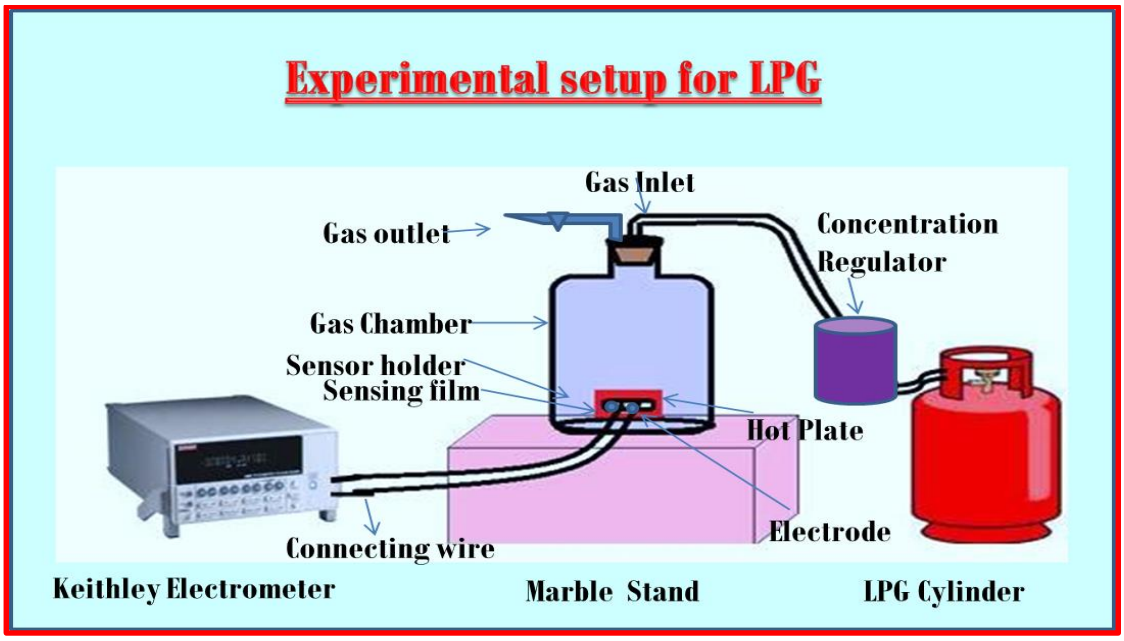

Fig. 2.3 Experimental set-up for LPG Sensing

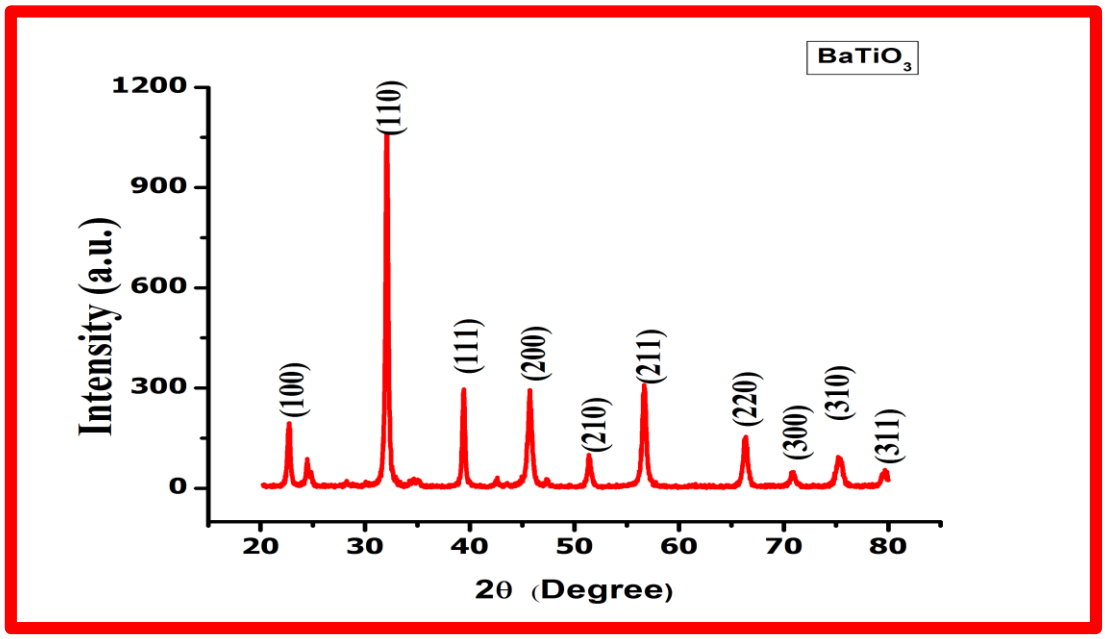

Fig. 2.4 XRD pattern of Barium titanate showing polycrystalline nature of the film.

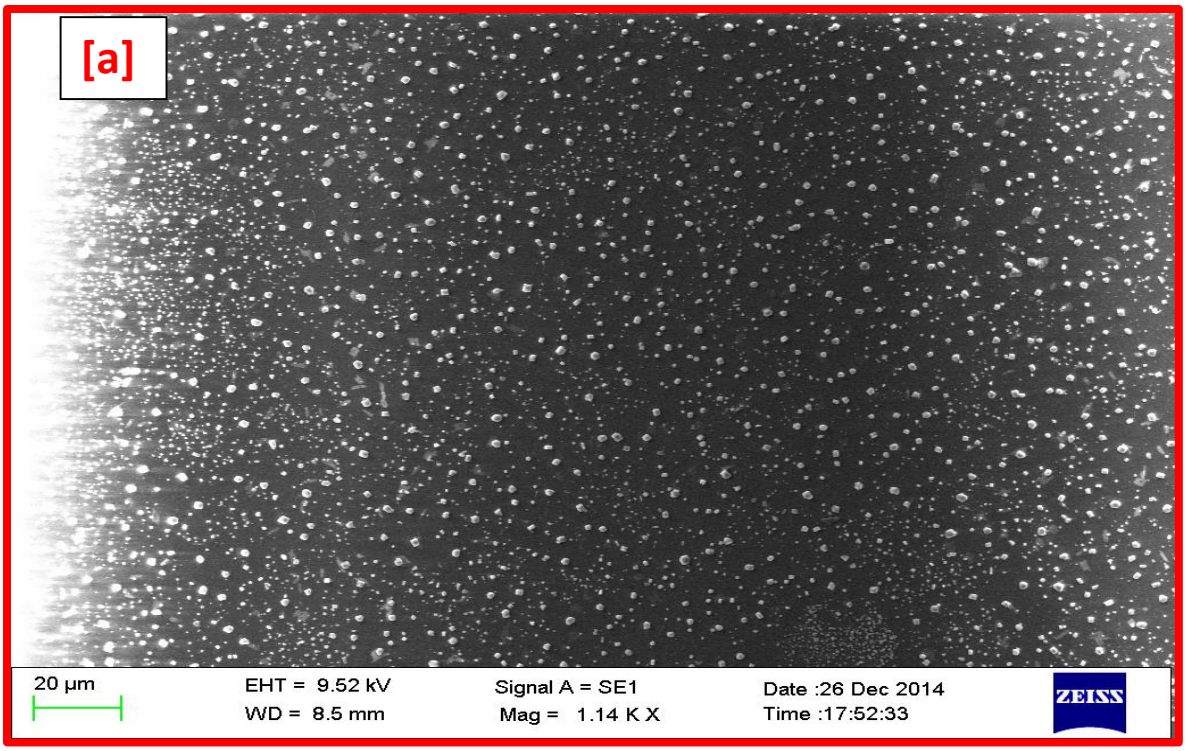
[a]
20 µm
EHT = 9.52 kV
WD = 8.5 mm
Signal A = SE1
Mag = 1.14 K X
Date :26 Dec 2014
Time :17:52:33
ZEISS

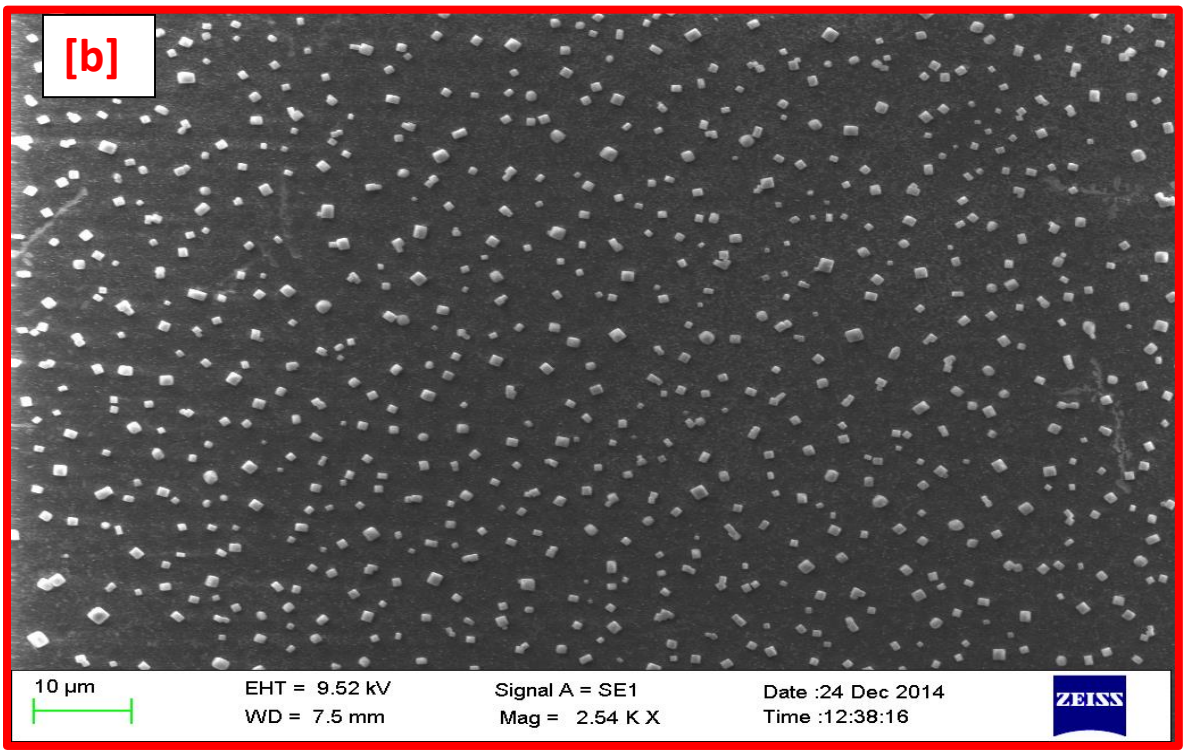
[b]
10 µm
EHT = 9.52 kV
WD = 7.5 mm
Signal A = SE1
Mag = 2.54 K X
Date :24 Dec 2014
Time :12:38:16
ZEISS

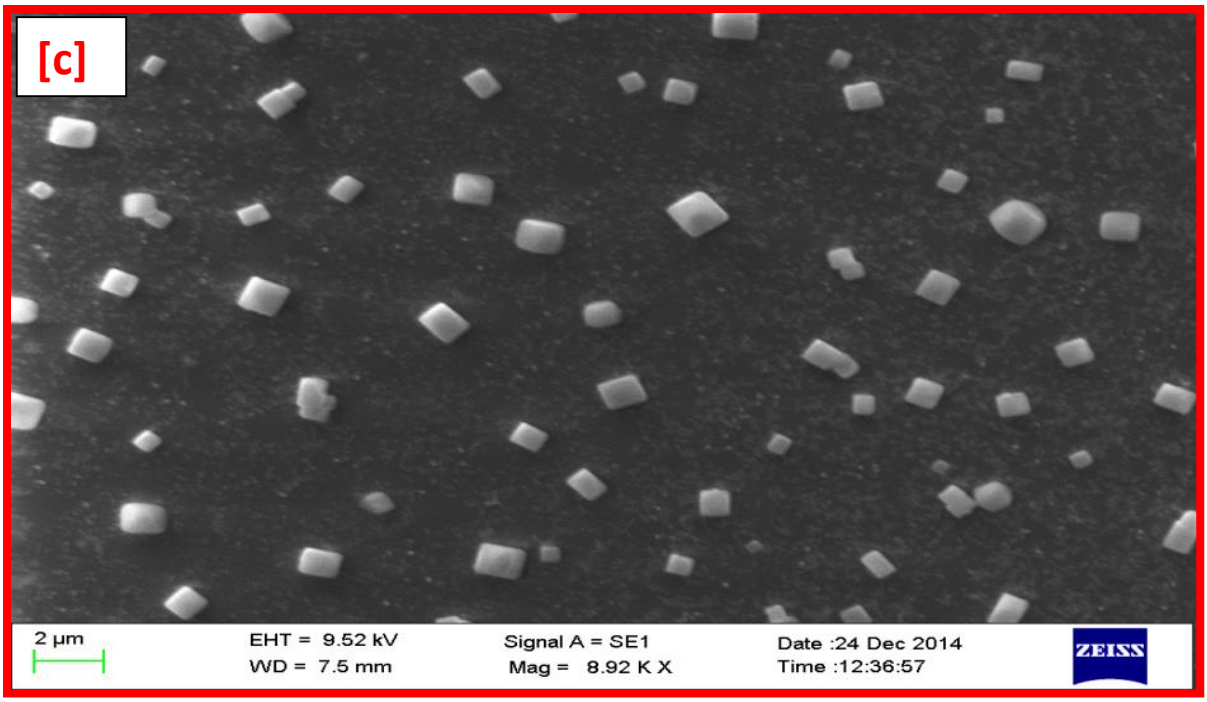

Fig. 2.5 SEM image of macroporous Barium titanate film at (a) 2 µm, (b) 10 µm and (c) 20 µm

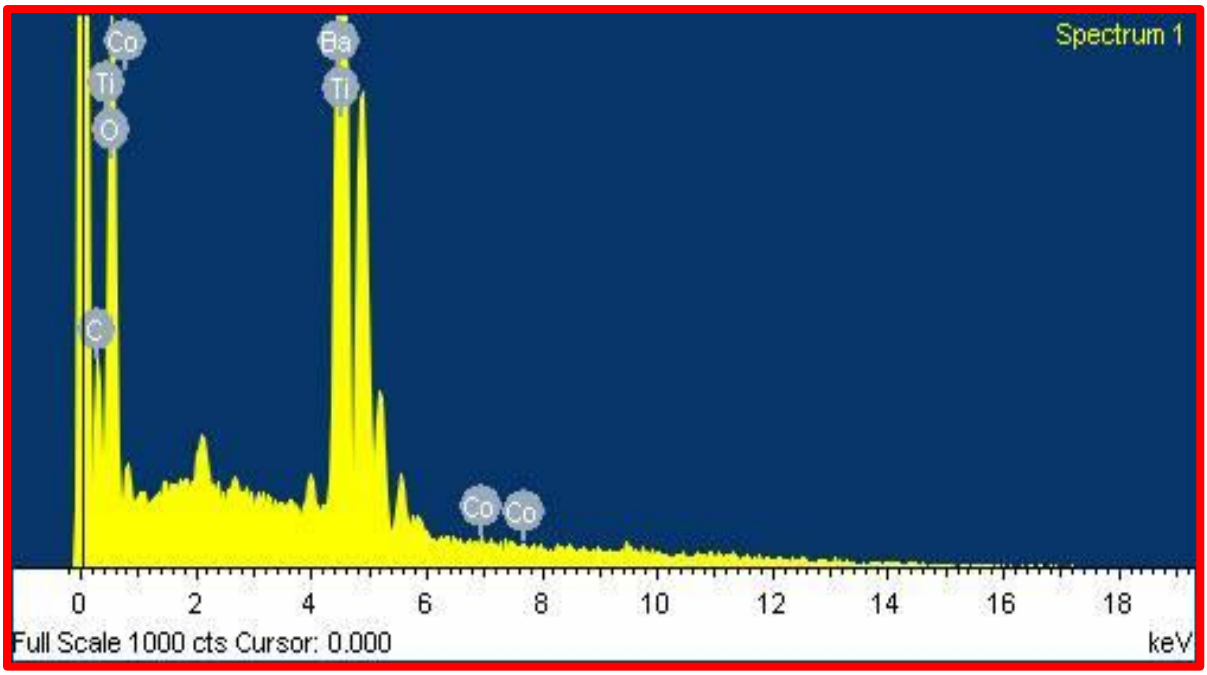

Fig. 2.6 EDAX of Barium titanate showing the presence of Ba, Ti and O element along with Co as a foreign element.

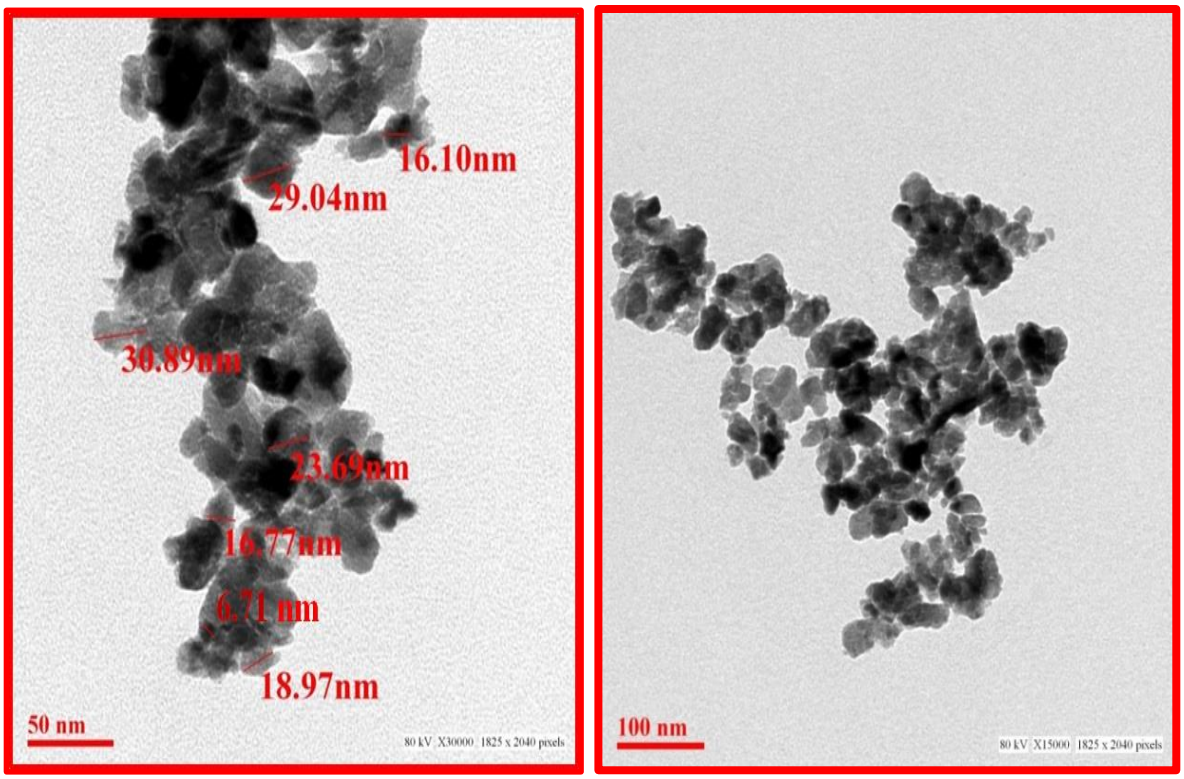

Fig. 2.7 (a) and (b) representing TEM micrographs of Barium titanate at different scales

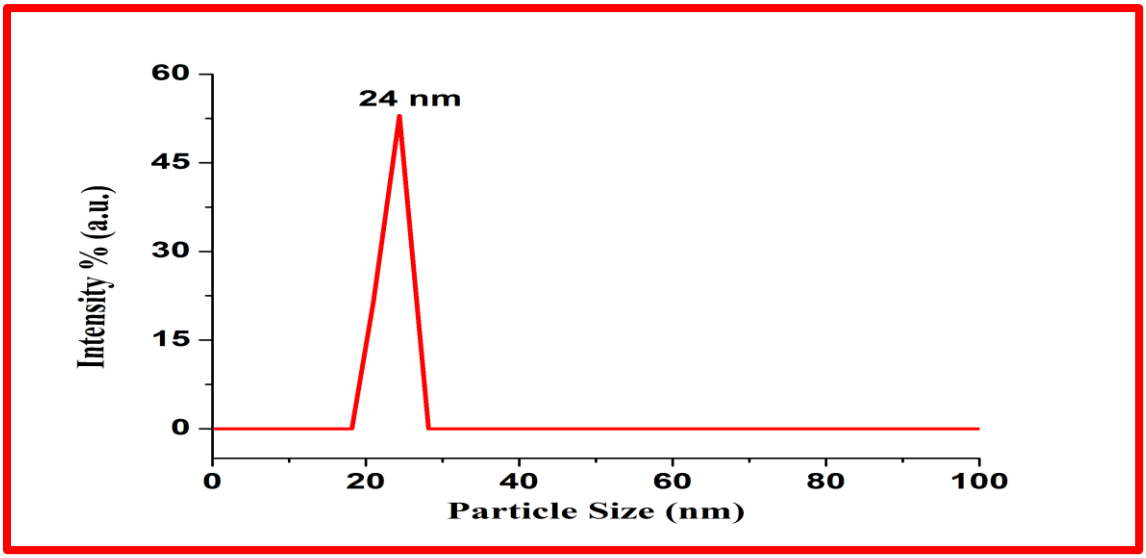

Fig. 2.8 Particle size distribution by Nano ZS90 showing average size of the particles confirming the above TEM result

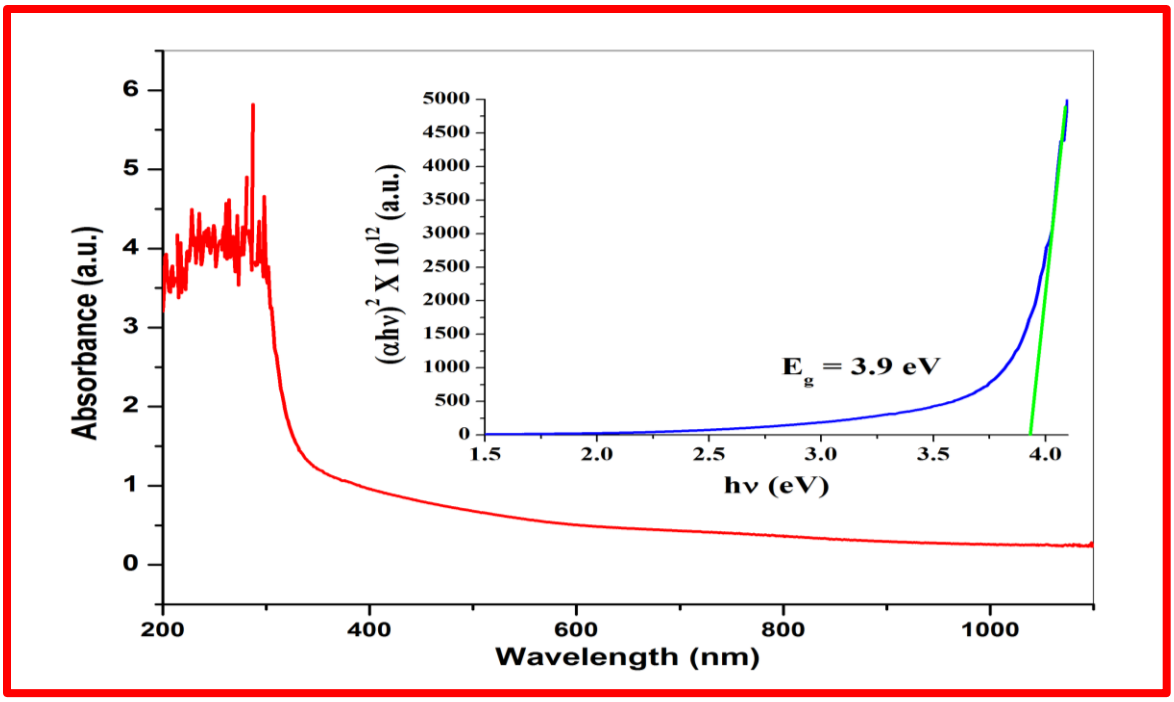

Fig. 2.9 UV-Absorption spectrum with insitu plot for band gap estimation

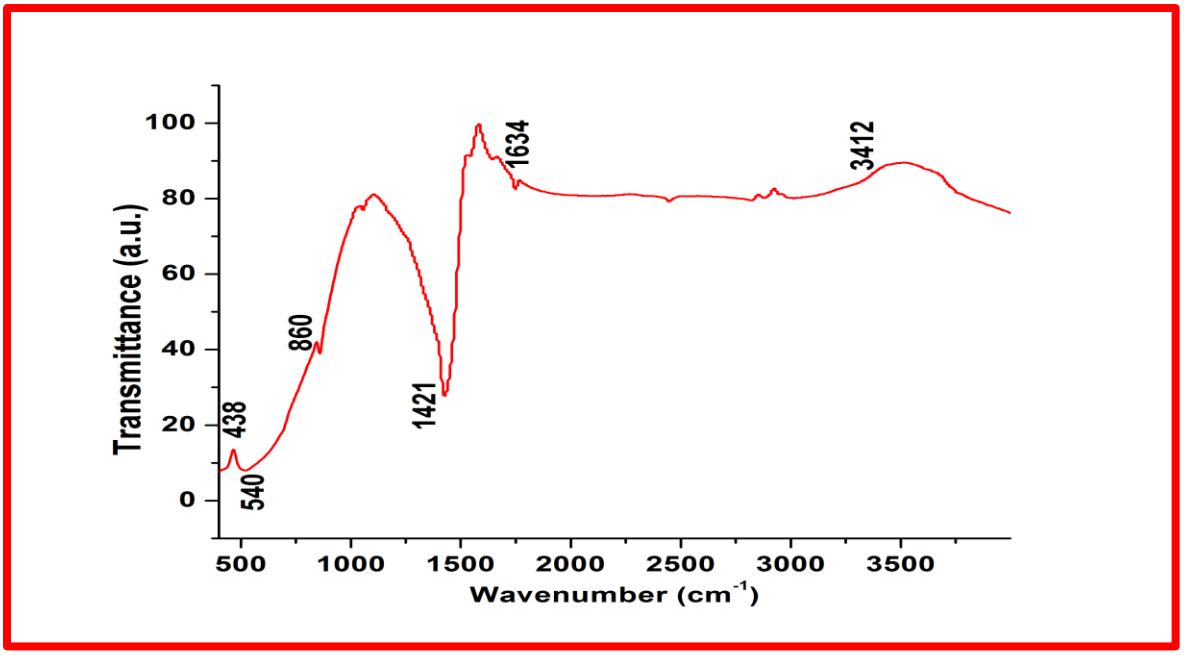

Fig. 2.10 FTIR spectrum of Barium titanate showing bending and stretching between the molecules in the form of peaks in Transmittance mode

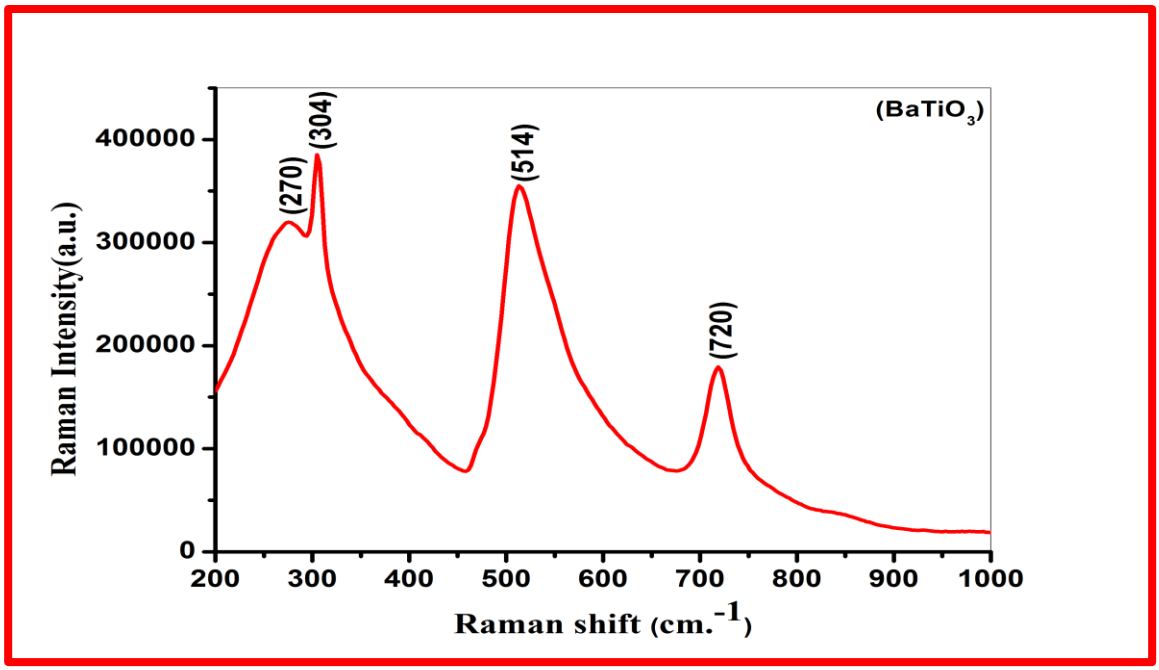

Fig. 2.11 Raman spectrum of polycrystalline Barium titanate

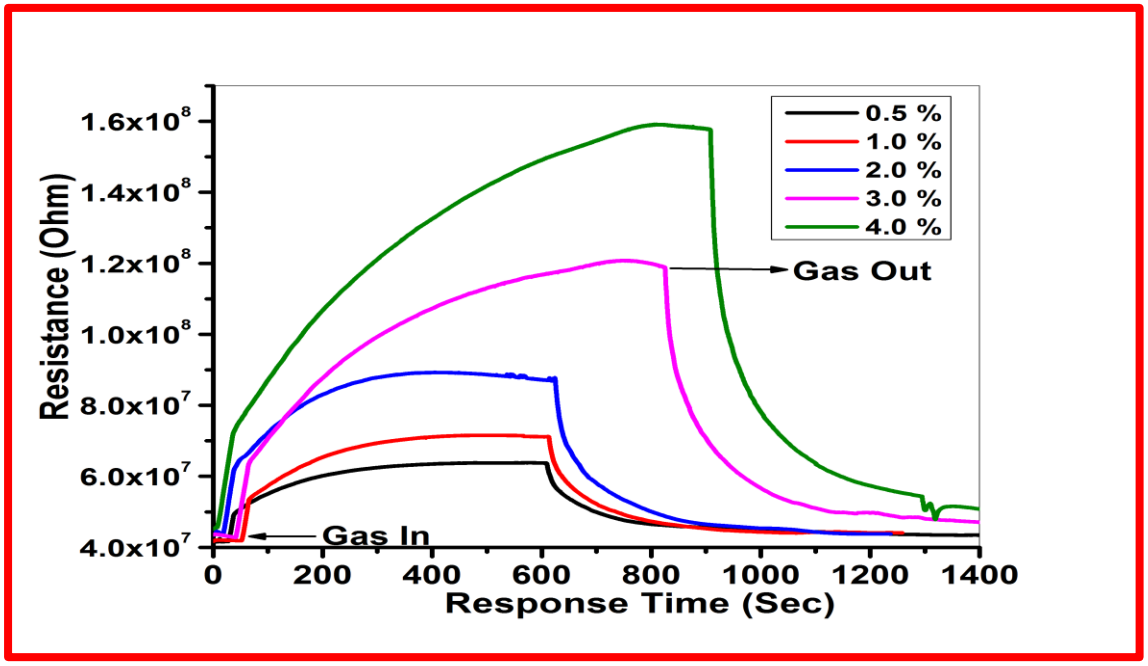

Fig. 2.12 Gas sensing behavior of Barium titanate thin film at different concentration varying from 0.5 vol% to 4 vol.% of LPG.

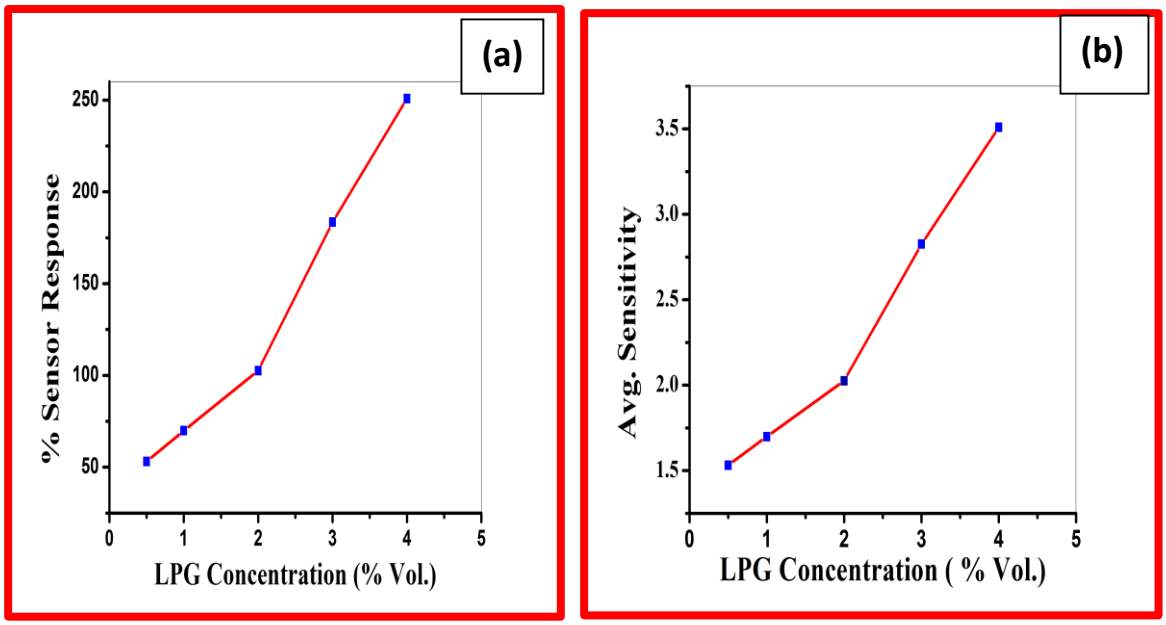

Fig. 2.13 (a) % Sensor Response vs LPG concentration and (b) Sensitivity vs LPG concentration

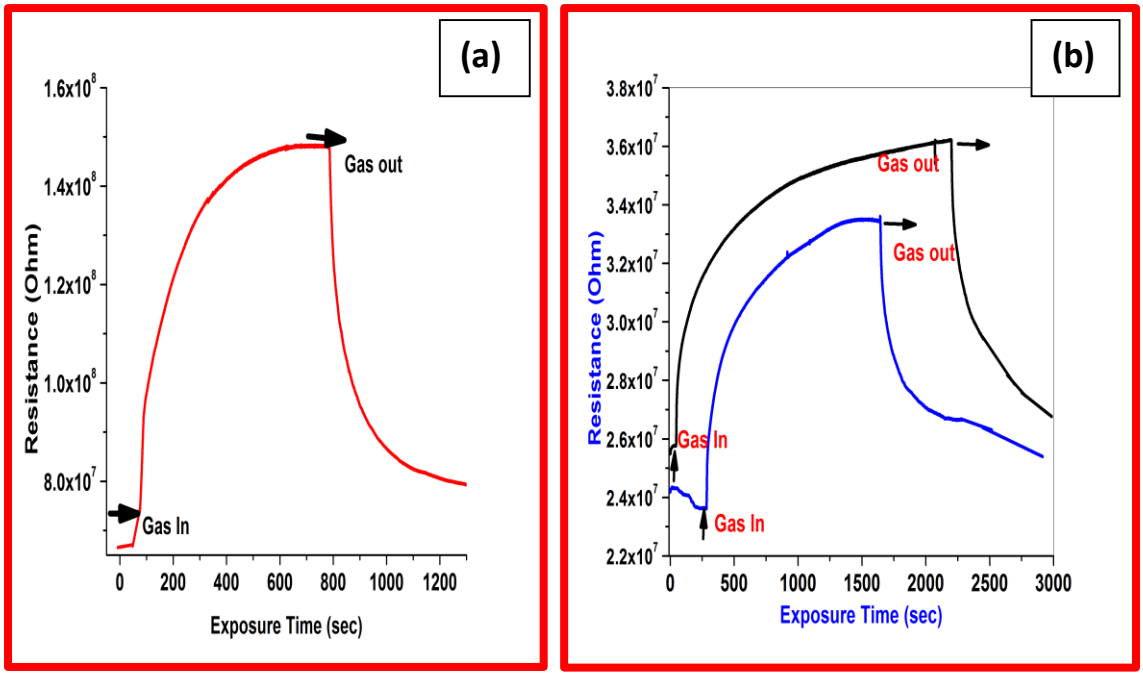

Fig. 2.14` Reproducibility curve of the $BaTiO_3$ thin film at 3 vol.% of LPG and aging effect after two weeks and four weeks for 0.5 vol.% of LPG

S.No.	LPG Concentration (in vol.%)	Sensitivity	% Sensor Response
1.	0.5	1.53	53.156
2.	1	1.69	69.84
3.	2	2.02	102.56
4.	3	2.82	182.55
5.	4	3.50	250.85

Table.2.1 Variation of sensitivity and % Sensor response with LPG concentration

Table 2.2 Comparative study of LPG sensing of Barium titanate from open literature

S. No.	Material for Synthesis	Materials Used	Operating Temp ^{o}C	Methods	Crystallite Size	Sensitivity	Ref.
1.	$BaTiO_3$	Barium chloride, titanium chloride	350	Spray pyrolysis	40 nm by XRD	3.03	[7]
2.	$BaTiO_3$	Barium hydroxide, titanium butaoxide	300	Solid state reaction	65 nm by XRD	0.45	[8]
3.	$BaTiO_3$	Barium Acetate, titanium tetraiso-propoxide	25	Sol- gel method	6.7 nm by TEM 11 nm by XRD	3.5	Present work

Chapter 3

Detection of Liquefied Petroleum Gas below lowest explosion limit (LEL) using nanostructured hexagonal Strontium ferrite thin film

This chapter reports the synthesis of nano crystalline hexagonal Strontium ferrite nanoparticles $SrFe_{12}O_{19}$ by chemical co-precipitation method in this chapter. Thin films of strontium ferrite were prepared on glass substrate and characterized by various techniques such as XRD, SEM, TEM, EDS, UV-spectroscopy and FTIR. XRD pattern revealed the phase transformation of M-type hexa-ferrite with the minimum crystallite size of 18 nm. Uniform macro porous surface structure of the film was revealed by SEM images. Existence of iron, strontium and oxygen in the material was confirmed by using EDX. Optical characterization of the material was done by UV-Spectroscopy and band gap was found as 3.2 eV. The liquefied petroleum gas (LPG) sensing behavior of Strontium ferrite film was investigated at room temperature. The variations in electrical resistance of the film were measured with the exposure of LPG with respect to time as a function of concentration (0.5-5 vol.%) of LPG. The maximum value of sensitivity was found 7 and maximum sensor response was 602.23.

CHAPTER 3

DETECTION OF LIQUEFIED PETROLEUM GAS BELOW LOWEST EXPLOSION LIMIT (LEL) USING NANOSTRUCTURED HEXAGONAL STRONTIUM FERRITE THIN FILM

3.1 Introduction

Surface to volume ratio and quantum confinement elucidate to nanostructure of materials. Ferrites are basically a class of material which contains iron oxides having enthralling magnetic and electric properties [1]. These are prepared by sintering various transition metal oxides along with the alkaline earth metal oxide. Development of new class of ferrites and studies on improvements in their properties began in early 90's. On the basis of technological application, magnets are distinguished as soft magnetic materials and hard magnetic materials [2]. Soft magnetic materials are those magnetic materials whose domains shift when a magnetic field is applied and hard magnetic materials are those magnetic materials with less mobility of domain wall. Magnetized hard ferrites possess a hexagonal structure with the high value of magnetization and magnetocrystalline anisotropy so these are termed as M phase ferrites, with M as Ba, Sr or Pb [3-4]. $SrO\text{-}Fe_2O_3$ binary system has few ternary oxides including $SrFe_{12}O_{19}$, $SrFe_2O_4$, $Sr_2Fe_2O_5$, $Sr_3Fe_2O_6$. Among these $SrFe_{12}O_{19}$ have attracted the attention of most of the researchers due to its vast area of applications besides stable characteristics, they have high electrical resistivity. Celesite is the natural ore of Strontium ferrite. Krik-othmer in 1993 called it M-Ferrite with P63/mmc space group. Strontium ferrite is used for LPG sensing because of relatively high resistance and special magnetic resonance properties for absorption. In Strontium ferrite, there are large interstitial sites which interact with the oxygen molecules in comparison to other ferrites. The dielectric properties of Strontium ferrite shed light on the charge carriers which are responsible for charge transport phenomenon. These ferrites can be prepared by different methods viz. as chemical co-precipitation, sol-gel, ball milling, solid-state reaction and reverse micelle process [5-9].

In this chapter, we report the synthesis of Strontium ferrite powder by co-precipitation method and its LPG sensing. This is characterized using XRD, SEM, TEM,

EDX, Zetasizer, UV Spectroscopy and FTIR. Due to large interstitial sites, $SrFe_{12}O_{19}$ has special magnetic resonance and absorbing properties, directed towards for better sensing properties.

3.2 The Structure of Strontium ferrite

Strontium ferrite contains strontium and iron where strontium is S block element belonging to group 2 period 5 with $5s^2$ electronic configuration and iron belonging to d-block element; group 8 period 4 with electronic configuration $3d^6 4s^2$ [10]. Crystal structure of M-phase ferrite is complex but can be described as hexagonal with the unique axis. Strontium ferrite possesses pyramidal or plate-like structure. $SrFe_{12}O_{19}$ possess 64 ions per unit cell along with 11 different symmetry sites. Oxygen atoms are closely packed at the interstitial position with Sr and Fe in ten layers along with the C-axis. The iron atoms are positioned at five different crystallographic sites 2a, 2b, 4f, 4k and 12k. Among them 12k, 4k, 2a are on octahedral site, 4f on tetrahedral site and 2b forming trigonal bipyramid surrounding by five oxygen atoms. There are five possible structure of Strontium ferrite which is shown in the Table 3.1.

3.3 Literature Review

Kanagesan et al. prepared the Strontium ferrite nanopowder by sol-gel method and carried out an investigation using XRD. The average particle size was found to be 80-100 nm and its thermal analysis revealed its endothermic and exothermic reaction peaks [11]. T.T.V. Nga et al. investigated the magnetic properties of $SrLa_xFe_{12-x}O_{19}$ (x = 0-1.5) prepared by sol-gel method. The material was characterized by XRD, TEM, VSM and the average crystallite size of the particle was reported as 80-100 nm by XRD and 200 nm particle size by TEM [12]. Azim et al. synthesized lanthanum-doped strontium hexaferrite with four different composition of $La_xSr_{1-x}Fe_{12}O_{19}$ (x = 0 - 0.2). His team worked on the structural and electrical characterization of the compositions. XRD confirmed the single hexagonal phase of the four compositions with an average size ranging from 29-35 nm [13]. Neil J. Shirteliffe et al. synthesized aluminum doped barium and strontium hexaferrite nanoparticles prepared by citrate auto-combustion method. Ferrite phase was confirmed by XRD analysis and shifting in diffraction peak was observed with variation in aluminum

concentration in strontium ferrite [14]. Lagorce et al. showed the magnetic and mechanical behavior of micromachined strontium ferrite polyimide composites which further applicable in developing microelectronics and micromachining [15]. J.V.A. Santos et al. prepared new sol-gel route to obtain high quality $BaFe_{12}O_{19}$ thin film with crystallite size 32 nm confirmed by XRD. Magnetization loop of $BaFe_{12}O_{19}$ with the large coercive field is obtained on the amorphous silica substrate at room temperature [16].

3.4 Experimental Method

3.4.1 Materials Required

Strontium nitrate and ferric nitrate were used as the starting materials. Aqueous ammonium hydroxide was used to get the precipitate. Distilled water and ethanol was used to wash the precipitate and glacial acetic acid was used to dissolve the strontium ferrite powder to obtain gel.

3.4.2 Synthesis of Strontium ferrite powder

Strontium nitrate and Ferric nitrate were used as the starting materials. Both the nitrates were taken and dissolved in distilled water in 1:12 molar ratio and stirred up for 2 h. Then 25% aqueous ammonium hydroxide was added drop by drop to maintain the pH level of the solution up to 11 to maintain the crystallite size and homogeneity of the material. After stirring, the sample was put for ageing for 24 h and then it was filtered and washed with distilled water several times till the pH approaches from 7 to 8. Then the sample was dried at 60°C for 2 h inside the oven and further, it was annealed at 900 °C for 2 h in a programmable electric furnace [17-18]. Reactions carried out during this process are given as below:

$$2Sr(NO_3)_2(aq.) + 4Fe(NO_3)_3(aq.) + 16NH_4OH(aq.) \longrightarrow Sr_2Fe_4(OH)_{16}.nH_2O + 16NH_4NO_3(aq.)$$

$$\downarrow$$

$$SrO + SrO.Fe_2O_3 + Fe_2O_3 + 8H_2O$$

$$\downarrow \Delta$$

$$SrFe_{12}O_{19}(Hexaferrite)$$

The crystalline powder was crushed into the fine powder by using mortar and pestle. The flowchart of synthesis of Strontium ferrite powder is given as under:

3.4.3 Preparation of thin film of Strontium hexaferrite

Sol-gel spin coating technique is one of the best methods used to deposit the uniform thin films. It is advantageous over to other conventional thin film techniques because it requires less equipment and is potentially cheap. Besides this, the microstructure and uniformity of the deposited film can easily be controlled by regulating the preparation condition namely, solution concentration/fluid density, fluid viscosity, the speed of the spinner. The glass substrate of dimension 1.5 x 1.5 cm^2 was cut and cleaned using distilled water and ethanol and followed by ultrasonic cleaning. A thick solution of $SrFe_{12}O_{19}$ was made by dissolving 0.20 gm. of powder in 40 ml glacial acetic acid and it was sonicated for 6 h. Then the solution was spun on the glass substrate using a photoresist spinner at a speed of 1000 rpm and for 30 s and dried at 60 ^oC for 2 min on a hot plate. Again spin coating at 1000 rpm for 30 sec was carried out and again dried for 2 min on the hot plate. This process was repeated for 3-4 times for obtaining homogeneous ferrite thin film and later it was dried at 80 ^oC for 5 min on the hot plate [19-20].

3.4.4 Gas sensing measurement

A gas chamber made of borosil glass along with the inlet and outlet knobs was fabricated in our lab. The inlet of the gas chamber was connected to the concentration measuring unit for measuring the exact vol.% of the gas inserted inside the chamber. The whole arrangement was placed on a marble slab. Sensing film with silver electrodes protruded outside was placed inside the chamber. The outer ends of the leads were connected to the Keithley electrometer model 6517B for measuring the electrical resistance of the film.

3.4.5 Characterization Techniques

XRD pattern of the prepared powder of Strontium ferrite ($SrFe_{12}O_{19}$) was recorded by glancing angle X-ray Diffractometer (Proto- Model- X-ray Diffractometer), equipped with monochromatic Cu-Kα as the radiation source (30 kV and 15 mA). Surface morphological study of the material has been done by ZEISS SEM equipped with W (Tungsten) hairpin filament & LaB_6 gun operated at 20 kV. EDAX spectra were obtained by in-situ Brooker element analyzer for qualitative chemical analysis. TEM analysis was carried out by FEI Technai G2 Spirit TWIN, Netherlands. Optical characterization of the sample was performed by using UV-Visible spectrophotometer (Evolution 201). The FTIR spectra of the strontium ferrite sample were recorded by the instrument, Thermo Nicolet, (Model No. 6700, USIC, BBAU, Lucknow, India).

3.5 Results and Discussion

3.5.1 X-Ray Diffraction (XRD) Analysis

X-ray diffraction is based on the constructive interference of the monochromatic X-rays. The interaction of incident rays with the sample produces constructive interference when it satisfies the Bragg's condition [21]. Fig. 3.3 shows the X-Ray diffraction pattern of strontium ferrite film. The analysis of XRD pattern matched with JCPDS no. #801197 reveals that the phase of the film is hexagonal M-type with lattice parameter a = 5.883 Å and c = 23.037 Å. The peaks at 2θ = 30.35 (110), 32.357 (107) and 34.198 (114) confirm the presence of ferrite phase. The minimum crystallite size of the hexagonal $SrFe_{12}O_{19}$ thin film was calculated as 18 nm by using Debye Scherer's equation through broadening of the intensity peak. [22-23].

3.5.2 SEM Analysis

SEM micrographs show the porous nature of the material at 10 KX and 20 KX magnification. Grains are unevenly distributed leaving vacant spaces among them. The size of pores lies in the range 0.1μm - 0.5μm. These pores serve as adsorption centers and play very important role in gas sensing [24].

The aggregation model suggests that if there is no barrier exists, aggregation due to Brownian motion and attractive Van der Walls forces will rapidly decrease the number of particles in the suspension. According to this theory, the particle will grow until they reach a stable size. At this point, they will grow by combining with smaller unstable nuclei and not by collisions with other stable particles. This shows that particle aggregation plays a significant role in the growth of particle size of the final product if initial nuclei are unstable. At the early stage of ageing, as the processing of the reaction, homogeneous nucleation occurred in the entire solution. As the temperature increases, more and more nuclei were formed, some of them combined to form primary spherical particles by an aggregation growth mechanism. At the final stage of ageing, a large no. of spherical particles were formed, and several particles together formed softly agglomerates. Evidence of the statement is also supported by the Transmission electron microscopy images shown in Fig. 3.6.

EDAX spectrum is shown in Fig. 3.5 and confirms the formation of strontium ferrite with compositions as Sr 51.25%, Fe 16.62%, and O 32.13% in our sample. These compositions confirm the theoretical properties obtained by calculations.

3.5.3 TEM Analysis

Fig. 3.6(a) & (b) shows the TEM images of strontium ferrite, loaded on the carbon coated copper grid at different scales. Sample preparation plays an important role in TEM analysis. The sample was prepared by dispersing very few amount of Strontium ferrite powder in ethanol and sonicated for many times. The ultrasonic waves produced during sonication reduce the size of the nanocrystals and also removes the agglomeration. Few drops of the floating solution were dipped on the grid. The image reveals the crystalline nature with plumbite hexagonal structure [25]. The grain size was found as 20 nm. Also, the dimensions of some particles are below 10 nm which can be seen clearly by zooming the image at large level.

3.5.4 UV-Visible Absorption Analysis

The graph represents the variation of optical absorbance for the thin film with the wavelength. The optical absorbance spectra of strontium ferrite film deposited separately

on the glass substrate were plotted with 200-1100 nm wavelength range. This data was further used for analyzing the optical bandgap energy (E_g). The optical band gap of strontium ferrite can be calculated from the intercept of energy axis obtained by extrapolating the plot on energy axis [hυ versus $(\alpha h\upsilon)^2$] as shown by the in-situ of Fig. 3.7. The bandgap of the film was estimated as 3.2 eV and it plays a vital role in gas sensing mechanism. The band gap of Strontium ferrite varies when the gas was injected into the chamber. As LPG reacts with the chemisorbed oxygen species on the surface of the Strontium ferrite film, electrons are released from the valence band to conduction band which changes the electrical resistance of the film constituting the sensitivity of the sensor [26].

3.5.5 Fourier Transform Infrared (FTIR) Analysis

FTIR spectra were obtained at room temperature for wave number 4000 to 400 cm^{-1}. The IR spectrum is obtained by using KBr pellet mixed in 1:20 ratio of the sample pressed with hydraulic pressure machine. FTIR spectrum of Strontium ferrite is presented in Fig. 3.8. The two absorption peaks between 400 cm^{-1} to 800 cm^{-1} represent the vibration band of iron and strontium with oxygen, revealing the metal-oxide bonding in Strontium ferrite. Bands at 443 cm^{-1} and 592.7 cm^{-1} are the characteristic absorption peaks of hexaferrite. The peaks at wave number 1141.34 cm^{-1} are related to the C-N bond formation during the synthesis process and the peaks at wave number 1377.7 cm^{-1} are due to stretching vibration of nitrates (NO_3^-) group indicating nitrate ions. The peaks around wave number 1634.615 cm^{-1} are attributed to υ (OH) stretching and bending vibration due to the presence of deformation vibrations of water molecules adsorbed during the compaction of powder specimens with KBr. The spectrum shows a stretching frequency within the region 3600-3400 cm^{-1} which corresponds to free –OH group and hydrogen bonded hydroxyl group [27-28].

3.5.6 Particle Size Analysis

The particle size of Strontium ferrite was analyzed by dissolving it in distilled water and methanol solution using Zeta nanosizer (Nano ZS90) and corresponding data are plotted as shown in Fig 3.9. It measures the acoustic wave attenuation (dB/cm) Vs

frequency in the range 1-100 MHz. From the particle size distribution curve, it was found that average size of the particle was 90 nm with 100% intensity. The average particle size is larger due to agglomeration of the particles.

3.5.7 LPG Sensing Investigations

3.5.7.1 Working principle of LPG sensing

LPG is a mixture of hydrocarbon gases with propane and butane as its main components. National Institute for Occupation Safety and Health (NIOSH) and Occupational Safety and Health Administration (OSHA) are the agencies that calibrated the LEL of propane as 2.2% and butane 1.8% gas in the air in vol. % [30-31]. Lower Explosive Limit (LEL) is the explosive range in which the concentration of a gas explode if any ignition source is introduced near to it. So as to avoid an emergency situation, LPG sensors are required for the detection of LPG leakage. This chapter deals with the gas sensing properties of Strontium ferrite at room temperature. Gas sensing measurements were done by the experimental setup as discussed in Sec. 2.4.4. As dry film surface having several random orientations and vacant sites associated with high electrostatic force, atomic oxygen was attracted; as a result, there was an increase in conductivity. After getting stabilized with an open atmosphere, the LPG gas was injected into the chamber and the components of hydrocarbons were dissociated. H^+ atoms were adsorbed by the lattice oxygen forming the water vapours as a combustible product which forms a depletion layer. This layer is responsible for the increase in resistance of the film [32-33]. As the concentration of gas inside the chamber increases, the potential barrier becomes stronger and further constant. As the resistivity with the exposure of gas increases, consequently, the sensitivity of the film also increases. The sensitivity is the measure of physical or chemical properties of the sensing material when it is exposed to the desired gas. Significant and sequential variations in electrical properties of the sensing element under investigation will cause the higher sensitivity. The sensitivity of LPG sensor may be defined as the ratio of the resistance in presence of the target gas (R_g) to the resistance in the presence of the air (R_a) [34-35] i.e.

$$S = \frac{R_g}{R_a}$$

The sensor response (SR) may be defined as under:

$$\%SR = \frac{|R_a - R_g|}{R_a} * 100$$

3.5.7.2 Sensing behaviour of Strontium ferrite thin film

Sensing behaviour of Strontium ferrite thin film was studied by focusing on its sensing parameters with exposure to the gas. Response time, recovery time, sensitivity, % sensor response and selectivity are the parameters of a gas sensor [36-37]. Response time is the time in which sensor reaches to its 90% of the maximum resistance of the film when exposed to the LPG. Recovery time is the time required for the sensor to come back approximately to its initial stage [38]. Variations in the resistance of the Strontium ferrite film with the exposure time were recorded through Keithley electrometer. Since Strontium ferrite is a hexaferrite so it has more active sites for adsorption phenomenon. Therefore a fast response with change in resistance of the film is observed when the film was exposed to the LPG. Similarly, it also recovers easily when the outlet of the chamber was opened. From the Fig. 3.9 for 0.5 vol. % of LPG the resistance of the film in the air was around 52.45 MΩ. When the film was exposed to LPG, the resistance was increased rapidly up to saturation level and became constant at 89.74 MΩ. Later the outlet of the chamber was opened and the LPG was eliminated from the chamber. Then there was a rise in resistance of the film from 52.45 MΩ to 53.78 MΩ. Thus, the exposure of different concentration of LPG may be presented by various other curves.

Variations in sensor response with time for different concentrations of LPG were recorded and plotted in Fig. 3.10 (a). Each curve shows that on the exposure of LPG, the resistance of the film increases very sharply and as the exposure time increases, it attains a constant position. As the outlet of the chamber was opened, the resistance of the film was found to be decreased and finally attained its initial value. There is a linear change in sensitivity as gas concentration increases from 0.5 to 5 % vol. Sensitivity for each concentration was estimated and plotted in Fig. 3.10(b) which also exhibits the linear

increase with the gas concentration in the chamber. The lower concentration tends to the weaker interaction of adsorbed oxygen species to LPG gas molecules. As the concentration of LPG increases, a number of gas molecules increases in the chamber and finally they were adsorbed by the dangling bonds present on the surface of the film as a result resistance of the film increases. The value of maximum sensitivity was found as 7.022 and % sensor response was 602.23 for 5 vol.% LPG. Response time was found 40 sec and recovery time was found 120 s for 0.5 vol.% LPG. The sensing characteristics of the film were repeated after two months of fabrication, a minute change (±%) was observed indicating the stability and reliability of the sensor.

3.5.7.3 Repeatability curve and selectivity graph

The Repeatability of a sensor is defined as the ability to produce the same output over an interval of time for the same measurand. The repeatability graph of the Strontium ferrite film was as shown in Fig. 3.11 for 0.5 vol.% of LPG. The ageing effect of the film was also observed in the same graph after two weeks for 0.5 % LPG with $\pm$ 5% error. The % error in the result is due to the effect of moisture on the film which deteriorates the power of adsorption on the surface [39-40].

Selectivity of the sensing film was done by the exposure of 1 vol.% of other target gases like C_2H_5OH, NH_3 and NO_2 inside the chamber. Maximum sensitivity was found for the LPG. It was found nil approximately very low for nitrous oxide and ammonia gas. The film responded to the ethanol gas but fruitful results were found for LPG. Hence these graphs support the statement that strontium ferrite is a good sensor for the detection of LPG in comparison to NO_2, NH_3 and C_2H_5OH, gases at room temperature.

3.6. Conclusions

Nanostructured Strontium ferrite was successfully synthesised by coprecipitation and the thin film was prepared by a sol-gel spin coating method. The process used here is inexpensive and environment-friendly. The XRD revealed the formation of hexagonal Strontium ferrite and the minimum crystallite size was found as 18 nm. Peaks in FTIR spectra between 400 cm^{-1} to 600 cm^{-1} elucidated the characteristic peak of hexaferrite. The

SEM image showed the macroporous film with complex magnetoplumbite structure. TEM confirmed the hexagonal structure of the material with a minimum grain size < 20 nm. The value of maximum sensitivity was found as ~ 7 and % sensor response was ~ 602.23 for 5 vol.% LPG. The linear sensing characteristic of Strontium ferrite-based LPG sensor is quite appropriate for developing a commercial LPG sensor below LEL operable at room temperature.

REFERENCES

1. J.F. Wang, C.B. Ponton, I.R. Harris, A Study of Sm- Substituted SrM Magnets sintered Using Hydrothermally Synthesized Powders, Journal of Magnetism and Magnetic Materials, 298 (2006),122-131.
2. B.D. Cullity, Introduction to Magnetic Materials, Addition Wesley, Reading, M.A., (1972).
3. J. Livage, M. Henry, C. Sanchez, Sol-gel chemistry of transition metaloxide, Progress in Solid State Chemistry, 18 (1988) 259-341.
4. Z. Zhuang, B. Bian. R.M. White, D.E. Laughlin, Barium and Strontium Ferrite perpendicular thin film media with a sandust soft magnetic under layer, IEEE Transactions on Magnetics, 37 (2001) 4.
5. Y. Wang, Q. Li, C. Zhang, B. Li, Preparation and Magnetic Properties of different Morphology Nano-$SrFe_{12}O_{19}$ particle prepared by sol-gel method, Journal of Alloys and Compounds, 467(7) (2009) 284-287.
6. A. Javidan, S. Rafizadeh, S.M. Hosseinpour-Mashkani, Strontium ferrite nanoparticle study: Thermal decomposition synthesis, characterization, and optical and magnetic properties, Materials Science in Semiconductor Processing, 27 (2004) 468-473.
7. S. Thompson, N.J. Shirtcliffe, E.S.O. Keefe, S. Appleton, C.C. Perry, Synthesis of $SrCo_xTi_xFe_{(12-2x)}O_{19}$ through sol-gel auto ignition and its characterization, Journal of magnetism and magnetic materials, 292 (2005) 100-107.
8. P. Rao, R.V. Godbole, D.M. Phase, R.C. Chikate, S. Bhagwant, Ferrite thin films: Synthesis, characterization, and gas sensing properties towards LPG, Materials Chemistry and Physics, (2015) 333-338.
9. W.M.S. Silva, N.S. Ferreira, J.M. Soares, R.B. da Silva, M.A. Macedo, Investigation of structural and magnetic properties of nanocrystalline Mn- doped $SrFe_{12}O_{19}$ prepared by proteic sol-gel process, Journal of Magnetism and Magnetic Materials, 395 (2015) 263-270.

10. R.C. Pullar, Hexagonal Ferrite: A review of the synthesis, properties and applications of hexaferrite ceramics, Progress in Material Science, 57(7) (2012) 1191-1334.

11. K. Samikannu, J. Sinnappan, S. Mannarswamy, T. Cinnasamy, Synthesis and magnetic properties of conventional and microwave calcined Strontium Hexaferrite Powder, Materials Sciences and Applications, 2 (2011) 638-642.

12. T.T.V. Nga, T.D. Hien, N.P. Duong, T.D. Hoang, Structural and magnetic properties of $SrLa_xFe_{12-x}O_{19}$ (x= 0-1.5) prepared by using the sol-gel method, Journal of the Korean Physical Society, 52(5) (2008) 1474-1477.

13. M. Azim, S. Atiq, S. Naseem, Structural and Electrical Characterization of Lanthanum doped Strontium Hexaferrite, Sci. Int. Lahore, 24(4) (2012) 341-345.

14. N.J. Shirt-lifter, S. Thompson, E.S. O'Keefe, S. Appleton, C.C. Perry; Highly aluminum doped barium and strontium ferrite nanoparticles prepared by citrate auto-combustion synthesis, Materials Research Bulletin, 42 (2007) 281-287.

15. L.K. Lagorce, M.G. Allen, Magnetic and Mechanical Properties of Micromachined Strontium ferrite/Polyimide Composites, IEEE, Journal of Microelectromechanical System, 6 (1997) 4.

16. J.V.A. Santos, M.A. Macedo, F. Cunha, J.M. Sasaki, J.G.S. Duque, $BaFe_{12}O_{19}$ thin film grown by an aqueous sol-gel process, Microelectronics general, 34 (2003) 565-567.

17. C. Thirupathi, M. Jose, S. Nithiyananthan, Synthesis and Characterization of Strontium ferrite Nanopowder, Asian Journal of Chemistry, 25 (2013) S160- S162.

18. R.K. Tiwary, S.P. Narayan, O.P. Pandey, Preparation of Strontiumhexaferrite magnets from celestite and blue dust by mechanochemical route, Journal of Mining and Metallurgy, 44 (2008) 91-100.

19. A. Ghasemi, A. Morisako, X. Liu, Magnetic properties of hexagonal strontium ferrite thick film synthesized by sol-gel processing using SrM nanoparticle, Journal of magnetism and magnetic material, 320(18) (2008) 2300-2304.

20. M. Kapoor, Characterization, Fabrication of Strontium Ferrite Thin Films and their applicability in thetunable bandstop filter, Shodhganga, Chapter 5, 122-140 (2013).

21. B.D. Culty, Elements of X-Ray Diffraction, second edition, Addison-Wesley Publishing Company, Inc., (1978).

22. T. Xie, L. Xu, C. Liu, Y. Wang, Magnetic composite $ZnFe_2O_4$/ $SrFe_{12}O_{19}$: Preparation,characterization and photocatalytic activity under visible light, Applied Surface Science, 273(2013) 684-691.

23. G. Coffee, J. Hardy, O. Marina, L. Pederson, P. Rieke, E. Thomsen, Copper doped lanthanum strontiumferrite for reduced temperature solid oxide fuel cells, Solid State Ionics, 175 (2004) 73-78.

24. T. Li, Y. Li, R. Wu, H. Zhou, X. Fang, S. Su, A. Xia, C. Jin, X. Liu; A solution for the preparation of hexagonal M-type $SrFe_{12}O_{19}$ ferrite using egg-white :structural and magnetic properties,Journal of Magnetic and Magnetic material, 393 (2015) 325-330.

25. A. Drmota, M. Drofenik, A. Znidarsic, Synthesis and characterization of nano-crystalline strontiumhexaferrite using co-precipitation and microemulsion methods with nitrate precursors; Ceramic International, 38 (2012) 973-979.

26. S. Singh, B.C. Yadav, M. Singh, R. Kothari, A review report on Nanostructured ferrites as Liquefied petroleum gas sensor, International Journal of Science, Technology and Society, 1(1) (2015) 5-22.

27. J. Luo, Y. Xu, D. Gao, Synthesis, characterization and microwave absorption properties of polyaniline/Sm-doped strontium ferrite nanocomposite, Solid State Sciences, 37 (2014) 40-46.

28. S.M. Masoudpanah, S.A.S. Ebrahimi, Effect of citric acid content on the structural and magnetic properties of $SrFe_{12}O_{19}$ thin films, Thin Solid films, 520 (2011)199-203.

29. A.K. Jaiswal, S. Singh, A. Singh, R.R. Yadav, P. Tandon, B.C. Yadav, Fabrication of Cu/Pd bimetallic nanostructures with high gas sorption ability towards development of LPG sensor, Materials Chemistry and Physics, (2015) 16-21.

30. V.K.V. Jadhav, S.A. Patil, D.V.Shinde, S.D.Waghmare, M.K. Zate, R.S. Mane, S.H. Han, Hematite nanostructure, Morphology mediated Liquefied Petroleum gas sensor, Sens. Actuators B: Chem., 188 (2013) 669-674.

31. S. Singh, B.C. Yadav, R. Prakash, B. Bajaj, J.R. Lee, Synthesis of nanorods and mixed shaped copper ferrite and their applications as liquefied petroleum gas sensor; Applied Surface Science, 257 (2011) 10763-10770.

32. B.C. Yadav, S. Singh, A. Yadav, Nanonails structured ferric oxide thick film as room temperature liquefied petroleum gas LPG sensor, Applied Surface Science, 257 (2011) 1960-1966.

33. B.C. Yadav, S. Singh, A. Yadav, T. Shukla, Experimental investigations on nano-sized ferric oxide and its LPG sensing International Journal of Nanoscience,10(1)(2011)1-5.

34. D.A. Pomogailo, S. Singh, M. Singh, B.C. Yadav, P. Tandon, S.I. Pomogailo, G.I. Dzhardimalieva, K.A. Kydralieva, Polymer Matrix Nanocomposite Gas Sensing Materials; Inorganic Materials,50(3)(2014) 296–305.

35. A. Singh, A. Singh, S. Singh, P. Tandon, B.C. Yadav, R.R. Yadav, Synthesis, characterization and performances of zinc ferrite nanorods for room temperature sensing applications; Journal of alloy and compounds,618 (2015)475-483.

36. M. Singh, B.C. Yadav, A. Ranjan, M. Kaur, S.K. Gupta, Synthesis and characterization of perovskite barium titanate thin film and its application as LPG, Sens. Actuators B: Chem., sensor241, (2017). 1170-1178 (2016).

37. R.K Sonker, M. Singh, U. Kumar, B.C. Yadav, MWCNT Doped ZnO Nanocomposite Thin Film as LPG Sensing, J. of Inorg Organomet Polym, 26(6) (2016) 1434–1440.

38. Y.K. Mishra, G. Modi, V. Cretu, V. Postica, O. Lupan, T. Reimer, I. Paulowicz, V. Hrkac, W. Benecke, L. Kienle, R. Adelung, the Direct growth of freestanding ZnO Tetrapod Networks for multifunctional Applications in Photocatalysis, UV-Photodetection and gas sensor, Appl. Mater. Interfaces, 7(26), (2015), 14303-14316.

39. R. Srivastava, B.C. Yadav, M. Singh, T.P. Yadav, Synthesis, Characterization of Nickel Ferrite and Its Uses as Humidity and LPG Sensors, J. Inorg Organomet Polym, 26(6) (2016) 1404-1412.

40. O. Lupan,V. Cretu, V. Postica, N. Ababii, O. Polonskyi, V. Kaidas, F. Schutt, Y.K. Mishra, E. Monaico, I. Tiginyanu, V. Sontea, T. Strunskus, F. Faupel, R. Adelung,

Enhanced ethanol vapor sensing performances of copper oxide nanocrystals with mixed phases, Sens. Actuators B: Chem., 224 (2016) 434-448.

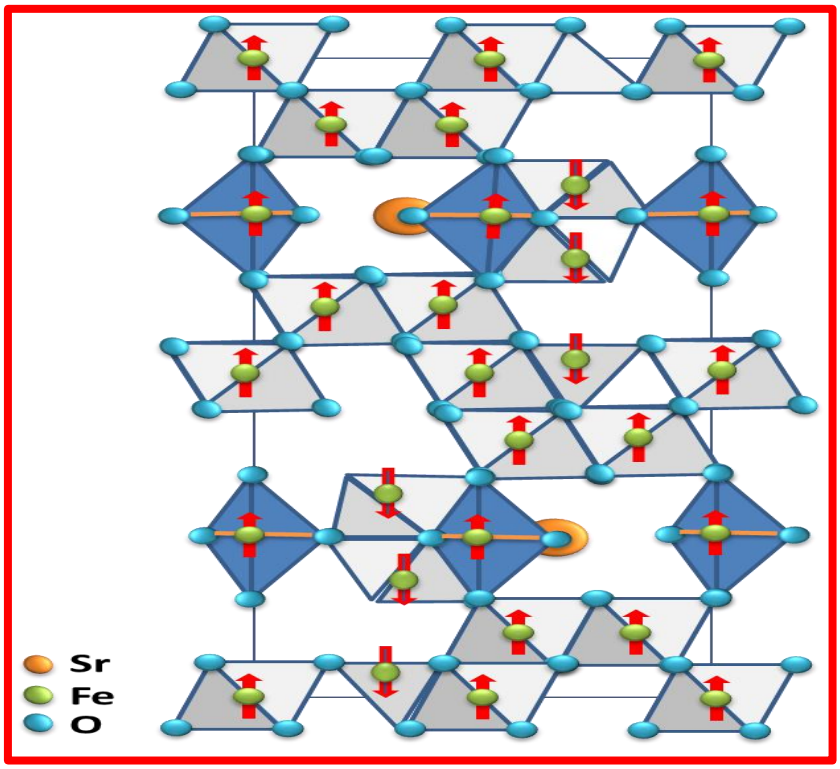

Fig. 3.1 Flowchart for preparation of Strontium ferrite powder

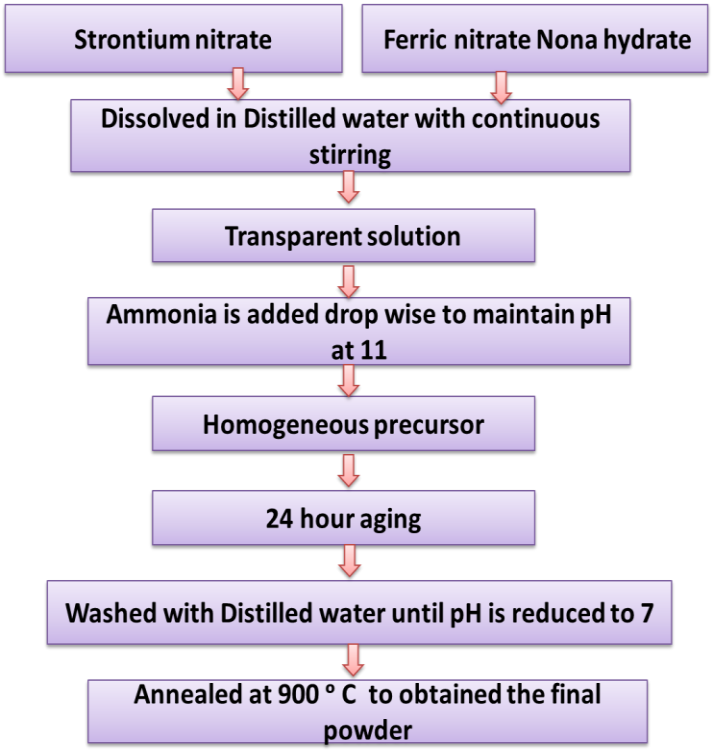

Fig. 3.2 Structure of hexagonal Strontium ferrite

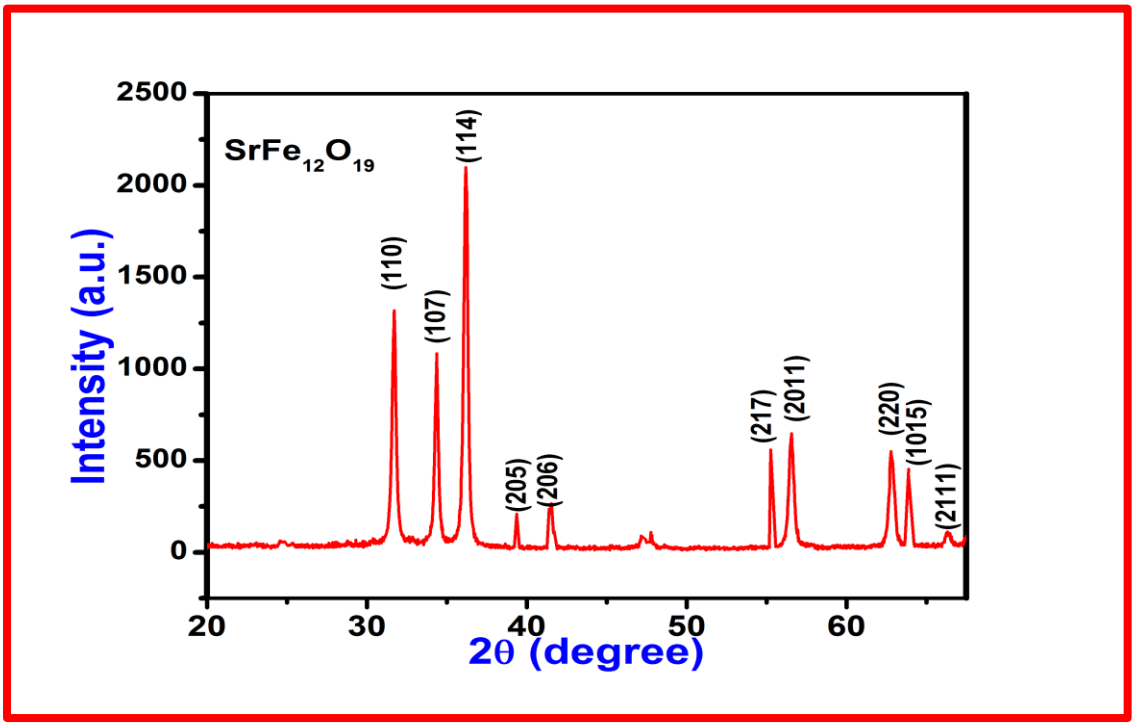

Fig. 3.3 XRD pattern of Strontium ferrite film

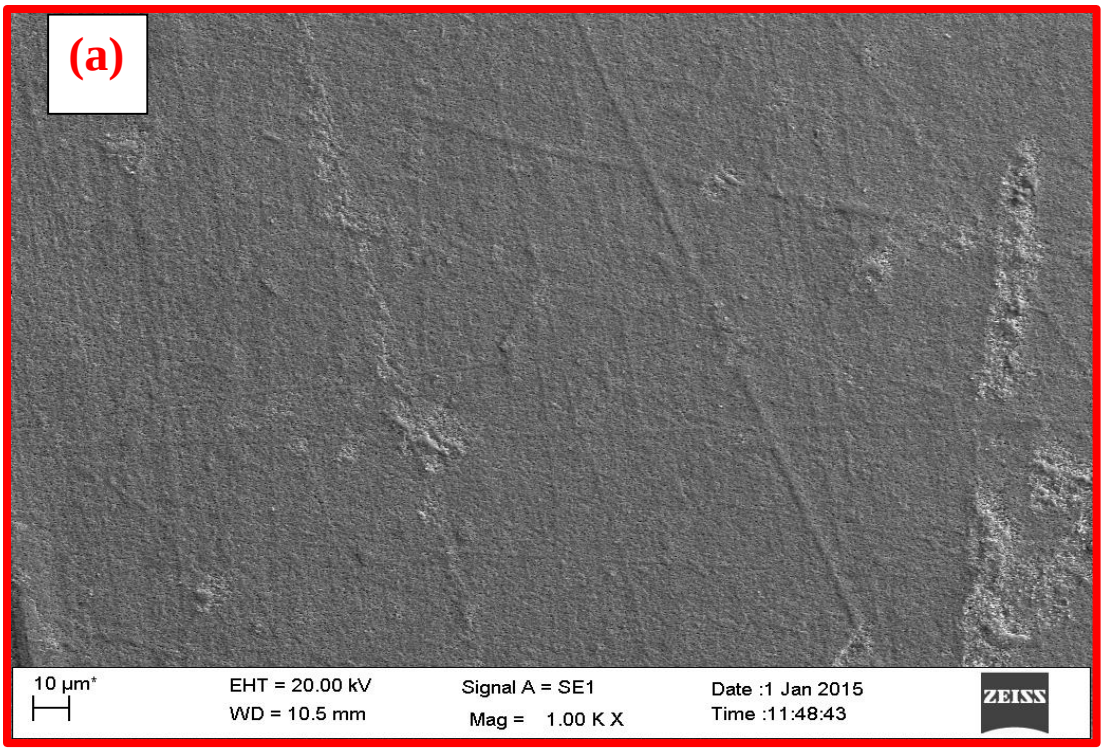
(a)
10 µm*
EHT = 20.00 kV
WD = 10.5 mm
Signal A = SE1
Mag = 1.00 K X
Date :1 Jan 2015
Time :11:48:43
ZEISS

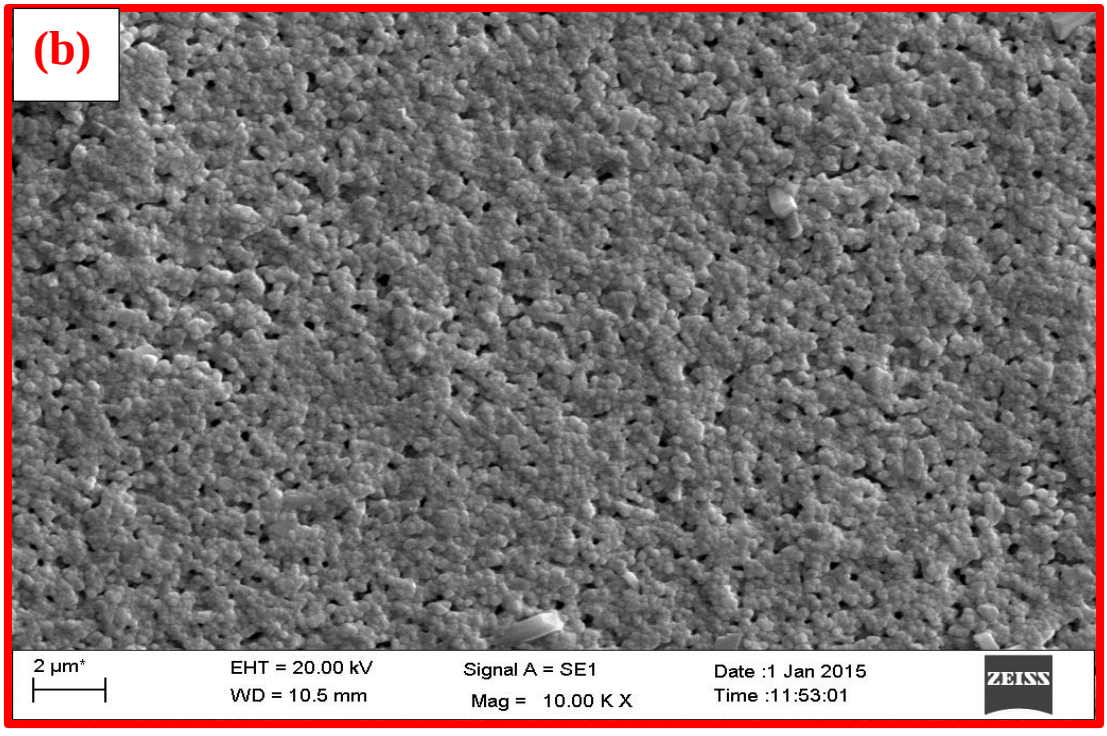
(b)
2 µm*
EHT = 20.00 kV
WD = 10.5 mm
Signal A = SE1
Mag = 10.00 K X
Date :1 Jan 2015
Time :11:53:01
ZEISS

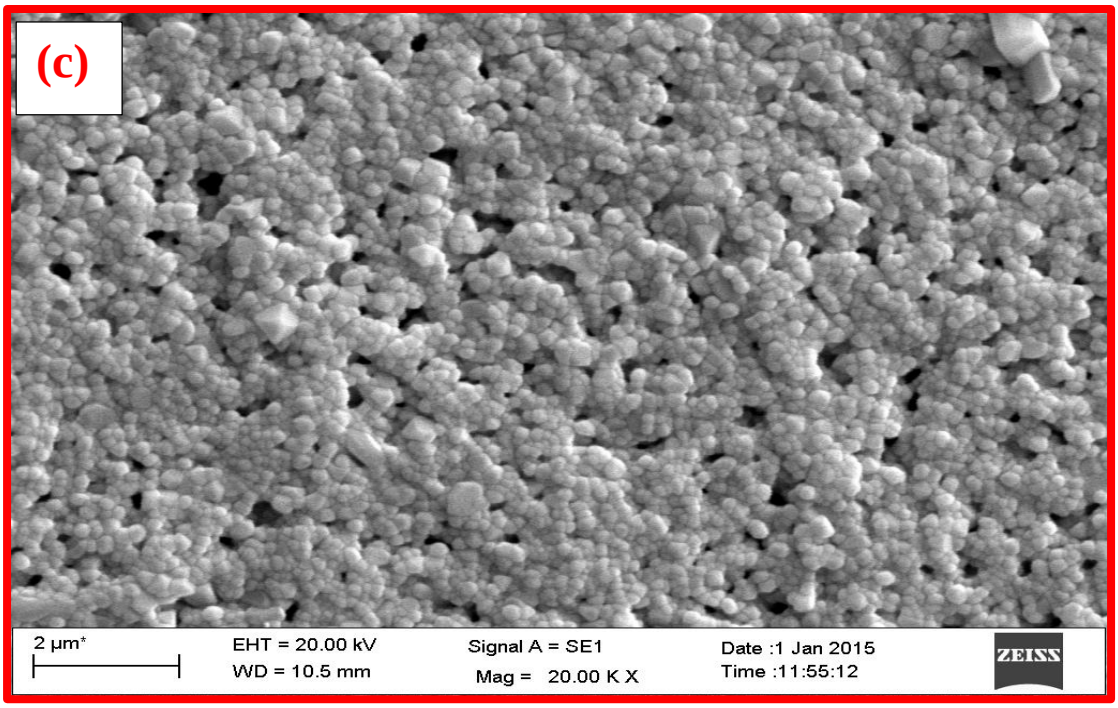

Fig. 3.4 (a) and (b) SEM image of macroporous Strontium ferrite at different magnification

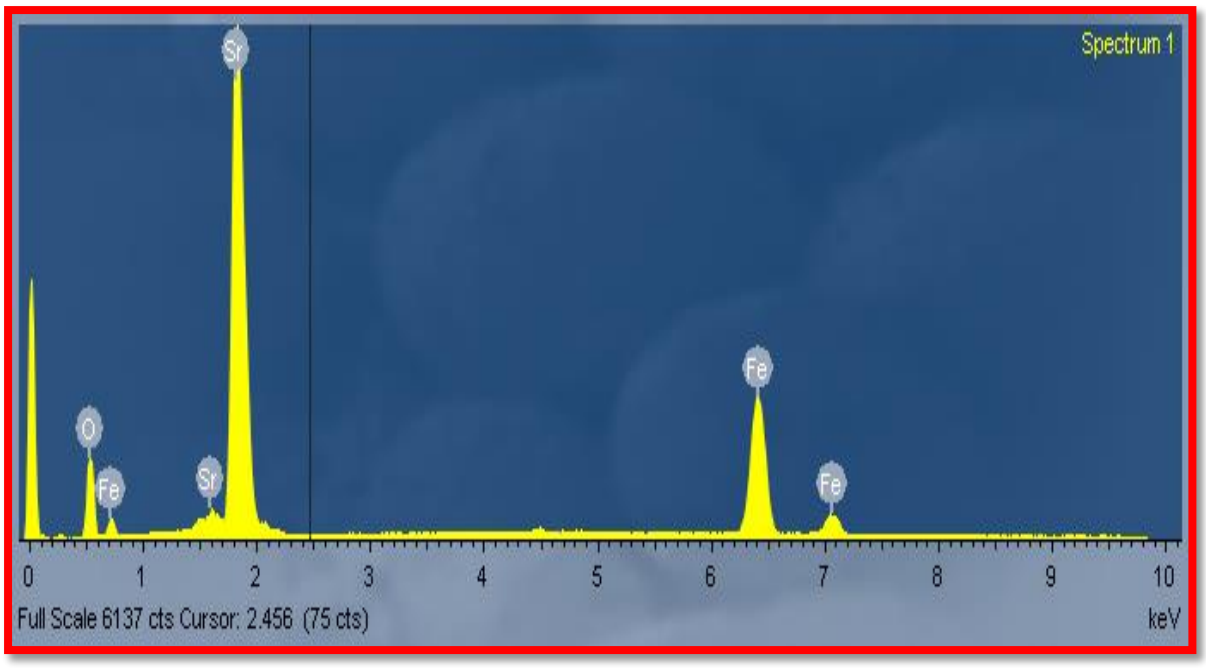

Fig. 3.5 EDAX of Strontium ferrite

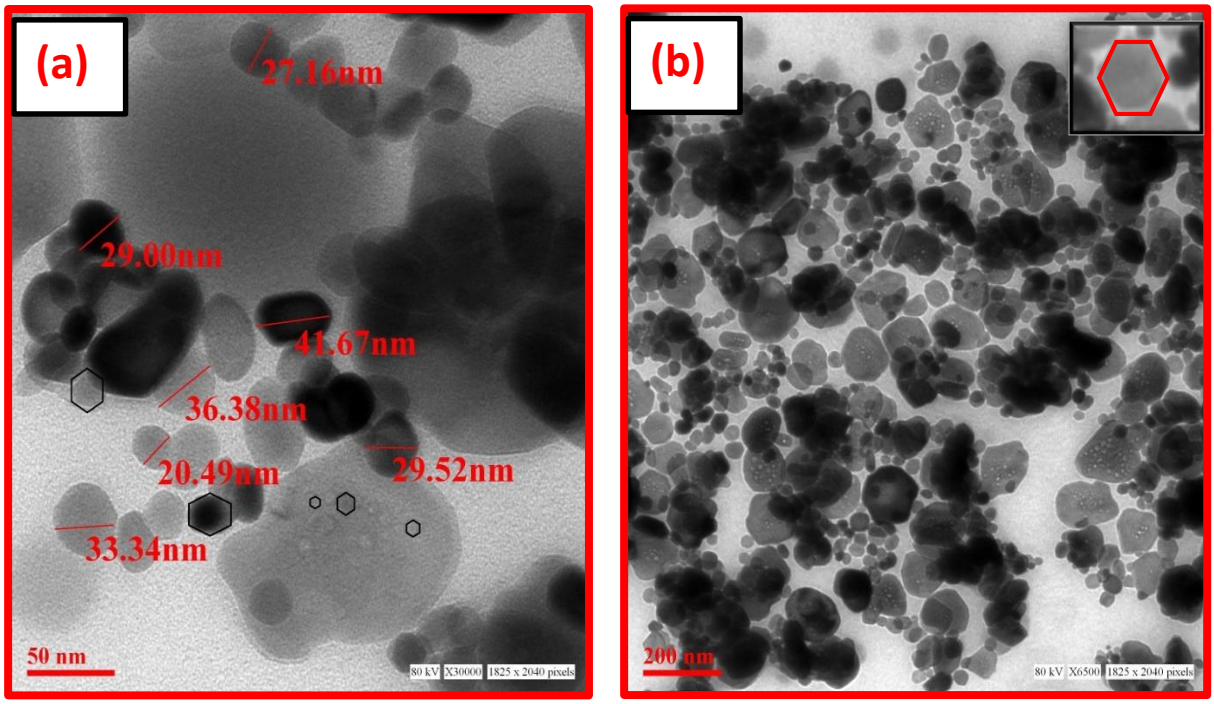

Fig. 3.6 (a) and (b) representing TEM micrographs of $SrFe_{12}O_{19}$ at different scales

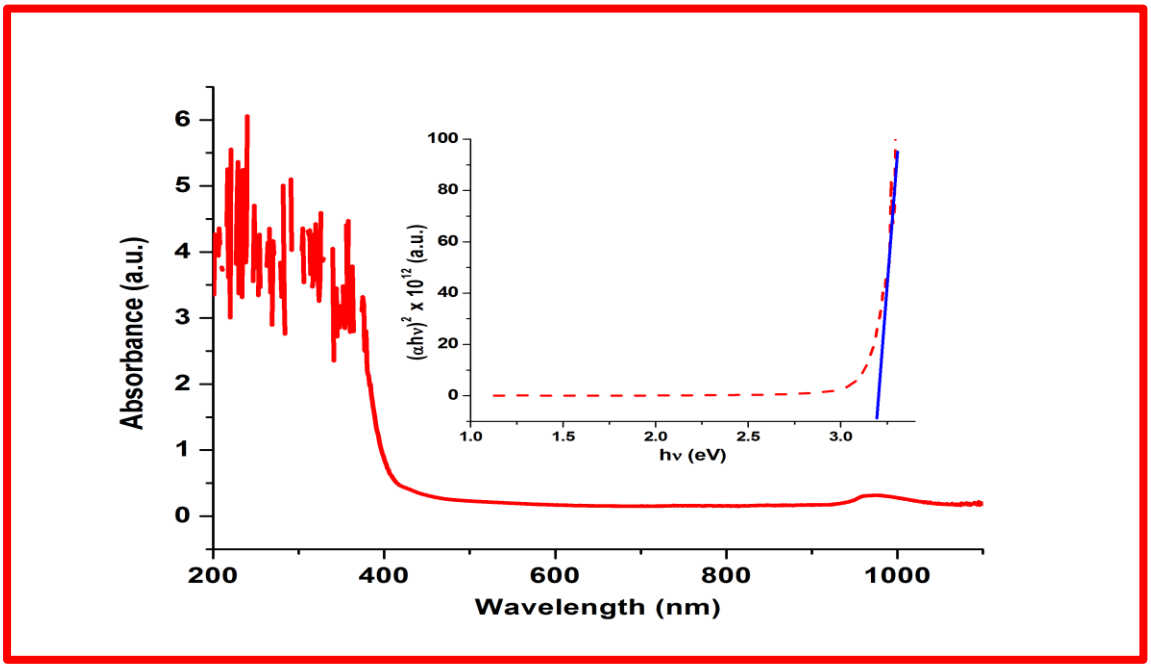

Fig. 3.7 UV-vis absorbance with the wavelength and in situ figure shows Tauc plot

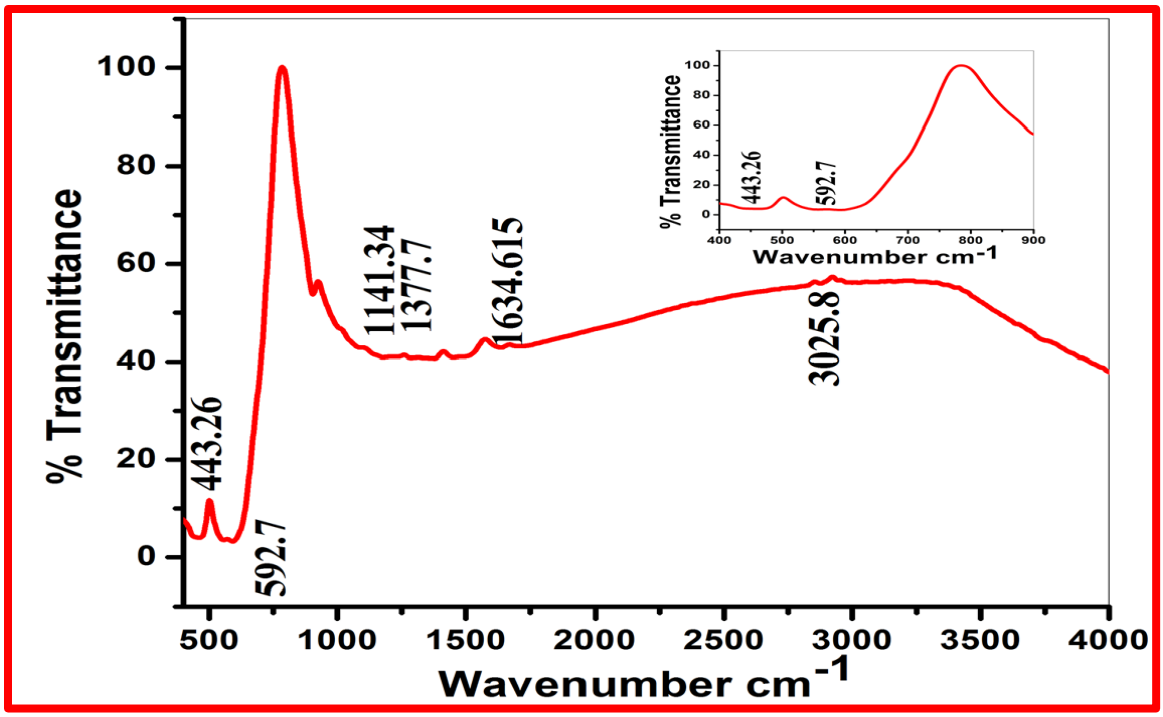

Fig. 3.8 FTIR spectrum of $SrFe_{12}O_{19}$

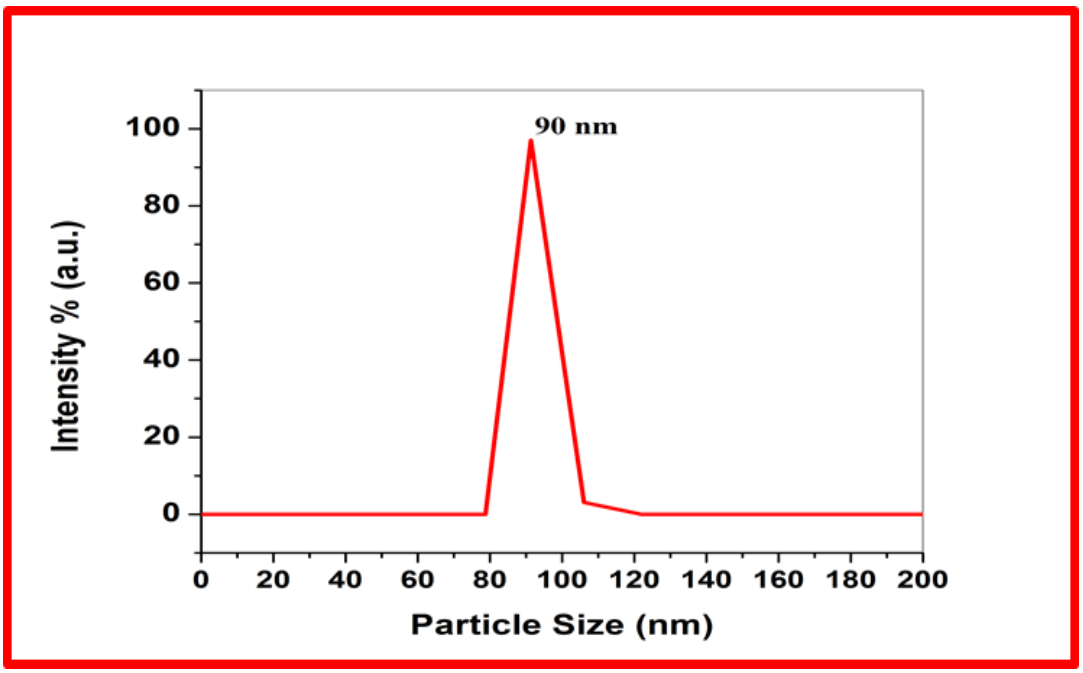

Fig. 3.9 Particle size distribution by nano ZS90

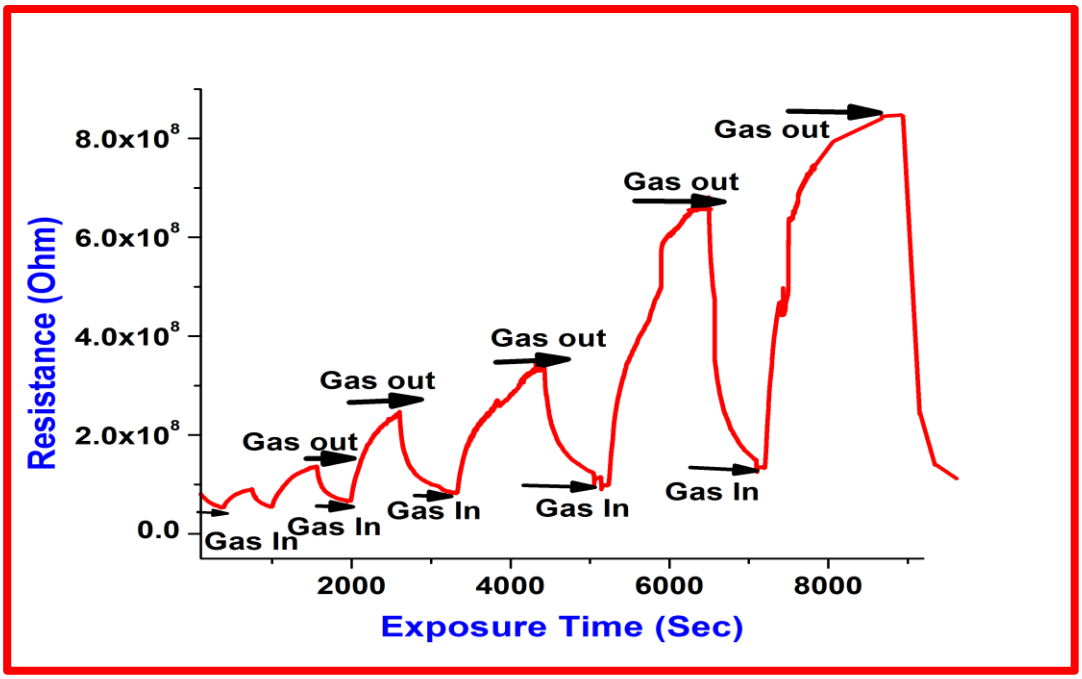

Fig. 3.10 Gas sensing behaviour of Strontium ferrite film with exposure time at different vol.% of LPG

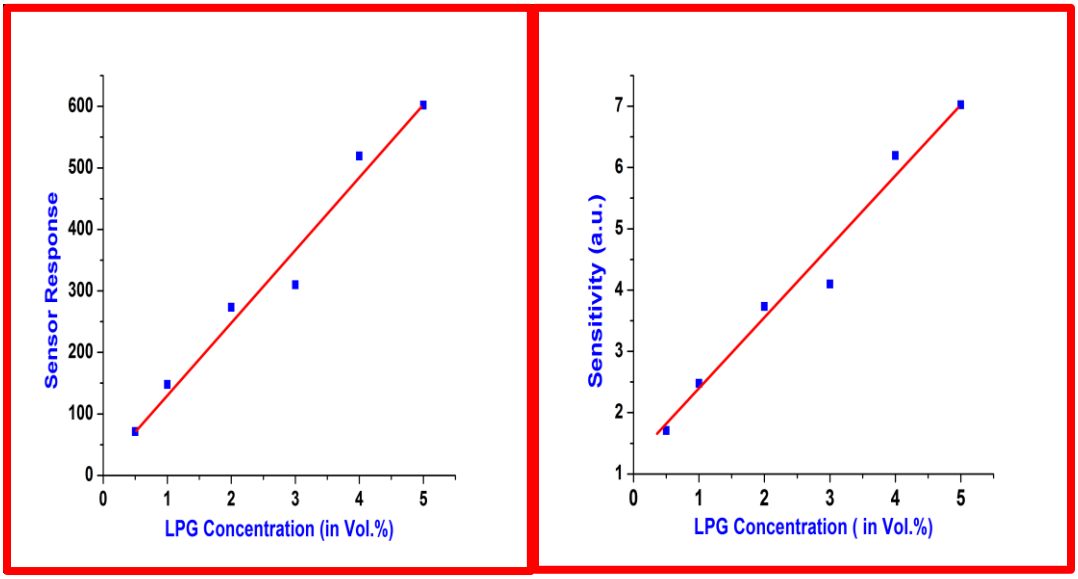

Fig. 3.11 (a) Sensor Response vs LPG concentration and (b) Sensitivity vs LPG concentration

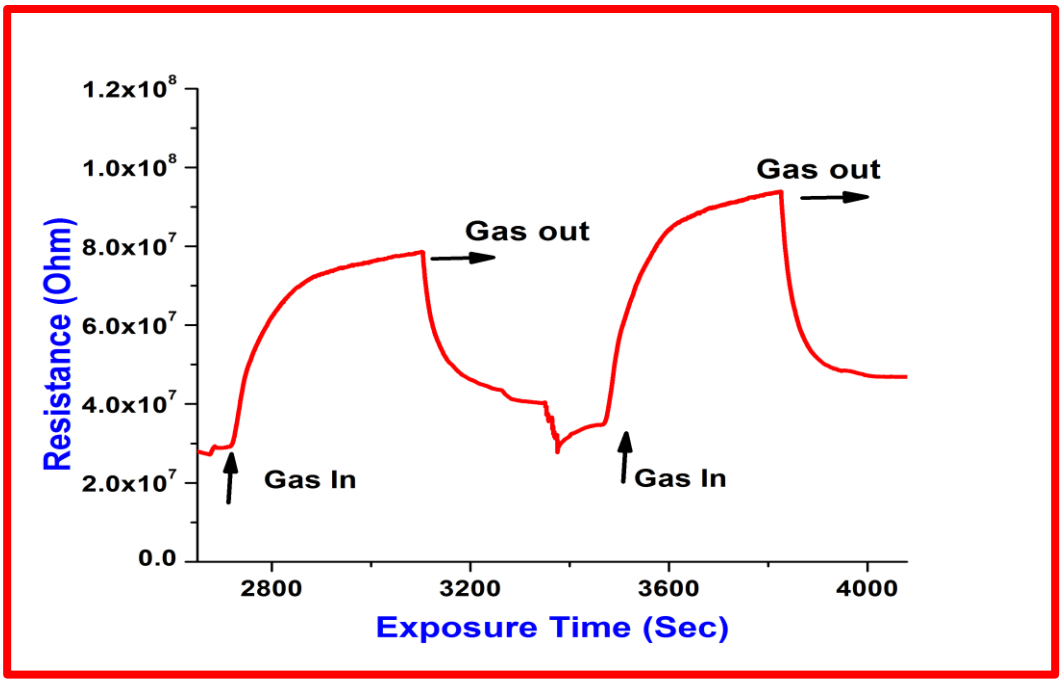

Fig. 3.12 Repeatability curve of the film after 15 days for 0.5 vol. % of LPG

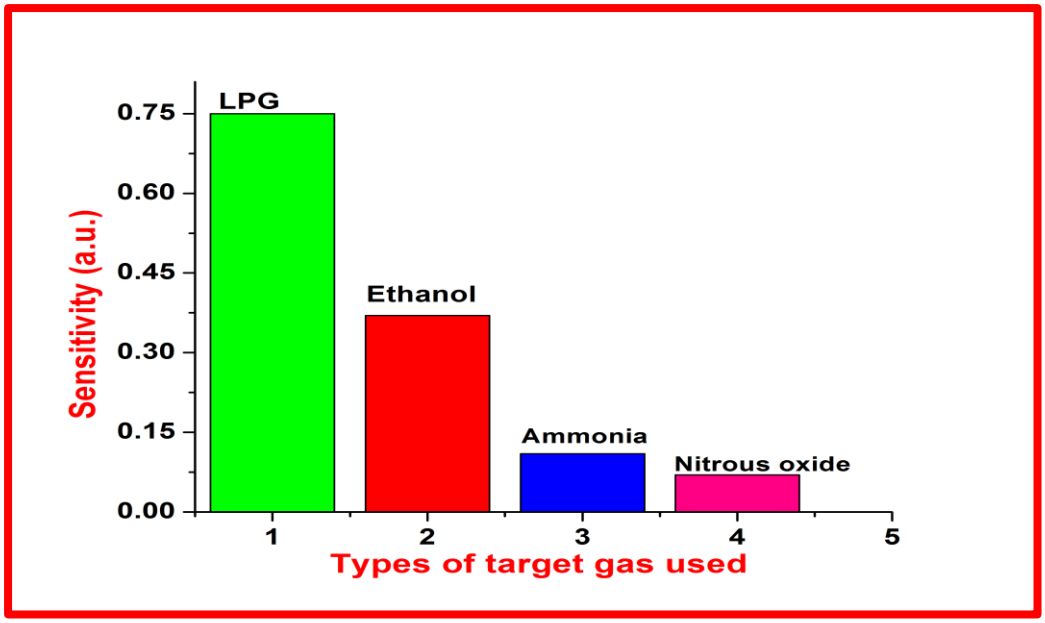

Fig. 3.12 Selectivity of Strontium ferrite film as LPG sensor

S.NO.	Type	Formula
1.	M-Type	$SrFe_{12}O_{19}$
2.	W- Type	$SrMe_2Fe_{16}O_{27}$
3.	Y- Type	$SrMe_2Fe_{12}O_{22}$
4.	X- Type	$Sr_2Me_2Fe_{28}O_{46}$
5.	Z- Type	$Sr_2Me_2Fe_{24}O_4$

Table 3.1 Classification of structure of hexaferrite

S.no.	LPG Concentration (in vol. %)	Sensitivity	% Sensor Response
1.	0.5	1.71	71.07
2.	1	2.47	147.82
3.	1.5	3.73	273.19
4.	2	4.09	309.96
5.	2.5	6.19	519.45
6.	3	7.02	602.23

Table 3.2 Variation of Sensitivity and % Sensor response with LPG concentration

Chapter 4

Study of Liquefied Petroleum Gas sensing properties of lead-free Bismuth sodium titanate prepared by sol-gel method

In the present chapter a study on bismuth sodium titanate (BNT) thin film based LPG sensor was carried out. The thin film was fabricated using sol-gel spin coating technique and was characterized by various techniques such as XRD, TGA, SEM, TEM, EDS, UV-Spectroscopy, Raman and FTIR. XRD analysis confirms the formation of BNT with minimum crystallite size of 9 nm. SEM images show the macro porous surface structure of the film. Optical characterization of the film was carried out by UV-visible spectrophotometer, Fourier transform infrared spectroscopy and Raman spectroscopy. Thermal analysis graph of BNT precursor via TGA was obtained. LPG sensing of bismuth sodium titanate was done at room temperature below LEL. Maximum sensitivity was found as 2.158 with response time of 22 s and recovery time 26 s for 0.25 vol.% of LPG.

CHAPTER 4

STUDY OF LIQUEFIED PETROLEUM GAS SENSING PROPERTIES OF LEAD-FREE BISMUTH SODIUM TITANATE PREPARED BY SOL-GEL METHOD

4.1 Introduction

During the period 1920-30 Rochelle salt lead the excavation of a new class of ferroelectric materials. Later in 1950's i.e. "Era of Proliferation" barium titanate and lead zirconate titanate (PZT) laid the foundation stone of ferroelectric perovskite materials at room temperature [1-2]. PZT was widely used in electronic industries such as touch sensor in microbiology for micromanipulation, a piezoelectric transformer, an electrostrictive material, ceramic, etc [3-4]. Lead +oxide is the major component of PZT which is hazardous to the human health [5]. So to overcome this problem scientists and researchers had been looking for any substitute of PZT [6]. Potassium sodium niobate and bismuth sodium titanate are widely used for the research work. Smolenskii et al. discovered the BNT as an important lead-free material with a perovskite structure and emphasized on the pyroelectric and piezoelectric properties of sintered ceramic of BNT [7]. It shows strong ferroelectric properties with a large remnant polarization, P_r = 38 $\mu C/cm^2$ and high Curie temperature (Tc = 320 ^oC). It has been considered as a promising candidate for lead-free piezoelectric ceramics, which is an alternative to the widely used lead-based piezoelectric materials [8]. BNT is a perovskite which is widely used in piezoelectric sensors and actuators and also they are used in active and passive electronic devices. Perovskite titanates are also useful for visible light photocatalytic activities [9-10]. Distorted perovskites are known as the member of orthoferrite family [11]. This report deals with synthesis and characterization of BNT and its application as LPG Sensor.

4.2 Literature review

Kiyoshi Kanie et al. synthesized spherical polycrystalline BNT by sol-gel method. Shape monitoring of BNT particles was performed due to the different mixing ratio of

Bi/Ti from a rod-like to tubular structure [12]. T. Yu. et al. discussed the preparation and properties of lead-free polycrystalline BNT by an improved sol-gel spin coating method on Pt/Ti/SiO_2/Si substrates. The resulting film was dense, well crystallized rhombohedral perovskite structure with 50 to 200 nm particle size and also having good dielectric and ferroelectric properties. Thus resulting as a promising candidate for piezoelectric applications [13]. Meera Rawat et al. synthesised rhombohedral Ba^{+2} doped BNT (BBNT) varying x = 0, 0.2, 0.4, 0.6, 0.8, 1 by conventional solid-state method. They have studied the microstructure, dielectric and electrical behaviour of BNT and found that Ba^{+2} compound is much smaller than undoped BNT. Further, they concluded that electrical conductivity with temperature shows the compound exhibit Arrhenius type of electrical conductivity with non Debye system concluded by its dielectric property [14]. Venkata Ramana Mudinepalli et al. prepared high temperature lead-free piezoelectric relaxor i.e. NBT by the conventional ceramic double sintered method and studied its dielectric and mechanical properties. He studied phase transformation of NBT from tetrahedral to rhombohedral and also found particle size around 100 nm [15]. A. Kundu et al. synthesized to Ba- Zr co-doped sodium bismuth titanate by wet chemical route citric gel method. Densification, the microstructural and electromechanical behaviour of sintered pellets were studied by them. Thermal analysis was done by TGA curve and overlapping of exothermic peaks was identified by DTA [16]. Conor J. Walsh et al. focused on a lead-free, high-temperature ceramic capacitor having base material as BNT prepared by a conventional ceramic method using oxides and carbonates. Dopants including barium, strontium and tin were used at a different temperature to modify the dielectric properties of the capacitor. Different compositional experiment, along with theoretical modelling has been investigated to modify BNT and to attain the goals set forth [17]. M. Raghavender et al. prepared to Sm-doped NBT ceramics with x = 0.05%, 0.1%, 0.015% by chemical route. XRD confirmed the single phase rhombohedral structure of BNT. They further studied the change in its behaviour of BNT as a percent of Sm increases and dielectric properties from temperature range 450-550 ^oC [18]. BNT can be synthesized by various methods like solid state, Penchini method, aerosol-gel, hydrothermal route method etc [19-20]. Bismuth sodium titanate ceramic requires high sintering temperature above 1200 ^oC to obtain a dense and pores free structure [21]. For gas sensing application we require porous film so

there is no need of very high temperature. In this chapter gas sensing properties of BNT has been carried out which depends upon the porosity of the film. Thus the film was annealed at 650 ^{o}C to obtain non-contaminated perovskite porous film. However, there has been no report published in the open literature on the LPG sensing of BNT prepared by a sol-gel spin coating technique.

4.3 Structure of BNT

BNT is an A-site distorted perovskite with bismuth and sodium both at A-site. BNT has two main phases transitions; one is from rhombohedral to tetragonal and other is from tetragonal to cubic [9]. The structure of BNT can be described in two ways first is barium and sodium at the corners of the cube and oxygen at face center and second structure titanate at the center of the oxygen get radon and other is 3D cubic network formed by sharing of TiO_6 octahedran with bismuth and sodium at the mid of the cube.

4.4 Experimental Details

4.4.1 Materials Required

Bismuth nitrate pent hydrate ($Bi(NO_3)_3.5H_2O$), titanium tetra-isopropoxide ($Ti\{OCH(CH_3)_2\}_4$) and sodium nitrate ($NaNO_3$) of AR grade were purchased from Sigma-Aldrich Chemical Co. 2 methoxy ethanol and acetic acid were used for the preparation of gel.

4.4.2 Preparation of Bismuth sodium titanate sol and powder

Bismuth nitrate pent hydrate ($Bi\ (NO_3)_3\ .5H_2O$), sodium nitrate ($NaNO_3$), titanium tetra-isopropoxide ($Ti\{OCH(CH_3)_2\}_4$) of AR grade were used as starting material. Bismuth nitrate pent hydrate and Titanium tetra-isopropoxide were dissolved in 20 ml of 2-methoxy ethanol. After stirring for 1 h BT solution was obtained and indexed as 1. Sodium nitrate was dissolved in 20 ml of acetic acid at 40 ^{o}C and gets stirred for 1 h to produce a transparent solution indexed as 2. Further, we mixed both the solutions 1 & 2 which gave a white clear sol of Bismuth sodium titanate. Later, this sol was kept under I.R. lamp to obtain the transparent gel of BNT. This gel was used for preparing a thin film of BNT by

spin coating technique. To obtain the powder of BNT, next part of the sol was dried under I.R. lamp. Further, this powder was annealed at 650 ^{o} C using the programmable furnace.

4.4.3 Thin film preparation of BNT

Sol-gel spin coating technique has been used to prepare the BNT thin film [22]. The glass substrate of dimension 1 × 1 cm^2 was taken and rinsed using distilled water, ethanol and acetone following the ultrasonic cleaning. A dilute solution of BNT was made by dissolving the BNT sol into acetic acid in 1:1 ratios and it was further sonicated for 2 h. The white transparent diluted solution was obtained and further, it was spun on the glass substrate using a photoresist spinner at a speed of 1000 rpm for 30 sec and dried at 60 ^{o}C for 5 min on a hot plate. Again spin coating and drying process were repeated three times for achieving the required thickness of the film. Finally, it was annealed at 650 ^{o}C for 2 h in a programmable furnace.

4.4.4 Characterization of Bismuth sodium titanate

XRD pattern of the prepared lead-free Bismuth sodium titanate (BNT) by sol-gel method was recorded by glancing angle X-ray Diffractometer (Rigaku Benchtop X-ray Diffraction, 5th generation Miniflex) with Ni-filtered CuK_{α} (λ=1.541Å) to study the phase formation of BNT. Thermal analysis of the dried BNT precursor via thermogravimetric analyzer was done in presence of air at the rate of 10 ^{o}C/min. Surface morphological study along with the elemental study of BNT thin film was carried out by SEM JEOL EV040 operated at 20 k and Microstructure analysis was carried by TEM model FEI Technai G2 Spirit TWIN, Netherlands. Optical characterization of the sample was done by using UV-visible spectrophotometer (Evolution 201) within a wavelength range from 200 nm to 1100 nm. FTIR and Raman identified the chemical modification of BNT. Raman spectrum of Bismuth sodium titanate was analyzed by En Spectr R532.

4.5. Result and Discussion

4.5.1 X-ray Diffraction analysis

BNT exists in rhombohedral, tetragonal, cubic and hexagonal phases depending upon the heat treatment. In the temperature range -260 °C to 255 °C exists in rhombohedral (R3c) phase and from 255 °C to 400 °C it is in the coexisting phase of rhombohedral /tetragonal. Further, from temperature 400 °C to 500 °C, it exists in tetragonal phase (P4bm) and from 500 °C to 540 °C intermediate phase of tetragonal/cubic and above 540 °C cubic prototype (Pm3m) phase exists. The phase identification of the BNT film and minimum crystallite size can be found through XRD [23-24]. Peak analysis of XRD pattern corresponding to BiO_3, TiO_3 and Bi_2O_3 matched with JCPDS card no. #36034 with lattice constant a = b = 5.476 Å, c = 6.778 Å. The characteristic peak at 2θ = 33.02 (110) confirms that the formation of cubic phase of the film. The peak at 2θ = 23.27 (100), 33.02 (110), 40.12 (111), 47.19 (200), 58.59 (211), 68.62 (220), and 78.07 (310) matched with the above reference data. The minimum crystallite size for BNT thin film was calculated as 9 nm using Debye Scherer's equation. Crystallite size corresponding to each peak was calculated and the average crystallite size was found as 15 nm.

4.5.2 Thermal Analysis

To study the decomposition process of dried BNT powder it was thermally analyzed by TGA. Only 2% loss was observed in TGA thermograph with temperature variation from 0 ° C to 900 °C. As shown in the figure a linear curve was obtained after 400 °C and there was a minor change in weight after 600 °C in thermography. This indicates that the powder was crystalline and of perovskite structure at 600 °C. The minor change observed in weight was due to the evaporation of the solvent content of the BNT powder.

4.5.3 SEM analysis and EDX

Morphology of the film plays an important role in gas sensing and it varies according to the sample preparation technique, doping at the interstitial site, catalyst, sintering temperature, pore size, etc [25]. The thin film of BNT prepared as discussed in section 4.2.2 was put in a desiccator to remove the moisture and further the film was coated

with palladium to make the surface conductive. The SEM micrographs clearly show the macroporous nature of the film. The film was porous with rectangular grains of different size which are non-uniformly distributed leaving vacant spaces among them. It is observed that the grain sizes range from small to large with a random distribution. Both the SEM images show that the particles are agglomerated with bimolecular grain growth i.e. grains are in hierarchical plate-like structure due to agglomeration and some are cubic in nature as shown in Fig 4.5. Fig 4.5(a) & (b) show the micrograph of BNT at scales: 5 μm and 1 μm with magnifications K5,000 and K10,000 respectively. Fig 4.5(c) shows the porous nature of the film at 1 μm scale. The porosity of the film lies in the range of 100 nm to 500 nm and average porosity of the film calculated from Fig 4.5(c) is 350 nm. Fig 4.5 (d) exhibits the micrograph at 500 nm scale and reveals the particle size range from 200 nm-400 nm.

The EDX spectrum of BNT thin film revealed that the theoretical amount of the elements calculated were nearly the same of the experimental amount of each element present in the thin film. Percentage of contents present in BNT is Bi 51.86% , Na 3.58%, Ti 26.93% and O 17.63%. It also shows that no foreign element was present in our sample.

4.5.4 TEM analysis and HRTEM with SAED pattern

Fig 4.6(a) and (b) shows the TEM image of BNT, loaded on the carbon coated copper grid at different scales. The image at 1μm scale and 200 nm reveal the cubic crystalline structure in agglomerated form. Fig 4.6(b) shows the plate-like structure with grain size 100 nm to 250 nm. Fig 4.6(c) shows the selected area electron diffraction pattern (SAED) of BNT and Fig.4.6 (d) exhibits the HRTEM of BNT. Bright spots with concentric rings reveal the regular periodic arrangement of atoms confirming the crystallinity of the nanocrystalline material. Also, it exhibits polycrystalline nature of the material. First ring (hkl) corresponds to (111). It is the most intensified ring. The second ring corresponds to (211), third correspond to (200) and fourth to (110). We have calculated the fringe spacing from HRTEM image along (111) and found as $d_{(hkl)}$ = 2..3666 Å.

4.5.5 Optical characterization

4.5.5.1 UV-visible Absorption Spectroscopy

The optical absorbance spectra of BNT film deposited separately on a glass substrate (200-1100 nm). The graph represents the variation of optical absorbance for the thin film with the variation in wavelength. The optical band gap of BNT can be calculated from the intercept of energy axis obtained by extrapolating the plot on energy axis [hυ versus insitu plot of $(\alpha h\upsilon)^2$] as shown in Fig 4.7. The bandgap of the film was found as 5.4 eV.

4.5.5.2. FTIR Analysis

The FTIR spectra of the BNT in transmittance mode are shown in Fig 4.8. At lower frequency ranging from 400-430 $cm^{-1,}$ a minute depth was observed which is due to Ti-O bending vibration of the compound. The asymmetry band around 629 cm^{-1} attributed to υ (Ti-O) stretching vibration mode representing the characteristic peaks of perovskite phase with the formation of TiO_6 [26]. Peak around 1164 cm^{-1} is attributed to υ (Ti-O-C) vibration mode. Peaks around 1420 cm^{-1}, 1559 cm^{-1} and 1734 cm^{-1} are attributed to υ (COO) vibration mode.

4.5.5.3 Raman Analysis

Raman spectroscopy provides information about the molecular vibration that can be used for sample identification and quantization. Raman spectrum of BNT was analyzed by EnSpectr R532 with a laser power of 30 mW and wavelength of 532 nm at room temperature. Absorption band of BNT appears at 275 cm^{-1}, 526 cm^{-1}, 583 cm^{-1} and 800 cm^{-1}. In the case of heat treatment below 500 ^oC, the material was polycrystalline in nature and distorted due to occupancy by Na/Bi cations at A-site. In this condition, the modes are found broad and there is no Raman active mode i.e. no Raman band is obtained. The broad and intense band at 275 cm^{-1} is associated with the vibration of the TiO_6 group [27]. Higher frequency bands at 532 cm^{-1} and 801 cm^{-1} bands are dominated by vibrations due to the displacement of oxygen.

4.5.6 LPG Sensing of BNT Film

LPG sensing is based on the surface morphology of the sample and nature of gas exposed to it [28-29]. The variations in electrical and other properties of the material with the exposure of gas are the basis of working of LPG sensor. The interaction of the gas with the material leads to transfer of electrons between the sample and the reducing gas. BNT film prepared was very porous with vacant spaces i.e. active sites which were measured by JSR porosity tester and the porosity was found as 205 cc/m . When the surface of the film comes into contact with the air, the atmospheric oxygen molecules get adsorbed on the surface of BNT film. During interaction of film with air, charge transfer from conduction band electrons from oxygen species by attaching themselves to the adsorbed oxygen molecules and thus a charge layer is formed and the resistance of the film becomes stable [30]. Thus we get the value of resistance of the film in the air (R_a). When LPG was exposed inside the chamber through inlet a complex reaction occurs and the hydrocarbons of LPG reacts with the adsorbed oxygen species [31]. Due to which there is a sudden rise in the resistance of the film. As the rate of the reaction increases the removal of electrons takes place which leads to the formation of a potential barrier that is further responsible for the constant resistance of the film. After a short interval of time the resistance of the film again becomes constantly resulting in the saturation, stabilized resistance was recorded as R_g. Now when the outlet knob was opened to remove the LPG from the chamber, there was a sudden fall in the resistance of the film and after some time it again recovered to its initial resistance.

To study the gas sensing properties of BNT the LPG concentration (in vol.%) was varied and obtained the different sensing curves correspondingly as shown in Fig. 4.10. Thus we studied its sensing behaviour by calculating its sensing parameters i.e. sensitivity, response time, recovery time and % sensor response. Sensitivity is defined as the ratio of Resistance of the film in LPG to the resistance of the film in the air [32]. Fig. 4.12 shows the variations in resistance of sensor with a different exposure time of LPG. The sensitivity of LPG sensor exhibited through bar diagram by Fig 4.11. Fig 4.12 represents the variation of % sensor response (SR) with LPG concentration from 0.25 to 3 vol. %. The value of maximum sensitivity was found 2.158 and percentage sensor response was found as 115.84

% for 3 vol.% LPG. The response time of the sensor is defined as the time in which sensor reaches 90% of the maximum resistance of the film in presence of target gas (R_g) [33-34]. The minimum response time of BNT was found as 22 sec for 0.25 vol.% of LPG. The recovery time of the sensor is the time interval during which the sensor again recovers to its initial stage [35]. The minimum recovery time was found as 26 sec for 0.25 vol.% of LPG.

The reproducibility response curve of BNT when continuously exposed to 1.5 vol.% of LPG was continuously exposed to the sensor for three consecutive cycles at room temperature is shown in Fig. 4.13(a). These sensing response curves show almost similar sensing response R_a to R_g and again from R_g to R_a repeated for three consecutive cycles which show the good reproducibility nature of the BNT film. Fig. 4.13(b) shows the ageing effect of the sensor was examined after two weeks of the previous experiment after the drying of the film under I.R. lamp for 1 vol.% of LPG. Sensing characteristic of the film was similar to the previously observed characteristic.

4.6 Conclusion

BNT powder was successfully synthesized by sol-gel method and a thin film on the glass substrate was prepared by spin coating method. XRD, FTIR and Raman confirm the formation of BNT and minimum crystallite size was calculated as 9 nm. Thermal analysis was done through TGA. The microstructural analysis was done by TEM, SEM and EDX. Optical Characterization was done and band gap was found 5.4 eV. FTIR reveals the information about the bond stretching between the molecules through transmittance spectra. Study of liquefied petroleum gas sensing properties of BNT was carried out. The value of maximum sensitivity was found 2.158 and percentage sensor response was found 115.84 % for 3 vol.% LPG. Minimum response time was found as 22 sec for 0.25 vol.% of LPG which is quite appropriate for developing a commercial LPG sensor operable at room temperature.

REFRENCES

1. L.E. Cross and R.E. Newnham, History of Ferroelectrics, High- Technology Ceramic- Past Present and Future: The Ceramics and Civilization, 3 (1987) 289-305.
2. M. Singh, B.C. Yadav, A. Ranjan, M. Kaur, S.K. Gupta, Synthesis and characterization of perovskite barium titanate thin film and its application as LPG Sens. Actuators B: Chem., 241 (2017) 1170-1178.
3. D. Alonso-Sanjose, R. Jimenez, I. Bretos, M.L. Calzada, Lead-Free Ferroelectric (Na1/2Bi1/2)TiO_3–$BaTiO_3$ Thin Films in the Morphotropic Phase Boundary Composition: Solution Processing and Properties, Jour. Am. Ceram. Soc., 92(10) (2009) 2218–2225.
4. L. Wang, W. Wang, Photocatalytic hydrogen production from aqueous solutions over novel $Bi_{0.5}$ $Na_{0.5}$ TiO_3 microspheres, International Journal of Hydrogen Energy 37 (2012) 3041-3047.
5. N. Setter, D. Damjanovic, L. Eng, G. Fox, S. Gevorgian, S. Hong, A. Kingon, H. Kohlstedt, N.Y. Park, G. B. Stephenson, I. Stolitchnov, A.K. Taganstev, D.V. Taylor, T. Yamada, S. Streiffer, Ferroelectric thin films: Review of materials, properties, and applications, Journal of Applied Physics 100 (2006) 051606.
6. S. Uddin, Y. Iqbal, A. Ullah, Phase, microstructure and dielectric properties of 0.94$Bi_{0.5}Na_{0.5}$ TiO_3–0.06BatiO_3 ceramics prepared by sol-gel technique, Materials Science-Poland, 31(3) (2013) 410-414.
7. G.A. Smolenskii, V.A. Isupov, N.N. Krainik, New ferroelectrics of complex composition. Sov Physics Solid State, 2 (11) (1961) 2651-2654.
8. A. Ullah, C.W. Ahn , K.B. Jang, A. Hussain, I.W. Kim, Phase Transition and Electrical Propertiesof BiAlO3-Modified (Bi0.5Na0.5)TiO3Piezoelectric Ceramics, Ferroelectrics 404 (2010) 167–172.
9. P. Kanhere, Z. Chen, A Review on Visible Light Active Perovskite-Based Photocatalysts, Molecules 19 (2014) 19995-20022.
10. R.L. White, Review of recent work on the magnetic and spectroscopic properties of the rare-earth orthoferrites, Journal of Applied Physics 40 (3) (1969) .

11. C.Y. Kim, The Synthesis of Lead-Free Ferroelectric $Bi_{1/2}Na_{1/2}TiO_3$ Thin Film by Solution-Sol–Gel Method, J. of Sol-Gel Science and Technology 33 (2005) 307–314.

12. K. Kanie1, H. Sakai, J. Tani, H. Takahashi, A, Muramatsu, Synthesis of Bismuth Sodium Titanate Fine particles with different shapes by the Gel-sol method, Materials Transactions, 48 (8) (2007) 2174- 2178.

13. T. Yu, K.W. Kwok, H.L.W. Chan, Preparation, and properties of sol–gel-derived $Bi_{0.5}Na_{0.5}TiO_3$ lead-free ferroelectric thin film, Thin Solid Films, 515 (2007) 3563–3566.

14. M. Rawat, K.L. Yadav, A. Kumar, P.K. Patel, N. Adhlakha, J. Rani, Structural, dielectric and conductivity properties of Ba^{2+} doped $(Bi_{0.5}Na_{0.5})TiO_3$ ceramic. Adv. Mat. Lett., 3 (4) (2012) 286-292.

15. V.R. Mudinepalli, N. Ramamanohar Reddy, W.C. Lin, K.V.S. Kumar, B.S. Murty, Phase transitions of the ferroelectrics $(Bi_{0.5}Na_{0.5})TiO_3$ by dielectric and internal friction measurement. Adv. Mater. Lett., 6 (1) (2015) 27-32.

16. A. Kundu, A.N. Soukhojak, Ba-Zr codoped sodium bismuth titanate by novel alkoxyless wet chemical route: processing and electromechanical behavior, Appl. Phys. A 82 (2006) 309–315.

17. C.J. Walsh, W.A Schulze, New York IEEE International Ultrasonics, Ferroelectrics and Frequency Control Joint 50th Anniversary Conf. (2004) 328-331.

18. M. Raghavendra, G.S. Kumar, G. Prasad, Modification of dielectric relaxations in sodium bismuth titanate with samarium doping, Journal of Physics and Chemistry of Solids 67 (2006) 1803–1808.

19. S. Kanagesan, C. Kumar, R. Velmurugan, S. Jesurani, sol-gel combustion synthesis of $Bi_{0.5}Na_{0.5}TiO_3{-}Zro_2$ ceramic composite Synthesis of Bismuth Sodium Titanate Fine Particles with Different Shapes by the Gel-Sol Method, Materials Science-Poland, 28(3) (2010) 1-7.

20. C.Y. Kim, T.Sekino, K. Niihara, Synthesis of bismuth sodium titanate nanosized powders by solution/ sol-gel process Journal of American Ceramic Society, 86(9) (2003) 1464-67.

21. D. Hu, X. Kong, K. Mori,Y. Tanaka, K. Shinagawa, Q. Feng, Ferroelectric Mesocrystals of Bismuth Sodium Titanate: Formation Mechanism, Nanostructure, and Application to Piezoelectric Materials, Inorg. Chem., 52 (2013) 10542−10551.

22. S. Singh, B.C. Yadav, M. Singh, R. Kothari, A review report on Nanostructured ferrites as Liquified petroleum gas sensor, International Journal of Science, Technology and Society, 1(1) (2015) 5-22.

23. W.L. Zhong, Y.G. Wang, P.L. Zhang, B.D. Qu, Phenomenological study of the size effect on the phase transitions in ferroelectric particles, Phys. Rev. B, 50 (1994) 698-703.

24. G.O. Jones, P.A. Thomas, Investigation of the structure and phase transitions in the novel A-site substituted distorted perovskite compound $Na_{0.5}Bi_{0.5}TiO_3$. Acta Crystallography. B-Struct. Sci., 58 (2002) 168-178.

25. G. Arlt, The influence of microstructure on the properties of ferroelectric ceramics, Feroelectrics, 104 (1990) 217-227.

26. S. Supriya, S. Kalainathan, S. Swaroop, Synthesis and Characterization of CeO_2 doped Bismuth sodium potassium titanate Ceramics International Journal of Chem. Tech Research, 3(1) (2011) 488-494.

27. J. Kreisel, A. M. Glazer, P. Bouvier, G. Lucazeau, High-pressure Raman study of a relaxor ferroelectric: The $Na_{0.5}Bi_{0.5}TiO_3$ perovskite, Physical Review B, 63 174106 1-10.

28. B.C. Yadav, S. Singh, A. Yadav, Nanonails structured ferric oxide thick film as room temperature liquefied petroleum gas LPG sensor, Applied Surface Science, 257 (2011) 1960-1966.

29. C.E. Simion, A. Sackmann, V.S. Teodorescy, C.F. Rasti, A. Stanoiu, Room temperature ammonia sensing with barium strontium titanate under humid air background, Sens. Actuator B: Chem. 220 (2015) 1241-1246.

30. S. Singh, B.C. Yadav, R. Prakash, B. Bajaj, J. Rock lee; Synthesis of nanorods and mixed shaped copper ferrite and their applications as liquefied petroleum gas sensor; Applied Surface Science, 257 (2011) 10763-10770.

31. A. Singh, A. Singh, S. Singh, P. Tandon, B.C. Yadav, R.R. Yadav; Synthesis, characterization and performances of zinc ferrite nanorods for room temperature sensing applications; Journal of alloy and compounds 618 (2015) 475-483.

32. M.R.A. Bhuiyan, M.M. Alam, M.A. Momin, M.J. Uddin, M. Islam, Synthesis and Characterization of Barium titanate ($BaTiO_3$) Nanoparticle, International Journal of Material and Mechanical Engineering, 1 (2012) 21-24.

33. R.K Sonker, M. Singh, U. Kumar, B.C. Yadav, MWCNT Doped ZnO Nanocomposite Thin Film as LPG Sensing Journal of Inorg Organomet Polym, 26(6) (2016) 1434–1440.

34. R. Srivastava, B.C. Yadav, M. Singh, T.P. Yadav, Synthesis, Characterization of Nickel Ferrite and Its Uses as Humidity and LPG Sensors, J. Inorg Organomet Polym, 26 (2016) 1404-1412.

35. M. Singh, B.C. Yadav, A. Ranjan, R.K. Sonker, M. Kaur, Detection of liquefied petroleum gas below lowest explosive limit (LEL) using nanostructured hexagonal strontium ferrite thin film, Sens. Actuators B: Chem., 249 (2017) 96-104.

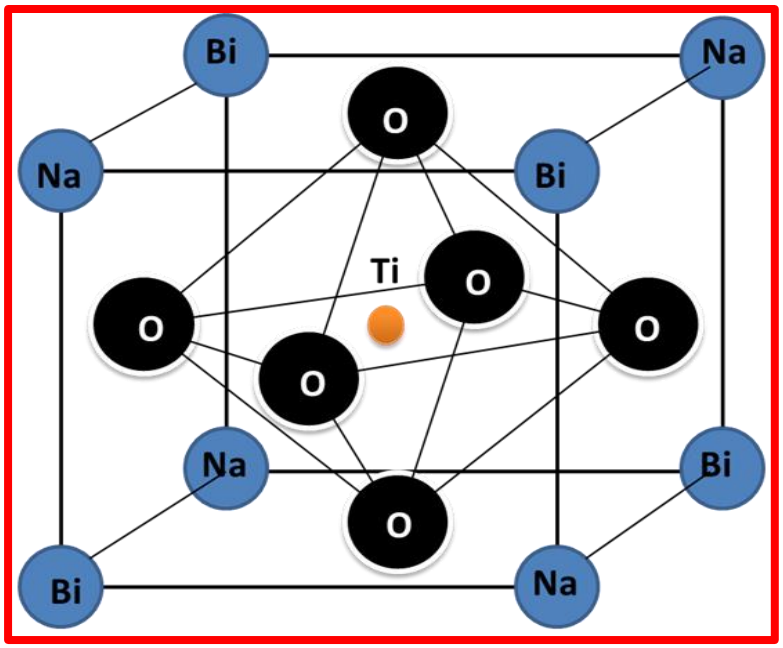

Fig. 4.1 Structure of bismuth sodium titanate

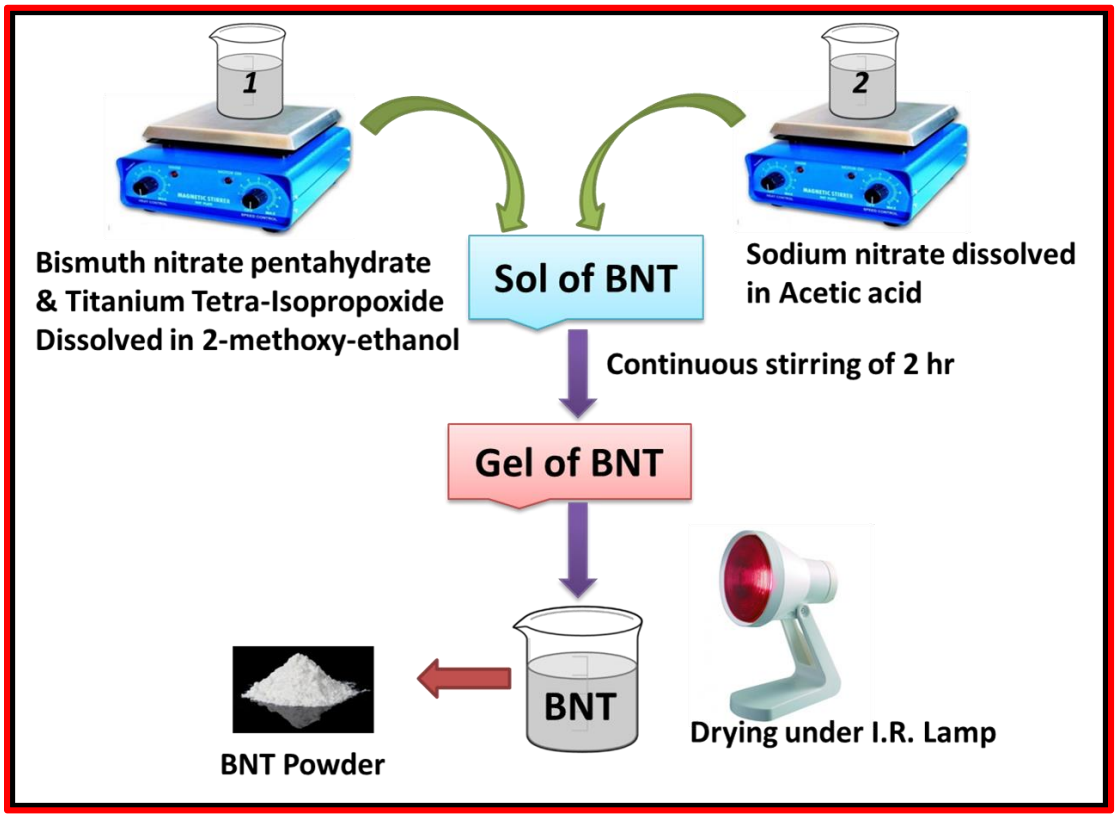

Fig. 4.2 Schematic representation of preparation of BNT by sol-gel method

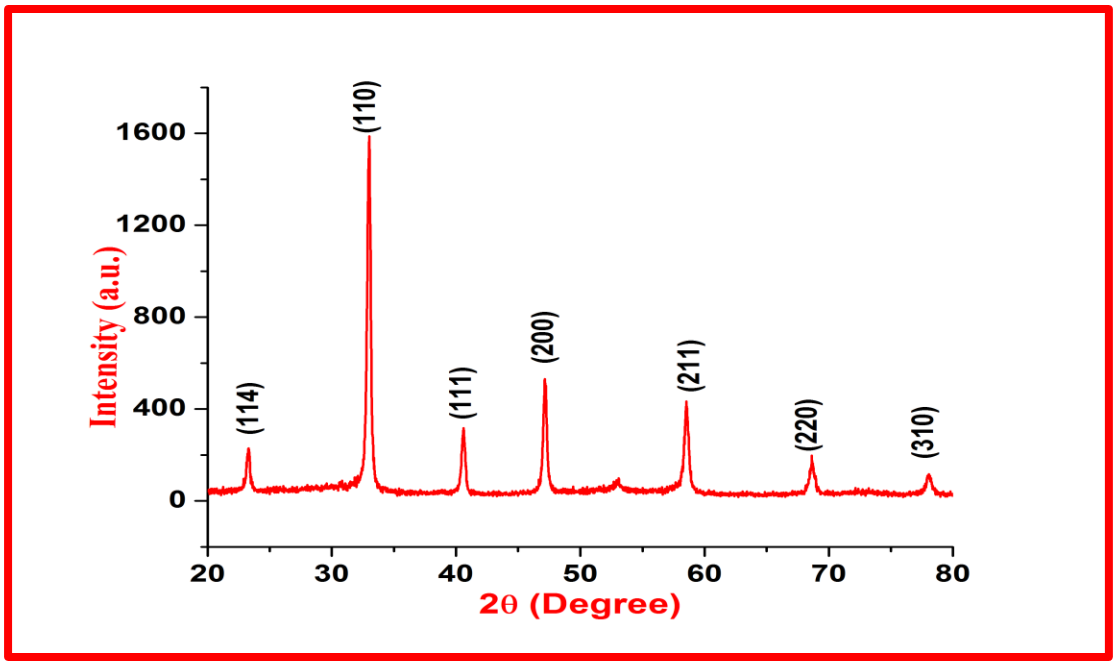

Fig. 4.3 XRD pattern of thin film of BNT

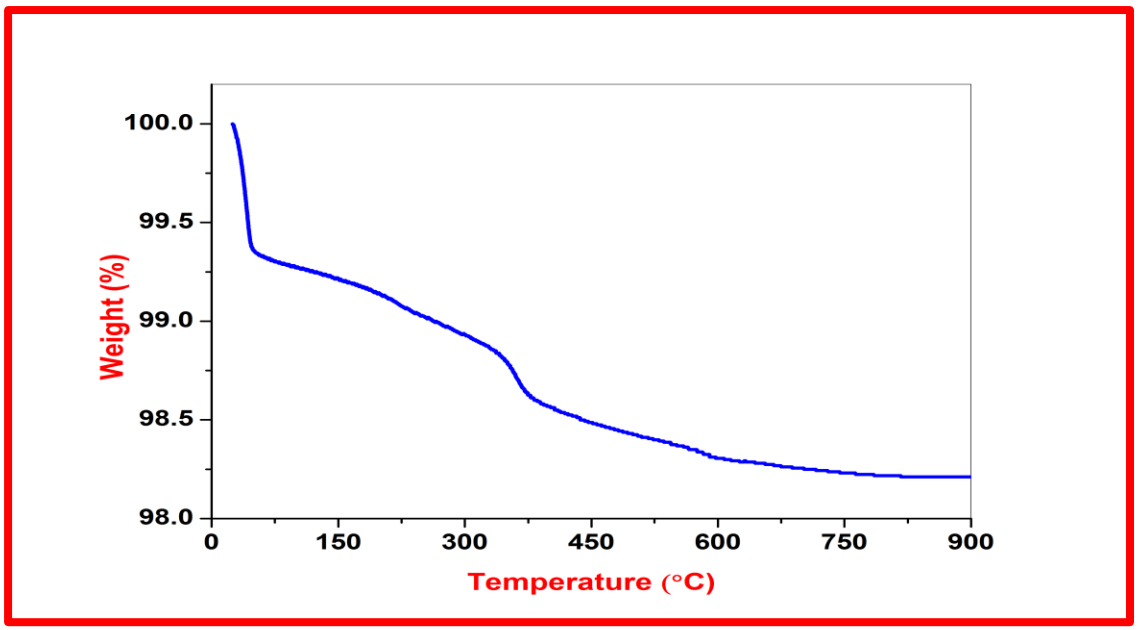

Fig. 4.4 TGA of BNT powder

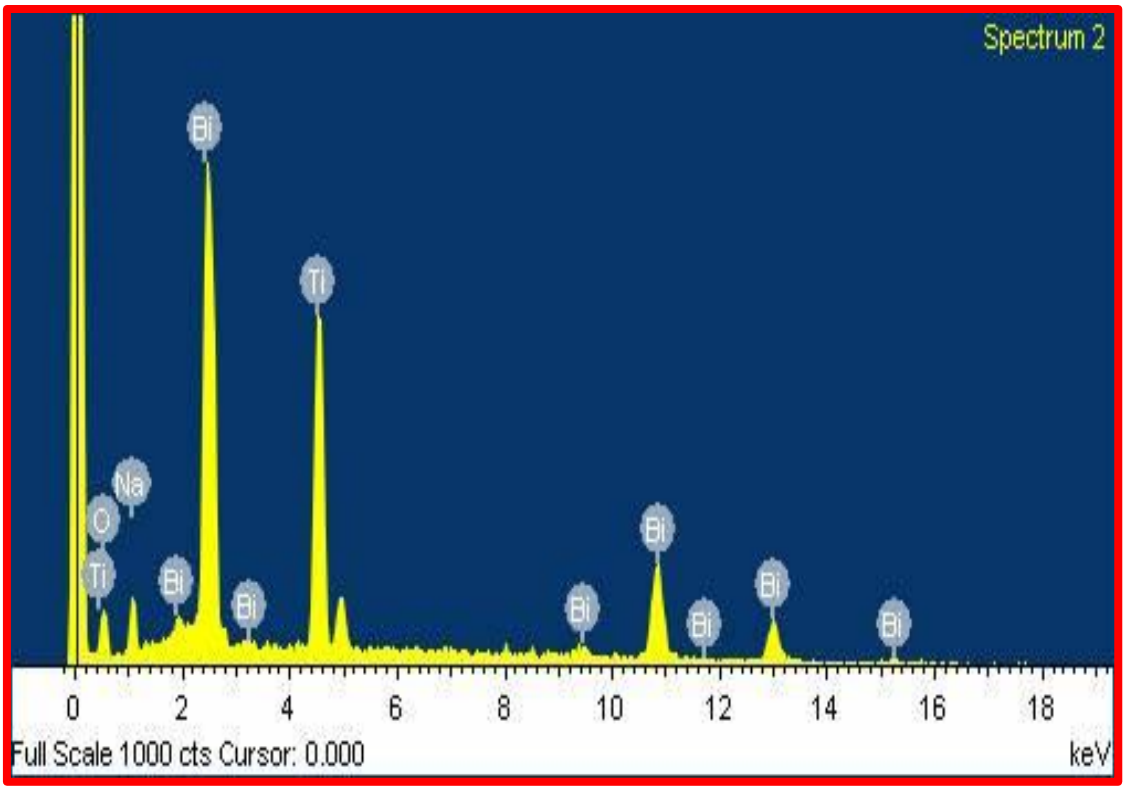

Fig. 4.5(e). EDAX of BNT

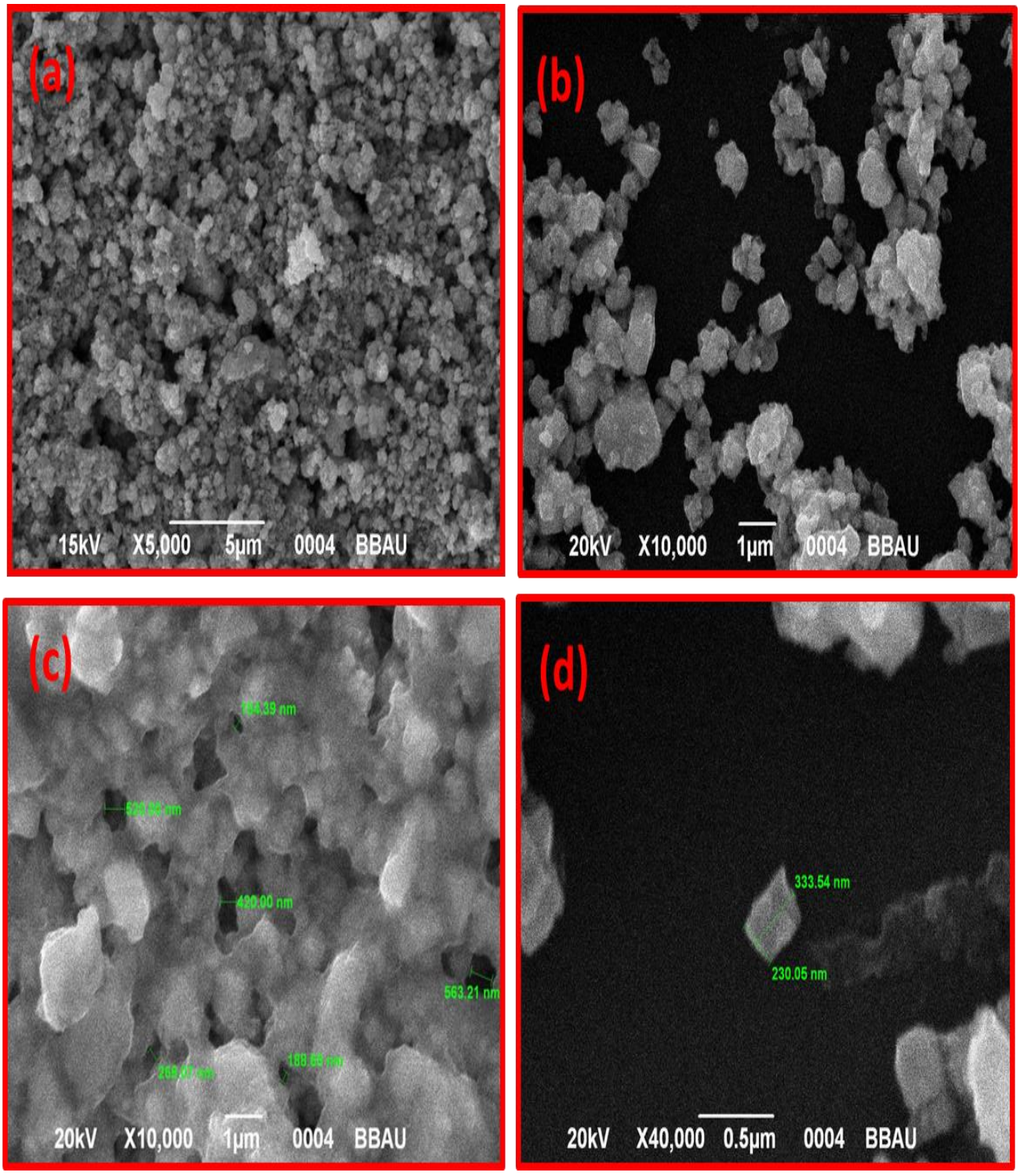

Fig. 4.5 (a), (b), (c) & (d) SEM image of macroporous BNT film at 1μm and 500 nm

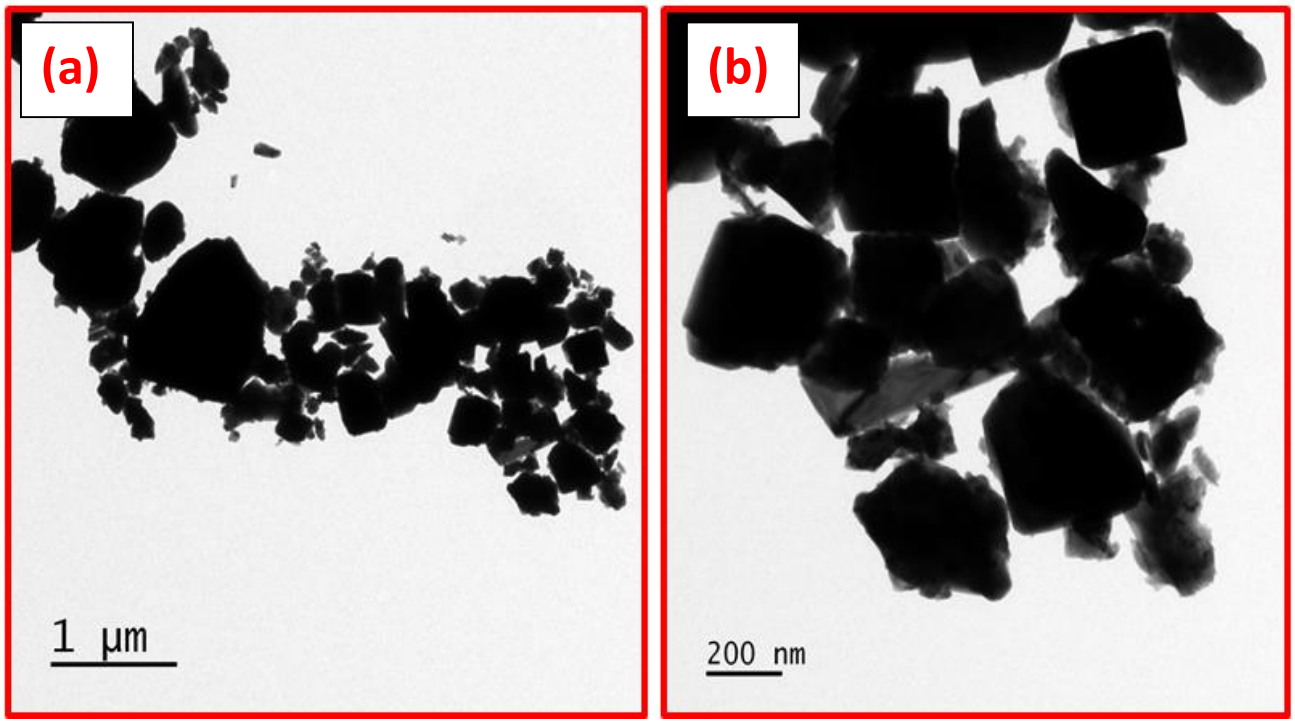

Fig. 4.6 TEM micrograph of BNT at different scales.

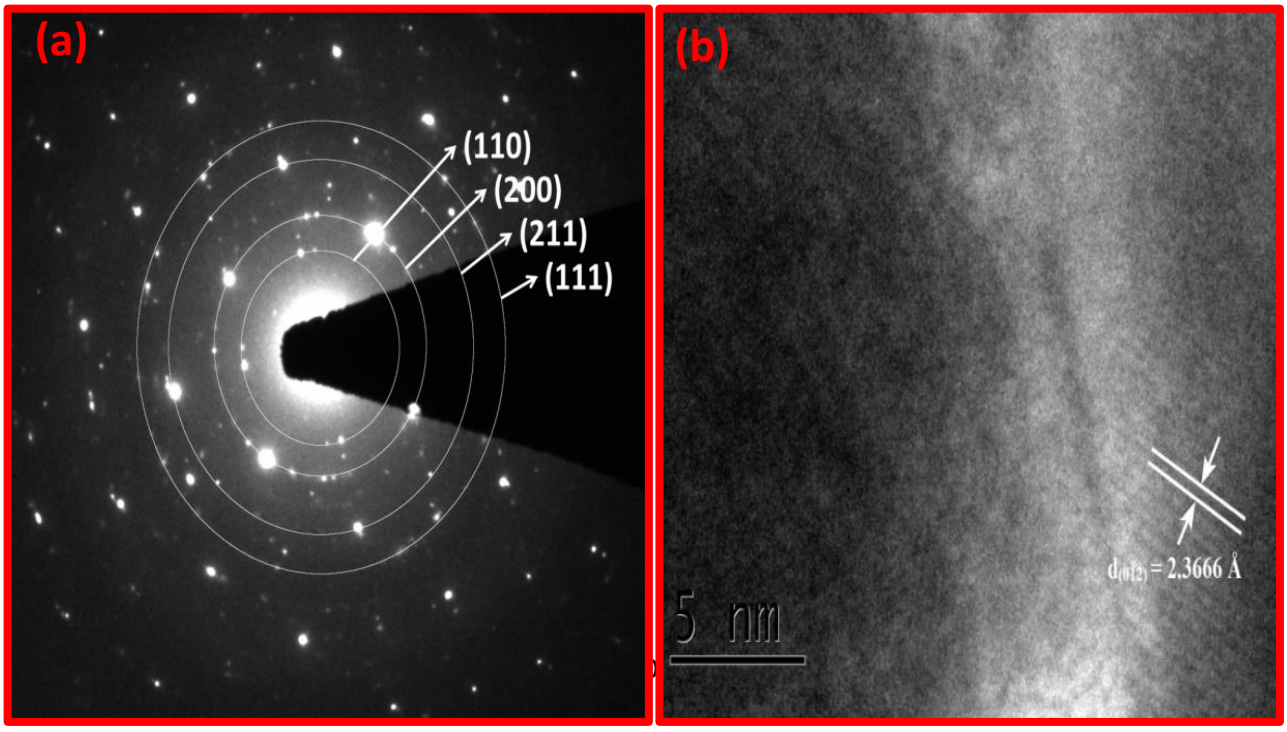

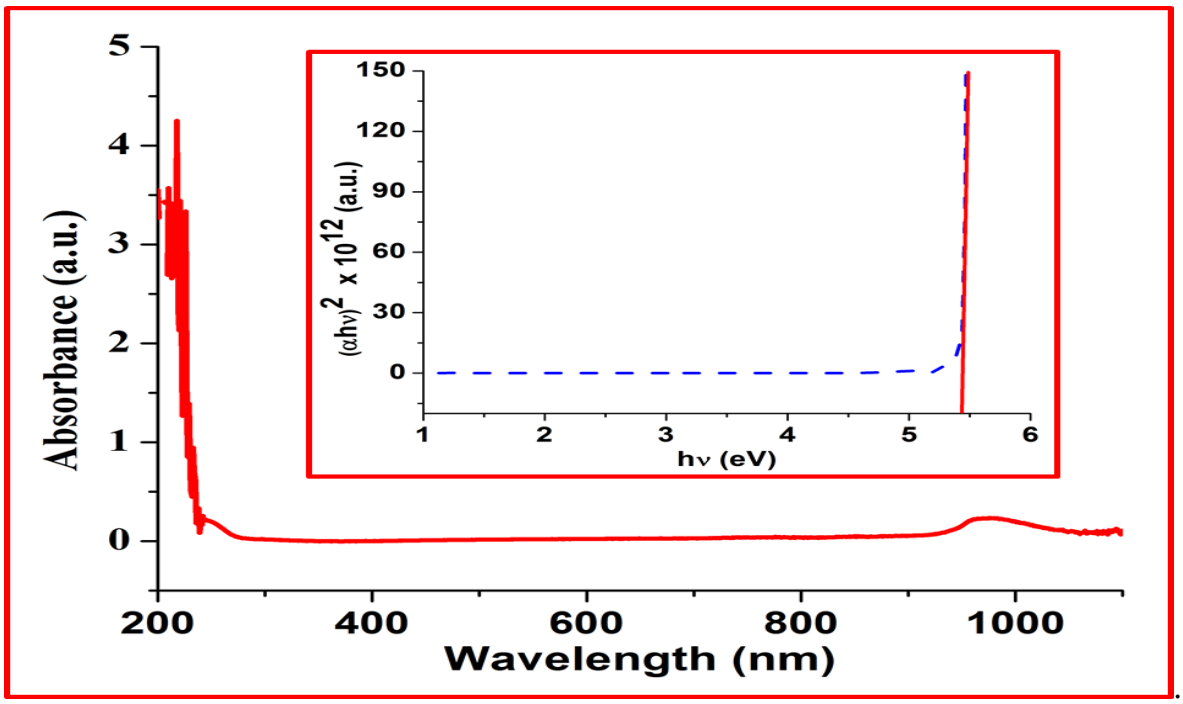

Fig. 4.7 Variation of UV-vis absorbance with the wavelength and in-situ figure shows Tauc plot

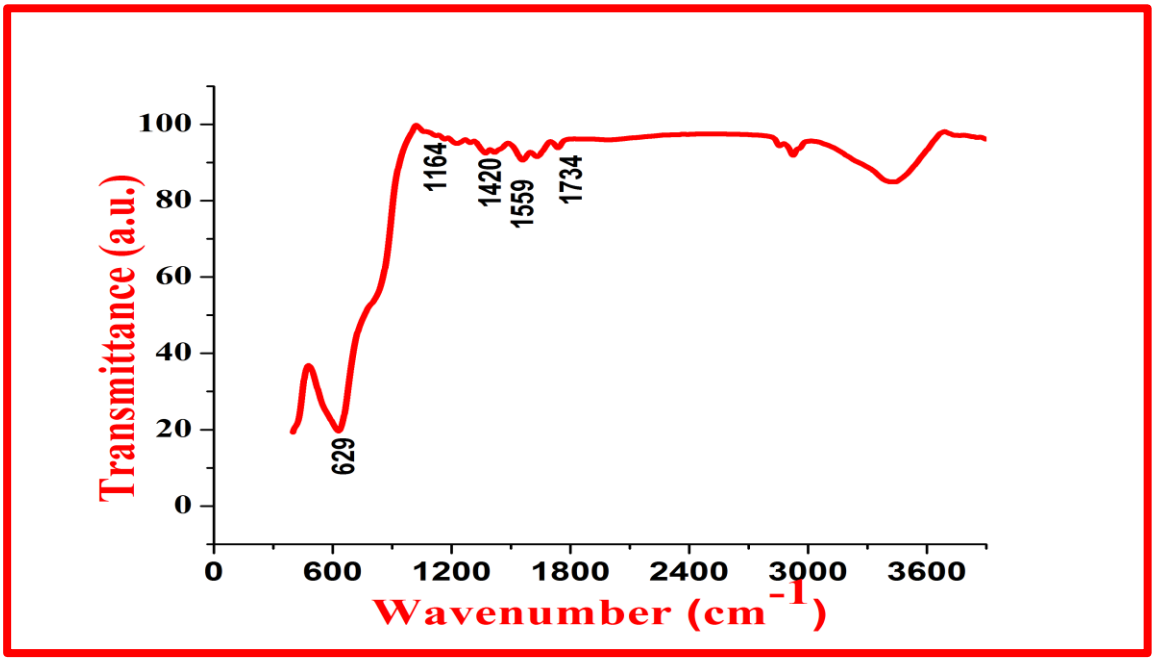

Fig. 4.8 FTIR spectrum of BNT

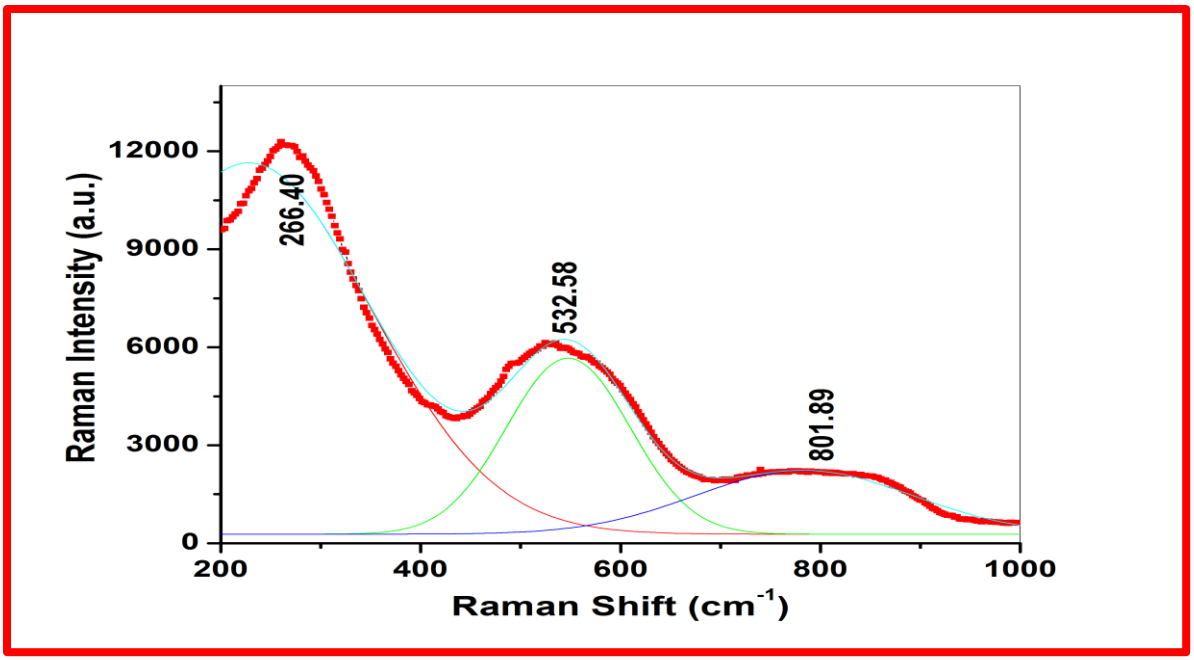

Fig. 4.9 Raman Spectrum of BNT

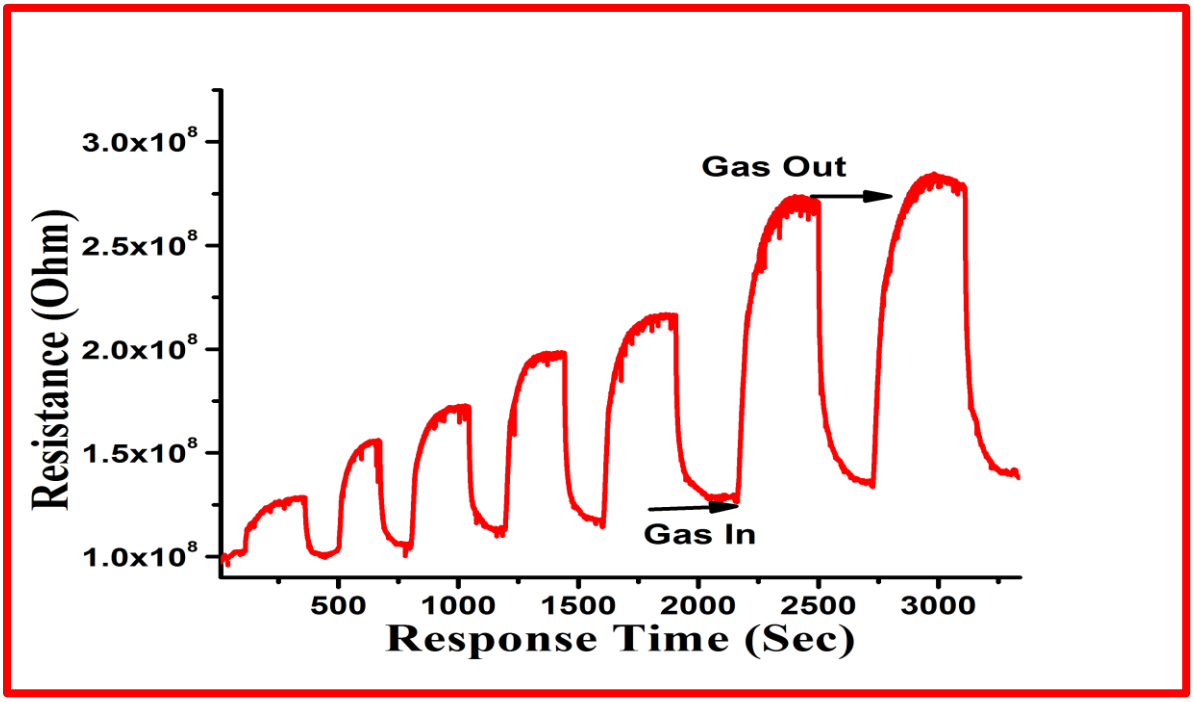

Fig. 4.10 Sensing response curve of BNT

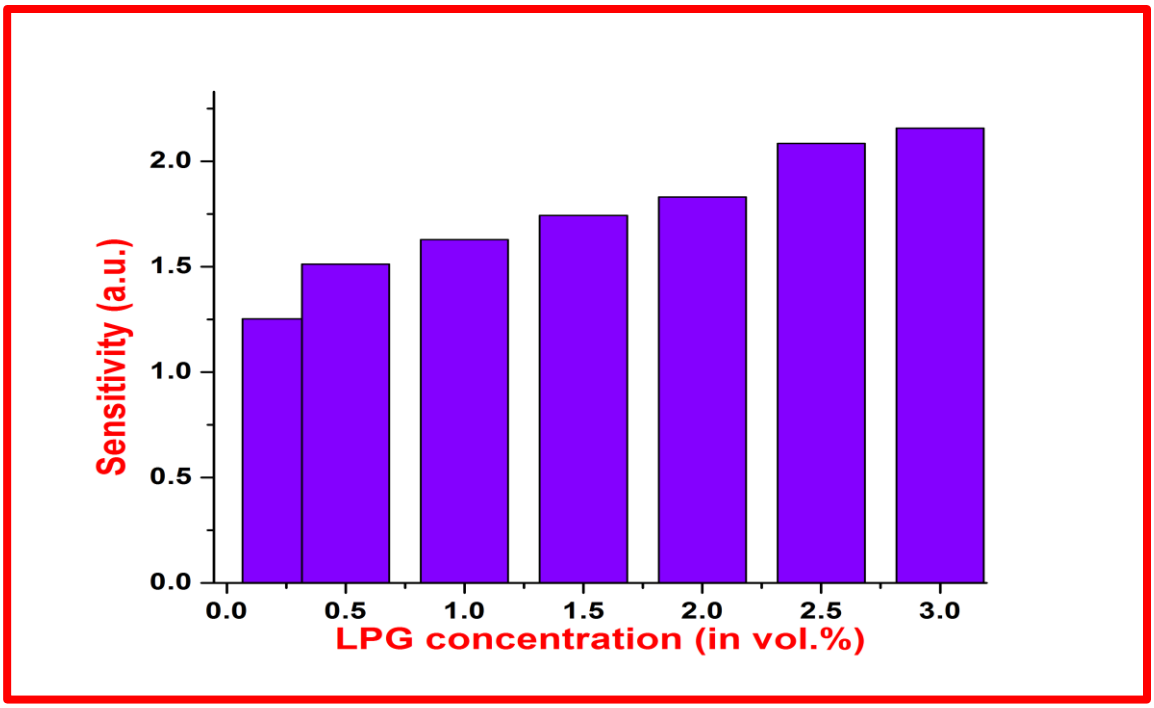

Fig. 4.11 Variation of sensitivity at different LPG conc. (vol.%)

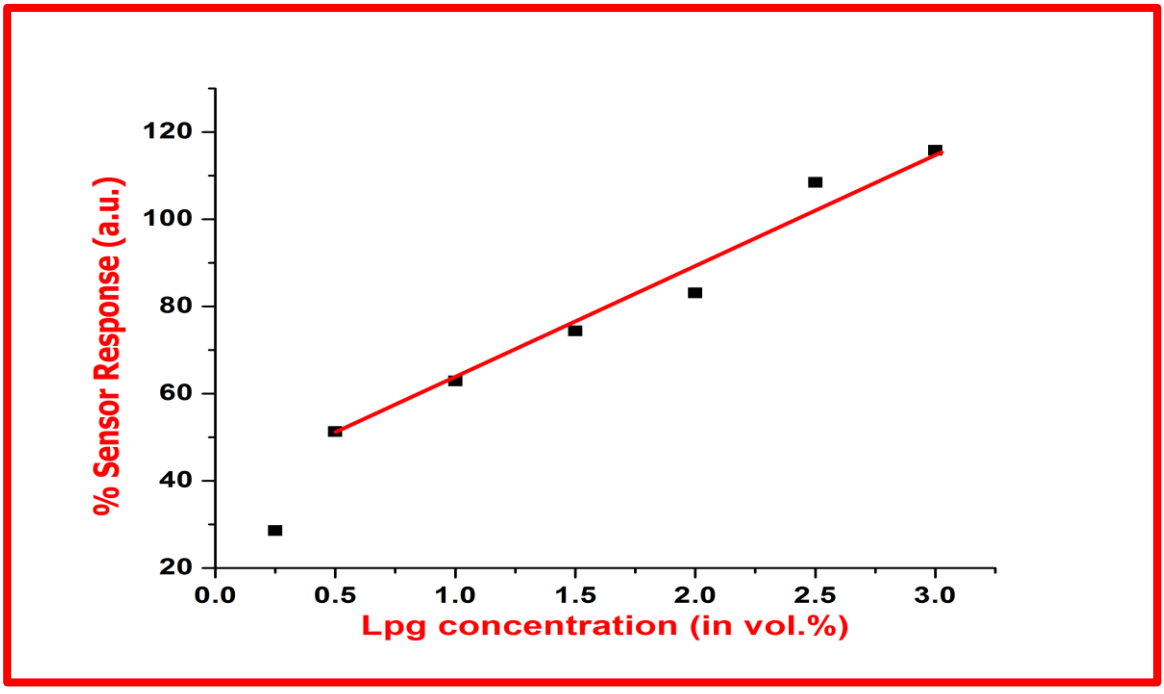

Fig. 4.12 % Sensor Response of BNT film sensor

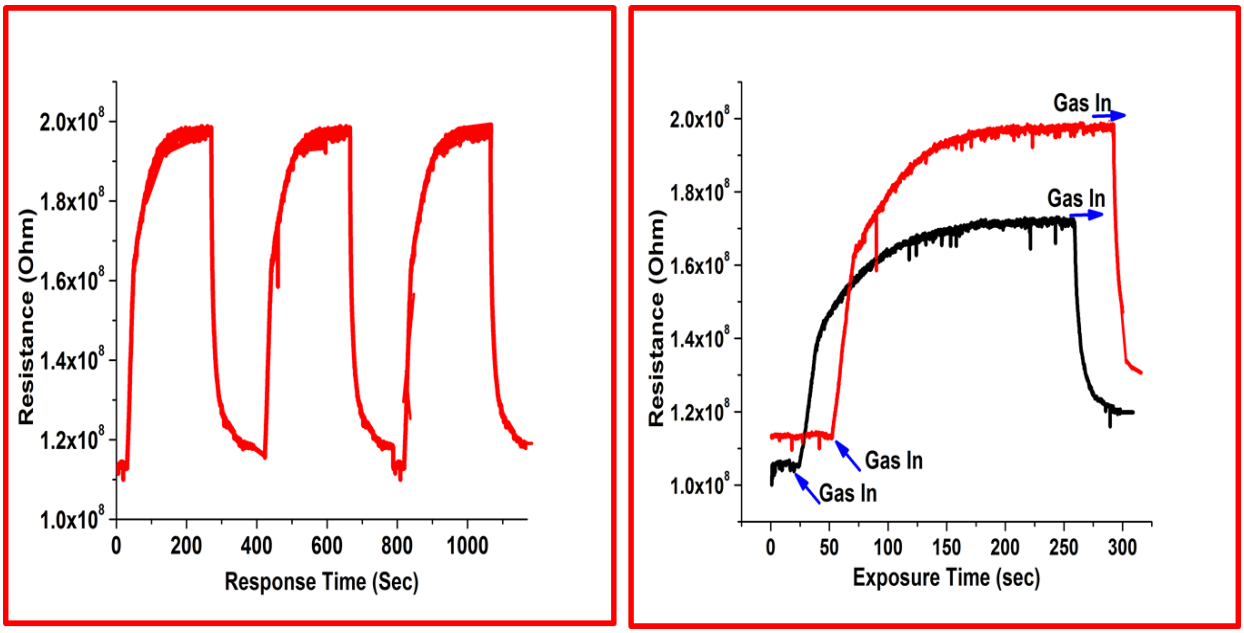

Fig. 4.13(a) & (b) Transient response curve of repeated cycle of BNT film sensor and (b) ageing effect after 2 weeks for 1vol.% of LPG

S.no.	LPG Concentration (in vol.%)	Sensitivity	% Sensor Response
1.	0.25	1.25	28.57
2.	0.5	1.51	51.26
3.	1	1.62	62.87
4.	1.5	1.74	74.38
5.	2	1.83	83.09
6.	2.5	2.08	108.47
7.	3	2.15	115.84

Table.4.1. LPG concentration versus the sensitivity and % sensor response

Chapter 5

Fabrication of perovskite Lanthanum ferrite film by sol-gel and its gas sensing properties

---

Present chapter describes a detailed study of pervoskite Lanthanum ferrite thin film based LPG sensor. The thin film was fabricated using sol-gel spin coating technique and was characterized by various techniques such as XRD, TGA, SEM, TEM, EDS, UV-Spectroscopy, Raman and FTIR. The minimum crystallite size was found as 8 nm and avg. crystallite size was found as 16 nm. Film was optically characterized by UV-visible spectrophotometer and Band gap was found 5.3 eV. Fourier transform infrared analysis and Raman analysis of the sample was done which shows the characteristic of ferrite. TEM show the polycrystalline nature along with the diffraction pattern. LPG sensing was done at room temperature below LEL. Maximum sensitivity was found as 3.3 with 313.85 % senor response. Response time 15 s and recovery time 20 s for 0.25 vol.% of LPG were observed.

CHAPTER 5

FABRICATION OF PEROVSKITE LANTHANUM FERRITE FILM BY SOL-GEL AND ITS GAS SENSING PROPERTIES

5.1 Introduction

LPG is a transparent gas which is stored in liquid form within a liquid cylinder under high pressure. It is used for the household purposes for cooking food, as a motor fuel due to soaring in the price of petrol and diesel, etc [1]. It is an odourless gas and ethanethiol is used as a powerful odorant in LPG so as to detect it. Another odorant like mercaptans, EN589, tetra-thiophene can be an alternative of ethanethiol. LPG is a highly flammable gas which consists of propane and butane. LPG helps to increase the red blood capsules but an excess amount of LPG is hazardous to the mankind. It may affect our lungs causing breathing problem. Some people do not have a sensible smelling power and they can't able to judge the leakage of LPG around our surrounding so artificial nose is developed to meet out their problem. Bhopal gas tragedy (India), Okishima (Japan), Chernobyl (Russia) were the places whose mishap-pending melt the mankind. These were the world's worst gas leakage accident in which a lot of people lost their lives. So to avoid such tragedies, lot of efforts has been done since ages [2]. There are several types of metal oxide sensor available in the market which is used for the detection of LPG. Now the major challenge is to detect the leakage of LPG for small leakage concentration and also to get rid of such the situation and get over it. Ferrite based sensors are gaining more attention of the researchers and technologist due to its phenomenal adsorption efficiency that occurs due to electronic transitions [3]. Ferrites show magnetic as well as electric properties and also show unpredictable behaviour and morphology by changing its macroscopic properties and parameters. This work deals with the perovskite material.

5.2 Structure of Lanthanum ferrite

Forestier and Guilt- Guillain identified rare earth ortho-ferrite of general formula $RFeO_3$, where R refers to trivalent Rare earth ion. In 1966, White et al. reported a review on orthoferrites consisting lot of literature on $RFeO_3$ [4]. In its first approximation ortho-ferrites are considered as perovskite but true symmetry is orthorhombic with one pseudo axis (c-axis). 90.6° angle exists between a-b plane and c-axis [5]. Koehlor and Wollen in 1957 synthesized functional ceramic with perovskite structure known as $LaFeO_3$ with 12:6 coordinate. Several methods are used to synthesise lanthanum ferrite such as microwave combustion method, polymerizable complex route, electro-spinning method, solid-state reaction, auto-combustion, a sol-gel method, sonochemical method, etc [6]. Although these techniques required heat treatment as well as the chelating agent, also for performing complex reactions to yield a complex solution which yields pure product. There are two ternary phases existing in the La-Fe-O system, first one is $LaFeO_3$ with an orthorhombic perovskite structure and another is $LaFe_{12}O_{19}$ with magnetoplumbite hexaferrite structure [7].

5.3 Literature Review

At the end of 90's pulse laser techniques was very popular and frequent used technique to deposit orthoferrite films of Dy, Sm, Gd and Y. It required a very high temperature of 860 °C for post-deposition of the film which was very difficult for practical application in electronic devices. Later on, many methods were used for the preparation of the thin film of orthoferrites. M. Rajendran et al. used aqueous sol method to prepare various orthoferrite films like $LaFeO_3$, $YFeO_3$, $ErFeO_3$, $SmFeO_3$ at 650 °C by dip coating method, particles ranging from 4-7 nm and also studied its spectral transmittance suitable for use in optical devices. Due to the facile synthesis of $LaFeO_3$ and abundance applicability in different devices, it attracted the researchers and scientist to work on it. Perovskite $LaFeO_3$ shows excellent discharge capacity at a higher temperature so due to this features it has been used for hydrogen storage [8]. Recently Yaru Pei et al. used PANI pyrolysis

method to prepare negative terminal of MH-Ni batteries using carbon coating on $LaFeO_3$ using the same property. Further, they investigated the effect of carbon coating by morphology produced by FESEM and found core-shell model also [9]. R. Dinesh Kumar et al. studied on the photocatalytic properties and magnetic properties $LaFeO_3$/ TiO_2 composite of average size 60 nm, prepared by hydrothermal method [10]. Peng Song et al. used simple synthesis route to prepare $LaFeO_3$ by using nitrates and sorghum straw. The reported particle size by this technique was around 20-30 nm with biomorphic porous structure and further, it was used for sensing application of gases like acetone, formaldehyde, methane, LPG, etc but the results were found better for acetone sensing. There were an immense number of researchers who focused on the gas sensing properties of $LaFeO_3$ [11]. Hong Xia Xiao et al. then also reported the acetone gas sensing properties of $LaFeO_3$ with particle size 19.21 nm prepared by hydrothermal method [12]. Hui Hui Zhang et al. used polycondensation of glucose and hydrothermal method to synthesize hollow nanosphere of 24 nm - 30 nm by using templates of carbon sphere. His team further studied the chloroform, HCHO, CH_4, NH_3, sensing and the results were found better for formaldehyde sensing. Later on, many modifications were done and catalysts were used to increase the sensing properties [13]. Y.M. Zhang et al. synthesized Ag - $LaFeO_3$ –SWCNTs nanocomposite of size 28-45 nm by sol-gel and microwave technique. The results were found good for formaldehyde sensing with very fast response time and recovery time [14]. In the present work sol-gel [15-16] and spin coating technique is used to prepare sensor on a glass substrate and further investigated its LPG sensing behaviour.

5.4 Experimental details

5.4.1 Materials Required

Lanthanum nitrate and Ferric nitrate were used as the starting materials. Oleic acid was used as a capping agent. Glacial acetic acid was used to dissolve the Lanthanum ferrite powder to obtain a gel.

5.4.2 Synthesis of Lanthanum ferrite powder

Sol-gel technique was used for the preparation of Lanthanum ferrite nanopowder. Lanthanum nitrate and ferric nitrate materials were taken and dissolved in 50 ml distilled water in 1:2 molar ratios and stirred for 2 h. After stirring, few drops of oleic acid was dissolved in the prepared solution, the sample was put for stirring along with heating temperature about 40 °C. Then we obtained a glossy dark brown sol. This sol was further put on the hot plate to dry. After some time the solvent evaporates continuously with time and the dense gel was obtained. As the time passes after ½ h, this gel was converted into yellowish powder. Then the sample was dried at 650 °C for 2 h in a programmable electric furnace. The obtained powder was crushed into fine particles by mortar and pestle.

5.4.3 Fabrication of Lanthanum ferrite thin film

Firstly the glass substrate was washed with distilled water and acetone following with the ultrasonic cleaning. Then 0.5 gm of the sample was dissolved in a solvent of 2 ml, containing distilled water and PEG in 1:1 ratio. Then the solution was put on a magnetic stirrer for half an hour and further, it was put inside the sonication bath for 1 h which yielded a yellowish sol. Spin coating technique was used to prepare a thin film of the material by pudding the solution on the substrate. Further, the film was dried on the hot plate at 80 °C for 5 min. After this, the film was kept inside the electric furnace for 1 h for good adhesion.

5.4.4. Characterization Techniques

XRD pattern of the prepared powder of perovskite Lanthanum ferrite was recorded by glancing angle X-ray Diffractometer (Proto- Model- An X-ray Diffractometer). Surface morphological study of the material has been done by ZEISS (IIT BHU) SEM equipped with a LaB_6 gun. EDAX was performed by in-situ Brooker element analyzer for qualitative chemical

analysis. TEM analysis was carried out by FEI Technai G2 Spirit TWIN, Netherlands. The sample was optically characterized by UV-Visible spectrophotometer (Evolution 201), FTIR recorded by the instrument, Thermo Nicolate, (Model No. 6700, USIC) and Raman analyzed by Renishaw.

5.5. Results and Discussion

5.5.1 X-ray Diffraction Analysis

Peak analysis of XRD pattern of Lanthanum ferrite was done and it matches with the JCPDF file no.37-1493. Characteristic peak found at $2\theta = 33.02^{\circ}$ (101) confirms the orthorhombic phase [17-19]. The other peaks at 22° (101), 40° (220), 46° (202) etc. as shown in the Fig.5.3 confirm the formation of Lanthanum ferrite. No extra peaks are found in the graph. The minimum crystallite size was found as 8 nm and avg. crystallite size as 19 nm.

5.5.2 SEM analysis and EDX

The surface morphology of the film was examined at 20 kX and 50 kX. The first image shows the surface morphology of the film at the micro scale. On magnifying it up to 200 nm scale it is clearly visible that the particle size ranges from 50 -150 nm. There are vacant spaces present on the surface of the film which will be responsible for whole kinematic in the gas sensing application. Fig. 5.4(c) shows the EDX of Lanthanum ferrite thin film and it confirms the elemental analysis of the material under investigation. The energy vs no. of counts graph shows that no foreign element was present in our sample.

5.5.3 TEM analysis and HRTEM with SAED diffraction pattern

TEM analysis has been done by sonicating the sample by dissolving it in distilled water in a sonication bath. The ultrasonic waves strike the particles and make the sample finer by breaking the bonds and thus removing agglomeration [20]. Later the sample was puddled on the copper grid.

The minimum particle size observed by TEM image is 2.8 nm. In the Fig.5.5, we can clearly see the spherical and oval particles range around 2.8 nm, 4.5 nm, 4.2 nm, 6.8 nm, 5.1 nm and 9.06 nm. The average range of the particle is around 5 nm. The SAED diffraction pattern of the sample presented in Fig 5.6 (a) shows the clear formation of a ring by joining the white dots. Thus the pattern indicates the polycrystalline nature of the film. In Fig 5.6 (b) exhibits the HRTEM image with different domain separations and atomic arrangement of the molecule at the scale of 20 nm. Boundaries are very clear showing the domain of lanthanum, iron and oxygen atoms.

5.5.4 Optical characterization

5.5.4.1 UV-visible Absorption Spectroscopy

The variation of optical absorbance with the wavelength is shown in Fig.5.7. Measurement of the electronic band gap of the $LaFeO_3$ film was carried out using the data obtained by the spectrophotometer. A ferrite material exhibits the minimum optical absorption for the photons with energies smaller than band gap and high absorption for photons with energies greater than the bandgap. As a result, there is a sharp increase in absorption at energies close to the bandgap that manifests itself as an absorption edge in the UV-vis absorption spectra. The optical absorbance spectra of Lanthanum ferrite were plotted with 200-1000 nm wavelength range. The figure shows that absorbance decreases with increase in wavelength. In the region approx. 5-6 eV, the curve shows a steep decrease in absorbance. Further, the data was analyzed and the bandgap energy (E_g) was estimated as 5.3 eV by the intercept of Tauc plot. The larger the band gap smaller will be the particle size of the sample.

5.5.4.2 FTIR Analysis

Variation in % Transmittance with wave number (400-3600 cm^{-1}) has been plotted and presented in Fig. 5.8, which shows that % transmittance sometimes increases and decreases later

becomes constant and finally decreases. A clear peak below 700 cm^{-1} is shown in FTIR graph in a separate box. This peak around 510 cm^{-1} confirms the formation of perovskite phase. This strong absorption peak lies between 433^{-1} and 576 cm^{-1} which is due to bond stretching vibration between the metal oxide bond i.e. Fe-O. The peak near to 1240 cm^{-1} and 1483 cm^{-1} are assigned as v1 and v2 and these are due to metal carbonate. Peak around 2800 is due to stretching in O-H vibration bond [21-23].

5.5.4.3 Raman analysis

The Raman spectrum is observed from the range 200 cm^{-1}-1200 cm^{-1}. The Raman shift around 220 cm^{-1}, 290 cm^{-1} and 404 cm^{-1} are due to Fe_2O_3. The peak around 616 cm^{-1} confirms the perovskite phase of the sample. The green lines and black lines are the curve fitting lines. The vibration bands are due to metal oxide vibration stretching between the L-O and due to FeO_6 [24].

5.6 LPG Sensing of Lanthanum ferrite Film

In this work LPG sensing properties of lanthanum ferrite has been studied at room temperature for concentration 0.25 vol.% to 3.5 vol.%. Electrical resistance was recorded with using Keithley Electrometer. Ionic and Electronic defects are seen to govern its sensing properties [26]. The preparation part of sensing element has been discussed in Chapter 2. Most of the perovskite materials behave as p- type semiconductor. In $LaFeO_3$, holes are responsible for the formation of the surface charge layer [27]. As La belongs to rare earth metal element so it is more interactive to the adsorbed oxygen species when it comes in contact with the film in air. Firstly the film contacts were prepared and connected to Keithley electrometer. Then it was allowed to attain stable position after 15-20 s. At stable condition, the resistance of the film becomes constant in presence of air which was recorded as R_a. $LaFeO_3$ possess good adsorption property so it adsorbs the oxygen molecule to form unstable oxygen ions [28-29]. These oxygen ions interact with the

LPG resulting into an increase of resistance of the film very rapidly. After a short span of time, the resistance of the film gains a constant resistance. This resistance is termed as R_g and when the chamber is opened again the resistance of the film decreases sharply and it almost recovers 95% of the previous resistance in the air [30]. Fig.5.10 shows the variation of resistance (ohm) with the Exposure time (s). It is observed that as LPG injection in the chamber increases, the resistance increases and later becomes constant. When gas was made in off state and outlet was opened the sensor regained its original position.

Table 5.1 shows the comparative change in sensitivity and % response that occurs for different vol.% of LPG. The data presented in the table has been plotted in Fig 5.11 (a) & (b). Fig. 5.11(a) shows that as the concentration of LPG increases, the sensitivity of the sensor increases and vice versa. Meaning that the amount of LPG exposed from 0.25 % to 3.5 % has a proportional reaction with the sensitivity and same as for sensor response shown by Fig 5.11(b). Beyond the concentration of 3.5%, sensitivity and % sensor response became constant.

After two weeks of the first observation, the ageing effect of the lanthanum ferrite thin film was examined and the respective curves are shown in Fig. 5.12 for 0.5 vol.% LPG. Firstly the film was dried under I.R. lamp to remove the humidity from the film. After this, the film was placed inside the LPG sensing setup and connected to Keithley electrometer for studying the stability. After 30 m., the film responded the constant resistance in presence of air. The resistance of the film in the air was observed 2.1 MΩ now, previously it was 1.97 MΩ. This change was due to the formation of more active sites due to the removal of water contents. Analogous to this, the resistance of the film was also varied in the presence of LPG. There was a minute change observed in sensing parameters of the material but the behaviour for 0.5 vol% of LPG was same.

6.6 Conclusion

Nanostructured Lanthanum ferrite film was prepared by facile sol-gel method followed by spin coating technique. The XRD confirmed the perovskite structure of the lanthanum ferrite and the minimum crystallite size was found as 8 nm with an average size of 19 nm. Peaks in FTIR spectra between 433cm^{-1} to 573 cm^{-1} showed the characteristic peak for perovskite material. The SEM image exhibited the macroporous film with agglomerated structure. HRTEM confirmed the polycrystalline nature of the material with a grain size < 10 nm. The minimum grain size of the particle was 2.8 nm. The value of maximum sensitivity was found ~3.31 and % sensor response was ~ 232 for 3.5 vol.% LPG. The response time was found of 12 s and recovery time as 14 s for 0.25 vol.% of LPG.

REFERENCES

1. C. Selvapriya, S.S. Prabha, M. Abdulrahim, K.C. Aarthi, LPG leakage monitoring and multilevel alerting system, International Journal of Engineering sciences & research technology, 2(11) (2013) 3287-3290.
2. A. Singh, A. Singh, S. Singh, P. Tandon, B.C. Yadav, R.R. Yadav, Synthesis, characterization and performance of zinc ferrite nanorods for room temperature sensing applications, Journal of Alloys and Compounds, 618 (2015) 475–483.
3. M. Singh, B.C. Yadav, A. Ranjan, M. Kaur, S.K. Gupta, Synthesis and characterization of perovskite barium titanate thin film and its application as LPG, Sens. Actuators B: Chem., 241 1170–1178 (2017).
4. R.L. White, Review of recent work on the magnetic and spectroscopic properties of the rare-earth orthoferrites, Journal of Applied Physics, 40 (3) (1969).
5. R. Krishnan, A. Lisfi, M. Guyot, V. Cagan, Preparation and some properties of pulse laser deposited $YFeO_3$ film, J. Magnetism and magnetic material, 147 (1995) L-221-224.
6. W.C. Koehler, E.O. Wollan, Neutron-diffraction study of the magnetic properties of perovskite like compounds $LaBO_3$. J. Phys. Chem. Solids., 2(2) (1957) 100-106.
7. K.T. Jacobi, R. Ranjani, Thermodynamic properties of $LaFeO_{3-\delta}$ and $LaFe_{12}O_{19}$, Materials Science and Engineering B, 176 (2011) 559–566.
8. M. Rajendran, M. Ghanashyam Krishna, A.K. Bhattacharya, Low-temperature preparation of orthoferrite thin-films by an inorganic sol-gel process, Thin Solid Films, 385 (2001) 230-233.
9. Y. Pei, Y. Li, J.Y. Che, W. Shen, Y. Wang, S. Yang, S. Han, Study on the high-temperature electrochemical performance of perovskite-type oxide $LaFeO_3$ with carbon modification, International journal of hydrogen energy, 40 (2015) 8742- 8749.
10. R.D. Kumar, R. Thangappanb, R. Jayavel, Synthesis and characterization of $LaFeO_3/TiO_2$ nanocomposites for visible light photocatalytic activity, Journal of Physics and Chemistry of Solids, 101 (2017) 25–33.
11. P. Song, H. Zhang, D. Han, J. Li, Z. Yang, Q. Wang, Preparation of biomorphic porous $LaFeO_3$ by sorghum straw-biotemplate method and its acetone sensing properties, Sens. Actuators B: Chem., 196 (2014) 140–146.

12. H. Xiao, C. Xue, P. Song, J. Li, Q. Wang, Preparation of porous $LaFeO_3$ microspheres and their gas-sensing property, Applied Surface Science, 337 (2015) 65–71.

13. H. Zhang, P. Song, D. Han, Q. Wang, Synthesis and formaldehyde sensing performance of $LaFeO_3$ hollow nanospheres, Physica E, 63 (2014) 21–26.

14. Y.M. Zhang, J. Zhang, J.L. Chen, Z.Q. Zhu, Q.J. Liu, Improvement of response to formaldehyde at Ag–$LaFeO_3$ based gas sensors through the incorporation of SWCNTs, Sens. Actuators B: Chem., 195 (2014) 509–514.

15. K. Suresha, T.S. Panchapagesanb, K.C. Patil, Synthesis, and properties of $La_{1-x}Sr_xFeO_3$, Solid State Ionics, 126 (1999) 299-305.

16. K.M.S. Khalil, W.A. Elhamdy, A.El-Aziz A. Said, A.A. Elsamahy, Porous $LaFeO_3$/Silica Nanocomposites via Sol-Gel Mixing Involving Citric Acid, Chemistry, Colloids and Surfaces A: Physicochem. Eng. Aspects, 506 (2016) 840–848.S. Acharya, P.K. Chakrabarti, Some interesting observations on the magnetic and electric properties of Al^{3+} doped Lanthanum orthoferrite ($La_{0.5}Al_{0.5}FeO_3$), Solid State Communications, 150 (2010) 1234-1237.

17. S. Phokha, S. Pinitsoontorn, S. Rujirawat, S. Maensiri, Polymer pyrolysis synthesis and magnetic properties of $LaFeO_3$ nanoparticles, Physica B, 476 (2015) 55–60.

18. Y. Yuan, Z. Dong, Y. Lia, L. Zhang, Y. Zhao, B. Wang, S. Han, Electrochemical properties of $LaFeO_3$-rGO composite, Progress in Natural Science: Materials International, 27 (2017) 88–92.

19. S. Acharya, P.K. Chakrabarti, Some interesting observations on the magnetic and electric properties of Al^{3+} doped lanthanum orthoferrite ($La_{0.5}Al_{0.5}FeO_3$), Solid State Communications 150 (2010) 1234-1237.

20. Q. Peng, B. Shan, Y. Wen, R. Chen, Enhanced charge transport of $LaFeO_3$ via transition metal (Mn, Co, Cu) doping for visible light photoelectron chemical water oxidation, International journal of hydrogen energy, 40 (2015) 15423-15431.

21. A. Mitra, A.S. Mahapatra, A. Mallick, P.K. Chakrabarti, Enhanced microwave absorption and magnetic phase transitions of nanoparticles of multiferroic $LaFeO_3$ incorporated in multiwalled carbon nanotubes (MWCNTs), J. of Magnetism and Magnetic Materials 435 (2017) 117–125.

22. P.A. Desai and A. A. Athawale, Microwave Combustion Synthesis of Silver Doped Lanthanum Ferrite Magnetic Nanoparticles, Defence Science Journal, 63(3) (2013) 285-291.

23. K.K. Bhargav, A. Maity, S. Ram, S.B. Majumder, Low-temperature butane sensing using catalytic nano-crystalline lanthanum ferrite sensing element, Sens. Actuators B: Chem., 195 (2014) 303–312.

24. P.V. Coutinho, F. Cunha, P. Barrozo Structural, vibrational and magnetic properties of the orthoferrites $LaFeO_3$and $YFeO_3$: A comparative study, Solid State Communications, 252 (2017) 59–63.

25. P. Song, Q. Wang, Z. Zhang, Z. Yang, Synthesis and gas sensing properties of biomorphic $LaFeO_3$ hollow fibers templated from cotton, Sens. Actuators B: Chem., 147 (2010) 248–254.

26. L. Zhang, J. Hu, P. Song, H. Qin, K. An, X. Wang, M. Jiang, CO-sensing properties of perovskite $La_{0.68}Pb_{0.32}FeO_3$ nano-materials, Sens. Actuators B: Chem., 119 (2006) 315–318.

27. X. Ge, Y. Liu, X. Liu, Preparation and gas sensitive properties of LaFe1-yCoyO3 semiconducting materials, Sens. Actuators B: Chem., 79 (2001) 171-174.

28. X. Liu, B. Cheng, H. Qin, P. Song, S. Huang, R. Zhang, J. Hu, M. Jiang, Preparation, electrical and gas-sensing properties of perovskite-type $La_{1-x}Mg_xFeO_3$ semiconductor materials, J. of Physics and Chemistry of Solids, 68 (2007)511–515.

29. P. Song, J. Hu, H. Qin, L. Zhang, H_2-sensing characteristics of nanocrystalline $La_{0.8}Pb_{0.2}FeO_3$ prepared by sol–gel method, Journal of Sol–Gel Science and Technology, 35 (2005) 65–68.

30. H.T. Fan, X.J. Xu, X.K. Ma, T. Zhang, Preparation of $LaFeO_3$ nanofibers by electrospinning for gas sensors with fast response and recovery, Nanotechnology, 22 (2011) 115502–115508.

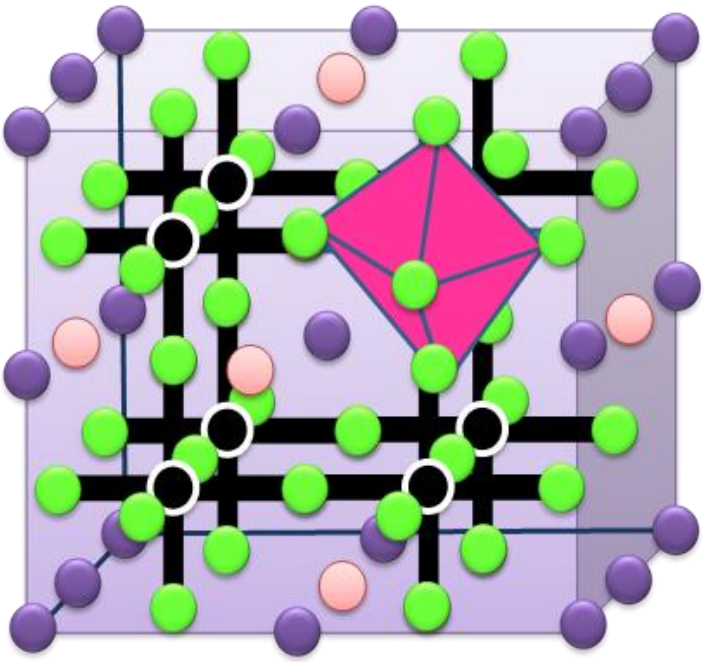

Fig.5.1 Structure of perovskite Lanthanum ferrite

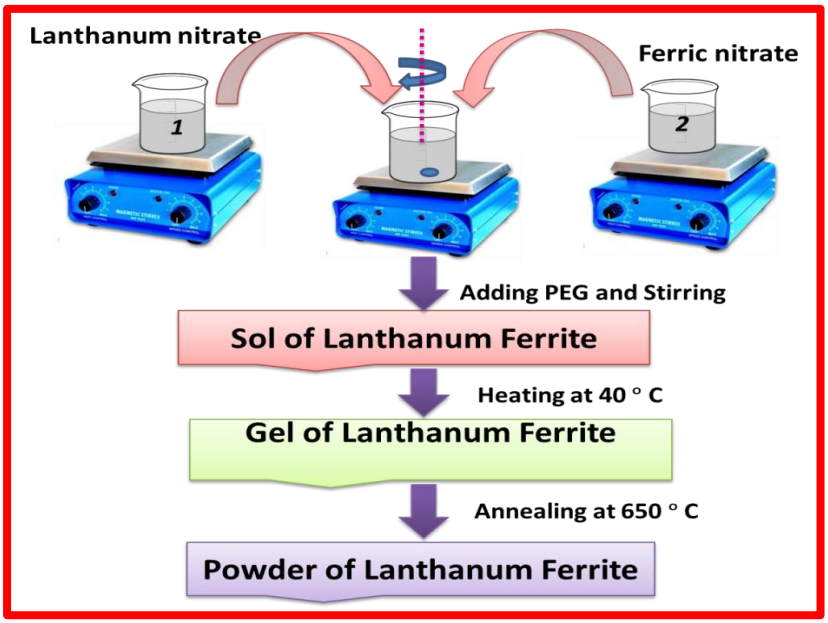

Fig.5.2 Flowchart for the preparation of the Lanthanum ferrite powder

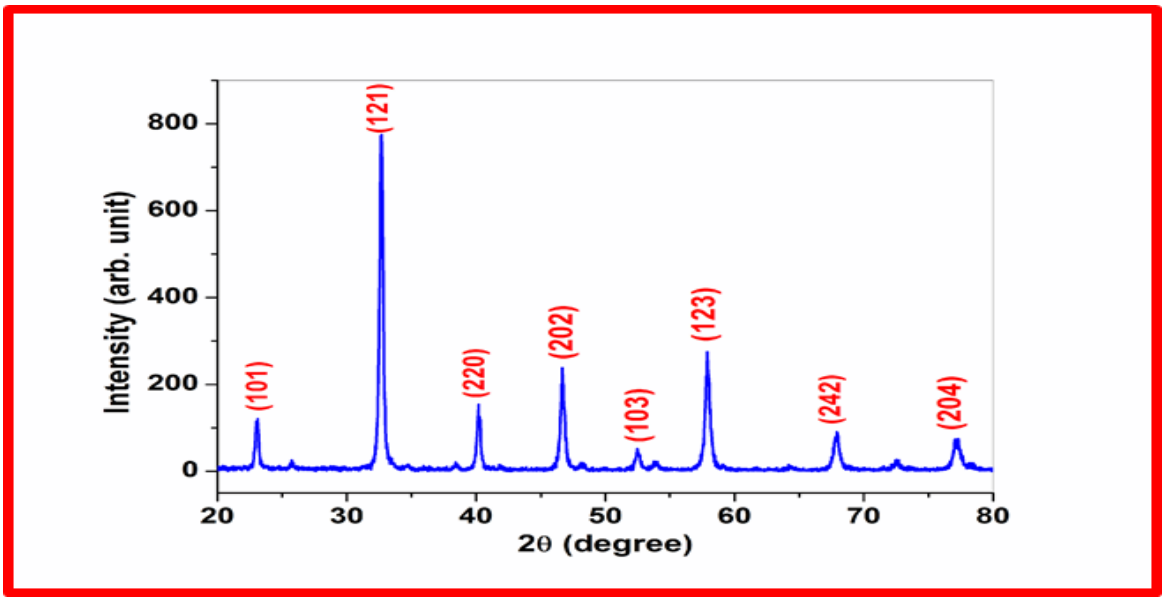

Fig.5.3 XRD pattern of thin film of Lanthanum ferrite

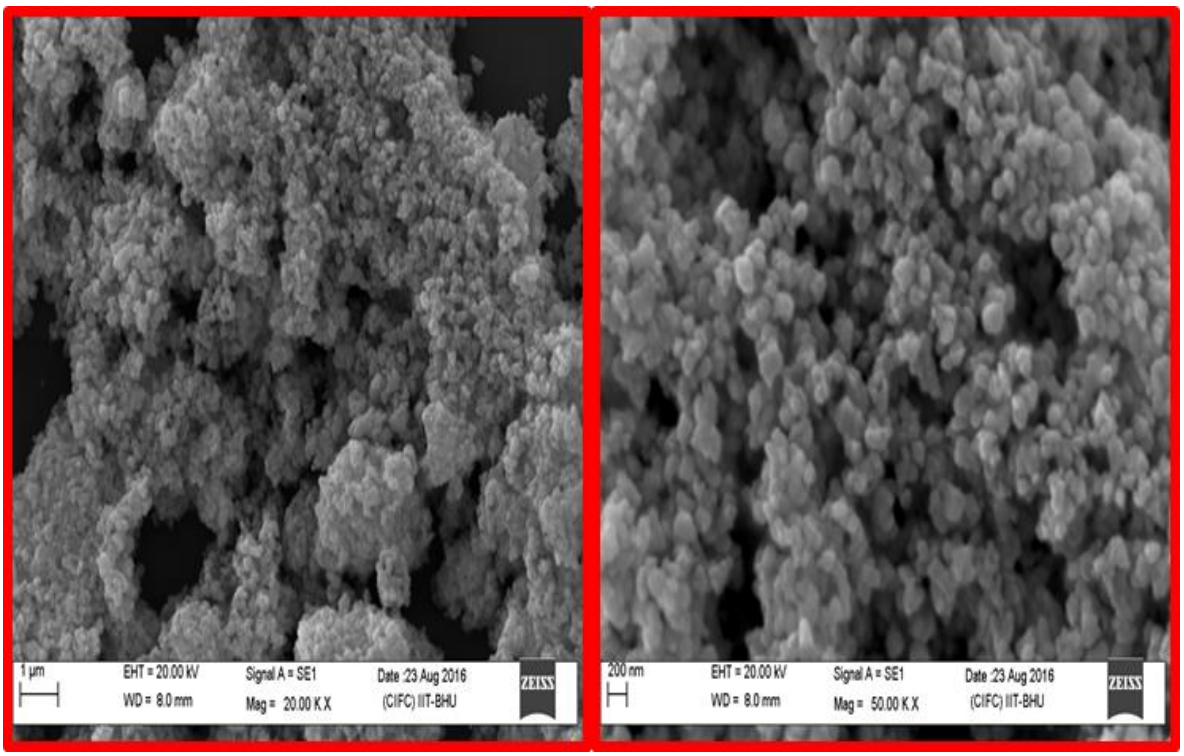

Fig 5.4 (a) & (b) SEM image of thin film of Lanthanum ferrite

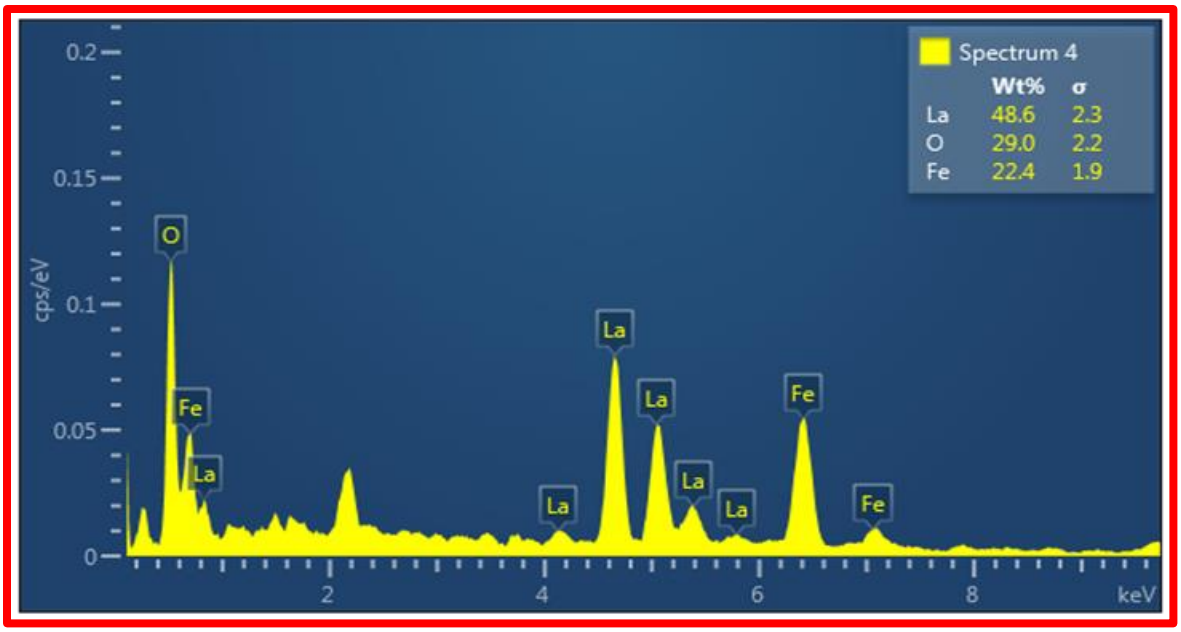

Fig.5.4 (c) EDX of thin film of Lanthanum ferrite

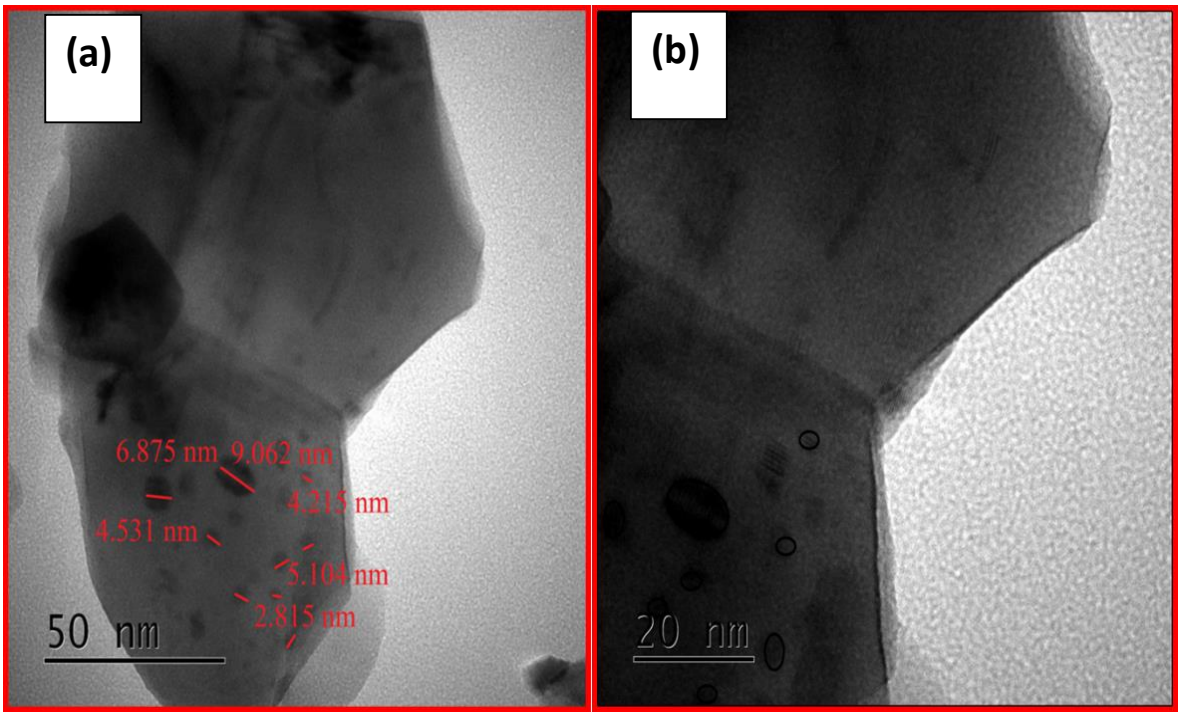

Fig.5.5 TEM image of thin film of Lanthanum ferrite

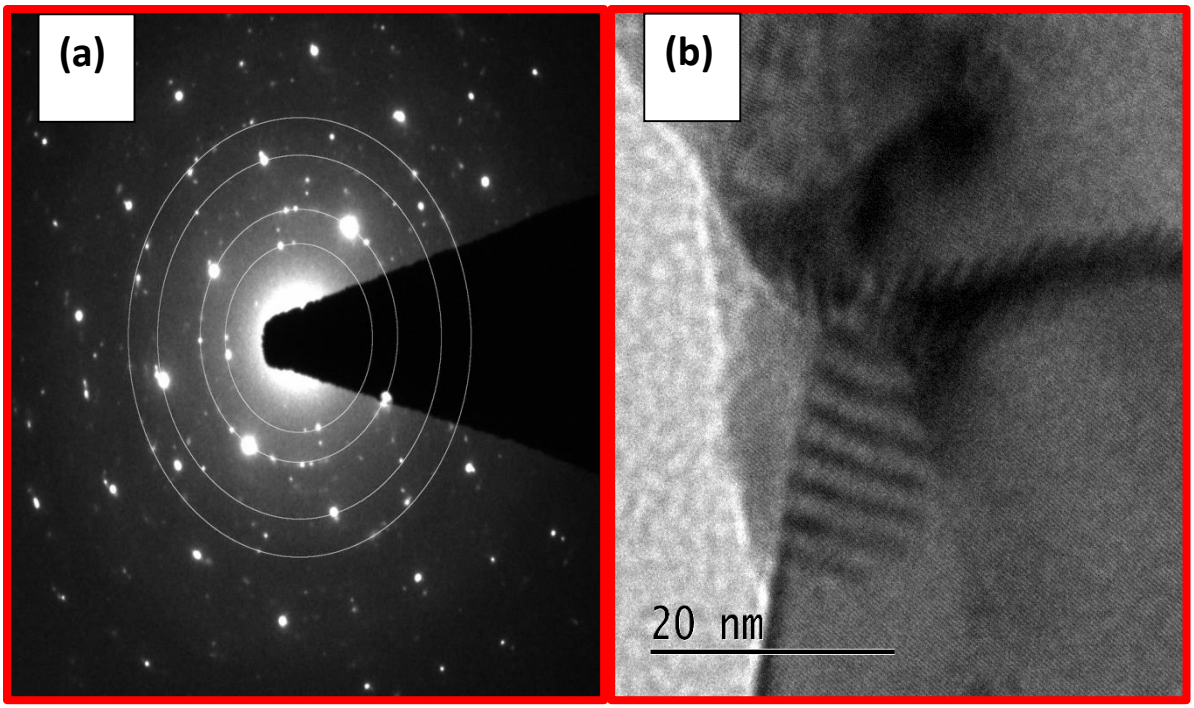

Fig.5.6 Diffraction pattern and HR image of Lanthanum ferrite

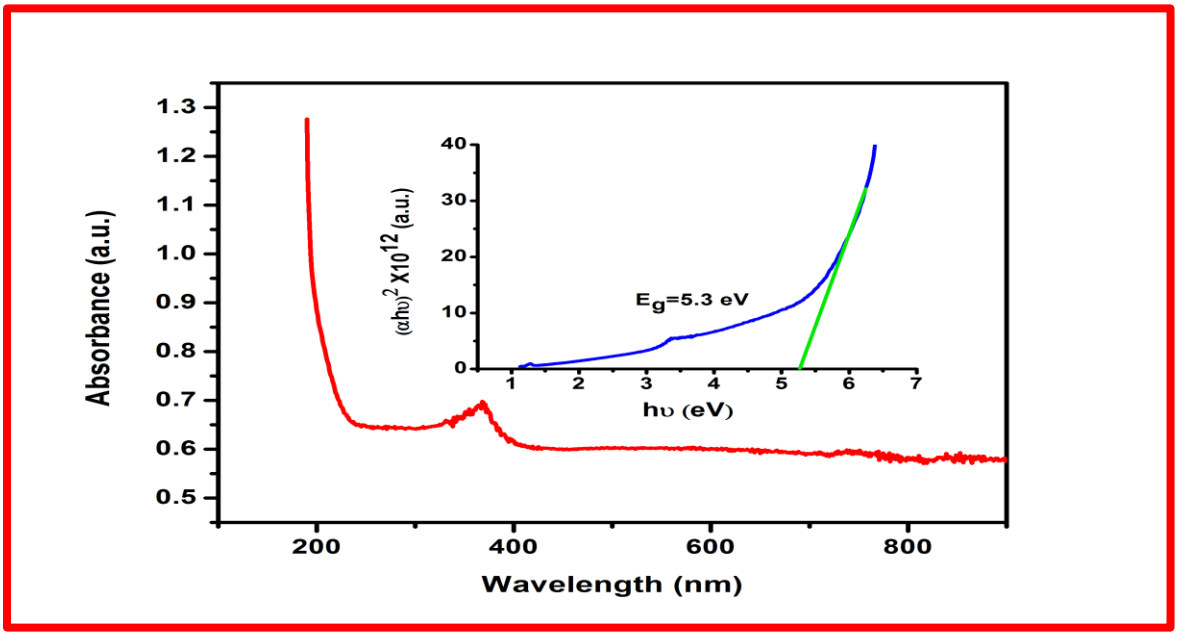

Fig. 5.7 Absorbance spectra of Lanthanum ferrite; *insitu* curve shows Tauc plot.

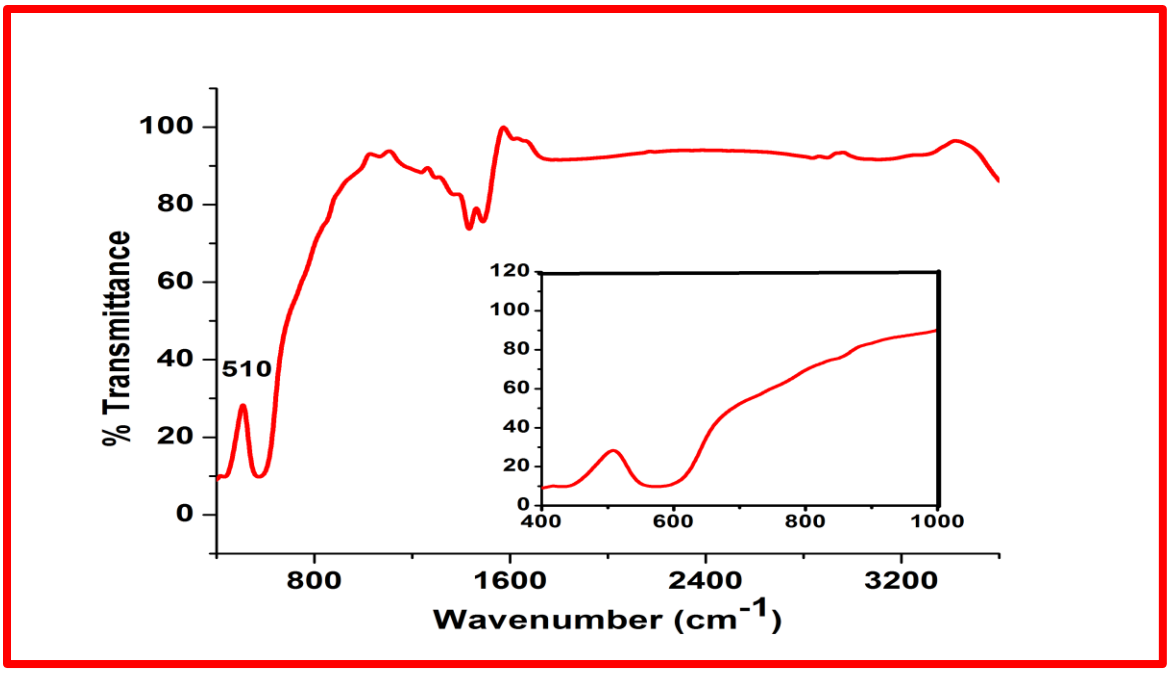

Fig.5.8 FTIR curve of the Lanthanum ferrite film

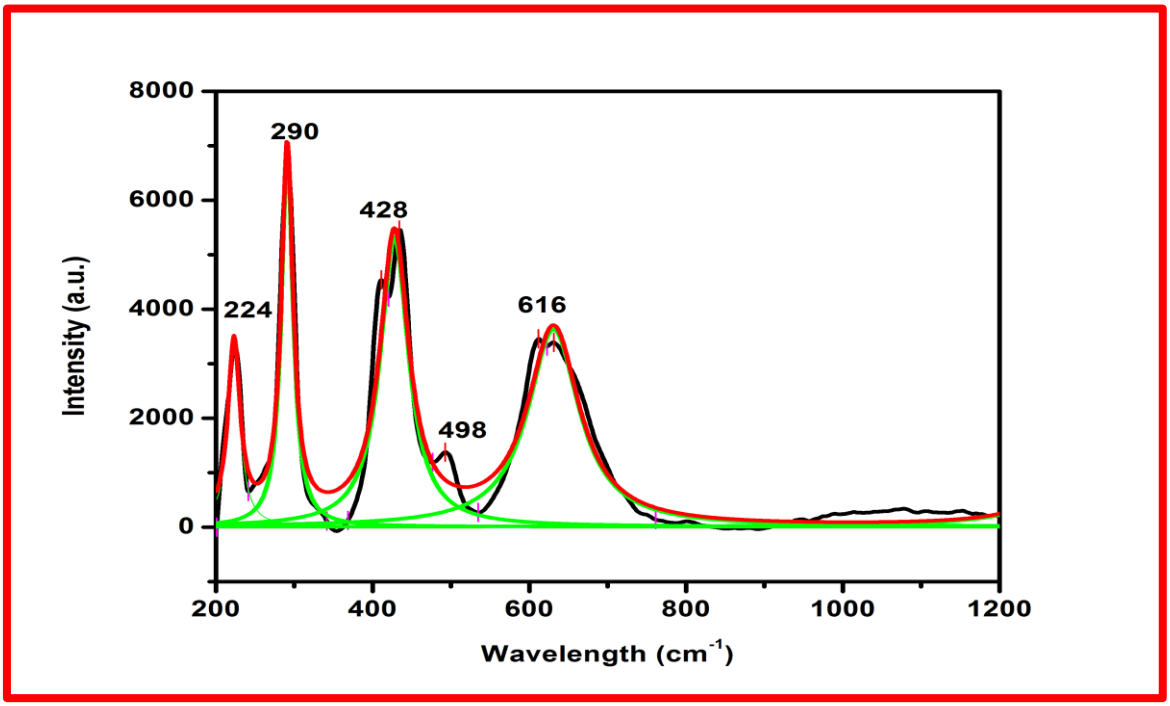

Fig.5.9 Raman curve of the Lanthanum ferrite

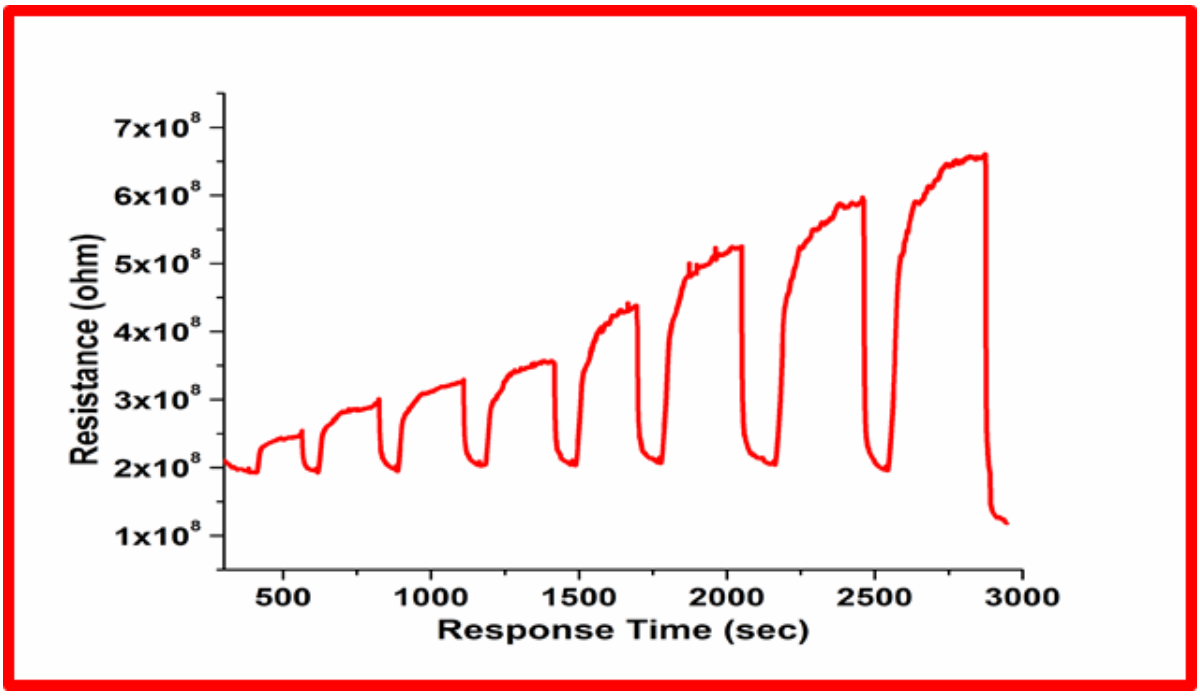

Fig.5.10 Sensing response curve of the Lanthanum ferrite film for different LPG concentration

.

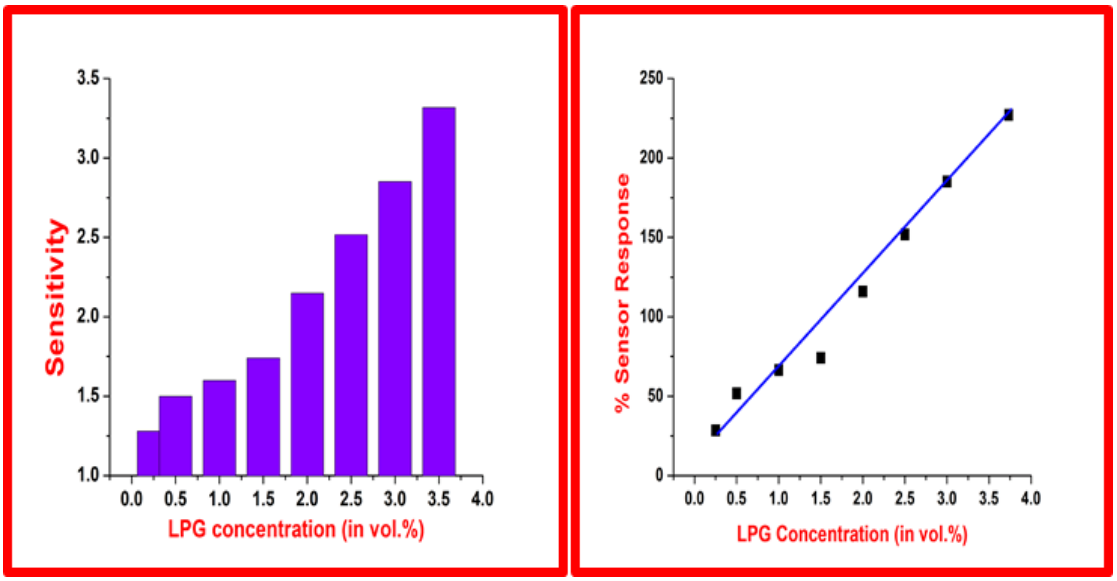

Fig 5.11(a) & (b) Sensitivity and % Sensing response curve of the Lanthanum ferrite film for different LPG concentrations

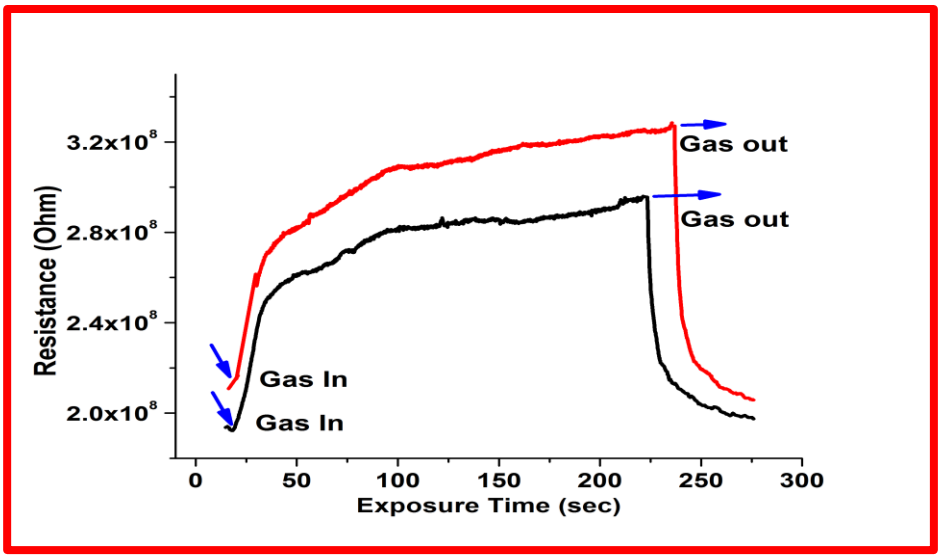

Fig.5.12 Aging effect on Lanthanum ferrite film sensor after 2 weeks

S. No.	LPG Concentration (vol.%)	Sensitivity	% Sensor Response
1	0.25	1.28	28.49
2	0.5	1.51	51.81
3	1	1.66	66.44
4	1.5	1.74	74.09
5	2	2.15	115.04
6	2.5	2.51	151.94
7	3	2.85	185.28
8	3.5	3.31	231.85

Table 5.1 The comparative change in sensitivity and % sensor response that occurs for 0.25 to 3.5% of LPG

Chapter 6

Ag (x = 0.2, 0.4) substituted Nickel ferrite thin film and its application as LPG sensor below LEL

In this chapter Ag (x = 0.2, 0.4) substituted Nickel ferrite thin film has been prepared using sol gel spin coating technique. Surface morphological, structural and optical properties of the film were investigated by various techniques such as XRD, SEM, EDS, UV-Spectroscopy and FTIR. The minimum crystallite size was evaluated as 6 nm and 7 nm for Nickel ferrite film by XRD. SEM images show the macro porous cubic structure of the film. The energy band gap of $Ni_{0.8}Ag_{0.2}FeO_4$ and $Ni_{0.6}Ag_{0.4}FeO_4$ was evaluated as 5.31 eV and 5.40 eV respectively. LPG sensing was carried out for vol.% (0.25-4) of LPG at room temperature. Maximum sensitivity was found as 2.578 and 4.57 and % sensor responses were found as 157.89 and 357.15 respectively. Ag (x = 0.2) substituted Nickel ferrite thin film exhibit better sensitivity and sensor response to LPG than Ag(x = 0.4) nickel ferrite.

CHAPTER 6

Ag (X= 0.2, 0.4) SUBSTITUTED NICKEL FERRITE THIN FILM AND ITS APPLICATION AS LPG SENSOR BELOW LEL

6.1 Introduction

Global warming and continuously rise in pollution has been the major issue of the environment which fetches the attention of the researchers to develop an effective system for detecting the hazardous gas and also quantification of these gases in our surrounding. Gas sensors have been the propitious choice for the quick response and reliable measurement to meet out to these issues [1]. Many metal oxide semiconductor gas sensors and their composites such as ZnO, I_2O_3, SnO_2, WO_3, Fe_2O_3, TiO_2, etc. had been used on the vast scale [2]. Ferrites are the most used material in the chemical gas sensor for gas investigation purpose as they possess high surface area and electromagnetic behaviour with versatile features. Complex ferrites in comparison to normal ferrites show more interesting behaviour as they have the tendency to change the cation composition and microstructure of the ferrite [3-4]. Doping and substitution inside any matrix of metal oxide are used to modify its structure and also to enhance the electrical properties and are of application. Nickel ferrites are the soft magnetic material with high electrical resistivity. Therefore $NiFe_2O_4$ has been extensively used in the field of sensors especially in humidity, acetone sensing etc. Our group have already investigated and reported Nickel ferrite for humidity and LPG sensing [5]. In this work, we have used silver substituted Nickel ferrite as a chemical gas sensor for detection of LPG below the lower explosive limit (LEL). Ag nanoparticles have vast application in nanotechnology. Hence in this work silver ions have been used to substitute Ni ions in $NiFe_2O_4$ to investigate its modified electrical, optical and sensing properties.

6.2 Structure of Nickel ferrite

It is an inverse spinel ferrite with cubic structure [6]. Ni has 10 valence electrons

with varying valency +2 and +3 and silver has +1 valency. Nickel ferrite has fcc crystal structure containing 32 oxygen ion, 16 iron and 8 nickel ions. 64 tetra position and 32 octa-positions are occupied by oxygen ions. Eight Ni ion and 8 Fe ions occupy the octahedral site and rest 8 iron ion occupy the tetrahedral site. The ferric ions are present at the tetrahedral sites in nickel ferrite and nickel ions and some ferric ions occupy the octahedral sites [7]. The crystal structure of spinel ferrite is cubic and it is shown in the Fig.6.1.

6.3 Literature Review

Seema Joshi et al. synthesized $NiFe_2O_4$ using co-precipitation method by using nitrate salt and particles ranging from 8-20 nm. Her team focused on the structural, magnetic, dielectric and optical properties. She also reported the effect of various annealing temperature and strain at 250 $^{\circ}$C, 350 $^{\circ}$C, 450 $^{\circ}$C and 550 $^{\circ}$C [8]. C.V. Gopal Reddy et al. explained the structure of Nickel ferrite and designed p-type gas sensor. His team used citric acid and co-precipitation method to synthesize the Nickel ferrite and further it was used as Chlorine gas sensor. He found response time as 20-30 s and recovery time as 60-90 s [9]. Rimi Sharma et al. designed Zn doped Nickel ferrite by using sol-gel method and particles were found around 15-20 nm. Further, Rimi used it as photocatalytic degradation [10]. M. Mozaffari et al. worked on Al-substituted nickel ferrite by sol-gel method. She reported the particle size of 20-31 nm and studied its magnetic behaviour [11]. K Nadeem et al. synthesized Si coated $NiFe_2O_4$ by sol-gel co-precipitation method. He used chloride salt of respective materials and silica gel matrix for obtaining the $NiFe_2O_4$ [12]. Andris Sutka et al. prepared Co-doped $NiFe_2O_4$ using the sol-gel auto-combustion method. He further reported acetone gas sensing and found response time > 2 min and recovery time > 5 min [13]. Deepshikha Rathore used co-precipitation for the synthesis of Zn doped $NiFe_2O_4$ by using chloride salt. Her team performed experimental investigation for different gases like ethanol, ammonia, LPG, chlorine for 30 to 350 ºC temperature and results were found better for ethanol [14]. L. Satyanarayanan et al. prepared n-type LPG sensor by incorporating Pd inside $NiFe_2O_4$. They used hydrothermal method for the synthesis and average size of the particle was reported as 11 nm. Sensitivity was found good for LPG in comparison to others at 250 $^{\circ}$C [15]. Pratibha Rao et al. also designed ethanol gas sensor using spray pyrolysis method. His team prepared petal-like a

microstructured thin film of different contents of Pd doped $NiFe_2O_4$. Further, they used it for ethanol, hydrogen, methanol and LPG sensor and found better results for LPG [16].

There are many synthesis techniques used for the preparation of ferrite like sol-gel [17], hydrothermal, Co-precipitation [18], spray pyrolysis, Chemical Vapour deposition [19], Ball milling, solid-state method, evaporation method [20-21], etc. Sol-gel is the best and suitable technique to control chemical composition in the preparation of complex ferrites. This work deals with detail analysis of the effect of Ag content on microstructure properties, optical properties and gas sensing properties of Nickel ferrite. As far as best of our knowledge no work has been reported yet on Ag-doped Nickel ferrite as LPG sensor.

6.4 Experimental details

6.4.1 Material Used

Sigma Aldrich A-grade material Silver nitrate, Nickel chloride and Ferric nitrate were used for the synthesis of $Ni_{0.8}Ag_{0.2}Fe_2O_4$ and $Ni_{0.6}Ag_{0.4}Fe_2O_4$ nanoparticles. Glacial acetic acid and distilled water were used as a solvent.

6.4.2 Preparation of Ag substituted Nickel ferrite sol and powder

Silver substituted Nickel ferrite was prepared by simple sol gel technique [22-23]. Nickel chloride and Ferric nitrate were used as a starting material. Firstly Nickel chloride and Ferric nitrate were taken in a definite amount by weight% and are dissolved in distilled water. The stoichiometric amount of Silver nitrate was added inside the precursor solution and solution was continuously stirred for 2 h. This sol was put under I.R. lamp for drying. The dried sample was contaminated powder of $Ni_{0.8}Ag_{0.2}Fe_2O_4$ and $Ni_{0.6}Ag_{0.4}Fe_2O_4$ containing impurities of chloride and nitrates. So the powder was annealed at 650 ºC for the removal of impurities. The annealed powder was ground to get fine nanoparticles of $Ni_{(1-x)}Ag_xFe_2O_4$. Fig.6.2. shows the synthesis method for the preparation of silver doped Nickel ferrite.

6.4.3 Preparation of thin film of Ag-doped Nickel ferrite on glass substrate

Both the powders were dissolved in acetic acid separately and sol was prepared by continuous stirring of 1 h. Spin coating technique was used and sol was puddled dropwise on the glass substrate mounted on a Photoresist Spin coater at 800 rpm for 30 s. Later the prepared thin film was put on the hot plate at 50 °C for drying. After five m. , the film was removed from the hotplate and it was placed inside the electric furnace at 100 ºC for 1 h for creating good adhesion between the substrate and the film.

6.4.4 Characterization of $Ni_{(1-x)}Ag_xFe_2O_4$

XRD was performed by (Proto- Model- An X-ray Diffractometer). Raman Analysis and peaks were obtained by Renishaw Instrument. SEM was performed by JEOL SEM, BSIP equipped with EDX. Evolution 201 Instrument was used for optimizing absorbance spectra and band gap. The FTIR spectra were recorded by the Thermo Nicolet Instrument, (Model No. 6700, USIC).

6.5 Results and Discussion

6.5.1 X-ray diffraction analysis

XRD pattern of the prepared samples was matched with the JCPDF no. # 800072, ICSD #067846. Both the pattern matches with standard data but the peaks are more intense and higher in 0.4 % Ag substituted Nickel ferrite due to silver content as shown in Fig.6.3. Highest intensity peaks were observed at 30.52º (311) in both the pattern only difference is of intensity; this confirms the spinel phase of the sample with the cubic crystal structure. Peaks at 30.28º (220), 37.67º (222), 43.61º (331), 53.79º (422), 57.43º (511), 63.4º (440) and 74.7º (533) are also the peaks obtained in nickel ferrite. The two small peaks obtained at 43.89º, 50.06º and a doublet around 64.23º represent the presence of Ag content. The peaks at 18.58° (111), 23.15° (400) are of very low intensity in $Ni_{0.8}Ag_{0.2}Fe_2O_4$. Peak obtained at 77.07 º must be near to 75.48º but it is shifted to a little bit due to Ag content.

The minimum particle size of $Ni_{0.8}Ag_{0.2}Fe_2O_4$ is 6 nm and $Ni_{0.6}Ag_{0.4}Fe_2O_4$ is 7 nm calculated by Debye Sherrer formula.

6.5.2 SEM analysis and EDX

The SEM micrographs of 0.2% Ag substituted Nickel ferrite and 0.4% Ag substituted Nickel ferrites are shown in the Fig.6.4. Figs. 6.4 (a) & (b) show the macroporous image of $Ni_{0.8}Ag_{0.2}Fe_2O_4$ at 15 kV and Fig 6.4(c) & (d) show macroporous image of $Ni_{0.6}Ag_{0.4}Fe_2O_4$ at 15 kV. In Fig 6.4 (b), it is evidently visible that the average particle size range of 20-50 nm and the particles are of the same dimension almost. But in Fig. 6.4 (d), the particle size ranges from 20- 70 nm, some particles are of a large size that's why average particle size is increased. We deduce that on increasing the silver content from 0.2 to 0.4 %, the grain size of some particles is enhanced. These large particles are due to silver content but the film of 0.4% Ag substituted Nickel ferrite is more porous than the 0.2% Ag substituted Nickel ferrite film.

EDX graph of both the prepared sample shows that no other element is present in the sample. The Ag content in Fig. 6.5 (b) is more in comparison to Fig. 6.5 (a) which is also according to our calculated value. Also, the Nickel content in the sample presented in Fig 6.5 (a) is more as compared to the sample presented in Fig 6.5 (b).

6.5.3 Optical characterization

6.5.3.1 Raman Analysis

Raman spectra of both the sample were obtained from 200 cm^{-1} to 1000 cm^{-1}. Group theory suggests that there are 42 vibrational modes of inverse spinel nickel ferrite with 5 Raman active modes. The peaks at 224 cm^{-1}, 290 cm^{-1}, 331 cm^{-1}, 481 cm^{-1}, 562 cm^{-1} are the characteristic peaks of inverse spinel structure [24]. Sharp peaks are visible in $Ni_{0.8}Ag_{0.2}Fe_2O_4$ sample, as we increase the Ag content there is a broadening of the peak shown by a reddish curve as presented in Fig.6.6.

6.5.3.2 UV-visible Absorption Spectroscopy

The absorbance curve of both the sample is shown in Fig 6.7 (a) & (b). The

absorbance spectra show the similar absorption behaviour. But there is a change in the bandgap of the material on increasing the silver content. Using extrapolation method by drawing tangent on the absorbance curve band gap of the sample was calculated. When the silver content was substituted about 0.2% in nickel ferrite, then the band gap was found 5.40 eV and on increasing the silver content from 0.2 % to 0.4 %, the bandgap is increased to 5.31 eV. As we know that the higher the bandgap of the film, the lower the particle size.

6.5.3.3 FTIR Analysis

The FTIR spectra of a prepared pellet of the material and KBr are shown in transmittance mode ranging from 400 to 4000 cm^{-1} in Fig 6.8. The reddish graph shows the curve for $Ni_{0.8}Ag_{0.2}Fe_2O_4$ and the black graph shows the curve for $Ni_{0.6}Ag_{0.4}Fe_2O_4$. Both the curves show almost similar peaks. In ferrites, two main absorption peaks are obtained at 442 cm^{-1} and 530 cm^{-1} due to stretching vibration in metal-oxygen bonds. The spinel ferrite has been categorized in two sub-lattice tetrahedral (A site) and octahedral (B site). The characteristic peaks in the second graph are more intense due to Ag content. The peak at 530 cm^{-1} is due to M-O bond assigned at the tetrahedral site and the absorption peak at 442 cm^{-1} is due to Ni-O bond at the octahedral site and complex group [25]. The peaks after 3000 cm^{-1} represent the O-H bond present in the sample.

6.5.4 LPG Sensing of Film $Ni_{0.8}Ag_{0.2}Fe_2O_4$ and $Ni_{0.6}Ag_{0.4}Fe_2O_4$

The gas sensing is a surface controlled mechanism depending upon many different factors [26-28]. The plausible gas sensing mechanism of LPG is already reported in Chapter 2. The same setup was used for the LPG sensing for both the samples. Firstly the resistance of the $Ni_{0.8}Ag_{0.2}Fe_2O_4$ film was around 2.8 MΩ but the resistance of another film was 43 KΩ in the air. When LPG was allowed to react with the film, its resistance increases very rapidly and after getting stabilized, the resistance marked as R_a. When the outlet of the setup was opened, the LPG was released from the chamber. Firstly, there was a rapid decrement in the resistance of the film, then, the rate of decrement of the resistance became slow and sensor recovered more than 95 % of the initial resistance. The data have been plotted as Fig. 6.9 (a) & (b). In the p-type chemical sensor, electrical resistance increases on the imposition of reducing gas. Conductivity is provided at the octahedral site by

hopping of holes between Ni^{3+} and Ni^{2+} ions and hence reduction of Ni^{3+} to Ni^{2+} ions occurs.

$$\mathbf{Ni^{2+} + h+ \leftrightarrow Ni^{3+}}$$

Cationic interchange and vacancies due to oxygen or cations occur due to hopping of Nickel ion and silver ion substitution [29-30]. The curves (a) & (b) show the gas sensing response curve from (0.25 - 4) vol.% of LPG. Sensing curve clearly shows the repeatability cycle of all the concentrations of LPG smoothly and in a very systematic way. The Tables 6.1 (a) & (b) show the sensitivity and % sensor response of both the LPG sensor. The maximum sensitivity was found as 2.57 and % Sensor response was found 157.8 for $Ni_{0.8}Ag_{0.2}Fe_2O_4$ and for $Ni_{0.6}Ag_{0.4}Fe_2O_4$ sensitivity was found as 4.57 and % Sensor response was found 357.15 for 4 % LPG. For LEL properties, the minimum concentration peak was considered. Here the minimum sensitivity was calculated as 1.15 and 1.87 for 0.25 vol.%, concentration for $Ni_{0.8}Ag_{0.2}Fe_2O_4$ and $Ni_{0.6}Ag_{0.4}Fe_2O_4$ respectively. Response time was found as 10 s and 30 s for 0.25 % LPG and recovery time was found as 60 s and 90 s for both the samples. The sensitivity and % sensor response was found better for 0.4% Ag substituted sample. But response time and recovery time was found better for the first sample.

Ageing effect on both the samples is shown in the Fig. 6.10 (a) & (b) after two weeks for 1 vol.% LPG. The sensing film adsorbed moisture due to the removal of water content during the first observation. So to remove this moisture the film was dried under I.R. lamp for 5 min. Due to the evaporation of moisture content, the adsorption on the film surface was increased and as a result, there was an increment in the resistance in presence of air and also in presence of LPG. Behavior and sensing results of both the film were found quite similar as in the previous experiment.

6.7 Conclusion

Nanostructured $Ni_{0.8}Ag_{0.2}Fe_2O_4$ and $Ni_{0.6}Ag_{0.4}Fe_2O_4$ were successfully synthesized by sol-gel method and thin films were prepared on glass substrates. These films were characterized by XRD, SEM, FTIR, UV-visible spectroscopy and Raman. The comparison in their microstructures can be easily observable by SEM. SEM exhibited the better surface

morphology of 0.4% Ag substituted Nickel ferrite than 0.2% Ag substituted nickel ferrite. As Ag substitution increases the porosity of material was found increased. XRD revealed the crystalline phase of Ag substituted nickel ferrite. Similarly, there was a change in energy band gap from 5.3 to 5.4 eV and also there was a corresponding change in the optical behaviour of the samples. The maximum sensitivity was found 2.57 and 4.57 with % sensor response of 157.8 and 357.14 for 4 vol.% of LPG. The investigated LPG sensor produces a repeatable curve one after the other experiment hence this sensor is reliable and worth to develop at commercial scale.

REFERENCES

1. C.J. Belle, A. Bonamin, U. Shimon, J.S. Salazar, M. Pauly, S.B. Colin, G. Pourroy, Size dependent gas sensing properties of spinel iron oxide nanoparticles, Sens. Actuators B: Chem., 160 (2011) 942-950.
2. K. Wetchakun, T. Samerjai, N. Tamaekong, C. Liewhiran, C. Siriwong, V. Kruefu, A. Wisitsoraat, A. Tuantranont, S. Phanichphant, Semiconductor metal oxides as sensors for environmentally hazardous gases, Sens. Actuators B: Chem., 160 (2011) 580-591.
3. A.P. Kazin, M.N. Rumyantseva, V.E. Prusakov, I.P. Suzdalev, A.M. Gaskov, Nanocrystalline ferrites $NiZn_{1-x}Fe_2O_4$: Influence of cation distribution on acidic and gas properties, Journal of solid state chemistry, 184 (2011) 2799-2805.
4. V.D. Kapse, S.A. Ghosh, F.C. Raghuwanshi, S.D. Kapse, U.S. Khandekar Nanocrystalline $Ni_{0.6}Zn_{0.4}Fe_2O_4$: A novel semiconducting material for ethanol detection, Talanta, 78 (2009) 19–25.
5. R. Srivastava, B.C. Yadav, M. Singh, T.P. Yadav, Synthesis, Characterization of Nickel Ferrite and Its Uses as Humidity and LPG Sensors, J. Inorg Organomet Polym., 26 (2016) 1404-1412.
6. B.A. Aldar, R.K. Pinjari, N.M. Burange, Electric and Dielectric behaviour of Ni-Co-Cd Ferrite, IOSR Journal of Applied Physics (IOSR-JAP). 2278-4861.6(4) (2014) 23-26.
7. C. Matei, D. Berger, S. Stoleriu, F. papa, V. Fruth, Synthesis of lanthanum ferrite nanopowder by combustion method Journal of optoelectronics and advanced materials 9(6) (2007) 1793 – 1796.
8. S. Joshi, M. Kumar, S. Chhoker, G. Srivastava, M. Jewariya, V.N. Singh, Structural, magnetic, dielectric and optical properties of nickel ferrite nanoparticles synthesized by co-precipitation method, Journal of Molecular Structure, 1076 (2014) 55–62.
9. C.V. Gopal Reddy, S.V. Manorama ,V.J. Rao, Semiconducting gas sensor for chlorine based on inverse spinel nickel ferrite, Sensors and Actuators B 55 (1999) 90–95.

10. R. Sharma, S. Singh, Structural, magnetic and electrical properties of zinc doped nickel ferrite and their application in photo-catalytic degradation of methylene blue Physica, B 414 (2013) 83–90.

11. M. Mozaffari, Z. Abooalizadeh, J. Amighian, Investigation of magnetic properties of Al substituted nickel ferrite nanopowders synthesized by the sol–gel method, J. of Magnetism and Magnetic Materials, 323 (2011) 2997–3000.

12. K. Nadeem, H. Krenn, W. Sarwar, M. Mumtaz, Comparison of surface effects in SiO_2 coated and uncoated nickel ferrite nanoparticles, Applied Surface Science, 288 (2014) 677– 681.

13. A. Sutka, R. Pärna, G. Mezinskis, V. Kisand, Effects of Co ion addition and annealing conditions on nickel ferrites response, Sens. Actuators B: Chem., 192 (2014) 173–180.

14. D. Rathore, R. Kurchania, R.K. Pandey, Fabrication of $Ni_{1-x}Zn_xFe_2O_4$ (x = 0, 0.5 and 1) nanoparticles gas sensor for some reducing gases, Sens. Actuators A: Phy., 199 (2013) 236–240.

15. L. Satyanarayana, K.M. Reddy, S.V. Manorama, Nanosized spinel $NiFe_2O_4$: A novel material for the detection of liquefied petroleum gas in air, Materials Chemistry and Physics, 82 (2003) 21–26.

16. P. Rao, R.V. Godbole, S. Bhagwat, Nanocrystalline Pd:$NiFe_2O_4$ thin films: A selective ethanol gas sensor, Journal of Magnetism and Magnetic Materials, 416 (2016) 292–298.

17. A. Ashok, T. Somaiah, D. Ravinder, C. Venkateshwarlu, C.S. Reddy, K.N. Rao, M. Prasad, Electrical Properties of Cadmium Substitution in Nickel Ferrites, World Journal of Condensed Matter Physics, 2 (2012) 257-266.

18. R. Asokarajan, A. Milton Franklin Benial, Structural, Optical And Surface Morphological Properties of Nanosized Nickel Ferrite Particles by Co-Precipitation Method, International Journal of NanoScience and Nanotechnology, 4(1) (2013) 113-120.

19. S. Manorama, G. Sarala-Devi, V.J. Rao, Hydrogen sulphide sensor based on tin dioxide deposited by spray pyrolysis and microwave plasma chemical vapour deposition, Appl. Phys. Lett. 64 (23) (1994) 3163–3166.

20. P. Rao, R.V. Godbole, S. Bhagwat, Copper doped nickel ferrite nano-crystalline thin films: A potential gas sensor towards reducing gases, Materials Chemistry and Physics, 171 (2016) 260-266.

21. J. Azadmanjiri, H.K. Salehani, M.R. Barati, F. Farzan, Preparation and electro-magnetic properties of Ni_{1-x} $Cu_xFe_2O_4$ nanoparticle ferrites by sol–gel auto-combustion method, Mater.Lett.61 (2007) 84–87.

22. R. Kumar, K. Asokan, S. Patnaik, B. Birajdar, Evolution of microstructure and relaxor ferroelectric properties in $(La_zBa_{1-z})(Ti_{0.80}Sn_{0.20})O_3$, Journal of Alloys and Compounds, (2016) 197-203.

23. G.B. McGarvey, D.G. Owen, Control of the morphology and surface properties of nickel ferrite, J. Mater. Sci. 33 (1998) 35–40.

24. A. Sutka, G. Mezinskis, A. Lusis, M. Stingaciu, Sens. Actuators B: Chem., Gas sensing properties of Zn-doped p-type nickel ferrite, 171–172 (2012) 354–360.

25. G. Dixit, J.P. Singh, R.C. Srivastava, H.M. Agrawal, R.J. Chaudhary, Structural, magnetic and optical studies of nickel ferrite thin films, Adv. Mat. Lett., 3(1) (2012) 21-28.

26. J.L. Gunjakar, A.M. More, V.R. Shinde, C.D. Lokhande, Synthesis of nanocrystalline nickel ferrite ($NiFe_2O_4$) thin films using low temperature modified chemical method, Journal of Alloys and Compounds, 465 (2008) 468–473.

27. E. Ranjith Kumar, P.S.Prasada Reddy, G.S.Devi, S.Sathiyaraj, Structural, dielectric and gas sensing behaviour of Mn substituted spinel, MFe_2O_4 (M¼Zn, Cu, Ni, and Co) ferrite nanoparticles, Journal of Magnetismand Magnetic Materials398 (2016) 281–288.

28. N. Iftimie, E. Rezlescua, P. D. Popaa, N. Rezlescua, gas sensitivity of nanocrystalline nickel ferrite, Journal of optoelectronics and advanced Materials, 8(3) (2006) 1016–1018.

29. M. Singh, B.C. Yadav, A. Ranjan, R.K. Sonker, M. Kaur, Detection of liquefied petroleum gas below the lowest explosive limit (LEL) using nanostructured hexagonal strontium ferrite thin film, Sens. Actuators B: Chem., 249 (2017) 96-104.

30. F. Tudorachea, P. D. Popab, M. D. F. Iacomia, Studies on the structure and gas sensing properties of nickel–cobalt ferrite thin films prepared by spin coating, Materials Science and Engineering B 178 (2013) 334– 1338.

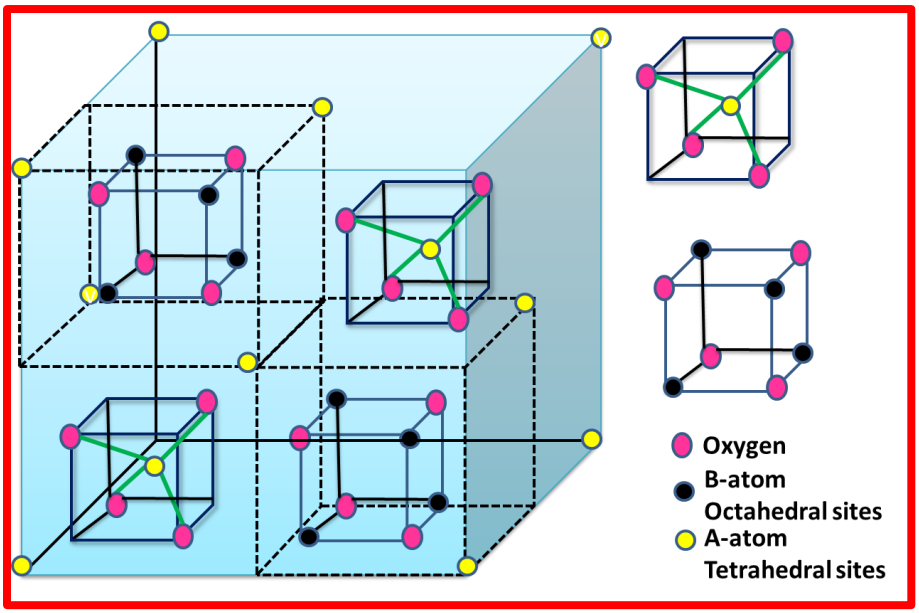

Fig.6.1 Cubic structure of Spinel Nickel ferrite

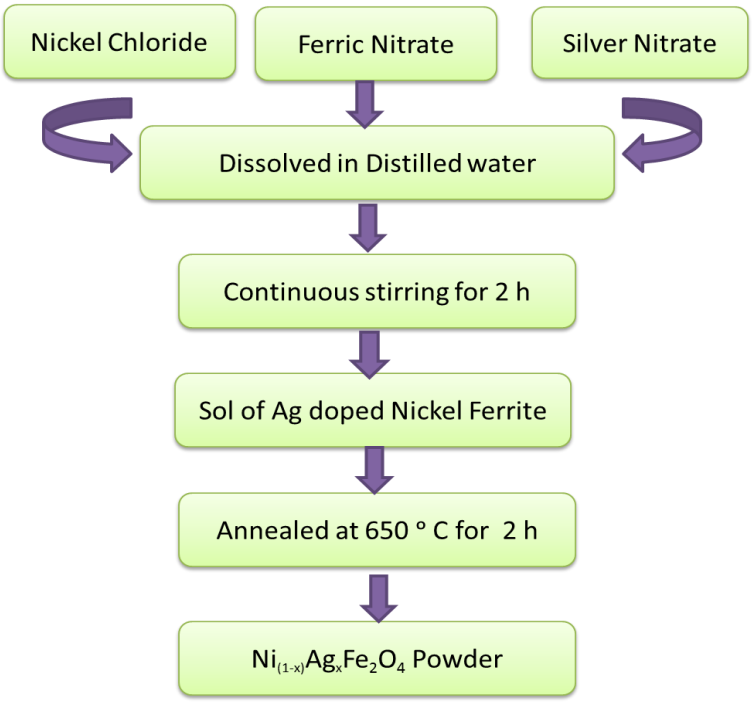

Fig.6.2 Flowchart for the preparation of $Ni_{(1-x)}Ag_xFe_2O_4$ nanopowder

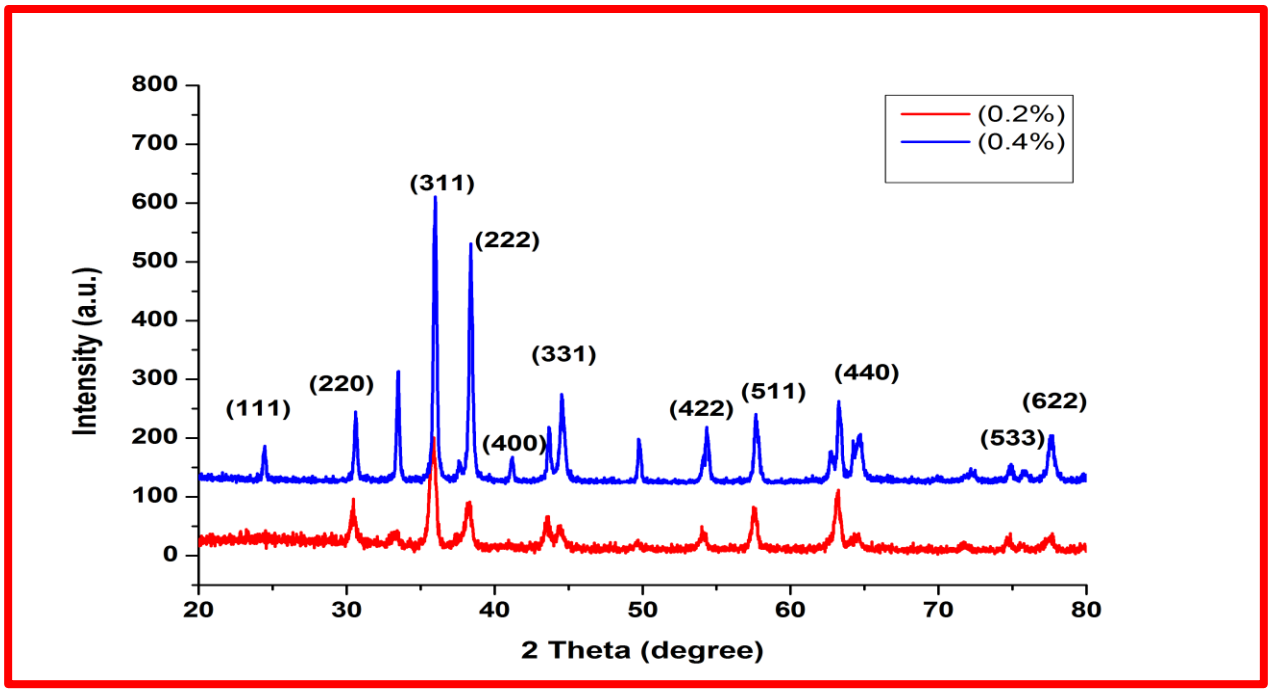

Fig.6.3 XRD pattern of $Ni_{0.8}Ag_{0.2}Fe_2O_4$ and $Ni_{0.6}Ag_{0.4}Fe_2O_4$

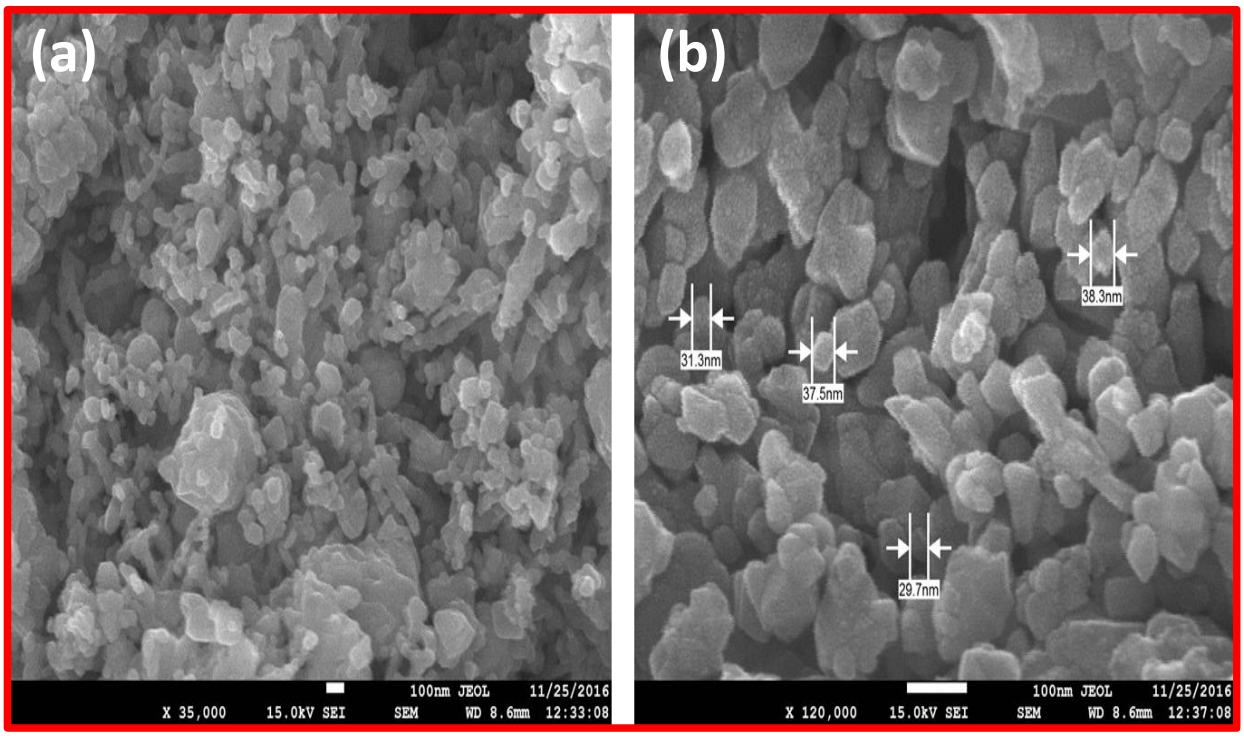

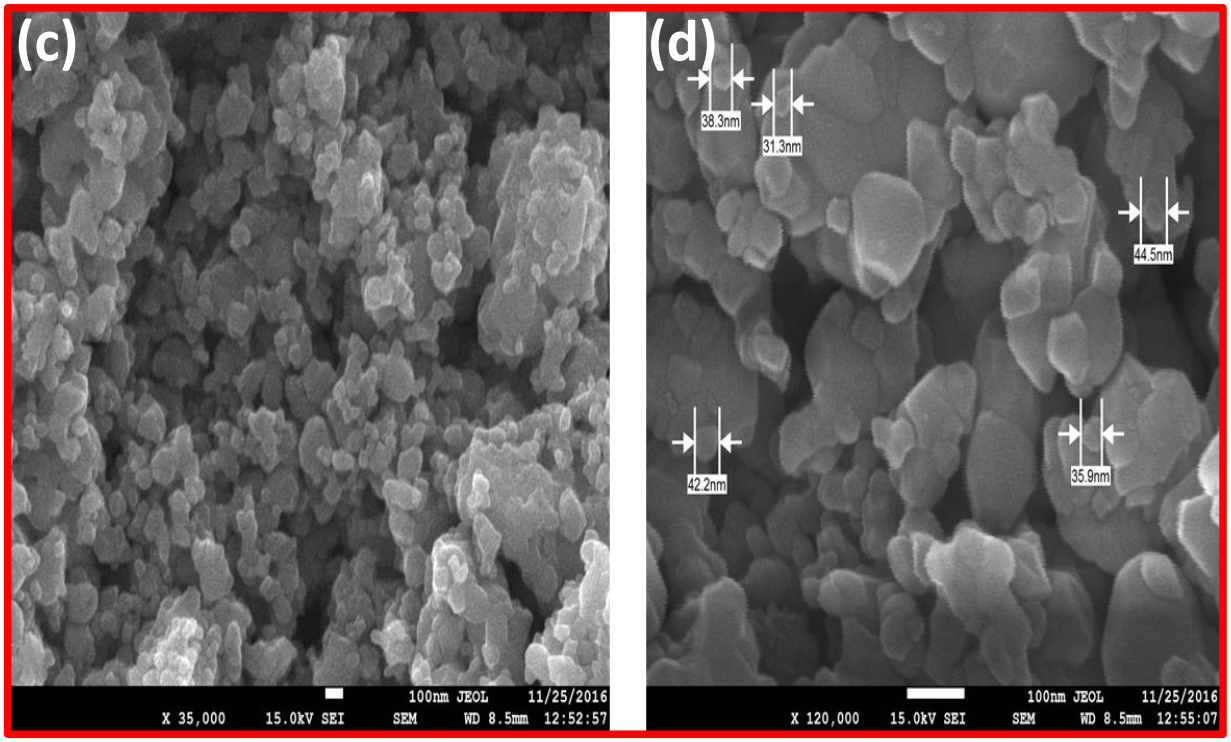

Fig.6.4 SEM micrographs (a) & (b) of $Ni_{0.8}Ag_{0.2}Fe_2O_4$ and (c) & (d) of $Ni_{0.6}Ag_{0.4}Fe_2O_4$

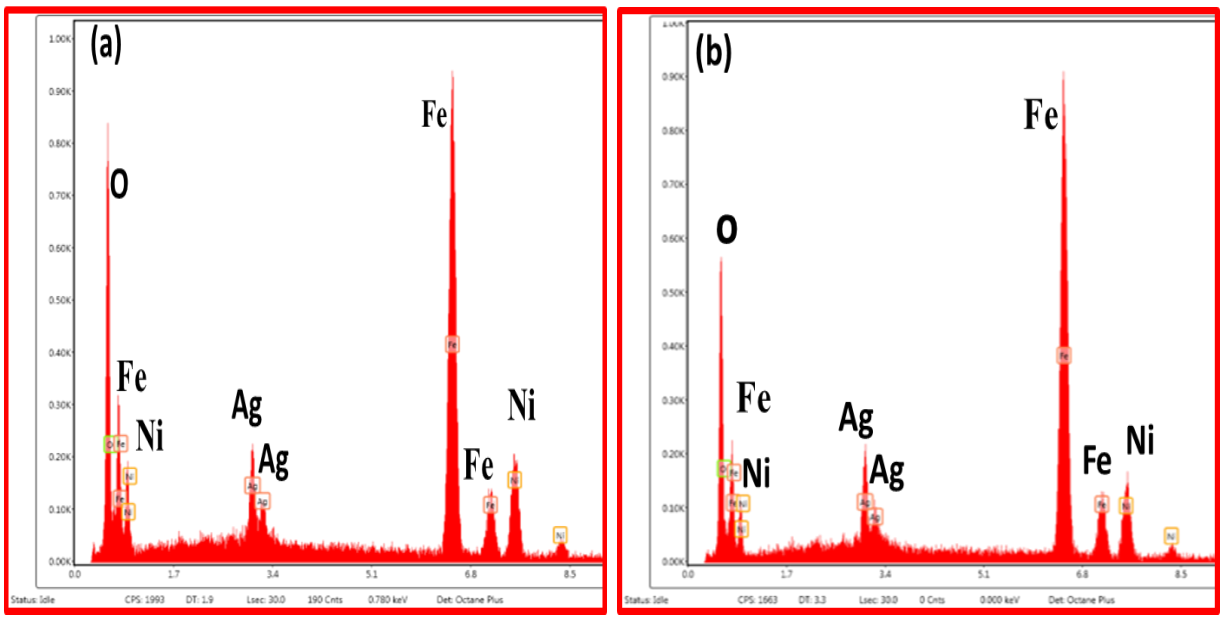

Fig.6.5 EDX of $Ni_{0.8}Ag_{0.2}Fe_2O_4$ and $Ni_{0.6}Ag_{0.4}Fe_2O_4$ s showing no foreign element inside

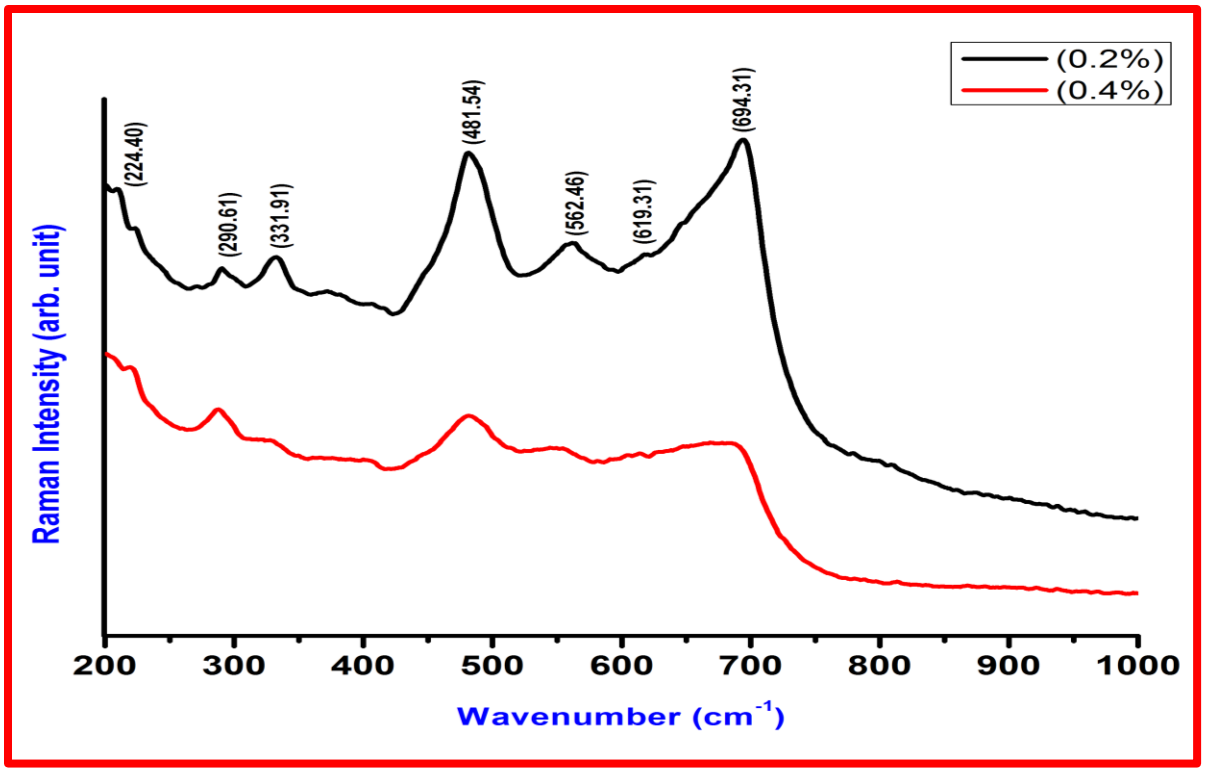

Fig.6.6 Raman spectra obtained for $Ni_{0.8}Ag_{0.2}Fe_2O_4$ and $Ni_{0.6}Ag_{0.4}Fe_2O_4$

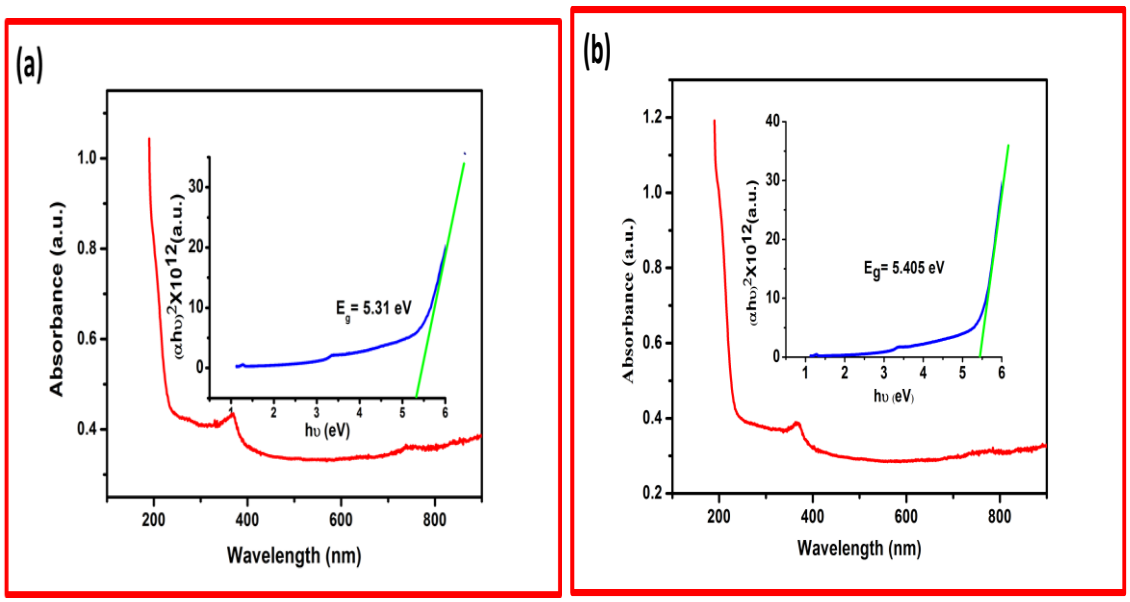

Fig.6.7 Absorbance spectra and band gap curve of (a) $Ni_{0.8}Ag_{0.2}Fe_2O_4$ and (b) $Ni_{0.6}Ag_{0.4}Fe_2O$

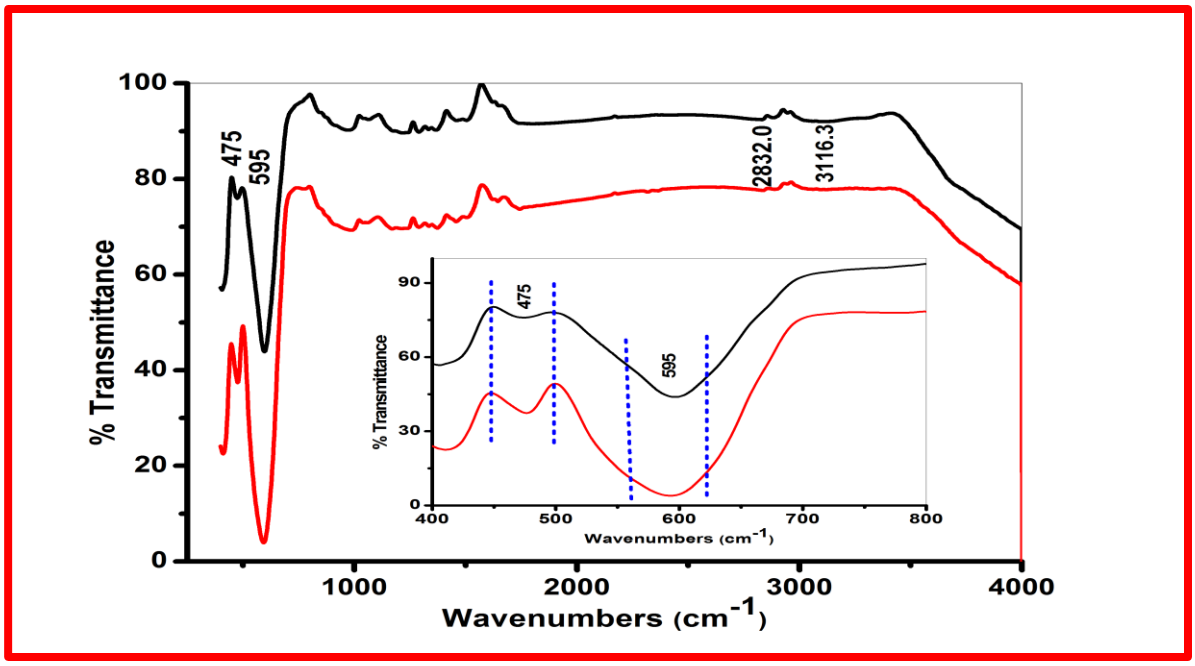

Fig.6.8 FTIR curve of of $Ni_{0.8}Ag_{0.2}Fe_2O_4$ and $Ni_{0.6}Ag_{0.4}Fe_2O_4$

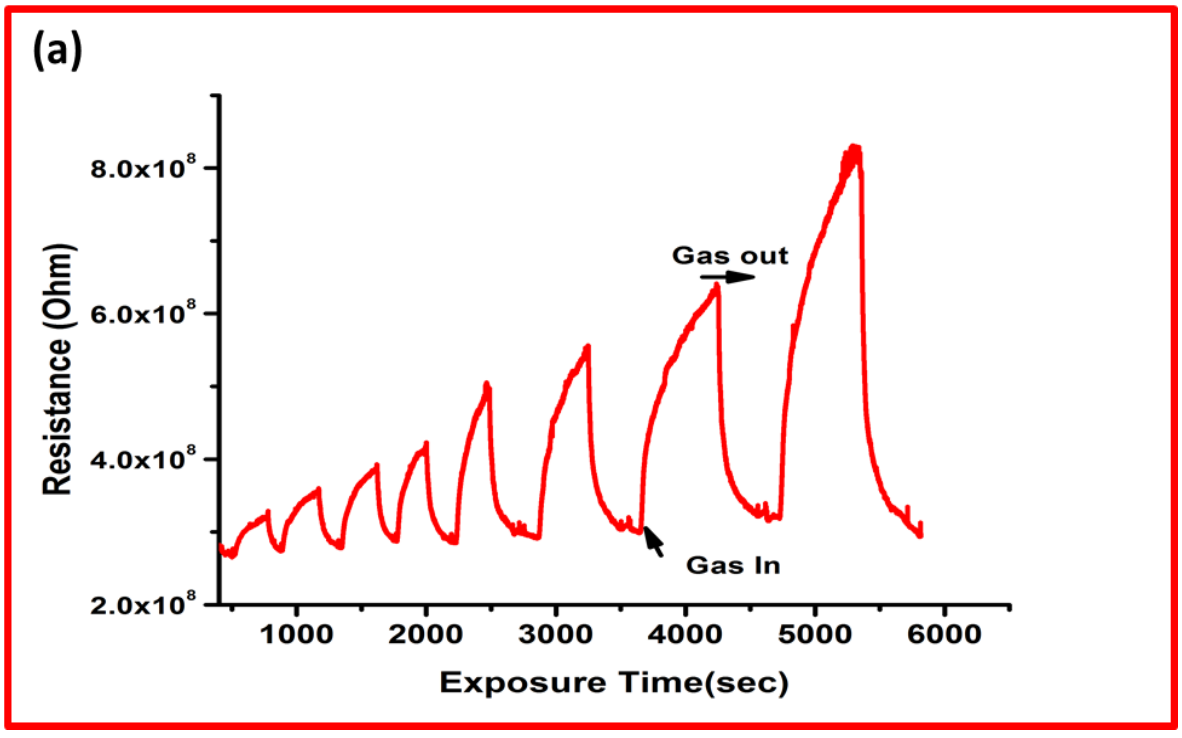

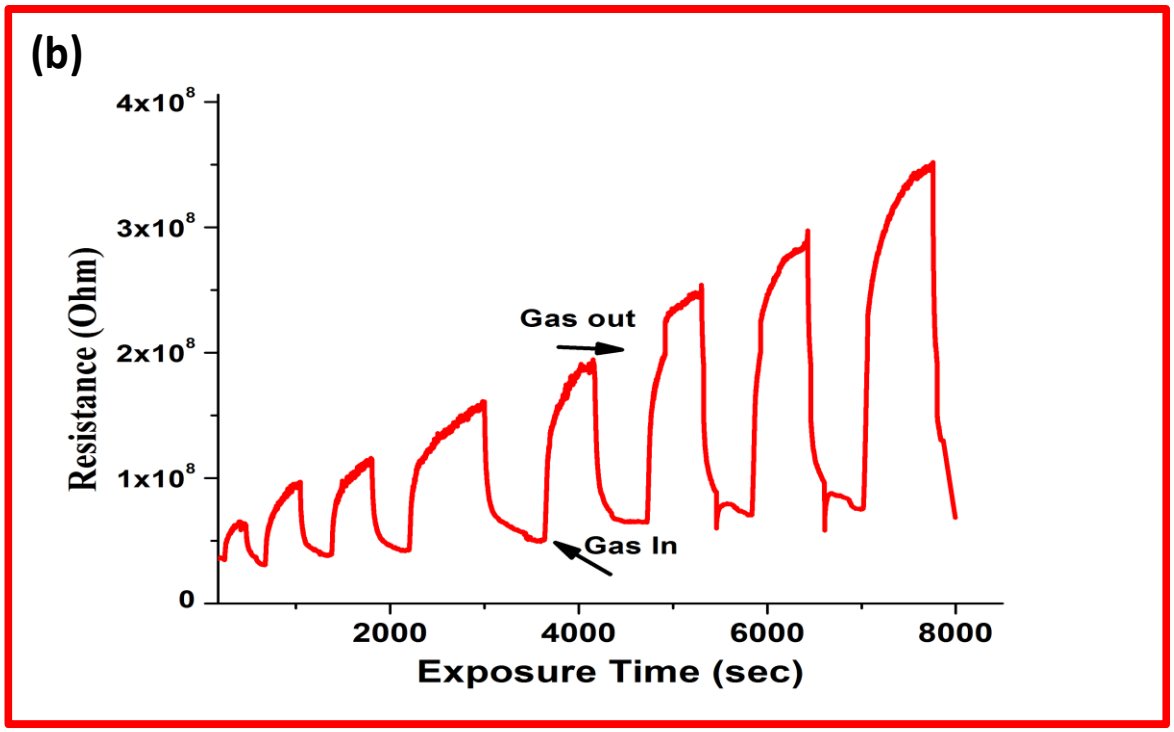

Fig.6.9 Gas sensing properties of $Ni_{0.8}Ag_{0.2}Fe_2O_4$ and $Ni_{0.6}Ag_{0.4}Fe_2O_4$

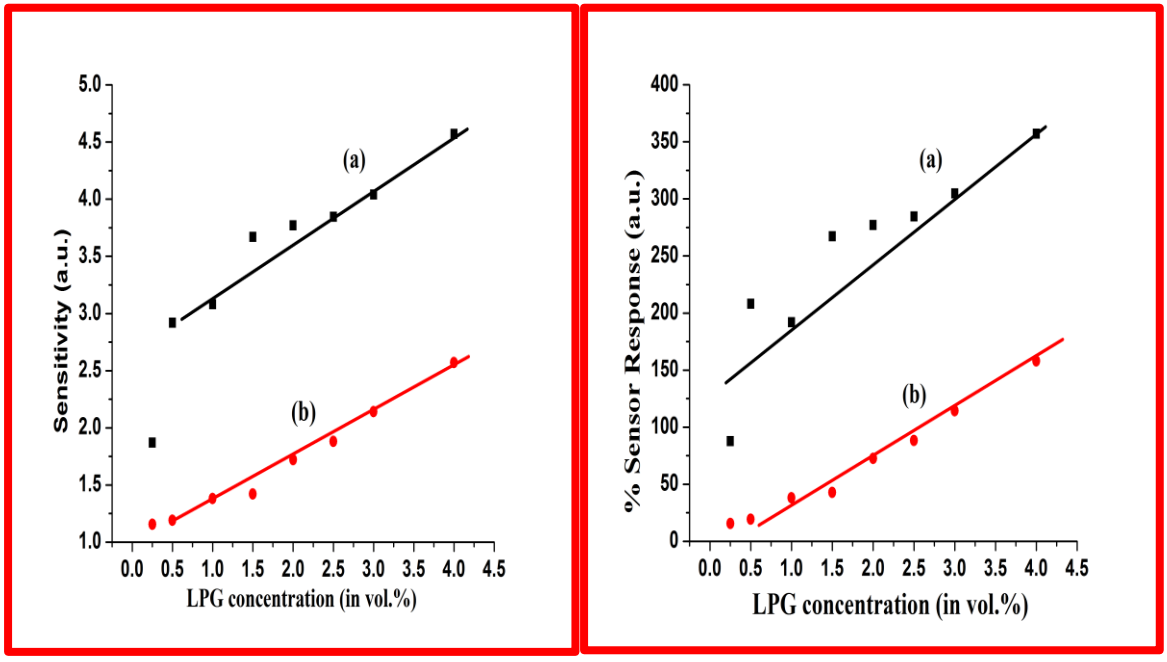

Fig.6.10 % Sensor response and Sensitivity curve of $Ni_{0.8}Ag_{0.2}Fe_2O_4$ and $Ni_{0.6}Ag_{0.4}Fe_2O_4$

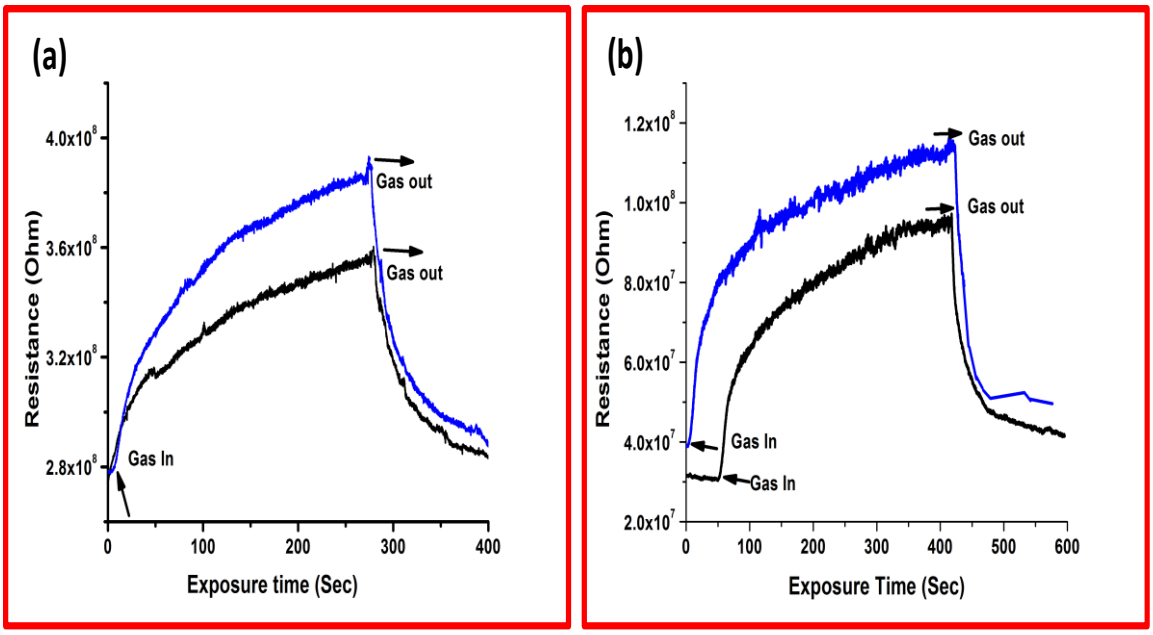

Fig.6.10 (a) & (b) Aging effect of $Ni_{0.8}Ag_{0.2}Fe_2O_4$ and $Ni_{0.6}Ag_{0.4}Fe_2O_4$ after 2 weeks

S. No.	LPG concentration (vol.%)	% Sensor Response	Sensitivity
1	0.25	15.64	1.156
2.	0.5	19.36	1.19
3	1	38.06	1.38
4	1.5	42.70	1.42
5	2	72.59	1.72
6	2.5	88.18	1.88
7	3	114.3	2.14
8	4	157.89	2.57

S. No.	LPG concentration (vol.%)	% Sensor Response	Sensitivity
1	0.25	87.82	1.87
2.	0.5	192.01	2.92
3	1	208	3.08
4	1.5	267.16	3.67
5	2	277.2	3.77
6	2.5	284.57	3.84
7	3	304.74	4.04
8	4	357.15	4.57

Table.6.1 LPG parameters of $Ni_{0.8}Ag_{0.2}Fe_2O_4$ and $Ni_{0.6}Ag_{0.4}Fe$

Chapter 7

Conclusion and Scope of Further Research Work

This chapter summarizes the results obtained from preparation and fabrication of thin film sensors, characterization and its LPG sensing properties at room temperature below Lower Explosive Limit. This chapter also gives the guidelines for future research work in the field of dielectric, magnetic and mechanical properties of ferrites and multiferroic and its application as Liquefied Petroleum Gas sensor.

CHAPTER 7

CONCLUSION AND SCOPE OF FURTHER RESEARCH WORK

7.1 Conclusion

Nanoscale materials are the materials having nanometer dimension and the scientific study of these objects, therefore, refers to the materials with sub-nanometer dimension and the scientific study of these objects are known as Nanoscience. It deals with the novel phenomenon of preparing, measuring its property and manipulating the dimension of an object up to the order of nanometer scale. Nanotechnology deals with using nanomaterials to develop products for practical application and for miniaturization of electronic devices. The maximum number of atoms lies on the surface of the nanoparticle which possesses huge surface energy and causes unstable or metastable stage. So there is a change in its chemical, mechanical, and optical properties resulting in the increase in the surface area per unit mass. This increased surface area made the nanomaterial for versatile application in electronic and technical industry.

Ferrites belong to a special class of magnetic material consisting of metal oxide particles and ferric oxide particles as their main compositions. The magnetic, electric and dielectric behaviours possessed by them have made ferrites more attractive to the current field of science and technology and from the research point of view. These important properties of ferrite find applications in micro-electric devices, magnetic switches, sensors, microwave devices, electromagnetic circuits, transformer core, optoelectronic devices, antenna rods and in the field of medicines for drug delivery to chemotherapy, etc. Generally, ferrites are ferrimagnetic materials having iron oxide as their main component along with the other metal oxides. The vast scope of ferrites and their composites for sensing applications may improve the working efficiency of liquefied petroleum gas sensors at room temperature. The large surface morphology, porosity, and reduced size of the nano materials are the properties of a reliable and a stable sensor. The pore plays a vital role in adsorption and desorption kinematics of the gas sensing phenomenon. Reduction of

the Fe^{+3} ion to Fe^{+2} ion increases the efficiency of the ferrite-based sensor by changing its electronic properties. This reduction enhances the efficiency of the LPG sensor.

In view of this, the Chapter 1 deals about the nanoscience and nanotechnology of spinel and orthoferrite materials along with the introduction of LPG sensor. Detailed investigation on nanostructured perovskite type Barium titanate thin film with synthesis, characterization and application as LPG sensor is depicted in Chapter 2. In Chapter 3, the synthesis, characterization and LPG sensing properties of nanostructured hexagonal Strontium ferrite thin film is described. Chapter 4 reports the study of liquefied petroleum gas sensing properties of lead-free Bismuth sodium titanate prepared by the sol-gel method at room temperature. In Chapter 5, fabrication of perovskite Lanthanum ferrite film by sol-gel and its gas sensing properties has been demonstrated. Chapter 6 describes the synthesis of porous Ag-substituted $NiFe_2O_4$ which were applied as LPG sensing material and has been demonstrated. A study of synthesis, characterization and LPG sensing properties of perovskite Barium titanate, hexagonal Strontium ferrite, lead-free Bismuth sodium titanate, perovskite Lanthanum ferrite and Ag-substituted $NiFe_2O_4$ is summarized in Chapter 7. This chapter also gives the guidelines for further research work in the field of spinel and orthoferrites materials and their applications as LPG sensor.

A study of synthesis, characterization and LPG sensing properties of $BaTiO_3$, $SrFe_{12}O_{19}$, $Bi_{0.5}$ $Na_{0.5}TiO_3$, $LaFeO_3$ and Ag-substituted $NiFe_2O_4$ is concluded as below:

7.1.1 Synthesis and characterization of perovskite Barium titanate thin film and its application as LPG Sensor

Nanostructured Barium titanate was synthesized by sol-gel method and thin film was prepared by spin coating technique. XRD, FTIR and Raman studies confirmed the formation of barium titanate and minimum size was calculated as 11 nm from XRD. SEM and TEM were used for surface morphological and phase analysis. Particle size calculated by TEM was varied from 6-30 nm. Optical characterization was done and band gap was found as 3.9 eV. The peak at 540 cm^{-1} in Raman spectra confirmed the formation of $BaTiO_3$. FTIR revealed the information about the bond stretching between the molecules. The film of barium titanate was further used as LPG sensor. The value of maximum sensitivity was found 3.5 and percentage sensor response was 250% for 4 vol.% LPG. The

linear sensing characteristic curve showed that the $BaTiO_3$ based LPG sensor is quite appropriate for developing a commercial LPG sensor operable at room temperature.

7.1.2 Detection of Liquefied Petroleum Gas below lowest explosion limit (LEL) using nanostructured hexagonal Strontium ferrite thin film

Nanostructured strontium ferrite was successfully synthesized by coprecipitation and followed by sol-gel spin coating method. The XRD revealed the formation of hexagonal strontium ferrite and the minimum crystallite size was found as 18 nm. Peaks in FTIR spectra between 400 cm^{-1} to 600 cm^{-1} elucidated the characteristic peak of hexaferrite. The SEM image showed the macroporous film with complex magnetoplumbite structure. TEM confirmed the hexagonal structure of the material with a minimum grain size < 20 nm. The value of maximum sensitivity was found as ~ 7 and % sensor response was ~ 602.23 for 5 vol.% LPG. The linear sensing characteristic of strontium ferrite-based LPG sensor is quite appropriate for developing a LPG sensor below LEL operable at room temperature.

7.1.3 Study of Liquefied Petroleum Gas sensing properties of lead-free Bismuth sodium titanate prepared by sol-gel method

BNT powder was successfully synthesized by sol-gel method and a thin film on the glass substrate was prepared by spin coating method. XRD, FTIR and Raman confirm the formation of BNT and minimum crystallite size was calculated as 9 nm. Thermal analysis was done through TGA. The microstructural analysis was done by TEM, SEM and EDX. Optical characterization was done and band gap was found 5.4 eV. FTIR revealed the information about the bond stretching between the molecules through transmittance spectra. Study of Liquefied petroleum gas sensing properties of BNT was carried out. The value of maximum sensitivity was found 2.158 and percentage sensor response was found 115.84 % for 3 vol.% LPG. Minimum response time was found 22 s for 0.25 vol.% of LPG which is quite appropriate for developing a commercial LPG sensor operable at room temperature.

7.1.4 Fabrication of perovskite Lanthanum ferrite film by sol-gel and its gas sensing properties

Nanostructured Lanthanum ferrite film was prepared by facile sol-gel method followed by spin coating technique. The XRD confirmed the perovskite structure of the Lanthanum ferrite and the minimum crystallite size was found as 8 nm with an average size of 19 nm. Peaks in FTIR spectra between 433 cm^{-1} to 573 cm^{-1} showed the characteristic peak for perovskite material. The SEM image disclosed the macroporous film with agglomerated structure. HRTEM confirmed the polycrystalline nature of the material with a grain size <10 nm. The minimum grain size of the particle was observed as 2.8 nm. The value of maximum sensitivity was found ~ 3.3 and % sensor response was ~ 231 for 3.3 vol.% LPG. The response time was found of 12 s and recovery time 14 s for 0.25 vol.% of LPG.

7.1.5 Ag (x = 0.2, 0.4) substituted Nickel ferrite thin film and its application as LPG sensor below LEL

Nanostructured $Ni_{0.8}Ag_{0.2}Fe_2O_4$ and $Ni_{0.6}Ag_{0.4}Fe_2O_4$ were successfully synthesized by sol-gel method and thin films were deposited on glass substrates. The films prepared were characterized by XRD, SEM, FTIR, UV-visible spectroscopy and Raman. The comparison in their microstructures were observed by SEM. Micrographs obtained, exhibited the better surface morphology of 0.45 Ag-substituted nickel ferrite than 0.2% Ag-substituted nickel ferrite. As Ag substitution increases, the porosity of material was found to be increased. XRD revealed the crystalline phase of Ag-substituted nickel ferrite. Similarly, there was a change in energy band gap from 5.3 to 5.4 eV and also in the optical behaviour of the samples. The maximum sensitivity was found 2.57 and 4.57 with % sensor response of 157.8 and 357.14 for 4 vol.% of LPG. The investigated LPG sensor produced a repeatable curve one after the other experiment hence this sensor was more reliable and a next step towards the development of a LPG sensor at commercial scale.

A chapter wise sketch of the Thesis including the sensing materials, dopants, band gap, sensitivity, crystallite size, average grain size, pore size is depicted in Table 7.1. The

main target of our research work was to design and fabricate an LPG sensor which would be robust, cost effective and more sensitive than previously reported sensors.

Table 7.1 A chapter wise sketch of the Thesis

Chapter No.	**Materials**	**Method of Preparation**	**Band Gap (eV)**	**Particle Size**	**Sensitivity/% Sensor Response**	**Response time**
Chapter 1	**Introduction**	**Method Used**	**Band gap**	**Particle size**	**Sensitivity/ % Sensor response**	**Response Time**
Chapter 2	$BaTiO_3$	Sol-gel	3.9 eV	11 nm	3.50/ 250.85	30 s
Chapter 3	$SrFe_{12}O_{19}$	Chemical Precipitation	3.2 eV	18 nm	7.02/ 602	40 s
Chapter 4	$Bi_{0.5}Na_{0.5}TiO_3$	Sol-gel	5.4 eV	9 nm	2.15/ 115.4	22 s
Chapter 5	$LaFeO_3$	Sol-gel	5.3 eV	8 nm	3.31/ 231	12 s
Chapter 6	Ag-substituted $NiFe_2O_4$	Sol-gel	5.3 & 5.4 eV	6 nm & 7 nm	2.57/ 157.89 & 4.57/ 357.15	10 s & 30 s
Chapter 7	Conclusion and future Scope	…….	……	……	…….	……

From the Table 7.1, we infer that Ag-substituted $NiFe_2O_4$ and $LaFeO_3$ are excellent materials as its response time is fast and produces better sensitivity for LPG sensing application at room temperature. Using these materials a commercialized model of LPG sensor applicable for both indoor and outdoor detection may be designed. Thus various configurations/systems described in the Thesis and the detailed specifications given for each of them are expected to prove useful in fabricating a sturdy, robust and cost-effective

LPG sensor suitable for operation over the entire range; from lower explosive limit (LEL) to upper explosive limit (UEL), even below LEL also.

7.2 Scope of Further Research Work

Future research works that would be productive in further understanding the role of nano-oxides for low-temperature applications are desirable. These include incorporation of the recovery aspects achieved by the incorporation of catalyst onto the surface of a nano-oxide being used to detect a reducing gas.

1. In the present work, Ag doping was done in Nickel ferrite structure and had been optimized to improve the sensing parameters, while there is scope for integration of modifiers like of similar radius or some nanocomposite or CNT's for reducing the response and recovery times of LPG sensor.
2. An effort may also be made for the synthesis of ferrites and multiferroic materials using other methods and their sensing applications.
3. The magnetic and dielectric behaviour of spinel and orthoferrites are an interesting area. So attention may be a focus on the twin character of ferrites.
4. The effects of higher annealing temperature on the thin films, substrate, doping, substitution, magnetic field, pH, along with the stability of material may be studied in future.
5. Detailed analysis of the evolution of the surface reactions with respect to temperature needs to be carried out, in order to exactly understand the reaction products from the surface interaction.
6. Growth simulations and reconstructions of the different surface species under different synthesis conditions would give rise to even more specific engineering of nanomaterials than what is currently known to the world of research within nanotechnology. Spectroscopic evaluation of the sensing mechanism has been important in future research.

Appendix

Experimental Methods and Characterization Techniques

The experimental techniques used throughout the whole work for the preparation and characterization of the nanomaterial and sensor are over-viewd in this part. The synthesis of ferrites and its composition was performed by sol-gel and co-precipitation method. Thin film was prepared by spin coating method. For the identification, the prepared sample was characterizated by XRD, SEM, EDX, TEM, UV-Visible spectroscopy, FTIR, Raman, particle size analysis techniques etc.. Further the variation of resistance corresponding to LPG concentration was observed by high resistance Keithley Electrometer.

EXPERIMENTAL METHODS AND CHARACTERIZATION TECHNIQUES

A.1.1 Introduction

The methodology and various experimental techniques used in the synthesis and modification of spinel ferrite, pervoskite and its nanocomposite thin films have been described. XRD, SEM, FTIR, TEM, BET, particle size analyzer and UV-Vis spectroscopy were used to characterize these films. A large number of techniques has been employed for getting the overall information about the properties, structure, shape and size, topology, composition etc. of the specimen. Some of the techniques which have been used in this thesis work is described in detail in this chapter.

A.1.2 Methodology of Present Work

Following steps were carried out for the present investigation:

1. Preparation and fabrication of the thin film
2. Characterizing techniques used for the optimization of the characteristics of the film to know phase, structure, size, functional group, band gap etc of the film are as follows:
    a) XRD: XRD is used for the study of phase identification and structural properties. It is also used to find particle size and grain size.
    b) SEM: SEM technique is used to know the surface morphology of the ferrite thin
    c) TEM: TEM is used to obtain the topography of the sample which deals with the internal structure of the sample, and its grain distribution and size of the particle.
    d) FTIR: FTIR technique is used for the identification of the types of the functional group present in the sample and type of chemical bonds shared by the molecules.

e) UV-Visible spectroscopy: This spectroscopy will provide information about the absorption spectra and about the band gap of the sample.

f) Raman Analysis: It is used for identifying the sample along with the nature of molecular vibrational bonds present in the molecules the sample.

g) Particle size analyzer: It is used to find out the average particle size of the sample.

h) Keithley Electrometer: It is used for measuring the resistance of the film.

A.1.3 Methods

A.1.3.1 Sol-gel Technique

Sol gel is the simplest, versatile, low temperature and economically cheap technique to prepare ferrites of the desired shape like spherical, cylindrical, flower like structure, petal like structure, etc. Colloids are the solid particle of any salt, oxide etc with dia 1-100 nm. When the colloidal particles are dispersed in liquid then the solution obtained is called 'So'l. 'Gel' is the interconnected rigid network ordered or disordered polymeric chain. Fig 1 shows the schematic diagram of the Sol-gel method.

Sol gel is the process of preparation of sol by dissolving metal alkoxide, inorganic salt in a suitable solvent. Hydrolysis followed by condensation are the two reactions that is carried out in whole sol-gel technique. When MOR alkoxide, where M is a metal ion, O is oxygen and R is organic group dissolved in an alcoholic solvent, the OR group which is highly electronegative in nature creates a partial positive charge metal ion. Due to the high reactivity of alkoxide into the water, water molecule attack central metal ion and thus how hydrolysis process takes place. The whole kinematics in the sol-gel process is dependant on the ratio of molar concentration (k) of alkoxide to water. For thin film formation the value of k is low (< 3) and to obtain powder value of k is large (>3). Catalyst also plays

an important role in the sol-gel process. Some base catalysts are amines, KOH, ammonia etc and some acid catalysts are HCl, HF, acetic acid, etc.

In brief, sol-gel is a controlled process for the preparation of the ferrite, easy to modify and disperse dopant. But every good thing has few limitations too as it requires significant effort and time to optimize stability and durability of the prepared sol.

A.1.3.2 Co-precipitation Method

Co- precipitation method is a convenient method for the synthesis of nanomaterial in a bulky amount. When the precipitator is added in the solution consisting of various multiple ions formation of the hydrate, hydrate oxide or salt form through precipitation. These oxide powder is further washed out and subsequently by hydrogenation. Ionic equilibrium of the solution is hindered by the precipitator and super saturation condition is observed. Solubility product K_{sp} for the solid precipitate C_aA_b (s), is written in expression form:

$$C_aA_b\,(s) = a\,C + bA$$

$$K_{sp} = [C]^a\,[A]^b$$

Where [A] and [C] are the unit of moles per liter. K_{sp} is the value of max. ion product formed at equilibrium condition for a given temperature.

To synthesize the narrow sized distribution nanoparticles there are some following requirements:

(1) The degree of supersaturation must be high,

(2) Spatial concentration distribution must be uniform side, the beaker in which the process takes place,

(3) There must be a uniform growth time for the particles,

(4) Accuracy should be maintained on synthesis parameters like concentration of metal ion, pH, precipitating agent, aging time, etc.

Chemical co-precipitation is widely used in industry and research to synthesize complex metal oxides such as $BaTiO_3$, $FeTiO_3$, $ZnFe_2O_4$, etc. An important advantage of this process is its simplicity. Atomic mixing of the constituents by chemical co-precipitation yields a final product of near perfect stoichiometry without high-temperature treatments. The final crystalline oxide is obtained by firing the precipitates at higher temperature. Colloidal chemistry plays a significant role in the precipitation of powders from solution. In chemical co-precipitation, the main control factor that causes individual particles bond to form larger agglomerates is an inter-particle force. The rate of agglomeration is largely dependent on the rate of particle collision per unit time. The collisions are caused by Brownian motion, thermal convection and shear forces. Shear forces caused by stirring is the main source of collisions in the co-precipitation process.

A.1.4 Fabrication Techniques for Thin Film

A.1.4.1 Spin Coating method

Spin coating is the technique used for several decades to prepare a thin film from a sol-gel. It is used to get the homogeneous thin film. In this method, a small amount of fluid (resin) is put onto the center of the substrate and that substrate is put on the arm rotator and for a small time interval approx. 30 sec the rotator is allowed to spin at 3000 Rpm. The value of rpm is set as per our need. Due to spin centripetal acceleration is produced which help the resin to distribute uniformly on the substrate so that it covers the edges of the substrate also. The thickness of the film and other properties depends on the viscosity of

the resin, rpm rate, time interval, surface tension, drying rate, single layering multi layering, substrate, etc.

A.1.4.2 Type of dispense technique used in spin coating method

Dispense of the resin plays an important factor in the preparation of thin film. For this, the substrate must be cleaned by ultrasonic clean. Then after loading the substrate on spin coater, the main task starts. There are two ways to dispense the resin fluid on the substrate these are as follows:

(a) **Static resin**: Static dispense is deposition of a small puddle of resin fluid on the center of the substrate. Highly viscous and larger substrate is needed in this process. Spinning speed is higher in this process. It also requires a large amount of fluid to cover the whole substrate and due to high spinning rate the fluid is waste.

(b) **Dynamic resin**: In this process speed of the arm rotator is slow around 500 rpm to 1000 rpm. This is more advantageous than static resins chances of void formation is low in this method. In this less amount of fluid is required and due to low speed, the wastage of fluid around the rotator is less.

A.1.5 Thin Film Characterization Techniques

Synthesis of Spinel ferrite, orthoferrite and its nano composite thin films were characterized by various characterization techniques such as XRD, SEM, TEM, FTIR, UV-Visible, Raman and particle size analyzer to study the phase identification, surface morphology, optical properties, and also the electrical properties.

A.1.5.1 Structural Characterization

A.1.5.1.1 X-ray Diffraction (XRD)

A.1.5.1.1.1 XRD Features and Basic principle

Max von Laue, in 1912, discovered that crystalline substances act as three-dimensional diffraction gratings for X-ray wavelengths similar to the spacing of planes in a crystal lattice. X-ray diffraction is now a common technique for the study of crystal structures and atomic spacing. X-ray diffraction is based on constructive interference of monochromatic X-rays and a crystalline sample. These X-rays are generated by a cathode ray tube, filtered to produce monochromatic radiation, collimated to concentrate, and directed toward the sample. The interaction of the incident rays with the sample produces constructive interference satisfying the Bragg's Law ($2d \sin \theta = 2n\lambda$). This law relates the wavelength of electromagnetic radiation to the diffraction angle and the lattice spacing in a crystalline sample. These diffracted X-rays are then detected, processed and counted. By scanning the sample through a range of 2θ angles, all possible diffraction directions of the lattice should be attained due to the random orientation of the powdered material. Conversion of the diffraction peaks to d-spacings allows identification of the mineral because each mineral has a set of unique d-spacings. Typically, this is achieved by comparison of d-spacings with standard reference patterns.

All diffraction methods are based on the generation of X-rays in an X-ray tube. These X-rays are directed at the sample, and the diffracted rays are collected. A key component of all diffraction is the angle between the incident and diffracted rays. Powder and single crystal diffraction vary in instrumentation beyond this.

A.1.5.1.1.2 Crystallite size calculation

The XRD spectra have been used to calculate the crystallite size by Scherrer's formula

$$D = \frac{K\lambda}{\beta cos\theta} \quad (1)$$

Where D is crystallite size, k is polarization factor, λ is the wavelength of CuK_α line and β is the full width half maximum (FWHM) of reflection peak and is the Bragg's angle about the peak. The value of crystallite size be calculated.

A.1.5.1.1.3 Applications:

X-ray powder diffraction is most widely used for the identification of unknown crystalline materials (e.g. minerals, inorganic compounds). Determination of unknown solids is critical to studies in geology, environmntal science, material science, engineering and biology.

Other applications include:

- Characterization of crystalline materials
- Identification of fine-grained minerals such as clays and mixed layer clays that are difficult to determine optically
- Determination of unit cell dimensions
- Measurement of sample purity.

With specialized techniques, XRD can also be used to:

- Determine crystal structures using Rietveld refinement
- Determine of modal amounts of minerals (quantitative analysis)
- Characterize thin films samples by:

- Determining lattice mismatch between film and substrate and to inferring stress and strain
- Determining dislocation density and quality of the film by rocking curve measurements
- Measuring super lattices in multilayered epitaxial structures
- Determining the thickness, roughness and density of the film using glancing incidence X-ray reflectivity measurements.

- Make textural measurements, such as the orientation of grains, in a polycrystalline sample.

A.1.5.1.1.4 Energy Dispersive Spectroscopy

The SEM is also capable of performing analyses of selected point locations on the sample; this approach is especially useful in qualitatively or semi-quantitatively determining chemical compositions (using EDS), crystalline structure, and crystal orientations. The design and function of the SEM is very similar to the EPMA(Electron micro probe Ananyser) and considerable overlap in capabilities exists between the two instruments. EDX is a qualitative tool for the detection of X-ray microanalysis. This means it gives the analysis based on the output signal of the height of the energy counts. EDX gives result in digitalized form. The X-axis represents Energy provided through the channel while Y-axis represents a number of counts. X-ray produces ionization and a solid state detector with better resolution is used to detect the information and further its result in terms of chemical composition which is further analyzed by the analyzer .

It performs the qualitative analysis by line identification and by qualitative ED analysis:

(a) **Line Identification:** line identification method is used to know the unknown specimen present in the sample by comparing the wavelength or energy of the spectrum from X-ray Spectrum.

(b) **Qualitative ED analysis**: In this, identification is done by superposition of the line spectra of the sample with the recorded spectra. The information of the results obtained is in tabular form or graphs or database.

A.1.5.2 Optical Characterization

A.1.5.2.1 UV- Visible Spectroscopy

Ultraviolet-visible spectroscopy (UV/ VIS) is the type of absorption spectroscopy which covers 200- 400 nm ranges. It is a spectral method which is used for the determination of the structure of the molecule. involves the spectroscopy of photons in the UV-visible region. It elucidates electronic properties by combining NMR and IR region. It uses light in the visible and adjacent near ultraviolet (UV) and near infrared (NIR) ranges. In this region of the electromagnetic spectrum, molecules undergo electronic transitions. UV/Vis spectroscopy is routinely used in the quantitative determination of solutions of transition metal ions and highly conjugated organic compounds. Solutions of transition metal ions can be colored (i.e., absorb visible light) because electrons within the metal atoms can be excited from one electronic state to another. The color of metal ion solutions is strongly affected by the presence of other species, such as certain anions or ligands. In the Fig.A.1.1.5 given below electronic transitions have been shown.

A.1.5.2.1.1 Basic Principle and Features of UV- Visible Spectroscopy

The principle of UV- visible is based on the electronic transition which occurs between the molecules containing π-electrons or nonbonding electrons (n-electrons). These π and n electrons can excite to higher anti bonding molecular orbital by absorption of energy in the energy in ultraviolet or visible light. When the electrons are excited more easily (i.e. lower energy gap between the HOMO and the LUMO), the wavelength of the absorbed light will be longer. This is the diagram showing the allowed transition that occurs in this phenomenon.

A.1.5.2.1.2 Instrumentation and block diagram of UV- Visible Spectroscopy

In a standard UV-Vis spectrophotometer, a beam of light is split; one-half of the beam (the sample beam) is directed through a transparent cell containing a solution of the compound being analyzed, and one-half (the reference beam) is directed through an identical cell that does not contain the compound but contains the solvent. The instrument is designed so that it can make a comparison of the intensities of the two beams as it scans over the desired region of the wavelengths. If the compound absorbs light at a particular wavelength, the intensity of the sample beam will be less than that of the reference beam. Absorption of radiation by a sample is measured at various wavelengths and plotted by a recorder to give the spectrum which is a plot of the wavelength of the entire region versus the absorption of light at each wavelength**.** And the band gap of the sample can be obtained by plotting the graph between ($\alpha h\nu$ vs $h\nu$) and extrapolating it along the x-axis**.** Ultraviolet and visible spectrometry are almost entirely used for quantitative analysis; that is, the estimation of the amount of a compound known to be present in the sample. The sample is usually examined in solution form.

A.1.5.2.2 Fourier Transform Infrared (FTIR) Spectroscopy

FTIR is most useful for identifying chemicals that are either organic or inorganic. It can be utilized to get information of some components of an unknown mixture. It can be applied to the analysis of solids, liquids, and gasses. The term Fourier Transform Infrared Spectroscopy (FTIR) refers to a fairly recent development in the manner in which the data is collected and converted from an interference pattern to a spectrum. Today's FTIR instruments are computerized which makes them faster and more sensitive than the older dispersive instruments.

FTIR can be used to identify chemicals from spills, paints, polymers, coatings, drugs, and contaminants. FTIR is perhaps the most powerful tool for identifying types of chemical bonds (functional groups). The wavelength of light absorbed is characteristic of the chemical bond as can be seen in this annotated spectrum. By interpreting the infrared absorption spectrum, the chemical bonds in a molecule can be determined. FTIR spectra of pure compounds are generally so unique that they are like a molecular "fingerprint". While organic compounds have very rich, detailed spectra, inorganic compounds are usually much simpler. For most common materials, the spectrum of an unknown can be identified by comparison to a library of known compounds. WCAS has several infrared spectral libraries including online computer libraries. To identify less common materials, IR will need to be combined with nuclear magnetic resonance, mass spectrometry, emission spectroscopy, X-ray diffraction, and/or other techniques.

Molecular bonds vibrate at various frequencies depending on the elements and the type of bonds. For any given bond, there are several specific frequencies at which it can vibrate. According to quantum mechanics, these frequencies correspond to the ground state

i.e. lowest frequency and several excited states i.e. higher frequencies. One way to cause the frequency of a molecular vibration to increase and to excite the bond by absorbing the light energy. For any given transition between two states, the light energy (determined by the wavelength) must exactly equal the difference in the energy between the two states [usually ground state (E_0) and the first excited state (E_1)].

Difference in the energy state = energy absorbed

$$E_1 - E_0 = hc/\lambda$$

Where,

h is the Planck's constant

c is the velocity of the light

λ is the wavelength of the light

2.5.4.2 Raman Analysis

A.1.5.4.2.1. Features and basic principle of Raman Spectroscopy

Raman spectroscopy provides information about molecular vibrations that can be used for sample identification. The technique involves shining a monochromatic light source (i.e. laser) on a sample and detecting the scattered light. The majority of the scattered light is of the same frequency as the excitation source; this is known as Rayleigh or elastic scattering. A very small amount of the scattered light (10^{-5}% of the incident light intensity) is shifted in energy from the laser frequency due to interactions between the incident electromagnetic waves and the vibrational energy levels of the molecules in the sample. Plotting the intensity of this "shifted" light versus frequency results in a Raman spectrum of the sample. Generally, Raman spectra are plotted with respect to the laser frequency such that the Rayleigh band lies at 0 cm^{-1}. On this scale, the band positions will lie at

frequencies that correspond to the energy levels of different functional group vibrations. The Raman spectrum can thus be interpreted similarly to the infrared absorption spectrum.

- When radiation passes through a transparent medium, the species present scatter a fraction of the beam in all directions.
- In 1928, the Indian physicist C. V. Raman discovered that the visible wavelength of a small fraction of the radiation scattered by certain molecules differs from that of the incident beam and furthermore that the shifts in wavelength depend upon the chemical structure of the molecules responsible for the scattering.
- The theory of Raman scattering shows that the phenomenon results from the same type of quantized vibrational changes that are associated with infrared absorption. Thus, the difference in wavelength between the incident and scattered visible radiation corresponds to wavelengths in the mid-infrared region.
- The Raman scattering spectrum and an infrared absorption spectrum of a given species often resemble one another quite closely.

A.1.5.4.2.2. Terminologies and basic component needed in instrumentation

When a monochromatic laser light with frequency υ_0 excites molecules and transforms them into oscillating dipoles. Such oscillating dipoles emit light of three different frequencies.A photon with frequency υ_0 is absorbed by a Raman-active molecule which at the time of interaction is in the basic vibrational state. Part of the photon's energy is transferred to the Raman-active mode with frequency υ_m and the resulting frequency of

scattered light is reduced to $\upsilon_0 - \upsilon_m$. This Raman frequency is called Stokes frequency, or just "**Stokes**".

- A photon with frequency υ_0 is absorbed by a Raman-active molecule, which, at the time of interaction, is already in the excited vibrational state. The excessive energy of excited Raman active mode is released, molecule returns to the basic vibrational state and the resulting frequency of scattered light goes up to $\upsilon_o + \upsilon_m$. This Raman frequency is called Anti-Stokes frequency, or just "**Anti-Stokes**".
- A molecule with no Raman-active modes absorbs a photon with the frequency υ_0. The excited molecule returns back to the same basic vibrational state and emits light with the same frequency υ_0 as an excitation source. This type of interaction is called an elastic **Rayleigh scattering**.

A Raman system typically consists of four major components:

1. Excitation source (Laser).
2. Sample illumination system and light collection optics.
3. Wavelength selector (Filter or Spectrophotometer).
4. Detector (Photodiode array, CCD).

A.1.5.4.2.2 Advantages of Raman Spectroscopy

Raman scattering is a spectroscopic technique that is complementary to infrared absorption spectroscopy. Raman offers several advantages over mid-IR and near-IR spectroscopy, including:

- Little or no sample preparation is required
- Water is a weak scatterer - no special accessories are needed for measuring aqueous solutions
- Water and CO_2 vapors are very weak scatterers - purging is unnecessary
- Inexpensive glass sample holders are ideal in most cases
- Fiber optics (up to 100's of meters in length) can be used for remote analyses
- Since fundamental modes are measured, Raman bands can be easily related to chemical structure
- Raman spectra are "cleaner" than mid-IR spectra - Raman bands are narrower, and overtone and combination bands are generally weak
- The standard spectral range reaches well below 400 cm^{-1}, making the technique ideal for both organic and inorganic species
- Raman spectroscopy can be used to measure bands of symmetric linkages which are weak in an infrared spectrum (e.g. -S-S-, -C-S-, -C=C-).

A.1.5.4.2 Raman Analysis

A.1.5.4.2.1 Features and basic principle of Raman Spectroscopy

Raman spectroscopy provides information about molecular vibrations that can be used for sample identification and quantitation. The technique involves shining a monochromatic light source (i.e. laser) on a sample and detecting the scattered light. The

majority of the scattered light is of the same frequency as the excitation source; this is known as Rayleigh or elastic scattering. A very small amount of the scattered light (ca. 10^{-5}% of the incident light intensity) is shifted in energy from the laser frequency due to interactions between the incident electromagnetic waves and the vibrational energy levels of the molecules in the sample. Plotting the intensity of this "shifted" light versus frequency results in a Raman spectrum of the sample. Generally, Raman spectra are plotted with respect to the laser frequency such that the Rayleigh band lies at 0 cm^{-1}. On this scale, the band positions will lie at frequencies that correspond to the energy levels of different functional group vibrations. The Raman spectrum can thus be interpreted similarly to the infrared absorption spectrum.

- When radiation passes through a transparent medium, the species present scatter a fraction of the beam in all directions.
- In 1928, the Indian physicist C. V. Raman discovered that the visible wavelength of a small fraction of the radiation scattered by certain molecules differs from that of the incident beam and furthermore that the shifts in wavelength depend upon the chemical structure of the molecules responsible for the scattering.
- The theory of Raman scattering shows that the phenomenon results from the same type of quantized vibrational changes that are associated with infrared absorption. Thus, the difference in wavelength between the incident and scattered visible radiation corresponds to wavelengths in the mid-infrared region.
- The Raman scattering spectrum and an infrared absorption spectrum of a given species often resemble one another quite closely.

A.1.5.3 Surface Morphological Characterization

A.1.5.3.1 Transmission Electron Microscopy (TEM)

Transmission Electron Microscopy (TEM) has become a mainstay in the repertoire of characterization techniques for materials scientists. Priebus and Hiller in 1938 built the first TEM whose magnification was 400000 times easier than many other objects. TEM's gives high lateral spatial resolution and its capability to provide both image and diffraction information from a single sample. It gives 2-dimensional Image with three-dimensional reconstructions. In addition, the highly energetic beam of electrons used in TEM interacts with sample matter to produce characteristic radiation and particles; these signals often are measured to provide materials characterization using EDS**,** backscattered and secondary electron imaging, to name a few possible techniques.

A.1.5.3.1.1 Principle, Construction and Working of TEM

. In TEM, a focused electron beam is an incident on a thin (less than 200 nm) sample. The signal in TEM is obtained from both undeflected and deflected electrons that penetrate the sample thickness. A series of magnetic lenses at and below the sample position are responsible for delivering the signal to a detector, usually a fluorescent screen, a film plate, or a video camera. Accompanying this signal transmission is a magnification of the spatial information in the signal by as little as 50 times to as much as a factor of 10^6. This remarkable magnification range is facilitated by the small wavelength of the incident electrons and is the key to the unique capabilities associated with TEM analysis. TEM offers two methods of specimen observation, diffraction mode and image mode.

In the diffraction mode, an electron diffraction pattern is obtained on the fluorescent screen, originating from the sample area illuminated by the electron beam. The

diffraction pattern is entirely equivalent to an X-ray diffraction pattern: a single crystal will produce a spot pattern on the screen, a poly-crystal will produce a powder or ring pattern (assuming the illuminated area includes a sufficient quantity of crystallites), and a glassy or amorphous material will produce a series of diffuse halos.

The image mode produces an image of the illuminated sample area. The image can contain contrast brought about by several mechanisms: mass contrast, due to spatial separations between distinct atomic constituents; thickness contrast, due to non-uniformity in sample thickness; diffraction contrast, which in the case of crystalline materials results from scattering of the incident electron wave by structural defects; and phase contrast (see discussion later in this article). Alternating between image and diffraction mode on a TEM involves nothing more than the flick of a switch. The reasons for this simplicity are buried in the intricate electron optics technology that makes the practice of TEM possible.

There are a number of drawbacks to the TEM technique. Many materials require extensive sample preparation to produce a sample thin enough to be electron transparent, which makes TEM analysis a relatively time-consuming process with a low throughput of samples. The structure of the sample may also be changed during the preparation process. Also, the field of view is relatively small, raising the possibility that the region analyzed may not be characteristic of the whole sample. There is potential that the sample may be damaged by the electron beam, particularly in the case of biological materials.

A.1.5.3.1.3 Advantages of TEM

- TEM is used to characterize the specimen with high spatial resolution
- It gives crystallographic and morphology related information

- Very thin slice of the specimen is needed to identify the presence of atomic species.
- It is also used to detect crystalline defects by strain contrast formation.
- Its diffraction pattern is used to study the amorphous and crystallinity of the material.
- It gives higher magnifying resolution result in comparison to SEM.
- The SAED (Selected Area Diffraction) is used to determine the internal crystal structure and bravis lattice and lattice parameter of the specimen.

A.1.5.3.2 Scanning Electron Microscopy (SEM)

The scanning electron microscope (SEM) uses a focused beam of high-energy electrons to generate a variety of signals at the surface of solid specimens. The signals that derive from electron-sample interactions reveal information about the sample including external morphology (texture), chemical composition, and crystalline structure and orientation of materials making up the sample. The SEM is also widely used to identify phases based on qualitative chemical analysis and/or crystalline structure. Precise measurement of very small features and objects down to 50 nm in size is also accomplished using the SEM. Backscattered electron images (BSE) can be used for rapid discrimination of phases in multiphase samples. SEMs equipped with diffracted backscattered electron detectors (EBSD) can be used to examine micro fabric and crystallographic orientation in many materials.

A.1.5.3.2.1 Principle and Working of SEM

Accelerated electrons in a SEM carry significant amounts of kinetic energy, and this energy is dissipated as a variety of signals produced by electron-sample interactions when the incident electrons are decelerated in the solid sample. These signals

include secondary electrons (that produce SEM images), backscattered electrons (BSE), diffracted backscattered electrons (DBSE) that are used to determine crystal structures and orientations of minerals), photons (characteristic X-rays that are used for elemental analysis and continuum X-rays), visible light (cathodoluminescence–CL), and heat. Secondary electrons and backscattered electrons are commonly used for imaging samples: secondary electrons are most valuable for showing morphology and topography on samples and backscattered electrons are most valuable for illustrating contrasts in the composition in multiphase samples (i.e. for rapid phase discrimination). X-ray generation is produced by inelastic collisions of the incident electrons with electrons in discrete orbitals (shells) of atoms in the sample. As the excited electrons return to lower energy states, they yield X-rays that are of a fixed wavelength (that is related to the difference in energy levels of electrons in different shells for a given element). Thus, characteristic X-rays are produced for each element in a mineral that is "excited" by the electron beam. SEM analysis is considered to be "nondestructive"; that is, x-rays generated by electron interactions do not lead to volume loss of the sample, so it is possible to analyze the same materials repeatedly.

A.1.2.3.2.2 Scanning Electron Microscopy (SEM) Instrumentation:

Essential components of all SEMs include the following:

- Electron Source ("Gun")
- Electron Lenses
- Sample Stage
- Detectors for all signals of interest

- Display / Data output devices
- Infrastructure Requirements:
    - Power Supply
    - Vacuum System
    - Cooling system
    - Vibration-free floor
    - Room free of ambient magnetic and electric fields

SEMs always have at least one detector (usually a secondary electron detector), and most have additional detectors. The specific capabilities of a particular instrument are critically dependent on which detectors it accommodates.

A.1.2.3.2.3 Applications of SEM:

The SEM is routinely used to generate high-resolution images of shapes of objects (SEI) and to show spatial variations in chemical compositions:

- Acquiring elemental maps or spot chemical analyses using EDS,
- Discrimination of phases based on the mean atomic number (commonly related to relative density) using BSE.
- Compositional maps based on differences in trace element "activators" (typically transition metal and Rare Earth elements).

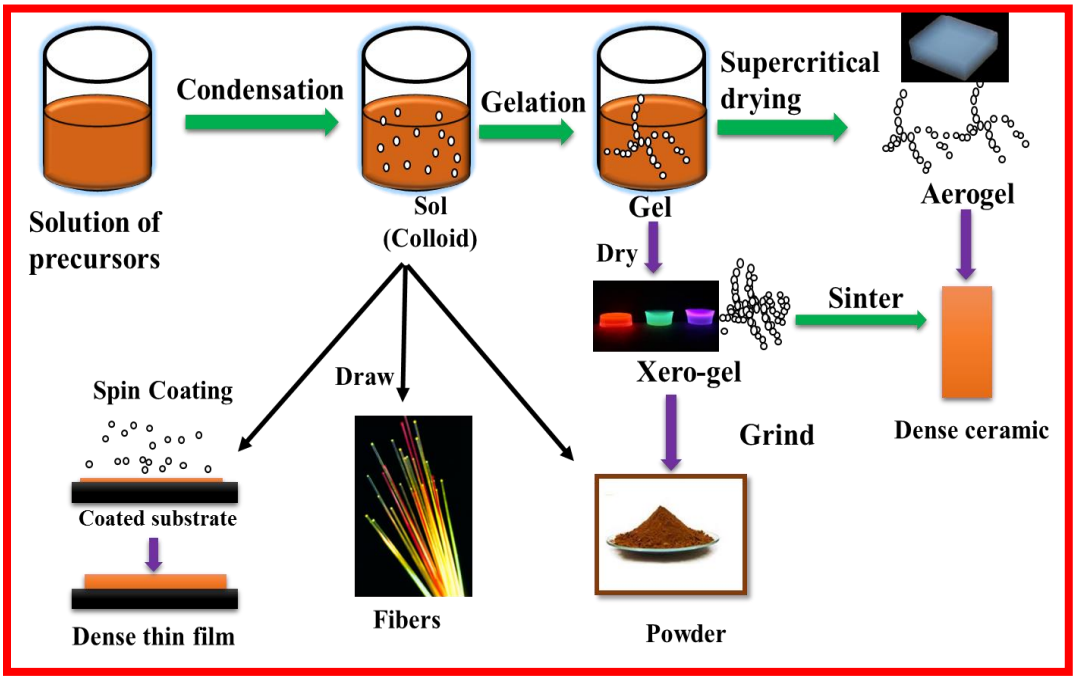

Fig.A.1.1 Schematic diagram of sol-gel process

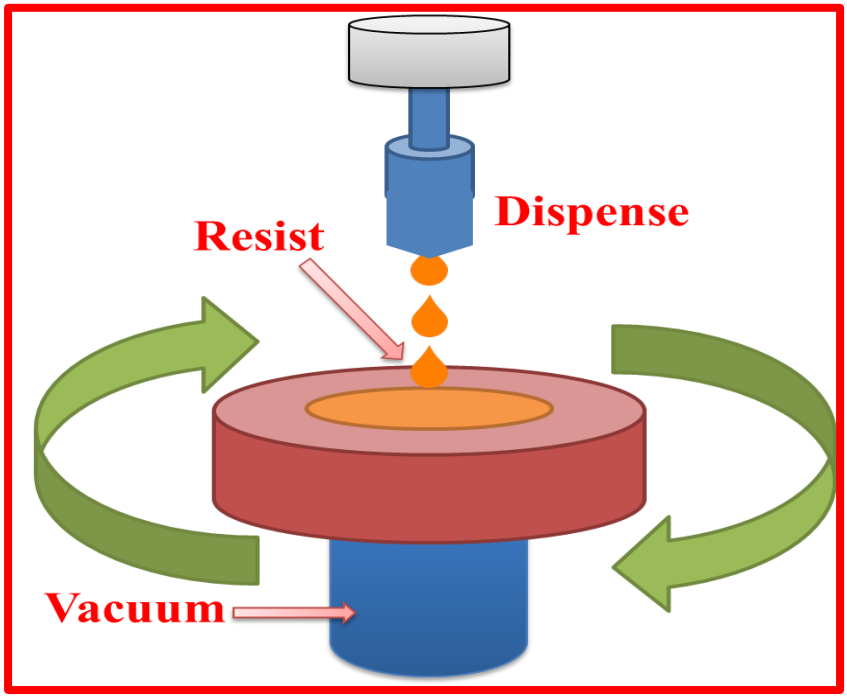

Fig. A.1.2 Schematic illustration of typical stage of spin coating process

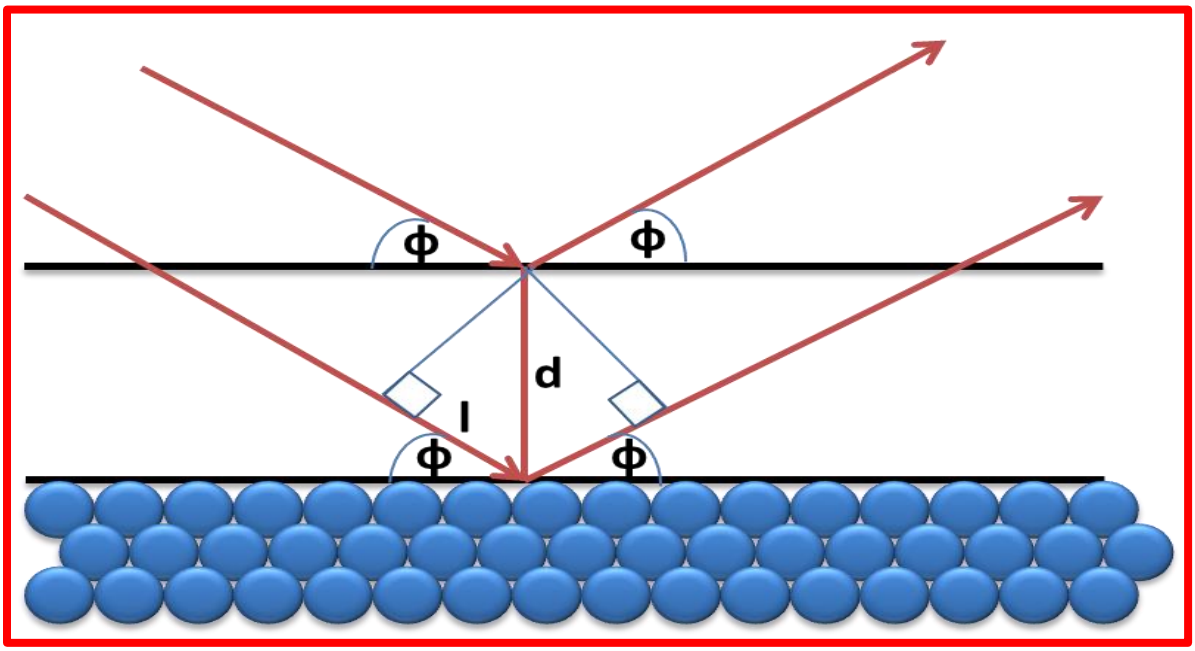

Fig.A.1.3 X-ray Diffraction occurs in two planes having phase difference

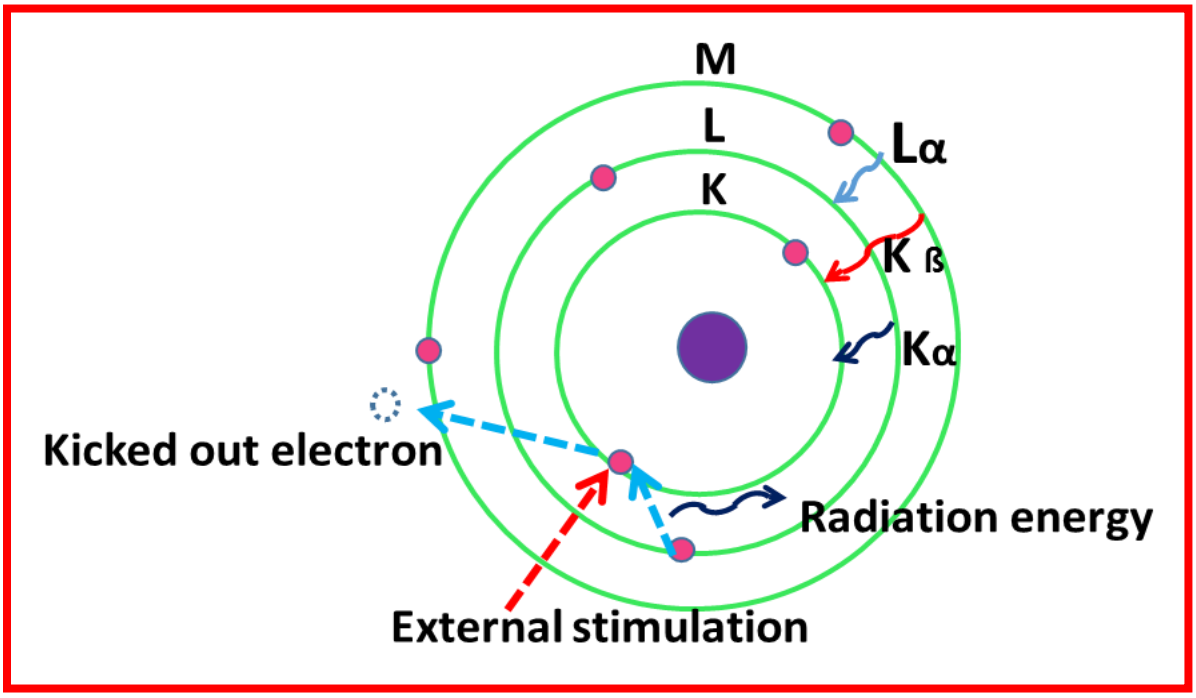

Fig.A.1.4 Generation of X-ray by electronic emission

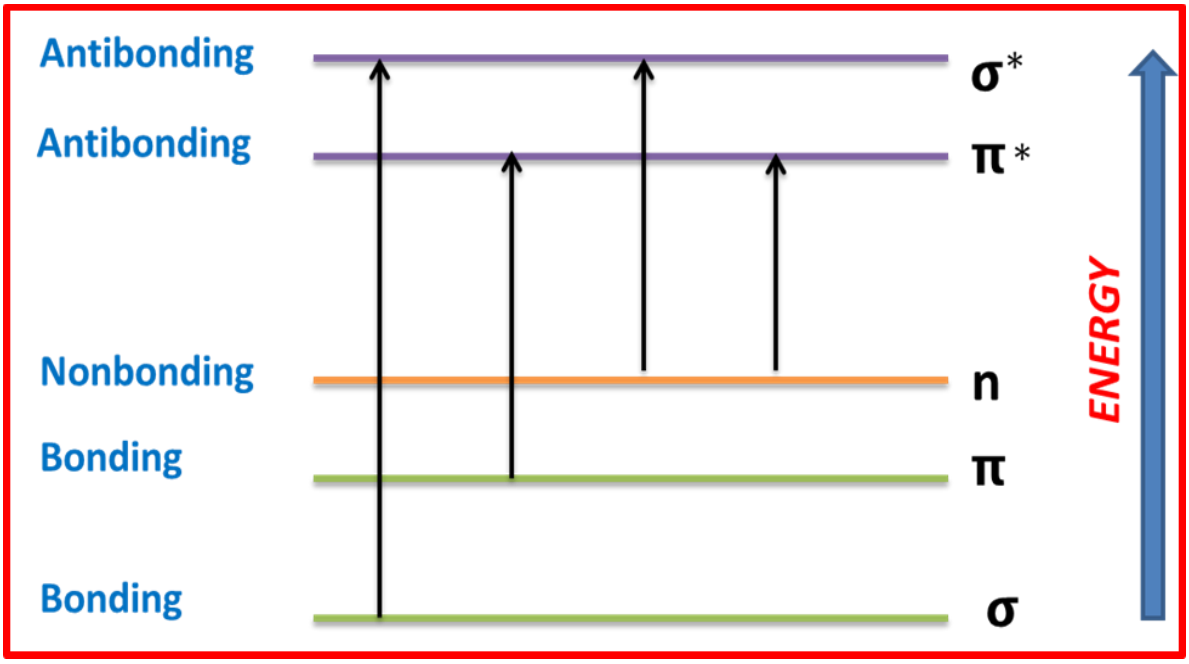

Fig.A.1.5 UV/ Vis Electronic Transitions

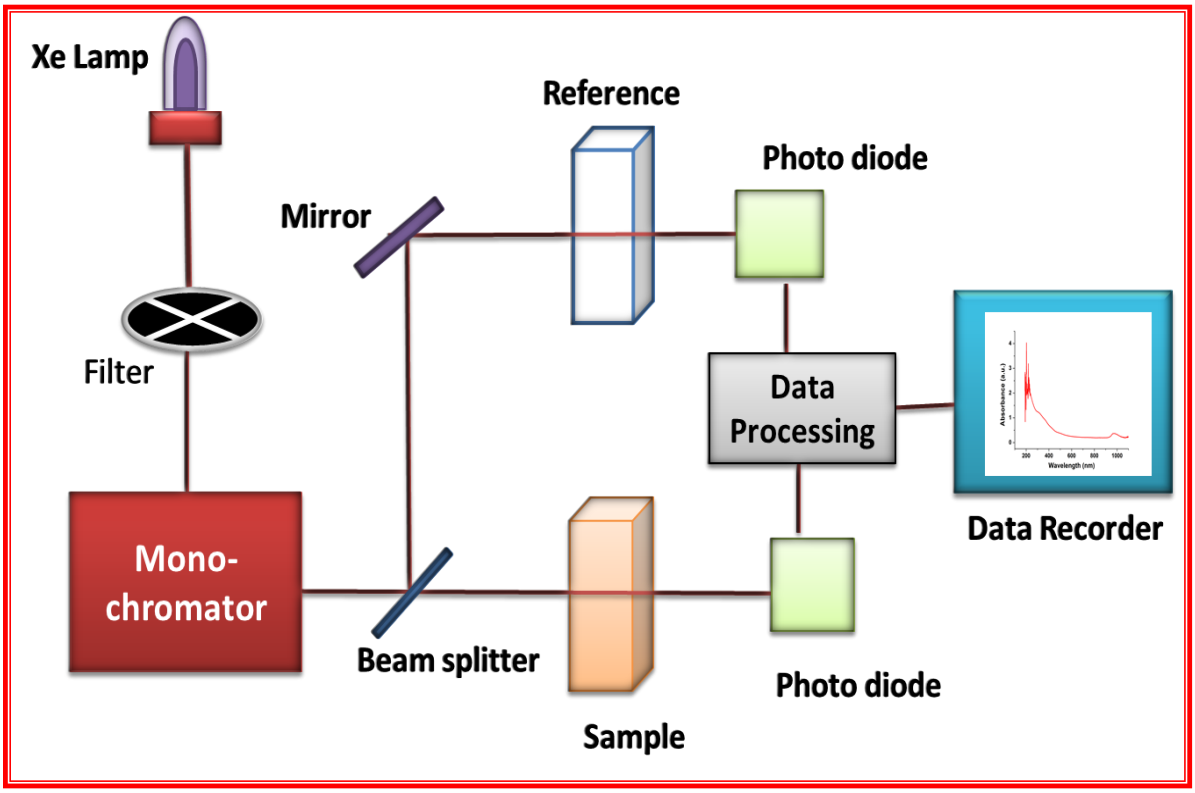

Fig. A.1.6 Schematic diagram of UV- vis spectrophotometer

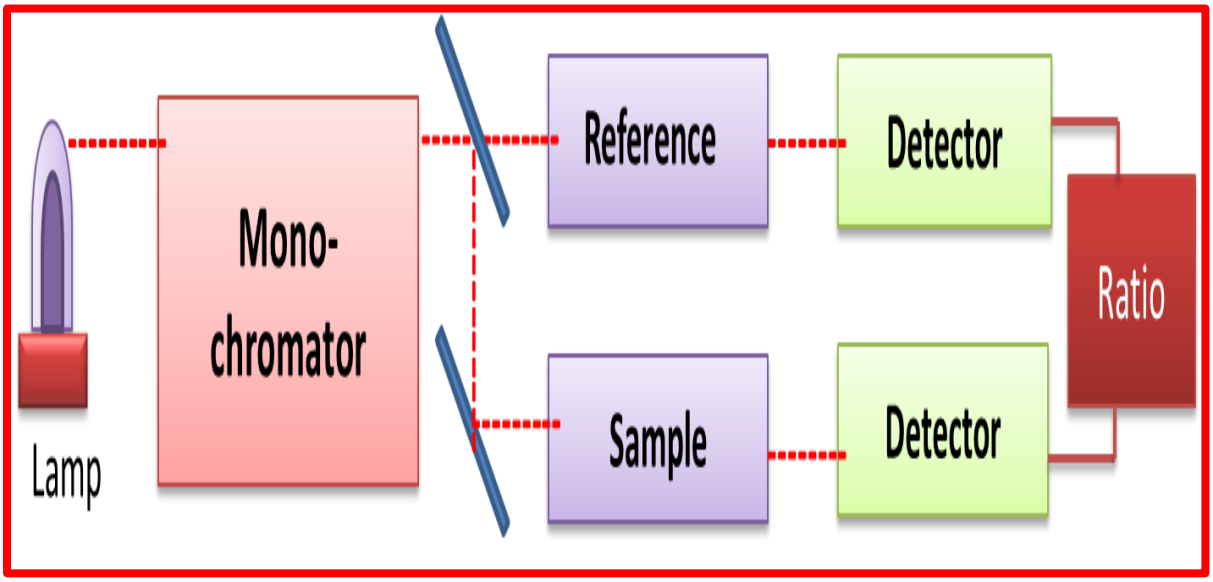

Fig.A.1.7 Block diagram of UV-vis Spectrophotometer

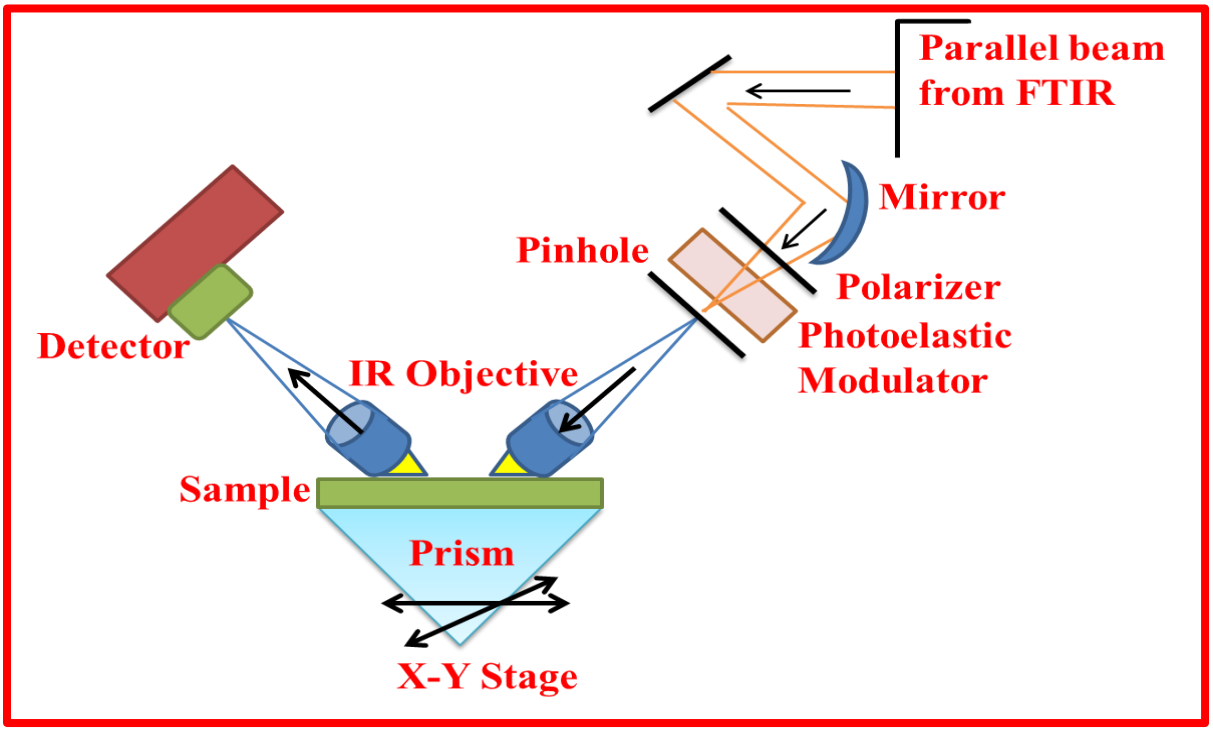

Fig.A.1.8 Schematic diagram of Fourier Transform Infrared (FTIR) Spectroscopy

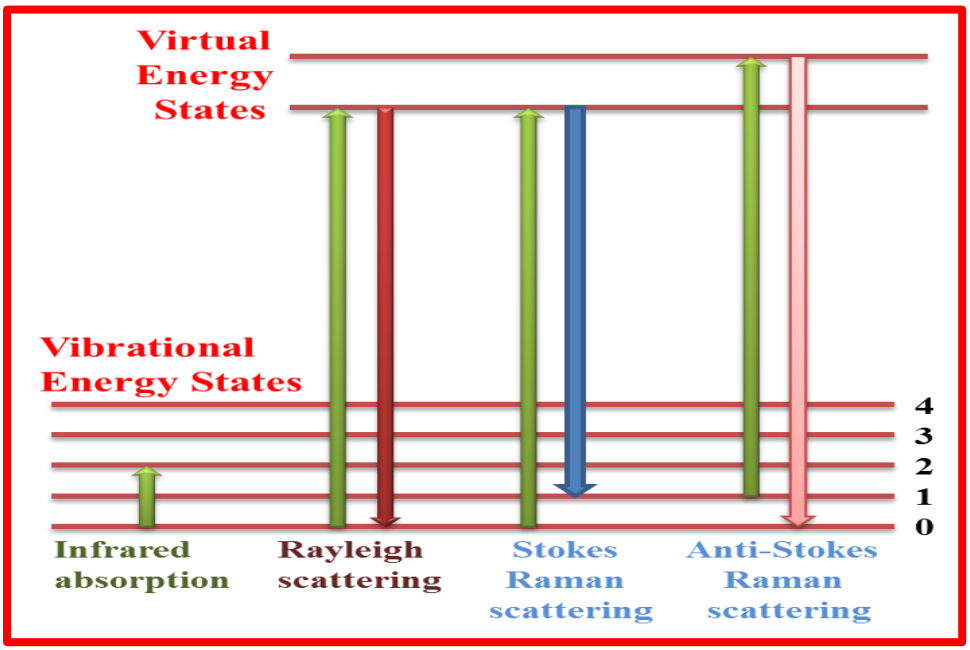

Fig.A.1.9 Emission of electrons in different type of scattering phenomenon

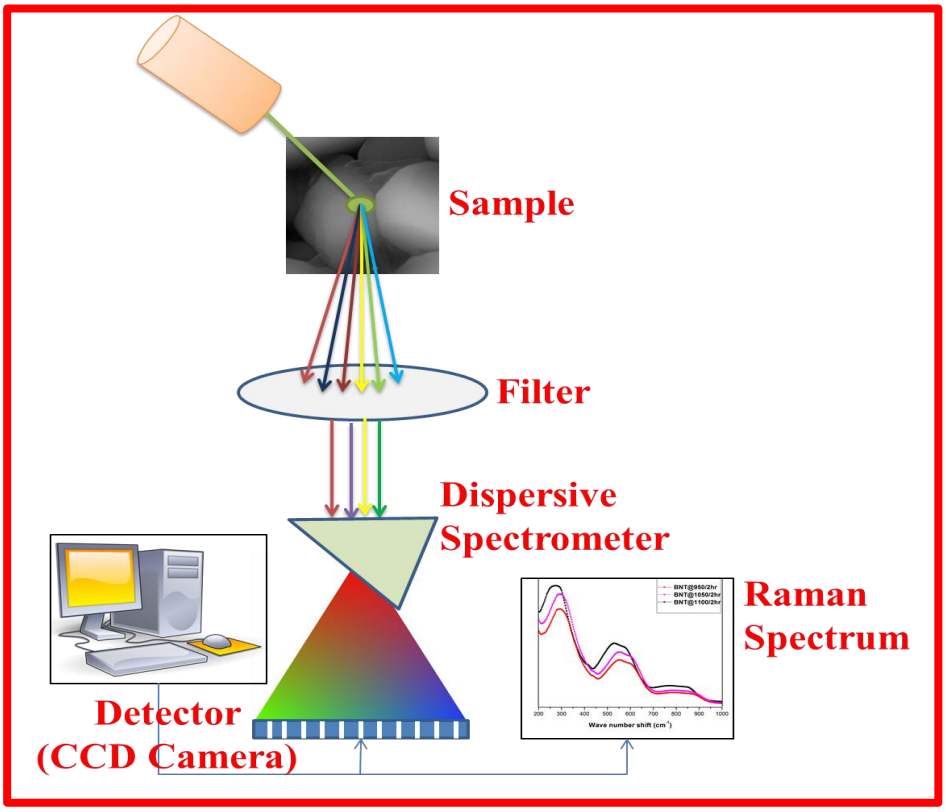

Fig.A.1.10 Schematic diagram of Raman spectroscopy

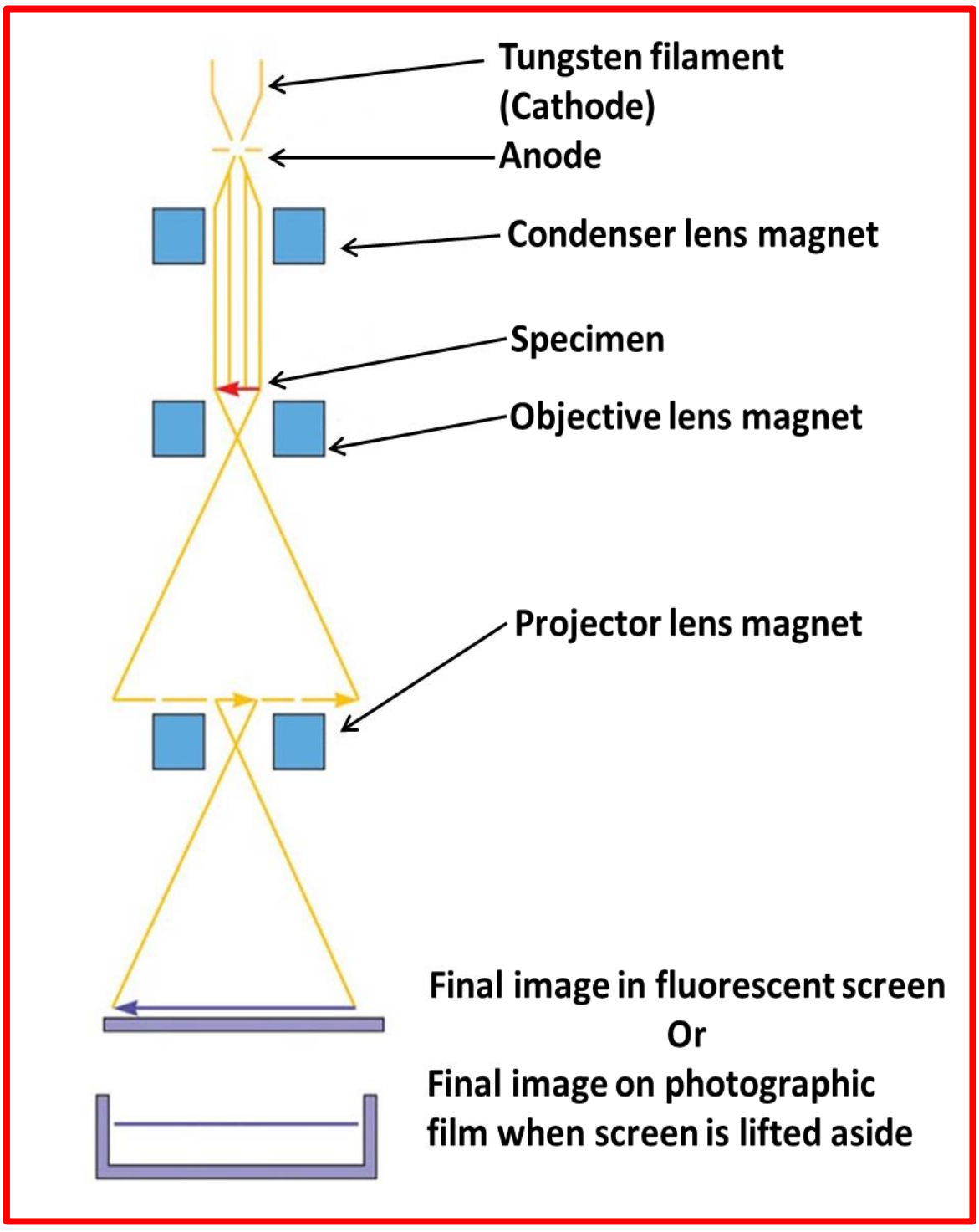

Fig.A.1.11 Schematic diagram of TEM

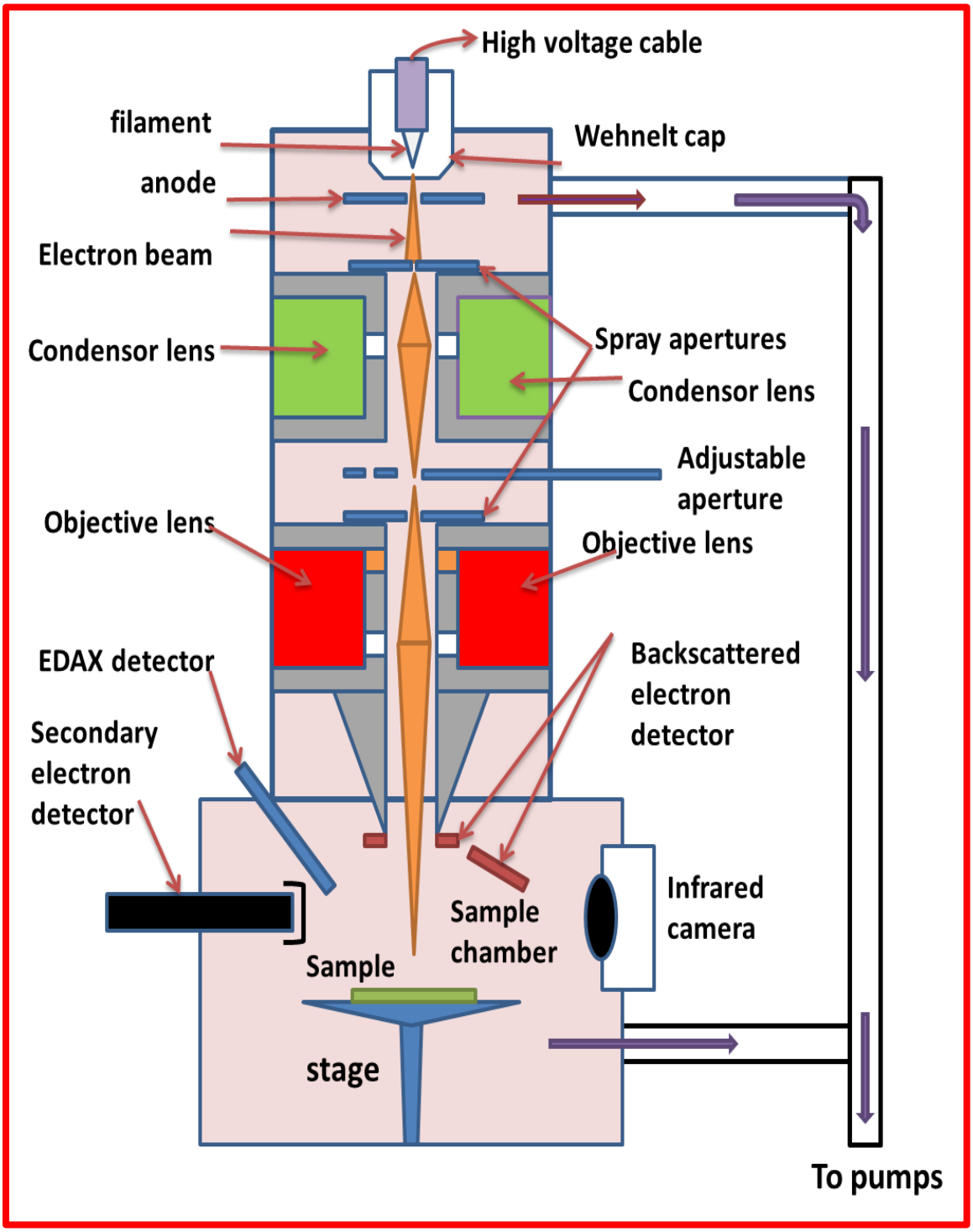

Fig. A.1.12 Schematic diagram of SEM

Sensors and Actuators B 241 (2017) 1170–1178

Contents lists available at ScienceDirect

Sensors and Actuators B: Chemical

journal homepage: www.elsevier.com/locate/snb

Synthesis and characterization of perovskite barium titanate thin film and its application as LPG sensor

Monika Singh [a], B.C. Yadav [a,*], Ashok Ranjan [b], Manmeet Kaur [c], S.K. Gupta [c]

[a] Nanomaterials and Sensors Research Laboratory, Department of Applied Physics, School for Physical Sciences, Babasaheb Bhimrao Ambedkar University, Lucknow 226025, India
[b] Department of Physics, University of Lucknow, Lucknow 226007, India
[c] Thin Film Division, Bhabha Atomic Research Centre, Mumbai, India

ARTICLE INFO

Article history:
Received 9 June 2016
Received in revised form
11 September 2016
Accepted 5 October 2016
Available online 6 October 2016

Keywords:
Perovskite
Barium titanate
Macroporous
LPG sensor

ABSTRACT

Perovskite barium titanate ($BaTiO_3$) nanocomposite thin film has been prepared using spin coating technique. Surface morphological, structural, compositional and optical properties of the film were investigated by various techniques such as SEM, XRD, TEM, EDS, UV-Spectroscopy, Raman spectroscopy and FTIR. SEM images showed the macroporous cubic structure of the film. The minimum crystallite size was evaluated as 11 nm by XRD and confirmed by TEM. Band gap of $BaTiO_3$ was evaluated as 3.9 eV. Raman Spectroscopy confirmed the formation of $BaTiO_3$ at 540 cm^{-1}. LPG sensings were carried out for vol.% 0.5–4 of LPG and sensor was found robust for the detection of LEL for LPG also.

1. Introduction

For more than 60 years barium titanate has attracted most of the researchers for practical interest and research work, due to its attractive properties. Rochelle salt and potassium dihydrogen phosphate instigated and accelerated the study on barium titanate. Then an era came when escalation in 100 of new ferroelectric materials occurred. Decade of 70's were known as the age of diversification in which concept of ferroelectric domain and its changing properties were studied and widely used in various applications [1,2].

$BaTiO_3$ is first piezoelectric perovskite ceramic transducer ever developed which is iso-structural with mineral perovskite ($CaTiO_3$) [3]. Perovskite consists of a transition metal ion in its centre with corner sharing of O_6 octahedral as shown in Fig. 1. Most of the ferroelectric pervoskite consists of non-magnetic transition element with empty d- shell. These non- magnetic elements form molecule by forming covalent bond with neighbouring oxygen ions. Barium titanate possesses a typical unit cell ABO_3 structure. A typical ABO_3 unit cell consists of corner linked network of oxygen octahedral with Ti^{4+} ion occupying B sites with octahedral cage and Ba^{2+} ions situated in A sites created by linked octahedral. Barium titanate is a ferroelectric perovskite ceramic which undergoes three phase transmission with its decreasing temperature from cubic phase to tetragonal and then from tetragonal to orthorhombic and from orthorhombic to Rhombohedral phase [4,5]. Chemically and mechanically $BaTiO_3$ is very stable as well as it exhibits ferroelectric properties at and above the room temperature.

Barium titanate is a porous ceramic formed by either ionic or covalent bonds. There are two type of porous ceramics i.e. reticulate ceramic and foam ceramic. Reticulate ceramic has voids surrounding by web of ceramic while foam ceramic has closed void into ceramic matrix [6]. Miniaturization of electronic devices enhanced the use of nanomaterial in daily life. Porous nanomaterials of $BaTiO_3$ have various applications in electro optics, laser frequency doubling, high capacitor memory cell, MEMS, MLC's, sensors, waveguide, etc [7]. Barium titanate also possesses amazing optical properties and ferroelectric polarization in presence of electric field so barium titanate is widely used in electro optics and photonic applications [8].

$BaTiO_3$ is used in photovoltaic devices. Conventional solar cell works on classical phenomenon of p–n junction but there were certain limitations such as lattice mismatch, band alignment etc. To overcome such problem ferroelectric photovoltaic cells are developed. $BaTiO_3$ is widely used as it is easy to sandwich between the electrodes to get rectifying behaviour and good performance solar

* Corresponding author.
E-mail addresses: balchandra_yadav@rediffmail.com, nano.bc71@gmail.com (B.C. Yadav).

http://dx.doi.org/10.1016/j.snb.2016.10.018
0925-4005/

Sensors and Actuators B 249 (2017) 96–104

Contents lists available at ScienceDirect

Sensors and Actuators B: Chemical

journal homepage: www.elsevier.com/locate/snb

Detection of liquefied petroleum gas below lowest explosion limit (LEL) using nanostructured hexagonal strontium ferrite thin film

Monika Singh[a], B.C. Yadav[a,*], Ashok Ranjan[b], Rakesh K. Sonker[a], Manmeet Kaur[c]

[a] Nanomaterials and Sensors Research Laboratory, Department of Applied Physics, School for Physical Sciences, Babasaheb Bhimrao Ambedkar University (A Central University), Lucknow 226025, U.P., India
[b] Department of Physics, University of Lucknow, Lucknow 226007, U.P., India
[c] Technical Physics Division, Bhabha Atomic Research Centre (BARC), Mumbai, M.H., India

ARTICLE INFO

Article history:
Received 10 November 2016
Received in revised form 11 April 2017
Accepted 12 April 2017
Available online 14 April 2017

Keywords:
Strontium ferrite
Co-precipitation method
Macroporous
LPG sensor

ABSTRACT

The nano crystalline hexagonal strontium ferrite nanoparticles $SrFe_{12}O_{19}$ were synthesized successfully by chemical co-precipitation method. Thin films of strontium ferrite were prepared on glass substrate and characterized by various techniques such as XRD, SEM, TEM, EDS, UV-spectroscopy and FTIR. XRD pattern revealed the phase transformation of M-type hexa-ferrite with the minimum crystallite size of 18 nm. Uniform macroporous surface structure of the film was exposed by SEM images. Existence of iron, strontium and oxygen in the material was confirmed by EDX. Optical characterization of the material was done by UV-Spectroscopy and band gap was found as 3.2 eV. The liquefied petroleum gas (LPG) sensing behavior of strontium ferrite film was investigated at room temperature. The variations in electrical resistance of the film were measured with the exposure of LPG with respect to time as a function of concentration (0.5–5 vol.%) of LPG. The maximum value of sensitivity for these films was found 7 and maximum sensor response was 602.23.

1. Introduction

Surface to volume ratio and quantum confinement elucidate to nanostructure of materials. Ferrites are basically a class of materials which contains iron oxides having fascinating magnetic and electric properties [1]. These are prepared by sintering various transition metal oxides along with the alkaline earth metal oxide. Development of new class of ferrites, and studies on improvements in their properties began in early 90's. On the basis of technological application, magnets are distinguished as soft magnetic materials and hard magnetic materials [2]. Soft magnetic materials are those magnetic materials whose domains shift when magnetic field is applied and hard magnetic materials are those with less mobility of domain wall. Magnetized hard ferrites possess hexagonal structure with high value of magnetization and magnetocrystalline anisotropy so these are termed as M phase ferrites, with M as Ba, Sr or Pb [3,4]. $SrO\text{-}Fe_2O_3$ binary system has few ternary oxides including $SrFe_{12}O_{19}$, $SrFe_2O_4$, $Sr_2Fe_2O_5$ and $Sr_3Fe_2O_6$. Among these, $SrFe_{12}O_{19}$ has attracted the attention of most of the researchers due to its vast area of applications beside a stable characteristic-sand having high electrical resistivity. Strontium ferrite contains strontium and iron where strontium is S block element belonging to group 2 period 5 with $5s^2$ electronic configuration and iron belonging to d-block element group 8 period 4 with electronic configuration $3d^64s^2$ [5]. Crystal structure of M-phase ferrite is complex but can be described as hexagonal with unique axis. $SrFe_{12}O_{19}$ posses 64 ions per unit cell along with 11 different symmerty sites. Oxygen atoms are closely packed at interstitial position with Sr and Fe in ten layers along with the C-axis. The iron atoms are positioned at five different crystallographic sites 2a, 2b, 4f, 4k and 12k. Among them 12k, 4k, 2a are on octahedral site, 4f on tetrahedral site and 2b forming trigonal bipyramid surrounding by five oxygen atoms. Strontium ferrite is used for LPG sensing because of relatively high resistance and special magnetic resonance properties for adsorption. In strontium ferrite, there are large interstitial sites which interact with the oxygen molecules in comparison to other ferrites. The dielectric properties of strontium ferrite shed light on the charge carriers which are responsible for charge transport phenomenon. These ferrites can be prepared by different methods viz. as chemical co-precipitation, sol-gel, ball milling, solid state reaction and reverse micelle process [6–10].

Kanagesan et al. prepared the strontium ferrite nano powder by sol-gel method and carried out investigation on the crystalline $SrFe_{12}O_{19}$ powder using XRD. The average particle size was found to be 80–100 nm and its thermal analysis revealed its endothermic and exothermic reaction peaks [11]. T.T.V. Nga et al. investigated

* Corresponding author.
E-mail address: balchandra_yadav@rediffmail.com (B.C. Yadav).

http://dx.doi.org/10.1016/j.snb.2017.04.075
0925-4005/

J Inorg Organomet Polym (2016) 26:1404–1412
DOI 10.1007/s10904-016-0425-4

Synthesis, Characterization of Nickel Ferrite and Its Uses as Humidity and LPG Sensors

Richa Srivastava[1] · B. C. Yadav[1] · Monika Singh[1] · T. P. Yadav[2]

Received: 15 May 2016 / Accepted: 22 July 2016 / Published online: 4 August 2016

Abstract Nanostructured nickel ferrites (sample B_1 and B_2) were synthesized by chemical precipitation method using two different precipitating agents; sodium and ammonium hydroxides. The samples were characterized by using powder X-ray diffraction, scanning and transmission electron microscopy techniques. The X-ray diffraction revealed the formation of nickel ferrite with lattice parameter a = 8.3 Å and the average crystallite sizes of the samples B_1 and B_2 were 50 and 15 nm respectively. Surface morphology of the sample B_2 exhibited the higher number of adsorption sites in comparison to B_1. Transmissions electron microscopy observations confirmed the formation of nanostructured nickel ferrite. Further the pellets, thick and thin films of materials B_1 and B_2 were prepared and investigated with the exposition of humidity and LPG. Maximum average sensitivity for humidity was formed as 53.74 MΩ/%RH. Also the maximum value of sensitivity was found 62.3 for 4 vol% of LPG. The results were found to be reproducible up to 96 % after 3 months. Response and recovery times for LPG sensing were found to be 220 and 250 s. Best sensitivity, less hysteresis, small activation energy and good reproducibility identify that fabricated humidity and LPG sensors (B_2) are promising and challenging.

Keywords Humidity · SEM · Sensitivity · LPG sensor · Nanostructure · Pores

✉ Richa Srivastava
richadolly@rediffmail.com; richadolly826@gmail.com

[1] Department of Applied Physics, Babasaheb Bheemrao Ambedkar University, Lucknow 226025, India

[2] Department of Physics, Banaras Hindu University, Varanasi 221005, India

1 Introduction

Effects of humidity on various materials are well known for a long time in many ways. It affects to mankind directly and indirectly both. The irreversible effect due to humidity eventually causes permanent damage to the exposed surfaces. Therefore, there is an essential need to measure and control precisely the humidity levels in various environments [1]. Generally, for magnetic or electrical applications, ferrites have been widely used [2]. But, there are new applications of materials as gas or humidity sensors, for which lower density and nanosized structures are preferred. As suggested by several authors [1, 2] nanosized grains of sensing materials are preferred due to increased specific surface area for exposure of gas. The ferrites have demonstrated to be excellent materials for gas and humidity sensors [3–10]. The synthesis of spinel ferrite nanoparticles has been studied in the recent years and the principal role of the preparation conditions on the morphological and structural features of the ferrites is discussed [4–20].

Nickel Ferrite ($NiFe_2O_4$) has a wide range of applications as magnetic material [10–19] with an inverse spinel structure with the Fe^{3+} cations equally distributed between the two kinds of sites, Ni^{2+} cations being located in octahedral sites and the magnetic ordering in the spinel structure of $NiFe_2O_4$ is ferromagnetic. These types of materials are also considered to be the most promising among highly sensing properties due to the temperature dependent surface morphology and photo catalytic activity [4, 8–12]. Spinel ferrites, with common formula of MFe_2O_4 (M: a divalent metal ion), have wide technological applications, e.g. in multilayer chip inductor (MLCI), ferrofluids, high-speed digital tape or recording disks, rod antenna, and humidity sensor [13–21]. Ferrite nanocrystals

J Inorg Organomet Polym
DOI 10.1007/s10904-016-0442-3

MWCNT Doped ZnO Nanocomposite Thin Film as LPG Sensing

Rakesh K. Sonker[1] · Monika Singh[1] · Utkarsh Kumar[1] · B. C. Yadav[1]

Received: 24 March 2016 / Accepted: 30 August 2016

Abstract A compound material of multi-walled carbon nanotubes (MWCNTs) coated with ZnO was synthesized at ambient conditions. The X-ray diffraction, UV–visible spectroscopy, scanning electron microscope (SEM) and transmission electron microscopy results confirmed that the existence of ZnO nanoparticles inside the MWCNTs. The gas sensing properties of the material were studied. ZnO-based composites on MWCNTs treated at room temperature shows enhanced performance as sensors, making them suitable for practical applications. Sensor structure showed a better sensing response (S ~61.57) at operating room temperature towards 1500 ppm LPG with an average sensitivity 41.95. Furthermore, the gas sensor responses increased linearly with the increment of the gas concentrations of LPG.

Keywords ZnO-MWCNT composite film · Chemical route · XRD · TEM · LPG sensing

1 Introduction

Liquefied Petroleum Gas (LPG), a blend of hydrocarbons mainly propane and butane is an explosive gas. The lower explosive limit (LEL) as specified by National Institute for Occupational Safety and Health (NIOSH) and Occupational Safety and Health Administration (OSHA) standards for chemical hazards is 21,000 ppm (2.1 % by volume in air) for propane and 19,000 ppm (1.9 % by volume in air) for butane. The permissible exposure limit (PEL) for LPG as specified by NIOSH and OSHA standards is 1000 ppm. LPG is primarily used as fuel for vehicles and as cooking gas for household applications. Precise monitoring of leakages of LPG even at low concentrations can be beneficial to prevent accidental explosions [1]. Sensors have become an integral part of the modern civilization owing to its significance, where metal oxides have played a major role as reliable sensor materials [2–5]. Zinc oxide (ZnO), a wurtzite n-type semiconductor which is in its different forms with unique properties, such as, direct band gap (3.37 eV), high exciton binding energy (60 meV), and good resistivity (10^{-3} to 10^{5} Ωcm) is one amongst the widely explored functional metal oxide semiconductor [6, 7]. High surface area composite hetero-structures based on zinc oxide and carbon nanotubes (CNTs) exhibit unique electrical properties that are related to the presence of a p–n heterojunction. Their electric conductivity can be influenced by the surrounding atmosphere. Therefore, these structures present a substantial potential as new gas sensing materials [8]. In order to study these hetero-systems, thin films of ZnO have been deposited by atomic layer of surface, a surface-gas phase process based on sequential and self-limiting surface reactions. A fine control of the morphology and thickness of the deposited films can be achieved by this technique [9]. In view of gas sensor applications, great interest is devoted on SnO_2, TiO_2, ZnO semiconductor layers with a thickness in the order of the Debye length [10–12]. More recently have shown a portable electronic nose based on hybrid CNT-SnO_2 gas sensors [13]. It was shown that doping of CNT improved the sensitivity of hybrid gas sensors, while quantity of CNT had a direct effect on the selectivity to volatile organic compounds like methanol and ethanol [14, 15], but didn't show selectivity to a particular gas. In 2011 Dai et al., reported SnO_2/MWCNTs nanocomposites exhibiting highly sensitive H_2S sensing at

B. C. Yadav
balchandra_yadav@rediffmail.com

[1] Nanomaterials and Sensor Research Laboratory, Department of Applied Physics, School for Physical Sciences, Babasaheb Bhimrao Ambedkar University, Lucknow, U.P., India

Published online: 07 October 2016

A review Report on Nanostructured Ferrites as Liquefied Petroleum Gas Sensor

Satyendra Singh[1], B.C. Yadav[2]*, Monika Singh[2] and Richa Kothari[3]

[1]Department of Physics, University of Allahabad, Allahabad 211002, U.P., India
[2]Department of Applied Physics, Babasaheb Bhimrao Ambedkar University, Lucknow-226025, U.P., India
[3]Department of Environmental Science, Babasaheb Bhimrao Ambedkar University, Lucknow-226025, U.P., India
*(*E-mail - balchandra_yadav@rediffmail.com*)

Abstract

The present review paper reports the synthesis methods, status, prospects for further development, and sensing applications of spinel ferrites. It introduces the inspiration of the nanostructured ferrites as gas sensors. It also explains the types of gas sensors, sensing mechanism and requirement of liquefied petroleum gas sensor.

Keywords: *nanomaterials, ferrites; microstructure; LPG sensor; sensitivity.*

1. Introduction

1.1 Nanomaterials and Nanotechnology

In the recent years, a new branch of research has raised up, broadly referred as "nanotechnology". The term nanotechnology is used to describe the creation and exploitation of materials with structural features in between those of atoms and bulk materials, with at least one dimension in the nanometer range i.e. within 1-100 nm [1-3]. Such type of materials are known as nanomaterials. Nanotechnology allows the extensive understanding of the unusual physical and chemical properties characterizing the matter at the nanometer scale revealing the way to the use of nanomaterials in a wide variety of applications involving materials science, engineering, physics, chemistry and biology [4-8]. An aspect of nanotechnology is vastly increased the ratio of surface area to volume present in many nanostructured materials which makes possibly new quantum mechanical effects, for example the "quantum size effect" where the electronic properties of solids are altered with great reductions in the particle size. This effect does not come into play by going from macro to micro dimensions. However, it becomes pronounced when the nanometer scale has reached. Broadly speaking, nanotechnology is the synthesis and applications of ideas from science and engineering towards the understanding and production of novel materials and devices. These products generally make use of physical properties associated with small scales.

As mentioned above, materials reduced to the nanoscale can suddenly show very different properties compared to what they exhibit on a macroscale, enabling unique applications. For instance, opaque substances become transparent (copper); inert materials attain catalytic properties (platinum); stable materials turn combustible (aluminum); solids turn into liquids at room temperature (gold); insulators become conductors (silicon). Materials such as gold, which is chemically inert at normal scales, can serve as a strong chemical catalyst at nanoscale. Over the past decade, nanomaterials have been the subject of enormous interest. These materials, notable for their extremely small feature size, have the potential for wide-ranging industrial, biomedical, and electronic applications [9-12].

1.2 Fabrication of Nanostructured Materials

Suitable control of the properties of nanometer-scale structures can lead to new science as well as new products, devices, and technologies [13-14]. In recent years, the most effective industry methods to fabricate nanostructures are top-down strategies [15-16]. Based on photolithography, the top-down technology challenges the physical limits of microelectronics miniaturization with the